

## PDF hosted at the Radboud Repository of the Radboud University Nijmegen

The following full text is a publisher's version.

For additional information about this publication click this link.

<http://hdl.handle.net/2066/92732>

Please be advised that this information was generated on 2017-12-06 and may be subject to change.

# **The second $\text{Ca}^{2+}$ -binding domain of the $\text{Na}^+/\text{Ca}^{2+}$ -exchanger**

## ***A biophysical study***

Een wetenschappelijke proeve op het gebied van de  
Natuurwetenschappen, Wiskunde en Informatica

### **Proefschrift**

ter verkrijging van de graad van doctor  
aan de Radboud Universiteit Nijmegen  
op gezag van de rector magnificus, prof. mr. S.C.J.J. Kortmann,  
volgens besluit van het college van decanen  
in het openbaar te verdedigen op dinsdag 10 april 2012  
om 13:30 uur precies door

### **Vincent Breukels**

geboren op 19 november 1982  
te Rotterdam

Promotor:

prof. dr. Geerten W. Vuister

Manuscriptcommissie:

prof. dr. Gert Vriend

prof. dr. Marcellus Ubbink (Leiden University)

dr. Hans A. Heus

The second  $\text{Ca}^{2+}$ -binding domain of the  $\text{Na}^+/\text{Ca}^{2+}$ -exchanger

A biophysical study

Vincent Breukels

ISBN: 978-94-6191-206-0

Printed by Ipskamp Drukkers

# Table of Contents

List of abbreviations	4
Chapter 1. Introduction <i>The Na<sup>+</sup>/Ca<sup>2+</sup>-exchanger</i>	5
Chapter 2. <i>Overview on the use of NMR to examine protein structure</i>	15
Chapter 3. <i>Binding of calcium is sensed structurally and dynamically throughout the second calcium-binding domain of the sodium/calcium exchanger</i>	71
Chapter 4. <i>The second Ca<sup>2+</sup>-binding domain of NCX1 binds Mg<sup>2+</sup> with high affinity</i>	95
Chapter 5. <i>Solution structure of the second Ca<sup>2+</sup>-binding domain of the B variant of the third isoform of the Na<sup>+</sup>/Ca<sup>2+</sup>-exchanger</i>	121
Chapter 6. Discussion <i>Structural and dynamic aspects of Ca<sup>2+</sup> and Mg<sup>2+</sup> binding of the regulatory domains of the sodium-calcium exchanger</i>	135
Chapter 7. References	145
Chapter 8. Summary	161
Chapter 9. Samenvatting	165
Chapter 10. Epilogue	169

## List of abbreviations

ATP	Adenosine-5'-TriPhosphate
BMRB	Biological Magnetic Resonance dataBank
CAX	cation/anion exchanger
CBD	Ca <sup>2+</sup> -binding domain
CCX	Ca <sup>2+</sup> /cation exchanger
CD	Circular Dichroism
CING	Common Interface for NMR structure Generation
CLD	$\alpha$ -Catenin Like Domain
CSA	Chemical Shift Anisotropy
CSP	Chemical Shift Perturbation
DSS	Dimethyl-Silpentane-Sulfonate
EDTA	EthyleneDiamineTetraAcetic acid
FID	Free Induction Decay
HEPES	4-(2-HydroxyEthyl)-1-PiperazineEthaneSulfonic acid
HSQC	Heteronuclear Single Quantum Coherence
ITC	Isothermal Titration Calorimetry
IUPAC	International Union of Pure and Applied Chemistry
KD	Dissociation Constant
kDa	KiloDalton
NCKX	K <sup>+</sup> -dependent Na <sup>+</sup> /Ca <sup>2+</sup> -exchanger
NCX	Na <sup>+</sup> /Ca <sup>2+</sup> -exchanger
NMR	Nuclear Magnetic Resonance
NOE	Nuclear Overhauser Effect
NOESY	Nuclear Overhauser Effect Spectroscopy
OD600	Optical Density at 600 nm
PDB	Protein DataBank
PFG	Pulsed Field Gradient
PIP2	Phosphatidylinositol 4,5-bisPhosphate
PMCA	Plasma Membrane Ca <sup>2+</sup> -ATPase
ppm	Parts Per Million
PRE	Paramagnetic Relaxation Enhancement
r.m.s.	Root Mean Square
r.m.s.d.	Root Mean Square Deviation
RDC	Residual Dipolar Coupling
RF	Radio-Frequency
S/N	Signal-to-Noise
SDS-PAGE	Sodium Dodecyl Sulfate PolyAcrylamide Gel Electrophoresis
SERCA	Sarco/Endoplasmic Reticulum Ca <sup>2+</sup> -ATPase
SR	Sarcoplasmic Reticulum
TCEP	Tris(2-CarboxyEthyl)Phosphine
TMS	TetraMethylSilane
TOCSY	Total Correlation Spectroscopy
Tris	Tris(hydroxymethyl)aminomethane
TRPC	Transient Receptor Potential Cation channel

# 1

## **Introduction**

*The Na<sup>+</sup>/Ca<sup>2+</sup>-exchanger*

## Introduction

### *Calcium*

The discovery of the calcium ion ( $\text{Ca}^{2+}$ ) as a signaling agent was purely coincidental. In a series of experiments using isolated frog heart, Ringer determined the influence of different constituents on heart contractility by replacing blood with a saline solution (Ringer, 1882). The experiments showed that both sodium ( $\text{Na}^+$ ) and potassium ( $\text{K}^+$ ) are essential for contraction. However, Ringer realized that the solutions were prepared from London's tap water, containing 38 parts per million of  $\text{Ca}^{2+}$  (Ringer, 1883). In a second series of experiments using saline solution prepared from distilled water, the heartbeats quickly diminished. Contraction could only be restored by the addition of  $\text{Ca}^{2+}$  to the solution and Ringer thereby showed for the first time the role of  $\text{Ca}^{2+}$  as a carrier of signals.

Nowadays  $\text{Ca}^{2+}$  is considered one of the most important cellular messengers (Carafoli, 2002). It not only triggers fast responses such as muscle contraction or exocytosis, but also mediates processes on a much slower time scale such as cell proliferation or gene transcription (Berridge *et al.*, 2003). This versatile role for  $\text{Ca}^{2+}$  is achieved through the interaction with many different proteins. Different  $\text{Ca}^{2+}$  binding motifs exist in proteins and the most common motif is the helix-loop-helix or EF-hand motif, which is present in hundreds of different proteins (Clapham, 2007). Other  $\text{Ca}^{2+}$  binding motifs, such as the Calx- $\beta$  motif can be structurally very different. However, they share one characteristic: binding of  $\text{Ca}^{2+}$  leads to conformational or electrostatic changes in the protein, which alters its function and triggers a specific cellular response.

Regulation of the  $\text{Ca}^{2+}$ -dependent processes demands an accurate control of intracellular  $\text{Ca}^{2+}$  concentration. Various types of  $\text{Ca}^{2+}$ -channels (*e.g.* voltage-operated  $\text{Ca}^{2+}$ -channels or store-operated  $\text{Ca}^{2+}$ -channels, Parekh and Putney, 2005) mediate  $\text{Ca}^{2+}$  entry into the cytosol either from the extracellular environment or internal  $\text{Ca}^{2+}$  stores like the sarcoplasmic reticulum (SR).  $\text{Ca}^{2+}$  entry is usually not directly translated into a cellular action but first processed by  $\text{Ca}^{2+}$ -sensor proteins (Fedrizzi *et al.*, 2008). For example, in cardiomyocytes  $\text{Ca}^{2+}$  binds to troponin, which enables myosin-actin contraction through ATP hydrolysis (Solaro and Rarick, 1998). To allow for muscle relaxation and to maintain  $\text{Ca}^{2+}$  homeostasis, the  $\text{Ca}^{2+}$  needs to be removed from the cytosol.  $\text{Ca}^{2+}$  is either sequestered into the cellular stores or expelled into the extracellular environment. This removal requires energy, because the intracellular  $\text{Ca}^{2+}$  concentration is very low compared to the extracellular concentration,  $\sim 200$  nM and  $\sim 1$  mM, respectively (Clapham, 2007). For this purpose the cell is equipped with ATPases and exchangers. The sarcoendoplasmic

reticulum Ca<sup>2+</sup>-ATPase (SERCA) and the plasma membrane Ca<sup>2+</sup>-ATPase (PMCA) hydrolyze ATP (Guerini *et al.*, 2005). The SERCA pump extrudes Ca<sup>2+</sup> into the SR, whereas the PMCA removes Ca<sup>2+</sup> from the cell. In contrast to pumps, exchangers do not consume ATP. Instead, Ca<sup>2+</sup>-exchangers utilize the energy stored in the gradient of other cations to transport Ca<sup>2+</sup> out of the cytosol.

### *The Na<sup>+</sup>/Ca<sup>2+</sup>-exchanger*

The best-studied Ca<sup>2+</sup>-exchanger in mammals is the Na<sup>+</sup>/Ca<sup>2+</sup>-exchanger (NCX) (Lytton, 2007). The first report of Na<sup>+</sup>/Ca<sup>2+</sup> exchange as a transport mechanism for Ca<sup>2+</sup> across the plasma membrane was published more than 40 years ago by two independent groups. Reuter and Seitz showed that Ca<sup>2+</sup> efflux of mammalian heart muscle was Na<sup>+</sup>-dependent (Reuter and Seitz, 1968) and at the same time Baker *et al.* obtained similar results using giant squid axons (Baker *et al.*, 1969). Na<sup>+</sup>/Ca<sup>2+</sup> exchange was almost immediately recognized as a general mechanism to remove Ca<sup>2+</sup> from the cytoplasm, whereas the PMCA mediated transport, discovered approximately at the same time, was mainly considered a special feature of red blood cells (Herchuelz, 2007). In fact, the PMCA and NCX work co-operatively to maintain homeostasis. The PMCAs have a high Ca<sup>2+</sup> affinity required to maintain low internal Ca<sup>2+</sup> concentration, whereas NCXs have a lower Ca<sup>2+</sup> affinity but much higher transport capacity required to rapidly restore low Ca<sup>2+</sup> levels after Ca<sup>2+</sup> influx (Clapham, 2007).

Na<sup>+</sup>/Ca<sup>2+</sup> exchange is the dominant Ca<sup>2+</sup> efflux mechanism across the plasma membrane in heart and neurons (Egger and Niggli, 1999). The Ca<sup>2+</sup> influx in these cell-types is high and needs to be balanced by Ca<sup>2+</sup> efflux through NCX activity. In a variety of diseases the Ca<sup>2+</sup> fluxes are impaired and exchanger activity is altered. For example, in chronic hypertension NCX activity is up-regulated, which eventually leads to heart failure (Menick *et al.*, 2007). Similarly, prolonged NCX activity is the major cause of cardiac ischaemia reperfusion injury (Murphy *et al.*, 1999). Controlled modulation of NCX activity could be beneficial and therefore the NCX is considered a possible drug target in these diseases (Tóth *et al.*, 2009). Better understanding of the function and regulation of the NCX will also increase our understanding in these diseases.

### *NCX function and regulation*

The exchanger transport cycle is completely reversible and whether the NCX exports Ca<sup>2+</sup> and imports Na<sup>+</sup> (so-called forward mode) or *vice versa* (reverse mode) de-



pendes solemnly on the electrochemical gradient. The transport is electrogenic (*i.e.* unequal amounts of charge exchanged)(Reeves and Sutko, 1980) and the exchange process can be measured by electrophysiology (Kimura *et al.*, 1986). Initial experiments measuring  $^{45}\text{Ca}^{2+}$  fluxes in cardiac membrane vesicles established that the NCX operates with a  $3\text{Na}^+ : 1\text{Ca}^{2+}$  stoichiometry (Reeves and Hale, 1984). The 3:1 stoichiometry is considered the dominant mode, however more recent findings suggest that a 4:1 ratio is possible too (Dong *et al.*, 2002; Fujioka *et al.*, 2000). In addition, the NCX can also catalyze  $\text{Na}^+/\text{Na}^+$  and  $\text{Ca}^{2+}/\text{Ca}^{2+}$  exchange (Reeves and Sutko, 1983; Slaughter *et al.*, 1983).

The development of electrophysiological recordings on giant excised patches greatly enhanced the understanding of NCX function and regulation. With this technique both the extracellular and the intracellular medium are experimentally controlled and varied (Hilgemann, 1989; 1990). This allowed determination of the activation and inactivation properties of NCX (cf. Figure 1.1). In two seminal papers Hilgemann *et al.* showed that the NCX is governed by at least two different activation and inactivation processes (Hilgemann *et al.*, 1992a; Hilgemann *et al.*, 1992b). To activate the exchanger, low levels of cytosolic  $\text{Ca}^{2+}$  are required. Activation occurs at a site distinct from the  $\text{Ca}^{2+}$ -transport sites. Activation is rapid and after the initial peak the exchange current decays exponentially to a steady state through a process called  $\text{Na}^+$  dependent inactivation. This  $\text{Na}^+$  dependent inactivation can be partially relieved by increased concentrations of  $\text{Ca}^{2+}$ .

The exchanger is regulated by more factors than  $\text{Na}^+$  and  $\text{Ca}^{2+}$  alone. These factors include  $\text{H}^+$ , MgATP and phosphatidylinositol bisphosphate ( $\text{PIP}_2$ )(Dipolo and Beauge, 2006).  $\text{H}^+$  influences the  $\text{Na}^+$ -dependent inactivation of NCX most likely through competition with the regulatory  $\text{Ca}^{2+}$  binding sites (Giladi *et al.*, 2010). ATP and  $\text{PIP}_2$  activate the exchanger (Condrescu *et al.*, 1995; Hilgemann and Ball, 1996). The interaction of

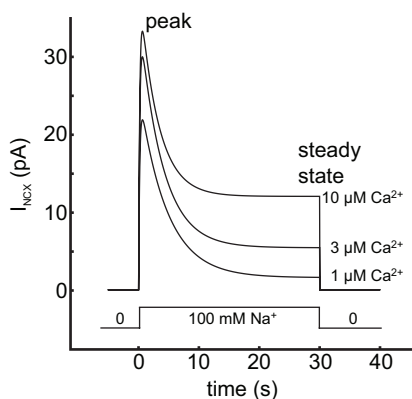


**Figure 1.1.** Simulated outward exchange currents (reverse mode) during the application of 100 mM  $\text{Na}^+$ . After the initial peak the exchange current decays to a steady state through a process called  $\text{Na}^+$ -dependent inactivation. The inactivation can be partially relieved by increased concentrations of cytosolic  $\text{Ca}^{2+}$ . Figure adapted from (Hilgemann *et al.*, 1992a).

ATP is indirect. ATP stimulates PIP<sub>2</sub> production and PIP<sub>2</sub> prevents Na<sup>+</sup>-dependent inactivation through a direct binding with NCX.

Besides ionic and metabolic regulators, many proteins are known to interact with NCX. Binding of the cytoplasmic tail of phospholemman with a cytosolic part of the NCX inhibits exchanger activity (Wang *et al.*, 2006). Interestingly, phospholemman also activates the Na<sup>+</sup>/K<sup>+</sup>-ATPase and the co-regulation of both the NCX and the Na<sup>+</sup>/K<sup>+</sup> ATPase might be to prevent high levels of intracellular Na<sup>+</sup>. More inhibitory proteins have been characterized *e.g.* calcineurin (Katanosaka *et al.*, 2005), 14-3-3 protein (Pulina *et al.*, 2006), and sorcin (Zamparelli *et al.*, 2010), but their physiological importance is not yet understood (Lytton, 2007). Lastly, ankyrin (Cunha *et al.*, 2007; Mohler *et al.*, 2005) and caveolin (Bossuyt *et al.*, 2002; Cavalli *et al.*, 2007a) associate with NCX, but they do not regulate the exchanger. Instead, they facilitate co-localization of NCX with the Na<sup>+</sup>/K<sup>+</sup>-ATPase (Lencesova *et al.*, 2004; Moore *et al.*, 1993), TRPC3 (Eder *et al.*, 2007; Goel *et al.*, 2007) and other membrane proteins. These complexes are important in confining Ca<sup>2+</sup> signals to a specific microdomain (Blaustein *et al.*, 2007).

### NCX family and topology

Since the molecular cloning of the first exchanger from canine sarcolemmal membrane (Nicoll *et al.*, 1990) two other genes of mammalian NCX have been identified; NCX2 (Li *et al.*, 1994) and NCX3 (Nicoll *et al.*, 1996b). NCX1 is found to be expressed in virtually every tissue, having at least seventeen different tissue specific splice variants, as opposed to NCX2 for which no splice variants have been found and NCX3 for which only three variants are known (Quednau *et al.*, 1996). NCX2 and 3 are mainly expressed in brain and skeletal muscle (Lee *et al.*, 1994; Nicoll *et al.*, 1996b). Together with a fourth isoform (NCX4)(Marshall *et al.*, 2005) only present in amphibian, fish and reptiles, they form the Na<sup>+</sup>/Ca<sup>2+</sup>-exchanger family, also referred to as solute carrier 8 (SLC8)(On *et al.*, 2008).

The NCX family is a member of a larger cation/Ca<sup>2+</sup> exchanger super-family (Cai and Lytton, 2004). The four other families of this super-family are the K<sup>+</sup>-dependent Na<sup>+</sup>/Ca<sup>2+</sup>-exchanger (NCKX) family, the YRGB family (named after the corresponding gene in *E. coli*), the cation/anion exchanger (CAX) family and the Ca<sup>2+</sup>/cation exchanger (CCX) family. The NCKX is present in mammals and is closely related to the NCX. NCKX exchanges four Na<sup>+</sup> ions for one K<sup>+</sup> and one Ca<sup>2+</sup> ion. Both the YRGB and CAX family catalyze H<sup>+</sup>/Ca<sup>2+</sup> exchange and are mainly present in yeast, plants and bacteria. In

the phylogenetic analysis the CCX family is a separate branch even though some members of the CCX family catalyze  $\text{Na}^+/\text{K}^+-\text{Ca}^{2+}$  exchange and are present in mammals (Cai and Lytton, 2004).

The exchangers share the presence of two highly conserved hydrophobic  $\alpha$ -repeat regions divided by a cytosolic loop (Schwarz and Benzer, 1997). Hydropathy analysis predicts nine transmembrane (TM) helices for NCX1 (cf. Figure 1.2) (Iwamoto *et al.*, 1999; Nicoll *et al.*, 1999a). A signal peptide resides at the N-terminus of the first TM helix and is thought to be necessary for the correct orientation of the protein in the membrane (Durkin *et al.*, 1991). Because this signal peptide is cleaved post translation, the N-terminus of the mature NCX resides at the extracellular side. The  $\alpha$ -repeat regions are formed by TM helices two, three, seven and eight and the connecting loops. In NCX1 these connecting loops form transmembrane re-entrant loops (cf. Figure 1.2) (Iwamoto *et al.*, 1999; Nicoll *et al.*, 1999a). Mutations of conserved residues within in the  $\alpha$ -repeat regions results in reduced or even loss of exchanger activity. This suggests that this part of the protein forms the ion translocation site (Iwamoto *et al.*, 2000; Nicoll *et al.*, 1996a; Ottolia *et al.*, 2005).

The large cytosolic loop between TM helix five and six is crucial for the correct regulation of the exchanger. Removal of this loop by chemotrypsin treatment abolishes all regulation and renders a constitutively active exchanger (Hilgemann, 1990). The loop starts with a 20-residue long exchanger inhibitory peptide (XIP) and further contains a domain tentatively named  $\alpha$ -catenin like domain (CLD) and two  $\text{Ca}^{2+}$ -binding domains (CBD1 and CBD2, cf. Figure 1.2). Application of exogenous XIP inhibits the exchanger (Li *et al.*, 1991), possibly through the binding with CBD2 (Maack *et al.*, 2005). Endogenous XIP

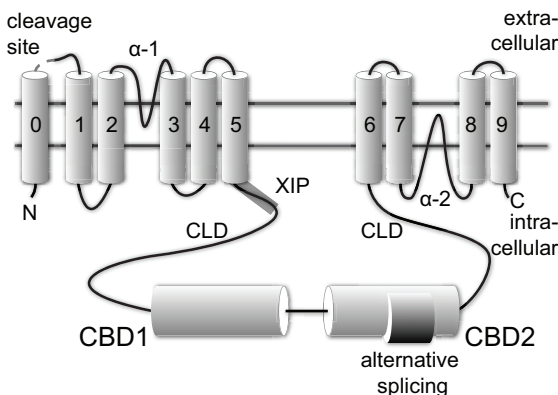


**Figure 1.2.** Membrane topology of the  $\text{Na}^+/\text{Ca}^{2+}$ -exchanger. A signal peptide resides at the N-terminus and is cleaved off, therefore the N-terminus of the mature exchanger resides at the extracellular side. The  $\alpha$ -repeat region is formed by transmembrane helices 2, 3, 7 and 8 together with the membrane re-entrant loops. The  $\alpha$ -repeat regions are thought to form the ion translocation site. The large cytosolic loop contains the exchanger inhibitory peptide region, the  $\alpha$ -catenin like domain and the two  $\text{Ca}^{2+}$ -binding domains.

is thought to be involved in PIP<sub>2</sub> regulation and Na<sup>+</sup> dependent inactivation (He *et al.*, 2000; Matsuoka *et al.*, 1997). Mutations in the endogenous XIP region remove the Na<sup>+</sup> dependent inactivation process. The CLD is modeled to have a structural similarity with  $\alpha$ -catenin (Hilge *et al.*, 2006). The role of CLD in the NCX is unknown, possibly the CLD forms the binding site of some of the regulatory proteins.

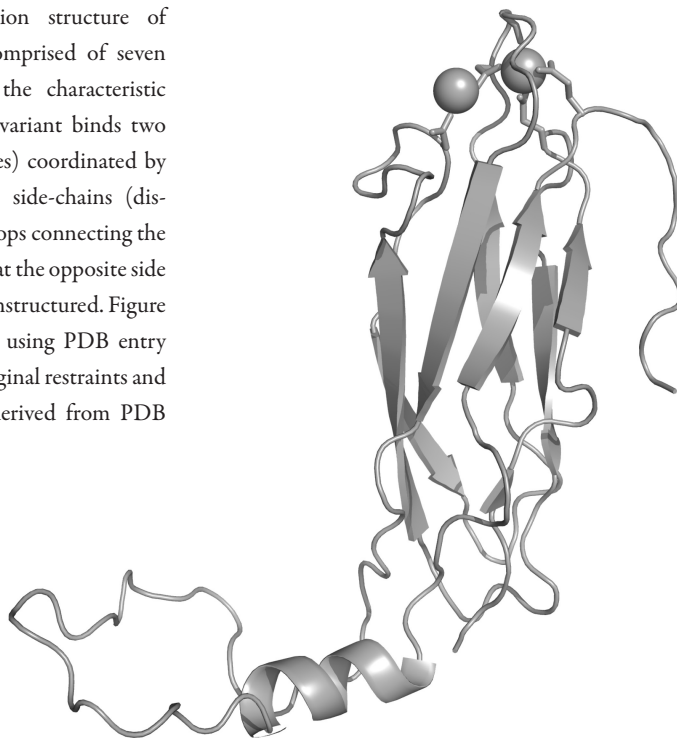
### *The Ca<sup>2+</sup>-binding domains*

The cytosolic loop holds two Ca<sup>2+</sup>-binding domains (CBD1 and CBD2). Binding of Ca<sup>2+</sup> to these allosteric Ca<sup>2+</sup> binding sites activates the exchanger. CBD1 binds Ca<sup>2+</sup> with highest affinity and is considered the primary Ca<sup>2+</sup> sensor (Hilge *et al.*, 2006). However, the more interesting domain is CBD2, because the region of alternative splicing of the NCX resides in CBD2. In NCX1 the alternative splicing comprises six exons labeled A to F. Exons A and B are mutually exclusive, whereas the C to F exons can be combined freely (Kofuji *et al.*, 1994; Quednau *et al.*, 1997). Alternative splicing does not occur in NCX2 whereas the three variants of NCX3 are AC, B and BC (Quednau *et al.*, 1997). The CBD2 variants have different responses to cytosolic Na<sup>+</sup> and Ca<sup>2+</sup> concentrations. For example, variants of NCX1-CBD2 containing exon A, but not exon B are able to overcome Na<sup>+</sup> dependent inactivation at elevated Ca<sup>2+</sup> concentration (Hurtado *et al.*, 2006). Importantly, the variants have distinct tissue specificity and this suggest that NCX activity is carefully tuned to cell-specific Ca<sup>2+</sup> needs.

To date, CBD1 and CBD2 are the only domains of the exchanger that have been structurally characterized (Besserer *et al.*, 2007; Hilge *et al.*, 2006; Hilge *et al.*, 2009; Nicoll *et al.*, 2006; Wu *et al.*, 2009; Wu *et al.*, 2010). Figure 1.3 shows the solution structure of NCX1-CBD2-AD. Both CBD1 and CBD2 display the Calx- $\beta$  motif comprised of seven  $\beta$ -strands. The strands form two  $\beta$ -sheets packed together as a  $\beta$ -sandwich. The Ca<sup>2+</sup> binding pocket is formed by distal loops connecting the  $\beta$ -strands. CBD1 has four Ca<sup>2+</sup> binding sites irrespective of the isoform (Hilge *et al.*, 2009). The conserved aspartic and glutamic acid residues coordinate the Ca<sup>2+</sup>, forming mainly polydentate interactions with two or even three Ca<sup>2+</sup> ions (Nicoll *et al.*, 2006). In contrast, the residue types at the coordinating positions in CBD2 vary between the splice variants and isoforms. As a consequence the number of Ca<sup>2+</sup>-binding sites varies between zero and three.

The Ca<sup>2+</sup> binding events at the CBDs need to be relayed to the ion translocation site in the membrane to activate the exchanger. To understand this mechanism, a model of the intact exchanger is required. In an initial model, CBD1 is packed together with

**Figure 1.3.** The solution structure of NCX1-CBD2-AD is comprised of seven  $\beta$ -strands and displays the characteristic Calx- $\beta$  fold. This splice variant binds two  $\text{Ca}^{2+}$  (displayed as spheres) coordinated by aspartate and glutamate side-chains (displayed as sticks) in the loops connecting the  $\beta$ -strands. The large loop at the opposite side of the domain is largely unstructured. Figure was created with Pymol using PDB entry 2FWU (refined using original restraints and the  $\text{Ca}^{2+}$  coordination derived from PDB entry 1QVM)



CBD2 in anti-parallel fashion. In this model the  $\text{Ca}^{2+}$  binding site of CBD1 points into the cytoplasm, away from the membrane (Hilge *et al.*, 2006). However, recent reports contradict this anti-parallel orientation. Instead, CBD1 with CBD2 form an elongated, rather flexible structure (Hilge *et al.*, 2009; Salinas *et al.*, 2011; Wu *et al.*, 2011). Binding of  $\text{Ca}^{2+}$  restricts the inter-domain flexibility and it is postulated that these changes could be part of allosteric  $\text{Ca}^{2+}$  regulation (Salinas *et al.*, 2011). Unfortunately, a structural view on the transfer of the  $\text{Ca}^{2+}$  binding events in CBD12 towards the ion transport sites near the membrane is still lacking.

I have studied the  $\text{Ca}^{2+}$ -binding domains in great detail with the aim to understand the processes involved in the  $\text{Ca}^{2+}$  regulation of the NCX. I have determined the structural and dynamical rearrangements of NCX1-CBD2 upon  $\text{Ca}^{2+}$  binding, investigated the role of  $\text{Mg}^{2+}$  in this domain, elucidated the structure of NCX3-CBD2-B and described the differences in  $\text{Ca}^{2+}$  binding between the different CBD variants from a structural perspective. This thesis, which is outlined in more detail below, is the result of these studies.

## Outline of this thesis

This chapter presents an introduction in Ca<sup>2+</sup> signaling and the role of the NCX in Ca<sup>2+</sup> homeostasis. It describes the general features of NCX function and regulation and indicates the importance of the Ca<sup>2+</sup>-binding domains. In the subsequent chapters of this thesis a detailed analysis of the CBDs is presented using Nuclear Magnetic Resonance (NMR) and other biophysical techniques. **Chapter 2** gives a general introduction of NMR as a tool to study proteins. **Chapter 3** describes the structural and dynamical effects of Ca<sup>2+</sup> binding to CBD2 and the results are compared with structures of splice variants and other Ca<sup>2+</sup>-binding proteins.

Divalent cations, such as Mg<sup>2+</sup>, compete with Ca<sup>2+</sup> for the Ca<sup>2+</sup> binding sites. The Mg<sup>2+</sup> concentration inside the cell is approximately a thousand times higher than the intracellular Ca<sup>2+</sup> concentration. Therefore, functional Ca<sup>2+</sup> sensors must have binding sites highly specific for Ca<sup>2+</sup>. **Chapter 4** shows that only one of the two binding sites of NCX1-CBD2-AD is specific for Ca<sup>2+</sup>. Mg<sup>2+</sup> always occupies the other binding site and the Mg<sup>2+</sup>-bound NCX1-CBD2-AD is structurally more stable and has an altered Ca<sup>2+</sup> affinity for the remaining binding site than apo NCX1-CBD2-AD.

A solution structure of NCX3-CBD2-B in the Ca<sup>2+</sup> bound form is presented in **Chapter 5**. This is the first structure of a domain of NCX3. The structure is highly homologous to NCX1-CBD2-AD. The new structure shows that the overall fold of CBD2, including the  $\beta$ -bulges and the  $\alpha$ -helix, are conserved between the different NCX isoforms. The orientation of the  $\alpha$ -helix with respect to the  $\beta$ -sandwich is determined for the first time using residual dipolar coupling measurements. The relevance of this orientation in the full-length exchanger is discussed.

The Calx- $\beta$  motif is compared to other motifs of the immunoglobulin fold in **Chapter 6**. A structural explanation is given for the distinct Ca<sup>2+</sup> binding properties of the different CBD variants and a gives a short outlook on NCX research. Finally, **Chapter 7** presents an overall summary of this thesis.



# 2

## *Overview on the use of NMR to examine protein structure*

Vincent Breukels, Albert Konijnenberg, Sanne M. Nabuurs, Jurgen F.  
Doreleijers, Nadezda V. Kovalevskaya and Geerten W. Vuister

*Curr. Protoc. Protein Sci.* (2011) **64**: 17.5.1-17.5.44



## Introduction

Nuclear Magnetic Resonance (NMR) is a versatile and important tool in biomolecular science, capable of yielding information on structure, dynamics and interactions. NMR spectroscopy and X-ray crystallography are the only techniques that can determine biomolecular structures at atomic resolution. In contrast to X-ray crystallography, liquid-state high-resolution NMR has the ability to study biomolecules in a more natural aqueous environment and does not require crystallization. Nowadays protein structures up to 15 kDa can be solved routinely. Solid-state NMR is emerging as an additional technique for biomolecular structure determination and appears particularly promising for membrane-bound proteins (Andronesi *et al.*, 2005; McDermott, 2009) and fibrous protein aggregates (Tycko, 2006). NMR also allows investigation of time-dependent processes such as enzyme kinetics (Henzler-Wildman *et al.*, 2007) and intramolecular dynamics (Ishima and Torchia, 2000; Palmer, 2004). A major limiting factor of NMR spectroscopy is its inherent low sensitivity and increasing technical complexity with increasing molecular size. As a consequence, the size of proteins that can be studied to atomic resolution is limited. With the development of stronger magnets, better probes and new spectroscopic techniques, proteins folds can be determined up to 80 kDa (Tugarinov *et al.*, 2005). For larger complexes NMR can still be useful yielding low-resolution structural data, especially in conjunction with other techniques such as small angle X-ray scattering (Grishaev *et al.*, 2005; Grishaev *et al.*, 2008; Sunnerhagen *et al.*, 1996; Wang *et al.*, 2009).

Protein structure determination by high-resolution NMR started with advent of two-dimensional spectroscopy in the early 1980s. The early procedures relied completely on homonuclear  $^1\text{H}$  NMR experiments and are nowadays referred to as the “Wüthrich approach” (Wüthrich, 2003). This approach allowed the determination of proteins up to  $\sim 12$  kDa. With the introduction of protein isotope labeling and heteronuclear spectroscopy in the early 1990s, the size of amenable proteins increased to about 30 kDa. The advances in heteronuclear spectroscopy have been so successful that the Wüthrich approach has become less common, even for proteins smaller than 12 kDa.

This chapter aims to give an overview of the current practices in the field of biomolecular high-resolution NMR spectroscopy. It describes the basic principles of NMR spectroscopy and gives an overview of all steps involved in protein structure determination. The focus is solely on soluble proteins and solution state heteronuclear NMR spectroscopy. The Wüthrich approach has been carefully reviewed in other texts (Cavanagh *et al.*, 2007). For recent advances on membrane proteins, nucleic acids and the use of solid-state NMR

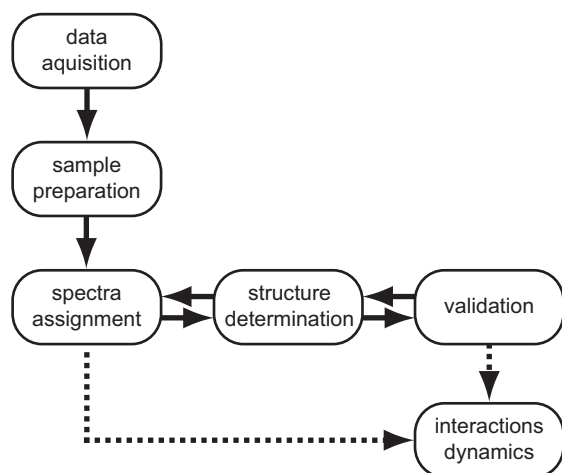


**Figure 2.1.** Flow chart of a NMR protein structure determination project. Such a project comprises several distinct steps, although some of these steps require iteration. A structure is not always required, as NMR is also a useful tool to study interactions or protein dynamics.

in protein science we refer to other texts (Flinders and Dieckmann, 2006; Kim *et al.*, 2009; McDermott, 2009). The intention of chapter 2 of this thesis is to show how NMR spectroscopy provides for a tool in protein science. It is not a “how-to” guide and we refer to more elaborate texts for the interested reader (Cavanagh *et al.*, 2007; Levitt, 2008).

### Outline

Any protein structure determination process contains several steps; it starts with obtaining a suitable sample, then acquiring data and spectral assignment and finally the structure determination and validation (cf. Figure 2.1). This review describes all these steps, starting with the basic physical principles behind the NMR and some of the most commonly measured and observed phenomena such as chemical shift, scalar and residual coupling and the nuclear Overhauser effect. Then in somewhat more detail, the process of spectral assignment and structure elucidation is explained. Furthermore, the use of NMR to study protein ligand interaction, protein dynamics or protein folding is described. Finally, a short outlook is given on how NMR will continue to play a vital role in protein science.

## Basic principles

NMR is based on a quantum mechanical property called spin angular momentum, or in short, spin. Spin is characterized by the quantum number  $I$  and is an intrinsic property of all particles including nuclei.  $I$  can adopt the values of  $0$ ,  $\frac{1}{2}$ ,  $1$ ,  $1\frac{1}{2}$ ,  $2$ , ..., depending on the nucleus type (cf. Table 2.1). In a simplistic, but incorrect classical-based view,

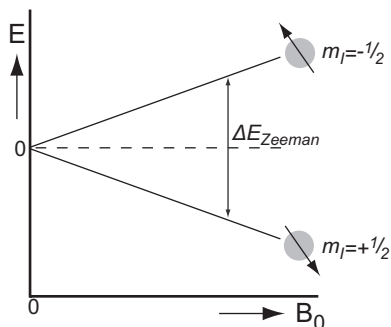


**Figure 2.2.** The energies of a nucleus with  $I = \frac{1}{2}$  and  $\gamma > 0$  as function of the magnetic field strength,  $B_0$ . The energy difference between the two states  $m_I = \frac{1}{2}$  and  $-\frac{1}{2}$  is called the Zeeman splitting and forms the basis of NMR spectroscopy.

spin can be considered as an electric charge revolving around its axis, thereby generating a small magnetic moment, with size  $m_I \hbar$ . As a consequence, any nucleus with  $I > 0$  will interact with an external magnetic field, just like a compass needle. Quantum mechanics dictates that the z-component of the magnetic moment cannot take any arbitrary orientation, but only discrete values, *i.e.*  $m_I = -I, -I+1, \dots, I-1, I$ . Consequently, a nucleus in an external magnetic field will have a different energy level depending on  $m_I$  (cf. Figure 2.2):

$$E = -m_I \hbar \gamma B_0 \quad (2.1)$$

with  $\hbar$  the reduced Planck's constant,  $B_0$  the static external magnetic field which is chosen along the z-axis and  $\gamma$  the gyromagnetic ratio of the nucleus. Table 2.1 shows the  $\gamma$  of several NMR nuclei commonly used in biomolecular NMR.

For practical purposes, nuclei with  $I = \frac{1}{2}$  are mostly used in solution-state protein NMR. In that case, only the  $m_I = +\frac{1}{2}, -\frac{1}{2}$  values exist and their corresponding energy states are usually denoted as  $\alpha$  and  $\beta$ , respectively. Depending on the sign of  $\gamma$ , either the  $\alpha$  or  $\beta$  state is the lowest in energy; however, for practical purposes this is not important as it is the energy difference that is actually observed in NMR. This energy difference is called the Zeeman splitting (cf. Figure 2.2) and is given by:

$$\Delta E = |E_{m_I=1/2} - E_{m_I=-1/2}| = \left| \left( \frac{1}{2} \hbar \gamma B_0 \right) - \left( -\frac{1}{2} \hbar \gamma B_0 \right) \right| = |\hbar \gamma B_0| \quad (2.2)$$

Differences in energy levels form the basis for any form of spectroscopy, including NMR. In contrast to optical spectroscopy, regular absorption or emission spectroscopy is not feasible for NMR. Instead, a slightly different approach, called pulsed Fourier transform NMR, is used. The Boltzmann distribution for thermal equilibrium dictates that in

**Table 2.1.** The gyromagnetic ratio ( $\gamma$ ) and frequency ratio ( $\Xi$ ) of several common spin-1/2 biomolecular NMR nuclei (Harris et al., 2002).

Isotope	$\gamma$ ( $10^7 \text{ rad s}^{-1} \text{ T}^{-1}$ )	$\Xi$	Natural abundance (%)
$^1\text{H}$	26.752 212 8	1.000 000 00	99.99
$^{13}\text{C}$	6.728 284	0.251 450 20	1.07
$^{15}\text{N}$	-2.712 618 04	0.101 367 67	0.37
$^{19}\text{F}$	25.181 48	0.940 940 11	100
$^{31}\text{P}$	10.839 4	0.404 807 42	100

a bulk sample, slightly more spins will be in the lower energy state than in the higher state. This results in a bulk magnetization in the direction of the static magnetic field, that behaves according to the laws of classical physics. Radio-frequency (RF) pulses are used to manipulate this magnetization; the RF pulses can rotate the magnetization, usually by  $90^\circ$  or  $180^\circ$ , although any arbitrary angle is possible. After a  $90^\circ$  RF-pulse, the initial magnetization will no longer point along the static magnetic field, but perpendicular to it and the magnetization is said to be “transverse”. Once such transverse magnetization has been created, it will start rotating around the static magnetic field in a motion called precession. This precession induces a small current in a receiver coil, which is the actual time-dependent signal recorded by the spectrometer and is called the free induction decay (FID)

As an example, Figure 2.3 shows the hypothetical FID of a single spin. The single cosine modulated signal decays slowly to zero by a process called transverse relaxation (cf. Relaxation). The frequency of the signal modulation is determined by the precession of the magnetization and thus depends on the energy difference given by Equation 2.2. Rewriting, using Planck’s law yields the frequency of the precession:

$$\omega = \Delta E/\hbar = \gamma B_0 \quad (2.3A)$$

$$\nu_L = \gamma B_0/2\pi \quad (2.3B)$$

Equation 2.3 shows that the observed frequency of the measured signal, called the Larmor frequency,  $\nu_L$ , is linearly proportional to the applied magnetic field and the gyromagnetic ratio,  $\gamma$ . To obtain the frequency encoded by the time-dependency of the signal of the FID, a mathematical procedure called (fast) Fourier Transformation (FFT) is performed. The resulting spectrum of the hypothetical FID is shown in Figure 2.3B.

Based on Equation 2.3, NMR would not be very useful technique, as only a single Larmor frequency would be observed for each type of spin nucleus in the sample.

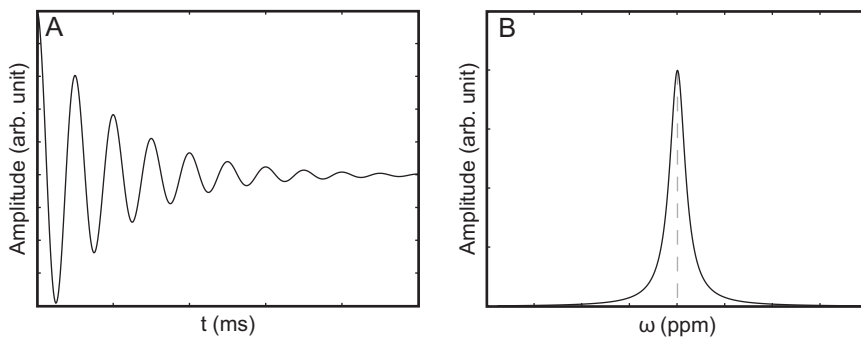


**Figure 2.3.** A simulated FID (A) showing a slowly decaying cosine signal. After Fourier transformation a single cosine would result in a single peak in the frequency spectrum (B). The rate of decay determines the width of the peak, a slow decay results in a sharp peak.

Fortunately, this is not true and what is actually observed are a multitude of frequencies, each corresponding to individual spins in the sample (Figure 2.4). The small variations in the Larmor frequencies,  $\nu_L$ , for the individual spins originate from the influence of the bond forming electrons in a molecule. These electrons induce small additional local magnetic fields that slightly differ at the respective nuclei. This effect is called shielding and can either augment or diminish the main static magnetic field. The effect is anisotropic (*i.e.* depends on the orientation with respect to the magnetic field), but in solution the molecules are tumbling rapidly, continuously re-orientating and averaging out any anisotropy. Thus, the shielding effect will cause the observed resonance frequency of any nucleus to deviate slightly from the predicted frequency of Equation 2.3:

$$\omega = \gamma(1 - \sigma)B_0 \quad (2.4A)$$

$$\nu = \gamma(1 - \sigma)B_0/2\pi \quad (2.4B)$$

with  $\sigma$  the isotropic shielding factor,  $\omega$  the resonance frequency in  $\text{rad s}^{-1}$  and  $\nu$  the resonance frequency in Hz.

Figure 2.4 displays the  $^1\text{H}$  spectrum of ubiquitin. Even a protein as small as ubiquitin already contains several hundred protons and each of these have their own resonance frequency and should be visible in the  $^1\text{H}$  spectrum. Unfortunately, the  $^1\text{H}$  spectrum is too crowded and the number of peaks that can be uniquely distinguished is in practice far less than the number of protons present in the sample. This unfortunate spectral crowding leads to loss in information and the solution to this problem lies in multi-dimensional spectroscopy.

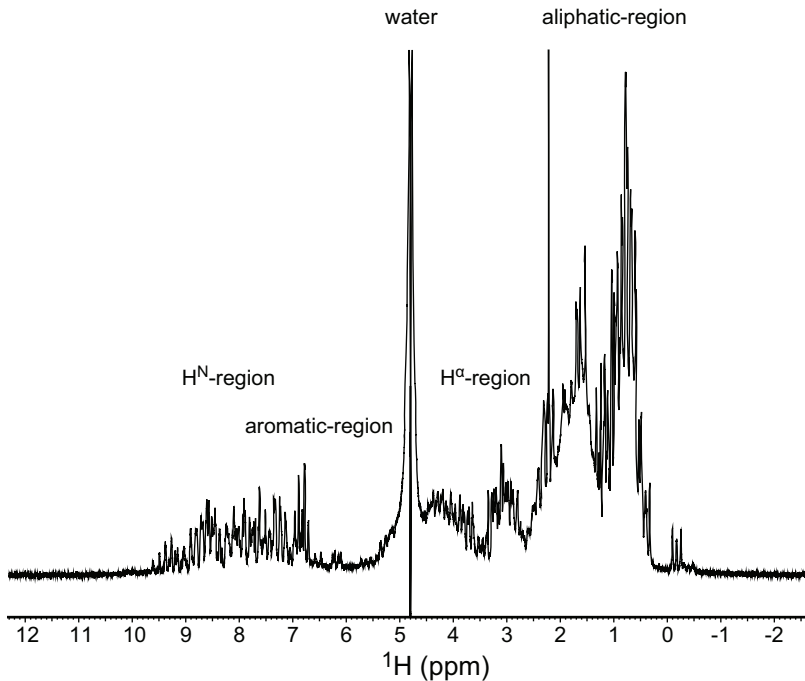


**Figure 2.4.** 1D proton spectrum of ubiquitin (8.5 kDa) in 95/5% v/v H<sub>2</sub>O/D<sub>2</sub>O solution. The strong H<sub>2</sub>O resonance is suppressed by pre-irradiation. Characteristic regions for different nuclei are indicated. Even for the typical example of the small, well-folded ubiquitin, the 1D-spectrum shows considerable peak overlap.

## Multi-dimensional Spectroscopy

In NMR spectroscopy multi-dimensional spectra are used to resolve the problem of spectral crowding and establish correlations between interacting nuclei (Jeener, 1971). Any interaction that allows for the transfer of magnetization from one nucleus to another can be exploited in multi-dimensional (nD) NMR spectroscopy. The concept is first explained for two dimensions (2D), but is easily generalized to multiple dimensions (3D, 4D, nD).

The general scheme of any 2D-NMR experiment is shown in Figure 2.5A and consists of four consecutive periods; preparation, evolution ( $t_1$ ), transfer or mixing and acquisition ( $t_2$ ). After the preparation period, transverse magnetization has been generated which is allowed to evolve during the evolution period  $t_1$ , precessing at a frequency specific for that particular nucleus (cf. Equation 2.4). The magnetization is then transferred to another nucleus during the transfer or mixing period. Subsequently, during the acquisition

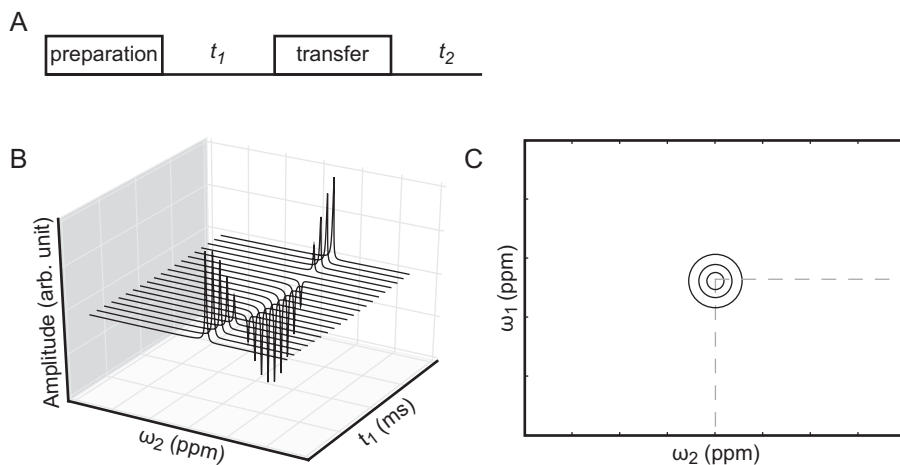


**Figure 2.5.** 2D NMR spectroscopy. (A) A schematic representation of a 2D-NMR experiment, comprising preparation, evolution ( $t_1$ ), transfer or mixing and detection ( $t_2$ ) periods. In a 2D-NMR experiment, the indirect dimension ( $t_1$ ) is recorded as a series of successive FIDs with incremented  $t_1$  values. (B) Fourier transformation of all FIDs along the  $t_2$ -axis, yields peaks that are modulated in intensity or phase along the  $t_1$  axis. (C) A second Fourier-transformation along  $t_1$  yields the 2D-NMR spectrum, displayed as a 2D contour plot where the contour lines connect points of equal amplitude.

period the signal originating from the second nucleus is encoded in the FID. The conventional 2D data are obtained from a series of  $n$  successive 1D measurements, in which the  $t_1$  value is incremented by a fixed amount. The resulting series of  $n$  FIDs are stored in a two-dimensional data matrix,  $S(t_1, t_2)$ . The rows in this data matrix represent data collected for a fixed  $t_1$  value and different  $t_2$  values, while the columns represent data collected for a fixed  $t_2$  value and varying  $t_1$  values. Fourier transformation of  $S(t_1, t_2)$  with respect to  $t_2$  gives  $n$  one-dimensional spectra that are modulated in intensity or phase along  $t_1$  (cf. Figure 2.5B). A second Fourier transformation, now with respect to  $t_1$ , will result in a 2D spectrum with two independent frequency axes. The conventional way to display such a spectrum is a contour plot that joins points of equal amplitude (Figure 2.5C).

### $^{15}\text{N}$ -HSQC

The advantage of multi-dimensional spectra over their 1D counterpart becomes obvious from examining Figure 2.6, which displays two  $^{15}\text{N}$ -HSQC spectra of *Azotobacter vinelandii* flavodoxine, a 179 residue long protein ( $\sim 20$  kDa). HSQC denotes Heteronuclear Single Quantum Coherence and the  $^{15}\text{N}$  prefix identifies that in this experiment the proton nucleus is correlated with the nitrogen nucleus. The magnetization

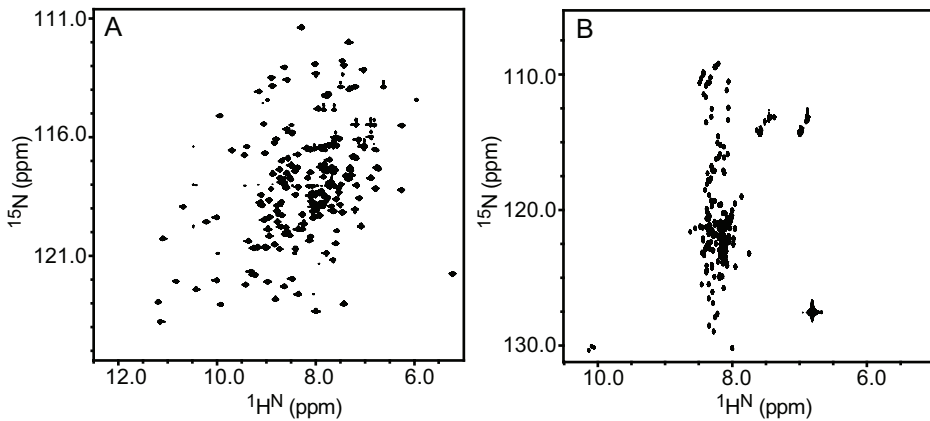


**Figure 2.6.** Contour plots of the  $^{15}\text{N}$ -HSQC spectra of *azotobacter vinelandii* flavodoxine (20 kDa) (A). Folded protein. Each peak in the spectrum corresponds to one amide of flavodoxine (B). The same protein, completely unfolded in 6M GuHCl. Note the clear differences in dispersion of the cross-peaks between the spectra of the folded and unfolded protein.

transfer in the HSQC experiment employs the scalar coupling: a through-bond interaction between nuclei that can correlate covalently connected nuclei up to four bonds away (see Scalar coupling for a more thorough explanation).

Compared to the 1D-spectrum (cf. Figure 2.4), the  $^{15}\text{N}$ -HSQC spectrum allows for a clear identification of individual peaks. For proteins each residue, with the exception of proline, contains at least one amide (*i.e.* the amide in the peptide bond) that gives rise to one peak in the  $^{15}\text{N}$ -HSQC spectrum. This feature renders the  $^{15}\text{N}$ -HSQC spectrum the “fingerprint” of a protein and the typical starting point of every new project. It can be used to identify if a protein is well folded and suitable for structural studies. As an example, Figure 2.6B shows the  $^{15}\text{N}$ -HSQC spectrum of the same protein as in Figure 2.6A, but in the presence of 6M guanidine hydrochloride (GuHCl). The spectrum of this fully unfolded protein is distinctly different, with almost all peaks clustering between 8.0 and 8.5  $^1\text{H}^{\text{N}}$  ppm. Another sign of malformed protein is the number of observed peaks. If this is far below the expected number based on the primary sequence of the protein, then this is a good indication of either dynamic processes such as chemical exchange or effects of protein aggregation. Furthermore, by measuring several  $^{15}\text{N}$ -HSQC spectra over a prolonged time, protein stability can be tested. Changes between the spectra indicate time dependent changes of the protein, such as degradation and aggregation. The  $^{15}\text{N}$ -HSQC experiment also forms the basis of many other three- and four-dimensional experiments.

The next step, after these first preliminary tests, is to identify which amide gives rise to which peak in the spectrum. This process is called assignment and requires addition-



al experiments (explained in detail in the Resonance assignment section). After assigning all amides, the  $^{15}\text{N}$ -HSQC experiment becomes a simple, yet powerful tool in many more applications such as the study of protein ligand interactions, protein folding and in slightly adjusted form, the study of backbone dynamics.

## Instrumentation

### *Magnet*

Biomolecular NMR requires a strong magnet in order to achieve sufficient resolution and sensitivity. For NMR, the strength of a magnet is usually given in mega-Hertz (MHz) rather than Tesla (T), referring to the Larmor frequency of protons at the particular field strength. To achieve reasonable resolution and sensitivity, most spectrometers used for protein NMR operate between 400 MHz (9.4 T) and 900 MHz (21.1 T). To obtain such high fields, magnets for biomolecular NMR are constructed using a solenoid of superconducting wire. This wire, usually made from an NbTi or NbSn<sub>3</sub> alloy, has zero electrical resistance at very low temperatures (2.2-4.2 K) (SchneiderMuntau, 1997). Once an electric current is applied through the solenoid, it will generate a constant magnetic field. As result of the superconductivity, the current in the solenoid will flow without resistance as long as it is kept below the critical temperature. Therefore, the magnet is immersed in liquid helium (4.2K) or even cooled liquid helium (2.2K). To prevent excessive boiling off of expensive helium, the helium bath and magnet are insulated by a cryostat and immersed in a bath of liquid nitrogen, a much cheaper cryogenic liquid.

Although the field strength of NMR magnets has steadily increased since the early '70s, the end of this development is almost reached. The highest field that can be produced with niobium alloys is  $\sim 1\text{GHz}$ , because the alloy cannot carry more electrical current required for even higher field strengths. Hence, the development of magnets for NMR is an active field of research and the focus lies on using different materials or combinations of low-temperature coils with high-temperature coils or external current coils (Kiyoshi *et al.*, 2006; Yanagisawa *et al.*, 2008).

### *Shims*

Every spectrometer contains additional so-called cryo- and room-temperature shimcoils. Shimming is the process of homogenizing the static magnetic field. The homogeneity determines the lineshape and intensity of the observed signals and influences the frequency resolution of the spectra. The insert, probe and the different samples and tubes

all have different magnetic susceptibilities that distort the magnetic field in slightly different ways, and the cryo- and room-temperature shim coils assure the required homogeneity of the magnetic field. Cryoshims of superconducting material are electrically charged during the installation of the magnet and exert a constant effect. In contrast, the current inside the room-temperature shimcoils can be controlled by the spectroscopist, thereby influencing the local magnetic field homogeneity on a sample-to-sample basis. As the geometry of each coil is different, they generate different local changes and the complete set is used to homogenize the magnetic field.

Because shimming is very tedious, most spectrometers utilize an (semi)-automated gradient shimming procedure. In this method, which found its origin in magnetic resonance imaging, special coils located inside the probe are used to temporarily introduce a small magnetic pulsed field gradient (PFG). The gradient allows mapping of both the magnetic field homogeneity, as well as mapping of the magnetic profiles generated by the various shimcoils. Together this allows for calculation of the optimal shim values that yield the most homogeneous magnetic field (Van Zijl *et al.*, 1994).

### Probe

To perform any form of spectroscopy, it is necessary for electromagnetic radiation to interact with the sample. The probe contains all the electric circuitry required to excite the nuclear spins and detect the NMR signal. It also contains the aforementioned PFG coil and the equipment to regulate the sample temperature. The probe is placed inside the magnet, such that the sample resides in the region of the highest and most homogenous part of the magnetic field. The resonance coil transmits the RF-pulses that perturb the magnetization and detects the NMR-signals. To obtain highest the signal-to-noise (S/N) ratio, the resonance coil needs to be tuned exactly at the correct Larmor-frequency (Equation 2.3). As most protein NMR experiments require the recording of multiple nuclei types in one experiment (*eg.*  $^1\text{H}$ ,  $^{15}\text{N}$ ,  $^{13}\text{C}$ ), most probes are equipped with several different coils, each specifically tuned to one or two nuclei. To further increase the S/N-ratio, some probes (called cryo- or cold-probes) are cooled using cold (20-25 K) helium gas. Cooling the probe reduces the thermal noise inside the coil and other electric components, thereby increasing the S/N-ratio. The gain in sensitivity is not completely free of cost, as it puts some restrictions on sample conditions (*cf.* Sample Preparation).

Finally, every probe used for biomolecular NMR contains a temperature control unit. Cooled gas flows through a heating unit and subsequently along the sample. It allows

control of the set temperature of the sample in the magnet.

### Console

The probe is too small to contain the amplifiers, frequency synthesizers and modulator boards that are used to detect the signals and transmit the RF-pulses. These are placed inside the so-called console, which also houses the power units, the controls for the room temperature shimcoils and temperature regulation, as well as a number of logic boards that control the NMR spectrometer. A probe suitable for biomolecular NMR typically contains multiple resonance coils; likewise, the console has multiple amplifiers and frequency generators too, each specifically tuned for the appropriate frequency. The console is connected to a computer from which the spectroscopist can operate the console and thus in essence all processes inside the probe. Finally, the console contains an analog-digital converter (ADC) that digitizes all acquired data, which are subsequently stored on the computer hard-disk.

### Software

The raw data, the FID, are time domain data and need to be processed into frequency spectra by means of Fourier transformation. Generally, the computer connected to the console also contains software from the console's manufacturer that can process the data. However, in biomolecular NMR, it is very common to use different, more specialized software packages. In addition to processing the raw experimental data, the resulting spectra need to be analyzed. A vast number of software packages are available and Table 2.2 shows a list of NMR software that is regularly used or has been used for multidimensional NMR. In academic institutions the packages Azara (Bouchner, 1993) and NMRPipe (Delaglio *et al.*, 1995) are nowadays the most common for the processing of the raw data and NMRViewJ and the collaborative computing project for NMR spectroscopy (CCPN) program Analysis for the analysis and assignment of the spectra (Vranken *et al.*, 2005). Due to the large number of software tools, almost an equal number of data formats have been developed and this leads to considerable difficulties converting from one program to the other. To overcome these issues, the CCPN provides for a framework that implements a common data format, linking existing NMR software and essentially creating a software pipeline that would streamline all steps starting from data-recording, analysis, up to structure calculation and validation (Vranken *et al.*, 2005).

**Table 2.2.** List of NMR of processing and displaying software packages.

Package	Processing	Display / Assignment	Operating system	Maintained	Free of use	Website
ANSIG	No	Yes	SGI	No	Acad. license	No maintained website
Azara	Yes	Yes	Linux, MacOS X	Yes	Acad. license	www.ccpn.ac.uk/ azara/
CCPN Analysis	No	Yes	Linux, MacOS X, Windows	Yes	Yes	www.ccpn.ac.uk/ ccpn
Felix	Yes	Yes	SGI, Linux, Windows	Yes	No	www.felixnmr. com/index
Gifa	Yes	Yes	Unix	No	Acad. license	www.cbs.cnrs.fr/ GIFA/
iNMR	Yes	Yes	MacOS X	Yes	No	www.inmr.net/
MNMR	Yes	No	SGI, Linux	No	Yes	www.crc.dk/ chem/mnmr/ intro
NMRPipe	Yes	Yes	Linux, MacOS X, Windows	Yes	Yes	spin.niddk.nih. gov/NMRPipe/
NMRViewJ	No	Yes	Linux, MacOS X, Windows	Yes	No	www.onemooon- scientific.com/ nmrview/install
Pronto /3D	No	Yes	SGI, Linux	Last update 2008	Yes	www.crc.dk/ chem/pronto/ welcome
Sparky	No	Yes	Linux, MacOS X, Windows	Last update 2008	Yes	www.cgl.ucsf.edu/ home/sparky/
Topspin	Bruker only	Yes	Linux, Windows	Yes	No	www.bruker- biospin.com/ topspin3
VNMRJ	Varian only	Display	Linux	Yes	No	www.varianinc. com
XEASY	No	Yes	SGI, Unix	No	No	No maintained website

## Sample Preparation

Obtaining a sufficiently large S/N-ratio is an ongoing struggle in NMR. Higher magnetic fields and more sensitive probes both increase the S/N-ratio. However, the most important factor for successful structure determination entails the needs for a high con-

centration sample that is soluble and stable over at least several days. Depending on the size of the protein (cf. Relaxation) a protein concentration of at least  $\sim 250 \mu\text{M}$  is necessary, although most studies are carried out at concentrations in the order of  $500 \mu\text{M}$ . To obtain such concentrations requires either the protein to be highly abundant in a specific cell-type or, more likely, overexpression in a host system or cell-free synthesis (Figure 2.7). The most common technique by far is overexpression in *E. coli*. It is advised to always start new expression trials with *E. coli*, because it is fast, cheap and easy to test multiple expression conditions (Graslund *et al.*, 2008).

### Solubility

Unfortunately, the insufficient solubility of proteins is often a bottleneck. Estimates show that 33-50% of all expressed non-membrane proteins are not soluble *in vitro* and circa 25-57% of the remaining soluble proteins precipitate at higher concentration (Golovanov *et al.*, 2004). To increase the solubility numerous different strategies have been deployed. For example, changing the exact N- and C-termini of the construct can alter the expression levels dramatically (Graslund *et al.*, 2008) and even specific point mutations have shown to increase the solubility (Ito and Wagner, 2004). In certain instances it is even possible to express the protein as bacterial inclusion bodies and subsequently denature, purify and refold the protein (Clark, 1998). However, all these strategies are protein specific, largely trial and error based and their successive results are difficult to translate to other proteins. Therefore, more general approaches are sought and much effort has been developed in so-called solubility-enhancement tags (SET; Figure 2.7B) (Zhou *et al.*, 2001). The tags are (small) proteins that are N- or C-terminally attached to the protein of interest. The idea originates from affinity tags such as maltose binding protein (diGuan *et al.*, 1988) or glutathione S-transferase (GST)(Smith and Johnson, 1988). It was observed that fusion proteins containing these tags showed an increased overexpression and solubility. After purification these tags are usually cleaved off due to their large size ( $\sim 30 \text{ kDa}$ ). However, without tag the protein of interest might precipitate again. As a result, smaller solubilizing tags that do not have to be cleaved, such as protein-G (GB1), are becoming more popular (Huth *et al.*, 1997; Zhou and Wagner, 2010). There are two potential drawbacks when using non-cleaved SETs: First, even small tags might influence the structure or function of the protein of interest and additional tests must be employed to exclude this possibility. Second, extra signals are observed in the NMR experiments as the SETs have the same isotopic labeling (*vide infra*) as the attached protein. However, the latter can be overcome

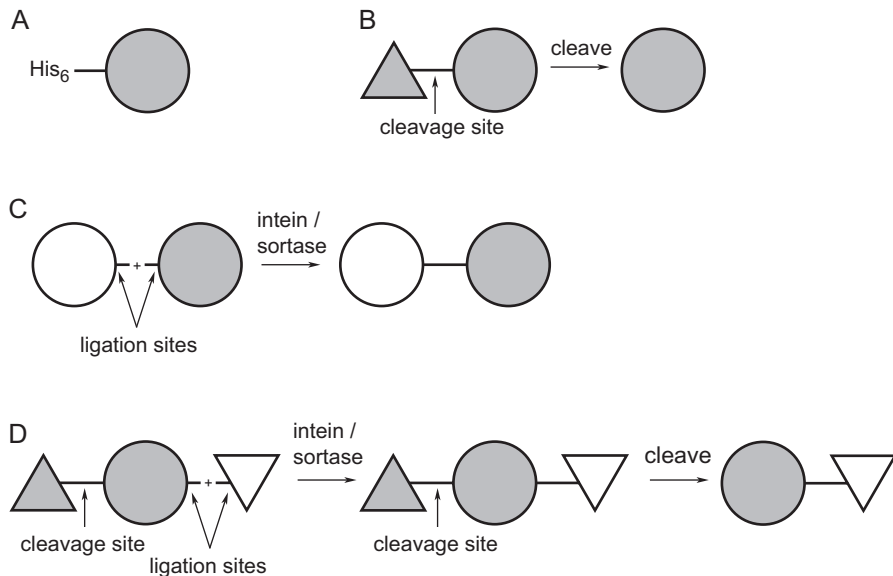


**Figure 2.7.** Schematic overview of labeling and solubilizing schemes. Protein domains of interest are indicated as circles, solubilizing or purification tags as triangles, grey color indicate isotopically labeled domain. Overexpression with (A) a  $\text{Ni}^{2+}$  affinity tag comprised of six histidines, (B) solubilizing / expression tag, (C) segmental labeling and (D) combined usage of solubility tags.

using a fusion protein with a cleavable tag at one terminus and a ligation site at the other (Figure 2.7D). Before cleavage, an NMR-invisible SET is attached to the fusion protein, using either sortase- or intein-based protein ligation. The NMR-visible tag can subsequently be cleaved off, while the NMR-invisible tag preserves solubility (Kobashigawa *et al.*, 2009; Züger and Iwai, 2005). A slightly different approach uses non-covalent protein-ligand binding instead of ligation. A very elegant example is the use of a small calmodulin binding peptide sequence. The peptide resides at the N- or C-terminus of the fusion protein and unlabeled calmodulin is then used as solubilizer (Durst *et al.*, 2008).

### Stability

Successful overexpression and purification still does not guarantee successful structure determination. Samples concentration needs to be in the 0.25 – 1.0 mM range, which usually requires some concentration step, *e.g.* by centrifugal filtration or freeze-drying. At these high concentrations the protein should not precipitate and must be stable for at least a few days and preferably a few weeks. Therefore, different buffer conditions such as pH, salts and additives usually have to be tested. Increasing salt concentrations

can prevent aggregate formation through electrostatic interaction (chaotropic salts) or increase protein stability (kosmotropic salts) (Bondos and Bicknell, 2003). Mild detergents, such as CHAPS, can prevent multimerization if the interaction is driven by hydrophobic interactions. The simultaneous addition of the charged amino acids L-arginine and L-glutamate also was shown to increase solubility (Golovanov *et al.*, 2004). When solvent accessible cysteines are present the addition of reducing agents such as dithiothreitol, tris(2-carboxyethyl)phosphine (TCEP) and  $\beta$ -mercaptoethanol prevents disulfide bond formation. Cryo-probes require extra consideration of the buffers used, as high salt concentrations increase the conductivity of the sample, which in turn results in decreased sensitivity. Fortunately, the conductivity is determined by both the concentration and the mobility of the ions and it is possible to choose salts that are most suitable for cryo probes (Kelly *et al.*, 2002).

Finding optimal conditions can be a lengthy process and it is crucial to have an assay for precipitation or aggregation. Different methods have been developed for the rapid screening of buffer conditions. Techniques originally developed for crystallography can be readily used for NMR, such as microdialysis cells (Bagby *et al.*, 1997) or microdroplets (Lepre and Moore, 1998). Both techniques screen the cell or droplet for precipitate by visual inspection under a microscope. More recently, a thermofluor-based method was proposed in which the thermal unfolding of a protein is monitored. Using a dye that becomes fluorescent upon binding to hydrophobic patches, thermal unfolding can be followed as it increases the number of accessible hydrophobic patches (Ericsson *et al.*, 2006). A high melting temperature is taken as an indication for a stable protein. The method can be performed in parallel for a large number of conditions using a commonly available 96-well plate real-time PCR machine, in which the thermal melting curves can be measured. As an

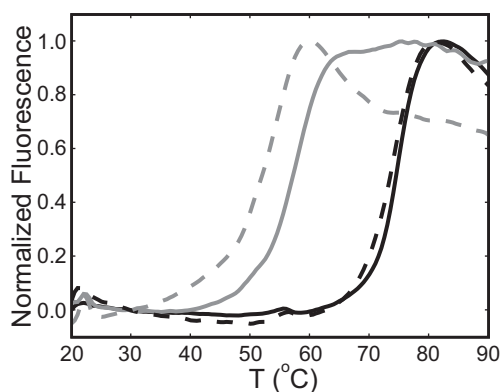


**Figure 2.8.** The thermal melting curves recorded for the second  $\text{Ca}^{2+}$  binding domain of the  $\text{Na}^+/\text{Ca}^{2+}$ -exchanger at 10 mM  $\text{CaCl}_2$  (black) or 10 mM EDTA (grey). Binding of  $\text{Ca}^{2+}$  increases the apparent melting temperature by 20 degrees. The addition of 100 mM NaCl (solid) has only an effect on the  $\text{Ca}^{2+}$  free form.

example, four thermofluor melting curves of the second  $\text{Ca}^{2+}$ -binding domain (CBD2) of the  $\text{Na}^+/\text{Ca}^{2+}$ -exchanger are shown in Figure 2.8. The addition of  $\text{Ca}^{2+}$ , an endogenous ligand, increases the apparent melting temperature of CBD2 by almost 20 °C. The addition of NaCl increases protein stability only in the  $\text{Ca}^{2+}$ -free form of CBD2.

A final test before engaging in a full structure determination is the  $^{15}\text{N}$ -HSQC measurement on a  $^{15}\text{N}$  labeled sample (*vide infra*). The resulting spectrum should reveal well dispersed peaks of equal intensity (cf. Figure 2.6A) and the number of peaks should match the number expected from the primary protein sequence. Low dispersion would indicate unfolded protein (cf. Figure 2.6B), whereas a too high number of peaks could indicate either degradation or conformational heterogeneity (Yee *et al.*, 2006). The  $^{15}\text{N}$ -HSQC spectrum also helps to identify peaks originating from the solubility or purification tags that have been attached to the protein. Lastly, a straightforward  $T_2$  experiment (cf. Relaxation, Figure 2.14) can be performed to test for multimerization. Short  $T_2$  values for individual peaks can indicate chemical exchange, whereas overall short  $T_2$  values are an indication for oligomers, such as dimer formation.

### High-throughput

In the late 1990's the foundation was laid for a systematic worldwide effort to determine the three-dimensional structures of proteins at atomic resolution (Terwilliger *et al.*, 2009). Rather than individual groups determining particular proteins, large initiatives or consortia were founded directed towards solving protein structures of whole genomes in an approach termed structural genomics. Over the last decade these consortia, such as the Protein Structure Initiative (American), SPINE (European) or RIKEN (Japanese), have solved 8,733 protein structures (September 15, 2010, <http://targetdb.pdb.org/>). The initiatives not only solved this large number of protein structures, but also generated new high-throughput, automated methods for cloning, expression and purifying protein samples. Furthermore, all these initiatives were committed to report the status of their targeted structures, which allowed for the first time to quantitatively determine the success rate of all these experimental steps. Analysis of these data clearly identified that purifying proteins and acquiring high concentration samples are the two major bottlenecks in protein structure determination (a success rate of ~30 and 35% respectively, Terwilliger *et al.*, 2009). More importantly to the individual researcher, these statistics have allowed new methods to estimate the probability of obtaining a suitable sample on the basis of the physical properties of the protein inferred from the amino acid sequence alone. This can help choosing



the optimal target from a set of similar proteins or identify other expression or purification methods in case of failure of either of these steps (Graslund *et al.*, 2008).

The structural genomics efforts have positively influenced the current practices in X-ray crystallography, for which automated methods on data collection and protein structure determination have been developed (Joachimiak, 2009). Unfortunately, the structural genomics effort on NMR has not achieved the same level of success (Billeter *et al.*, 2008). Although automated NMR methods have been developed and are continuously improved (cf. Automation), their usage is still rather uncommon in most NMR research laboratories and it is likely that human intervention and analysis will always prove to be necessary.

### *Isotopic labeling*

The type of isotopic labeling that is required for solution NMR structure determination depends on the size of the protein. The structure of proteins with a size smaller than 10 kDa can be solved using  $^1\text{H}$  spectra only and isotopic labeling is not absolutely required. It is however, advised to use isotope labeling to allow for application of the modern hetero-nuclear techniques that yield considerably better structures in less time. For larger proteins, isotopic labeling is absolutely necessary to implement multi-dimensional NMR experiments with sufficient sensitivity and to resolve the spectral overlap that occurs in  $^1\text{H}$  NMR spectra.

Growing the bacteria in minimal media containing  $^{15}\text{N}$  ammonium chloride or  $^{15}\text{N}$  ammonium sulphate and  $6\text{-}^{13}\text{C}$  glucose as the sole nitrogen and carbon sources, respectively, results in uniform  $^{15}\text{N}$  and  $^{13}\text{C}$  labeled proteins. When the molecular mass exceeds 25 kDa, deuterium labeling is also required in order to reduce the efficient  $^1\text{H}\text{-}^1\text{H}$  and  $^1\text{H}\text{-}^{13}\text{C}$  induced relaxation processes (e.g. dipolar relaxation *vide infra*). However, complete removal of all protons is undesirable, as there would be no  $^1\text{H}$  left to perform spectroscopy on. Therefore, a great variety of different isotope labeling schemes have been developed, all aimed at acquiring highly deuterated samples, while incorporating sufficient  $^1\text{H}$  to allow for the high sensitivity detection of this nucleus (see for two excellent reviews Gardner and Kay, 1998; Mittermaier and Kay, 2006).

The most straightforward technique for deuteration is random fractional deuteration, as first described by Lemaster and Richards (LeMaster and Richards, 1988) and subsequently used by many others (Nietlispach *et al.*, 1996; Zhou *et al.*, 1995). Bacteria are grown in minimal media containing around 85%  $\text{D}_2\text{O}$  and deuterated  $^{13}\text{C}$ -carbon sources. This results in deuteration levels of approximately 75% for non-exchangeable protons

whereas exchangeable protons, such as amides, become protonated as a result of the usage of protonated aqueous buffers.

The random deuteration of proteins results in more complex spectra, since the carbon chemical shift differs depending on the number of attached deuterium atoms. To alleviate this undesirable effect, other deuteration schemes were developed that yield better-defined labeling patterns. The simplest protocols involve growth in 100% D<sub>2</sub>O with a protonated carbon source (Lee *et al.*, 1997; Rosen *et al.*, 1996). This approach results in samples with highly deuterated C<sup>α</sup> and partially protonated methyl groups. The drawback of this technique is still the presence of different isotopomer compositions for the amino acid side chains. Each side-chain methyl group can contain zero, one, two or three deuteriums, causing peak doubling and unresolved line broadening (Rosen *et al.*, 1996; Shekhtman *et al.*, 2002). However, new optimized NMR techniques can alleviate these spectroscopic problems, increasing the feasibility of such samples (Otten *et al.*, 2010). Finally, the introduction of selective methyl group protonation strategies has become a prominent technique for high molecular mass proteins. Using deuterated glucose and α-ketoacid precursors it is feasible to obtain completely deuterated protein samples, with fully protonated methyl groups of either C<sup>δ</sup> of isoleucine residues (Gardner and Kay, 1997), C<sup>δ1/2</sup> of leucine or C<sup>γ1/2</sup> of valine residues (Goto *et al.*, 1999), C<sup>ε</sup> of methionine residues (Gelís *et al.*, 2007) or C<sup>β</sup> of alanine residues (Ayala *et al.*, 2009; Isaacson *et al.*, 2007). The main advantage is the very specific, almost completely controlled labeling scheme, where only a subset of the methyls is protonated.

In the stereo-array isotope labeling (SAIL) technique (Kainosho *et al.*, 2006) specifically deuterated proteins are produced through cell-free synthesis using synthetically produced, stereo-specifically deuterated amino acids as precursors. The SAIL method allows for the complete control of the labeling pattern of the protein. Unfortunately, the specific precursor amino acids are still very expensive and the technique has therefore not yet been widely applied.

### Segmental labeling

In segmental labeling only part of a protein is isotope labeled (Figure 2.7C). This is a completely different approach to reduce spectral complexity and can be especially useful for the study of interdomain interactions in multi-domain proteins (see for recent review Skrisovska *et al.*, 2010). These techniques are all based on ligation, either through native chemical ligation or expressed protein ligation. In the former, synthetically synthe-

sized peptides are ligated through the reaction of a C-terminal thioester and a N-terminal cysteine (Balambika *et al.*, 2007; Kochendoerfer *et al.*, 2004). However, this technique is limited by the possible length of synthesized peptides, which is approximately ~50 amino acids. In the expressed protein ligation technique, the segmental labeling is achieved through intein or sortase mediated ligation, in identical fashion as employed for the solubility tags (a step-by-step protocol is described by (Muona *et al.*, 2010), cf. Figure 2.7C).

## Chemical Shift

The observed resonance frequency is shown not only to be linearly dependent on the shielding constant, but also on the static magnetic field (cf. Equation 2.4). This causes the observed resonance frequency to be dependent on the experimental setup, which is very inconvenient as it makes tabulating impractical. Instead of frequency, it is the convention in NMR spectroscopy to use the unitless quantity chemical shift ( $\delta$ ) given in parts per million (ppm) and defined as:

$$\delta = \frac{\omega_0 - \omega_{ref}}{\omega_{ref}} \times 10^6 \quad (2.5)$$

in which  $\omega_0$  and  $\omega_{ref}$  denote the angular frequency of the signal of interest and reference compound, respectively. Equation 2.5 shows that the chemical shift in ppm is independent of the static magnetic field. The accepted  $^1\text{H}$  NMR reference is tetramethylsilane (TMS). Unfortunately, TMS is not soluble in aqueous solutions and the IUPAC recommendation for protein and nucleic acid NMR research is the use of the methyl  $^1\text{H}$  resonance of 2,2-dimethyl-2-silapentane-5-sulfonic acid (DSS;  $\delta = 0$ ) (Harris *et al.*, 2002). When even low concentrations of DSS are undesirable secondary reference compounds, including  $\text{H}_2\text{O}$ , can be used as well, as long as 0 ppm is kept at the theoretical (expected) zero of DSS. In practice, improper or neglect of this procedure has resulted in quite significant variations in the database of chemical shifts of biomolecules (Wishart *et al.*, 1995). For the other nuclei, such as  $^{13}\text{C}$  and  $^{15}\text{N}$ , reference compounds are not necessary, as the following relationship indirectly references these:

$$\nu_0^X = \Xi \nu_0^H \quad (2.6)$$

with  $\nu_0^X$  and  $\nu_0^H$  the absolute frequency of 0 ppm for the X nucleus and  $^1\text{H}$ , respectively and  $\Xi$  the relative frequency of the heteronucleus compared to  $^1\text{H}$ . Values of  $\Xi$  are listed

in Table 2.1.

Correctly referencing spectra is very important, as chemical shift databases are now a valuable tool in the process of structure determination (*vide infra*). In biomolecular NMR, quantitative NMR data such as chemical shifts are stored in the biological magnetic resonance databank (BMRB) (Ulrich *et al.*, 2008). It was estimated that more than 20% of the proteins in the BMRB are improperly referenced (Wang *et al.*, 2010). To increase the quality of these databases, several tools have been developed, such as CheckShift (Ginzinger *et al.*, 2009), LACS (Wang and Markley, 2009) and recently PANAV (Wang *et al.*, 2010) to correct referencing errors and the usage of such programs is strongly encouraged. Another approach has been the re-referencing of the almost complete BMRB database to aid the development of new chemical shift-based methods in NMR (Rieping and Vranken, 2010).

### *The structural information content of the chemical shift*

As the chemical shift depends on the local environment of the nucleus, it contains information on the local protein structure. This fact can be exploited in several ways. First of all, the specific chemical shift of the  $H^N$ , N,  $C^\alpha$  and  $C^\beta$  atoms can help identify the residue type. For example the  $^{13}C^\beta$  chemical shifts of Ser and Thr are characteristically high ( $\sim 64$  and  $\sim 70$  ppm, respectively), whereas the  $^{13}C^\alpha$  and  $^{15}N$  chemical shifts of Gly are very low ( $\sim 44$  and  $\sim 110$  ppm, respectively; cf. Figure 2.9).

Chemical shifts not only help identify the residue type, but also display sensitivity to the backbone torsion angles  $\phi/\psi$ . Especially, the  $H^\alpha$ ,  $C^\alpha$  and  $C^\beta$  chemical shifts are good reporters on local secondary structure and help identify secondary structure elements.  $C^\alpha$  chemical shifts are shifted downfield (to higher ppm) in  $\alpha$ -helices and upfield (to lower ppm values) in  $\beta$ -sheets. It is instructive to subtract the random coil value from the observed chemical shift, thus compensating for the amino-acid specific effects. The obtained value is called the secondary chemical shift and forms the basis of the well-known chemical shift index (CSI) (Wishart *et al.*, 1992), a method for indentifying secondary structure elements. A more local structure approach has been developed in the program TALOS (Cornilescu *et al.*, 1999) and its superior successor TALOS+ (Shen *et al.*, 2009), using a database of high-resolution protein structures with known chemical shifts. TALOS+ compares the observed backbone chemical shifts of triplets of adjacent residues to the database and uses the closest match to predict the  $\phi/\psi$  torsion angles of the unknown structure.

Chemical shifts are readily obtained, even for larger proteins and therefore much

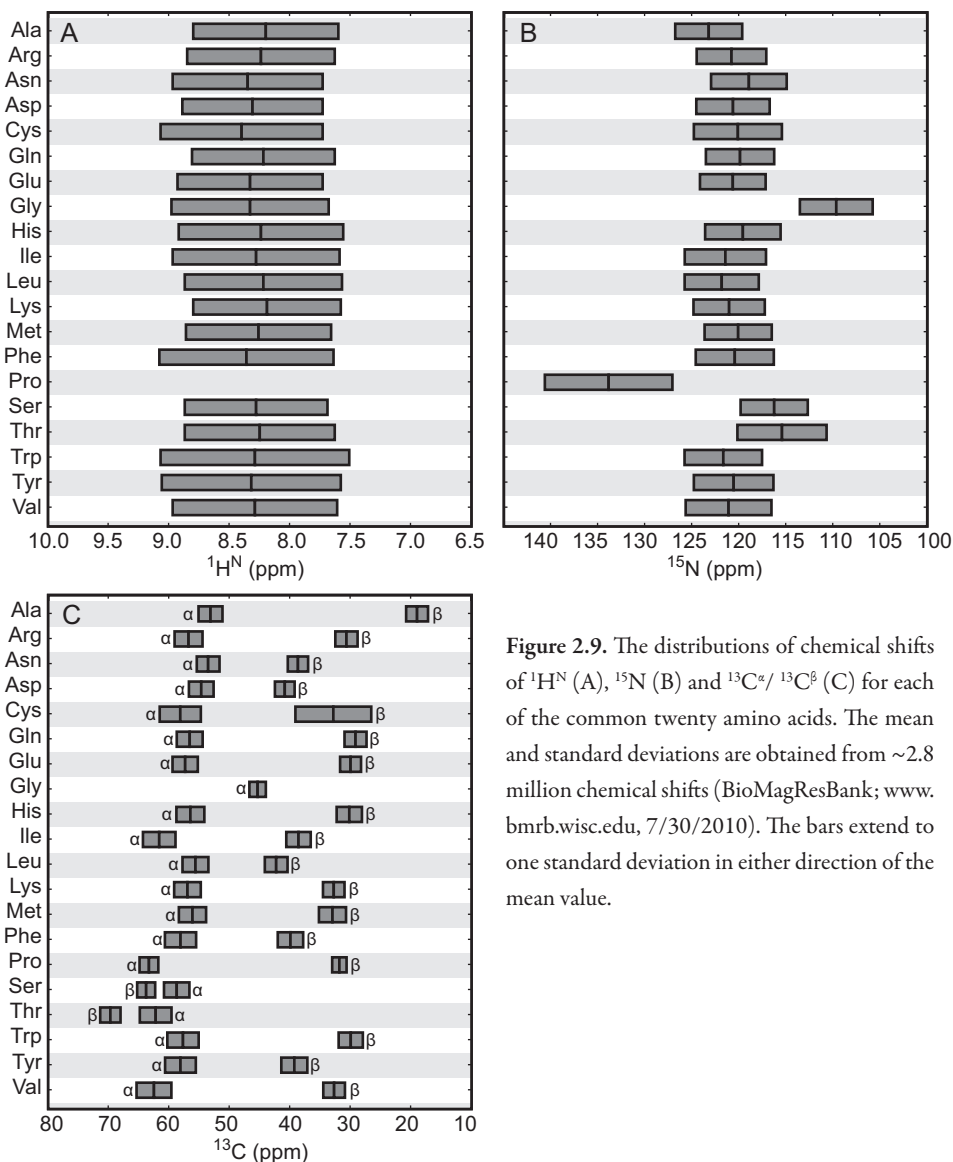


**Figure 2.9.** The distributions of chemical shifts of  $^1\text{H}^{\text{N}}$  (A),  $^{15}\text{N}$  (B) and  $^{13}\text{C}^{\alpha}/^{13}\text{C}^{\beta}$  (C) for each of the common twenty amino acids. The mean and standard deviations are obtained from  $\sim 2.8$  million chemical shifts (BioMagResBank; [www.bmrb.wisc.edu](http://www.bmrb.wisc.edu), 7/30/2010). The bars extend to one standard deviation in either direction of the mean value.

effort is directed towards obtaining the complete structure of a protein on the basis of chemical shifts alone. Although the backbone conformations are reasonably well predicted by programs such as CHESHIRE (Cavalli *et al.*, 2007b) and CS-ROSETTA (Shen *et al.*, 2008), the prediction of the side-chain conformation remains currently difficult due to the lack of accurate relationships between side-chain nuclei and conformation (Mulder and Filatov, 2010).

The reverse process, using a known structure to predict the chemical shift is

also possible. The two most commonly used programs are SHIFTX (Neal *et al.*, 2003) and SPARTA (Shen *et al.*, 2008). The approach of both programs is somewhat different. SHIFTX employs pre-calculated, empirically derived chemical shift hypersurfaces in combination with classical or semi-classical equations for ring current, electric field, hydrogen bond and solvent effects, whereas the SPARTA program uses a database approach similar to the one described for the TALOS programs. The performance of these programs is quite similar and predicts the backbone chemical shifts quite well (Mulder and Filatov, 2010).

## Scalar coupling, NOE and residual dipolar coupling

Equation 2.4 dictates that the observed frequency of a nuclear spin is proportional to the static magnetic field, the  $\gamma$  and the shielding factor. This equation, however, is not a complete description when other interacting spins are present. Nearby spins will interact with each other through scalar coupling, dipolar coupling and the nuclear Overhauser effect (NOE). All three interactions have important usage in NMR spectroscopy and a short theoretical description will be given.

### Scalar coupling

The  $J$ -coupling (or spin-spin coupling or scalar coupling) is a phenomenon of major practical importance. The spin state (*i.e.*  $\alpha$  or  $\beta$ ) of one nucleus can influence another nucleus through polarization of the electrons forming the chemical bonds between the interacting nuclei. The magnitude of the interaction between the two spins  $A$  and  $X$  is given by  ${}^nJ_{AX}$ , where  $A$  and  $X$  denote the two nuclei and  $n$  indicates the number of intervening bonds between  $A$  and  $X$ . Because the magnitude of  $J$  is independent of the static magnetic field strength, it is always expressed in Hz. Furthermore,  $J$  becomes smaller with increasing number of bonds and in biomolecules interactions with  $n > 3$  are typically not observed. A single  $J$ -coupling causes the splitting of a single resonance into two resonance lines that differ  ${}^nJ_{AX}$  Hz in frequency (Figure 2.10A).

The practical consequences of the  $J$ -coupling are threefold. First and most importantly, the  $J$ -coupling allows for the transfer of magnetization from one nucleus to the other, which forms the basis of multi-dimensional heteronuclear NMR. Thus, it allows multiple chemically connected nuclei to be spectroscopically connected as well. Introduction of  ${}^{15}\text{N}$  and  ${}^{13}\text{C}$  nuclei into the protein yields a network of spins connected by  ${}^1J$  interactions (cf. Figure 2.11), that greatly facilitates the spectral assignment (explained in Resonance Assignment). Second, active couplings during the measurement result in splitting of the

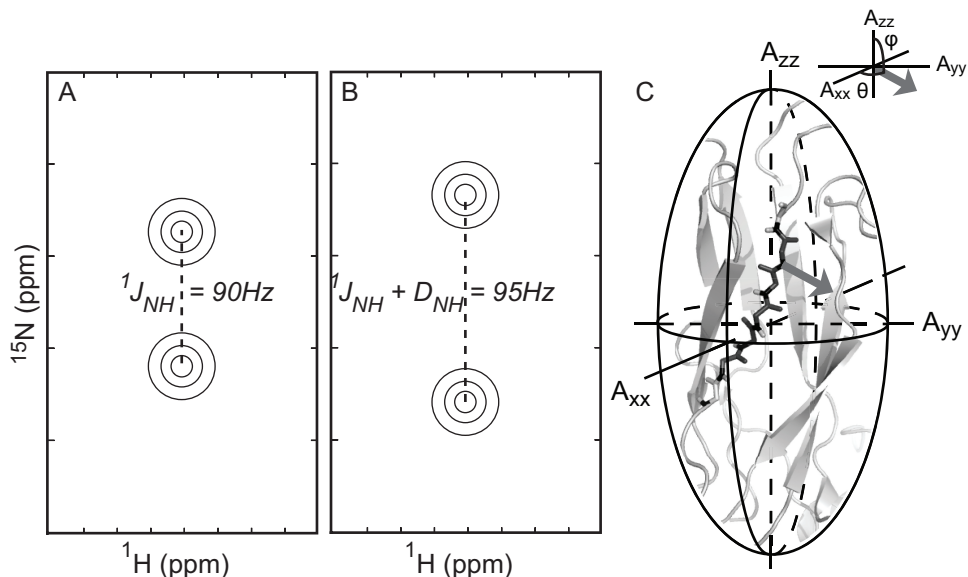


**Figure 2.10.** Schematic  $^{15}\text{N}$ -HSQC spectra showing the effects of  $J$ -coupling and residual dipolar coupling. (A) An active  $^1J_{\text{NH}}$ -coupling results in splitting with a separation  $^1J_{\text{NH}}$  (approximately 90 Hz). (B) The same spectrum in an alignment medium would result in a smaller ( $D_{\text{NH}} < 0$ ) or larger ( $D_{\text{NH}} > 0$ ) splitting as a result of the residual dipolar coupling (C). The size of  $D_{\text{NH}}$  depends on the orientation of the amide bond vector in the molecular frame

resonance signals into multiplets. For biomolecular spectra this is often undesired as the splitting results in more spectral crowding. Fortunately, specific spectroscopic techniques can often be used to prevent the occurrence of such multiplets. Finally, the magnitude of  $^nJ_{\text{AX}}$  depends also on the local structural conformation. Especially the  $^3J$  coupling constants can be used to derive structural restraints, as their magnitude correlates with the intervening dihedral angle,  $\vartheta$ , associated with the three bonds connecting the two nuclei. This correlation can be expressed through a so-called Karplus equation (Karplus, 1959; 1963):

$$^3J = A \cos^2(\theta) + B \cos(\theta) + C \quad (2.7)$$

where  $A$ ,  $B$ , and  $C$  denote empirically derived parameters for the specific  $^3J$  coupling and  $\vartheta$  denotes the dihedral angle.

The interpretation of  $^3J$ -coupling data into a structural restraint is unfortunately not straightforward. Equation 2.7 shows that a single  $^3J$  value translates to multiple possible  $\vartheta$  values. Furthermore, the estimated error on  $\vartheta$  can be quite large even though the coupling is measured very accurately, because the values  $A$ ,  $B$  and  $C$  are also empirically

determined. The error on  $\vartheta$  is even larger in situations where the protein adopts multiple conformations and it is impossible to differentiate between  $J$ -values of a static intermediate dihedral angle or the dynamic average of two extreme angles. To account for these problems, several different couplings related to the same dihedral angle need to be measured to resolve most ambiguity and reduce the experimental error. There are numerous experiments to measure both homo- and heteronuclear  $^1J$ ,  $^2J$  and  $^3J$  couplings and we refer the reader to more extensive texts on the subject (Cavanagh *et al.*, 2007; Vuister *et al.*, 1999).

### *The nuclear Overhauser effect*

Distance restraints derived from the Nuclear Overhauser effect (NOE) cross-peaks still constitute the primary source of structural information for solving a protein structure. The NOE originates from the dipolar interaction between nuclei. Each nucleus with  $I > 0$  acts as a small magnetic dipole that will interact with other nearby magnetic dipoles. This mutual interaction is called dipole-dipole interaction. In liquids the dipole-dipole interactions are usually not observed, because the interaction is angular dependent with respect to the static magnetic field and is averaged to zero through rapid isotropic tumbling. However, even in isotropic liquids, the dipole-dipole interaction remains the most efficient relaxation mechanism and the dipole-dipole induced cross-relaxation is an effective way to transfer magnetization from a spin  $I$  to a nearby spin  $S$ .

Experimentally, the NOE manifests itself as follows. After the initial perturbation from equilibrium, there is only observable magnetization on spin  $I$ , then gradually spin  $S$  becomes perturbed too as a result of the  $I$  to  $S$  cross-relaxation and becomes NMR observable. The strength of the NOE depends on the cross-relaxation rate  $\sigma_{IS}^{NOE}$ . For an isotropic tumbling, large (molecular weight  $> 3$  kDa) and rigid biomolecule the heteronuclear  $\sigma_{IS}^{NOE}$  is proportional to (Cavanagh *et al.* 2007):

$$\sigma_{IS}^{NOE} \sim \left( \frac{\mu_0}{4\pi} \right)^2 \frac{\hbar^2 \gamma_I^2 \gamma_S^2 \tau_c}{r_{IS}^6} \quad (2.8)$$

where  $\mu_0$  denotes the permeability of free space (a physical constant),  $\tau_c$  the rotational correlation time and  $r_{IS}$  the distance between spins  $I$  and  $S$ . For more elaborate expressions incorporating the effects of internal dynamic averaging, the reader is referred to more extensive texts (Cavanagh *et al.*, 2007). The variable  $\tau_c$  is a measure for the tumbling time of the molecule and for the typical proteins studied by NMR  $\tau_c$  is in the order of nanoseconds. Larger molecules will tumble more slowly, increasing the strength of the NOE.



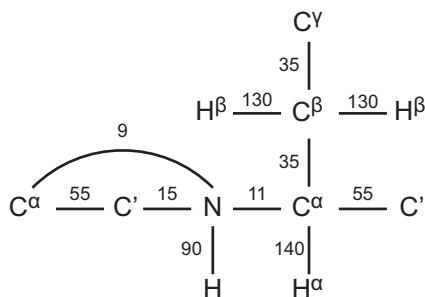


**Figure 2.11.** Typical  $|^1J|$  and  $|^2J|$  values between the nuclei of the peptide backbone and sidechain that are exploited in the triple resonance experiments (uniform  $^{15}\text{N}$  and  $^{13}\text{C}$  labeling assumed).

Another consequence of Equation 2.8 is the strong dependence of  $\sigma_{IS}^{NOE}$  on  $\gamma_I$  and  $\gamma_S$ . Due to the low  $\gamma$  values of  $^{13}\text{C}$  and  $^{15}\text{N}$ , only homonuclear proton-proton NOEs are measured in practice. Most importantly, Equation 2.8 shows the NOE to be inversely proportional to the sixth power of the distance between spins, rendering the NOE a powerful effect to yield structural information. In general, cross-peaks resulting from a proton-proton NOE interaction can be observed for spins with  $r < 5 \text{ \AA}$ .

In practice, the NOE effect is best measured by an experiment called transient NOE experiment. The two-dimensional version is commonly denoted as 2D-NOE or NOESY (from NOE spectroscopy); cross relaxation occurs during the mixing period (or transfer period; cf. Figure 2.5A). The resulting 2D NMR-spectra will show cross-peaks for all spins pairs for which cross-relaxation has occurred. The unambiguous identification of the spin pairs of the NOE cross-peak (the ‘NOE-assignment’) is greatly simplified by an increase in the resolution of the experiment using three or even four dimensions, by combining either a  $^{15}\text{N}$  or  $^{13}\text{C}$  HSQC experiment with a NOESY experiment. For example, the 3D  $^{15}\text{N}$ -HSQC-NOESY experiment (Marion *et al.*, 1989; Zuiderweg and Fesik, 1989) yields cross-peaks between a proton and a directly coupled amide  $^1\text{H}$ - $^{15}\text{N}$  pair. As this experiment eliminates all NOEs between two carbon-attached protons, the complementary  $^{13}\text{C}$ -NOESY-HSQC experiment (Marion *et al.*, 1989; Zuiderweg and Fesik, 1989) is usually also recorded. This experiment yields cross-peaks between a proton and a directly coupled proton, carbon pair. Figure 2.12A shows a schematic representation of the  $^{13}\text{C}$ -NOESY-HSQC spectrum. The cross-peaks can be conveniently depicted and analyzed using strips (Figure 2.12B), taken at the frequencies of the  $^1\text{H}$ - $^{13}\text{C}$  pair.

If spectral overlap is still limiting the proper analysis of the 3D-spectrum, increasing the dimensionality seems the logical approach and 4D-NOESY experiments can be constructed from two HSQC experiments and a NOESY experiment (Kay *et al.*, 1990a). Depending on the types of HSQCs the observed cross-peaks will indicate NOEs between

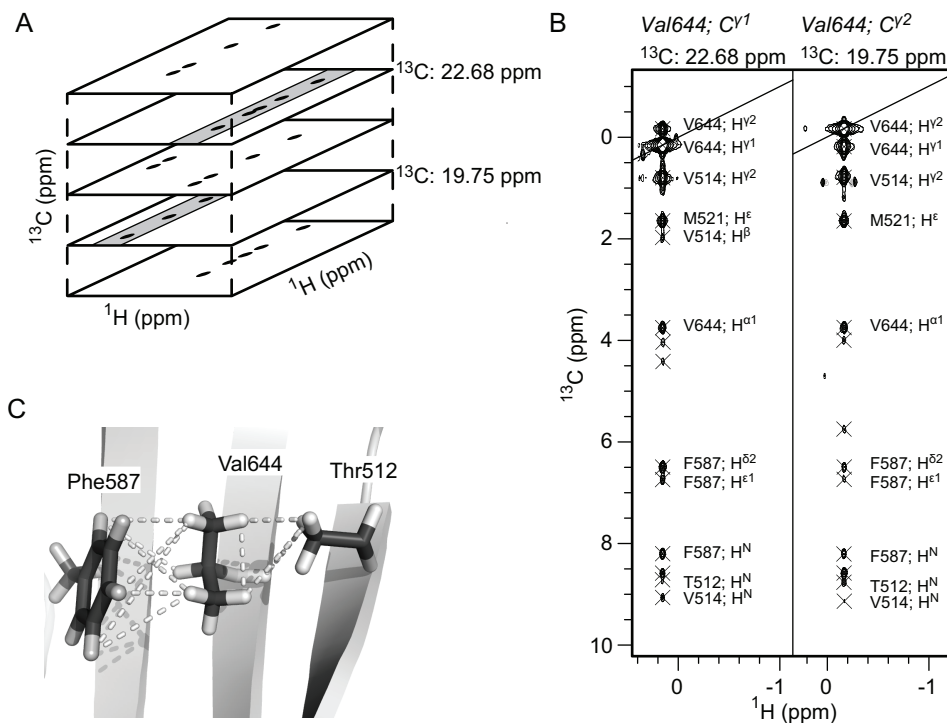


**Figure 2.12.** 3D NOE-experiments. (A) A 3D spectrum can be considered as a collection of several stacked 2D planes. The two indirect dimensions of the 3D experiment are recorded in exactly the same manner as the single indirect dimension of a 2D experiment (Figure 2.5). (B) Strips of the  $^{13}\text{C}$ -HSQC-NOESY spectrum of the calcium binding domain of the  $\text{Na}^+/\text{Ca}^{2+}$ -exchanger, taken at the frequencies of Val<sup>644</sup>  $\text{C}^{\gamma 1}$  and  $\text{C}^{\gamma 2}$  (also indicated in(A)). The cross-peaks to other protons are annotated (C). The assigned NOESY cross-peaks indicate the proximity of  $\text{H}^{\gamma 1}$  to  $\text{H}^{\delta 2}$  and  $\text{H}^{\epsilon}$  of Phe<sup>587</sup> and  $\text{H}^{\text{N}}$  of Thr<sup>512</sup>.

two nitrogen-proton pairs, or between a nitrogen-proton pair and a carbon-proton pair or between two carbon-proton pairs. However, the increased time needed to record such 4D spectra makes these often rather unpractical, which only can be remedied by special experimental adjustments (Vuister *et al.*, 1993). Furthermore, as a result of the introduction of an additional evolution period the S/N-ratio is decreased by a factor  $\sqrt{2}$  relative to the 3D counterpart recorded in an equal amount of time.

The NOE cross-peaks contain the actual structural information as only nuclei that are close enough in space will have a sufficiently large cross relaxation rate (cf. Equation 2.8). Figure 2.12B shows two strips from the  $^{13}\text{C}$ -NOESY-HSQC spectrum, taken at the  $^1\text{H}$ - $^{13}\text{C}$  frequencies of Val<sup>644</sup>  $\text{H}^{\gamma 1}$ - $\text{C}^{\gamma 1}$  and  $\text{H}^{\gamma 2}$ - $\text{C}^{\gamma 2}$  and cross-peaks to residues Phe<sup>587</sup> and Thr<sup>512</sup> are marked. All three residues are part of a  $\beta$ -strand structural element

(Figure 2.12C) and the corresponding short distances are indicated.

The cross-peak intensities are also dependent upon the mixing time  $\tau_m$ . A too short  $\tau_m$  value results in poor transfer and few cross-peaks in the spectrum. A too long  $\tau_m$  value will result in the observation of cross-peaks between two nuclei  $I$  and  $S$ , even when their distance is larger than  $5\text{\AA}$ , due to the indirect transfer of magnetization through an intermediate spin  $P$ , a process called spin-diffusion. Spin-diffusion will occur when both the  $I$  and  $S$  nuclei are close to  $P$ , but not to each other. Efficient NOE-transfer then exists for  $I$  to  $P$  and  $P$  to  $S$ , effectively relaying magnetization from  $I$  to  $S$ . Such cross-peaks may give rise to erroneous distance restraints, which potentially have disastrous effects on the calculated protein structure (cf. Validation).

There are multiple ways to extract distance information from a cross-peak. As the absolute intensity of a cross-peak is also dependent on other factors such as sample concentration, spectrometer, etcetera, the observed cross-peak intensity is related to a cross-peak between two nuclei with known, fixed distance,  $r_{ref}$ :

$$r_{IS} = \sqrt[6]{\frac{NOE_{ref}}{NOE_{IS}}} r_{ref} \quad (2.9)$$

Unfortunately, Equation 2.9 is over-simplified, as it does not take protein backbone and side-chain motions into account. Several theoretical models have been developed to account for the dynamic behavior and thus give more accurate distances. In practice, a more general approach is often followed, in which NOE cross-peaks are classified on the basis of intensity or volume into different groups. Each group has a defined lower- and upper bound value on the distance. This procedure avoids over-interpreting, while maintaining practical and computational simplicity. The classical protocol uses three groups, with the lower-bound set at  $1.8\text{\AA}$  and the upper-bound restraint at  $2.7\text{\AA}$  for strong intensity cross-peaks,  $3.3\text{\AA}$  for medium intensity cross-peaks and  $5\text{\AA}$  for weak intensity cross-peaks.

### *Residual dipolar coupling*

Whereas in liquids under normal conditions the dipolar interaction is averaged to zero, it can be partially restored through partial alignment of the protein molecules by using suitable alignment media (Tjandra and Bax, 1997; Tolman *et al.*, 1995). The resulting dipolar interaction will be much smaller ( $\sim 10^{-4}$ ) compared to that in fully ordered (solid) systems and is therefore called residual dipolar coupling (RDC). The spectroscopic effect of the RDC is identical to the  $J$ -coupling, and therefore it also results in splitting in the

NMR spectra (Figure 2.10B). The strength of the interaction between spin  $I$  and  $S$ , *i.e.* the width of the splitting  $D_{IS}$ , is given by Equation 2.10:

$$D_{IS} = -S \frac{\gamma_I \gamma_S \mu_0 \hbar}{16\pi^3 r_{IS}^3} \left[ A_a (3 \cos^2 \theta - 1) + \frac{3}{2} A_r \sin^2 \theta \cos \phi \right] \quad (2.10)$$

in which  $S$  denotes the degree of ordering,  $r_{IS}$  the distance between the nuclei,  $A_a$  and  $A_r$  the axial and rhombic components of the alignment tensor and  $\theta$  and  $\phi$  the vector orientation in this tensor (Figure 2.10C).  $S$ ,  $A_a$  and  $A_r$  are constant within one sample, because the degree of alignment is dependent on the protein and alignment medium. The distance between the nuclei is usually fixed too, as RDC values are commonly measured between bonded nuclei in a fixed geometry, for example H<sup>N</sup>-N or C <sup>$\alpha$</sup> -H <sup>$\alpha$</sup> . As a result, the observed RDC value is dependent only on the angle of the bond vector and orientation of the molecular frame. In essence, RDCs contain valuable long-range information not easily acquired otherwise.

To measure RDCs experiments similar to the  $J$ -coupling measurements are performed. A list of suitable experiments can be found in the excellent review of Prestegard *et al.* 2004. The splitting measured in the aligned state is the result of the  $J$ -coupling plus the dipolar coupling ( $D$ -coupling, Figure 2.10B). To obtain the RDC value, the  $J$ -value needs to be subtracted and identical experiments are recorded in isotropic medium to only measure the  $J$ -coupling. The RDC values can be translated into restraints used in the standard structure determination protocol (*cf.* Structure Determination) or for *de novo* structure determination (Andrec *et al.*, 2001b; a; Delaglio *et al.*, 2000). RDCs are particularly useful for the study of multi-domain proteins or complexes. The relative orientation of each domain or protein in such systems is usually difficult to determine because the number of inter-domain NOEs can be sparse (Prestegard *et al.*, 2004). As RDCs contain orientational information they can readily be used to determine relative domain orientations. Two programs that are useful for such analysis are MODULE (Dosset *et al.*, 2001) and REDCRAFT (Bryson *et al.*, 2008; Valafar and Prestegard, 2004).

Partial alignment of the protein is essential for the observations of RDCs. It is brought about by the alignment media, of which a large number exists (for a concise table see, Prestegard *et al.*, 2004). Most commonly used media are bicelles, bacteriophages and polyacrylamide gels. Bicelles are composed of mixtures of short and long phospholipids that form bilayered discs. These discs have anisotropic magnetic susceptibility and align with the magnetic field. The discs hinder protein tumbling through collisions and as re-

sult, any non-spherical protein will partially align with the discs. Like the bilayer discs, the negatively charged bacteriophages align with the magnetic field, but the ordering to the protein is imparted predominantly through electrostatic interactions instead of collisional interactions. Unlike the previous two alignment media, the alignment of compressed polyacrylamide gels is independent of the magnetic field. The compression leads to a highly anisotropic structure of the gel and order to the protein is imparted through collisional interactions.

In all instances, the alignment is highly dependent on the shape and charge distribution of the protein. Therefore, both magnitude and orientation of the alignment tensor can be predicted based on the three-dimensional structure. The ability to predict an alignment tensor can be used to validate 3D structures of protein complexes, determine relative orientation of domains and differentiate between monomeric and homodimeric states. Different tools and calculation methods, such as PALES (Zweckstetter and Bax, 2000; Zweckstetter, 2008), have been developed to perform this task in proteins (Almond and Axelsen, 2002; Berlin *et al.*, 2009; Fernandes *et al.*, 2001) and nucleic acids (Wu *et al.*, 2006).

## Resonance Assignment

NMR data can only be meaningfully interpreted when it is clear which peaks belong to which atom in the protein. The process of ascribing each observed resonance frequency to a specific atom is called assignment. The technique of assigning unlabeled proteins was developed by Wüthrich and co-workers in the early 80s and was based on a set of homonuclear 2D experiments. Although very successful, the Wüthrich approach can only be applied to proteins smaller than 10 kDa. The use of 2D homonuclear experiments becomes unfeasible for larger proteins due to increased complexity of the spectra and decreasing efficiency of the homonuclear through-bond magnetization transfer.

The introduction of (selective) isotope labeling combined with heteronuclear NMR experiments (Ikura *et al.*, 1990) increased the size of amenable proteins up to 25 kDa and has become the *de facto* standard technique. With the introduction of TROSY (cf. Relaxation) in combination with deuterium labeling, the size of proteins suitable for NMR has even increased up to ~70 kDa. In this section we will describe the process of assigning  $^{13}\text{C}/^{15}\text{N}$  labeled and  $^2\text{H}/^{13}\text{C}/^{15}\text{N}$  labeled samples.

### Sequential backbone assignment

The interpretation and assignment of NMR data of a protein usually starts with the assignment of the backbone (N, H<sup>N</sup>, H<sup>α</sup>, C<sup>γ</sup>) and C<sup>β</sup> atoms. For this purpose several different experiments need to be recorded that will link these atoms with their sequential neighbors. The experiments exploit the existing *J*-couplings between bonded nuclei (cf. Figure 2.11) to transfer magnetization from one nucleus to another, and the resulting experiments are usually called ‘triple resonance experiments’ (cf. Table 2.3) (Ikura *et al.*, 1990; Kay *et al.*, 1990b; Kay *et al.*, 1990a). The basis of all triple-resonance experiments is the <sup>15</sup>N-HSQC. As previously explained, in the <sup>15</sup>N-HSQC experiment <sup>1</sup>H<sup>N</sup> magnetization is transferred to a covalently attached <sup>15</sup>N and therefore each cross-peak in the 2D <sup>15</sup>N HSQC spectrum depicts a proton-nitrogen pair. The H-N correlation is a useful reference point since it is present in all amino acids (except proline). In the triple resonance experiments a third or even a fourth dimension is added to the <sup>1</sup>H and <sup>15</sup>N dimensions (Figure 2.13). This ‘extra’ dimension can either be a <sup>1</sup>H or <sup>13</sup>C dimension and allows the measurement of correlations between the proton-nitrogen and other nuclei in the backbone. Depending on the type of experiment (cf. Table 2.3), the observed resonances in the ‘extra’ dimension belong to the same residue as the amide (*i*) and/or previous residue (*i-1*).

The names of the triple resonance experiments reveal which nuclei are recorded and which nuclei are passively involved: the NH encodes for the amide proton and nitrogen, CA and CB for the C<sup>α</sup> and C<sup>β</sup>, CO for the carbonyl carbon and HA and HB for the

**Table 2.3** Summary of the different triple resonance NMR experiments used in protein assignment. The S/N ratio is relative to the HNC(O) experiment. Table adapted from (Sattler *et al.*, 1999)

Experiment	Nuclei Observed	Maximum Size
HNCO	H( <i>i</i> ),N( <i>i</i> ),C <sup>γ</sup> ( <i>i-1</i> )	<20 kD
HNCA	H( <i>i</i> ),N( <i>i</i> ),C <sup>α</sup> ( <i>i</i> ),C <sup>α</sup> ( <i>i-1</i> )	<20 kD
HN(CO)CA	H( <i>i</i> ),N( <i>i</i> ),C <sup>α</sup> ( <i>i-1</i> )	<20 kD
HN(CA)CO	H( <i>i</i> ),N( <i>i</i> ),C <sup>γ</sup> ( <i>i</i> )	<20 kD
CBCA(CO)NH	H( <i>i</i> ),N( <i>i</i> ), C <sup>α</sup> ( <i>i-1</i> ),C <sup>β</sup> ( <i>i-1</i> )	<20 kD
HBHA(CO)NH	H( <i>i</i> ),N( <i>i</i> ),H <sup>α</sup> ( <i>i-1</i> ),H <sup>β</sup> ( <i>i-1</i> )	<20 kD
CBCANH/HNCACB	H( <i>i</i> ),N( <i>i</i> ),C <sup>α</sup> ( <i>i</i> ),C <sup>β</sup> ( <i>i</i> ),C <sup>α</sup> ( <i>i-1</i> ),C <sup>β</sup> ( <i>i-1</i> )	<15 kD
(H)CC(CO)NH-TOCSY	H( <i>i</i> ),N( <i>i</i> ), C <sup>aliph</sup> ( <i>i-1</i> )	<15-20 kD
H(CC)(CO)NH-TOCSY	H( <i>i</i> ),N( <i>i</i> ), H <sup>aliph</sup> ( <i>i-1</i> )	<15-20 kD
HCCH-TOCSY	H <sup>aliph</sup> , C <sup>aliph</sup>	<25 kD

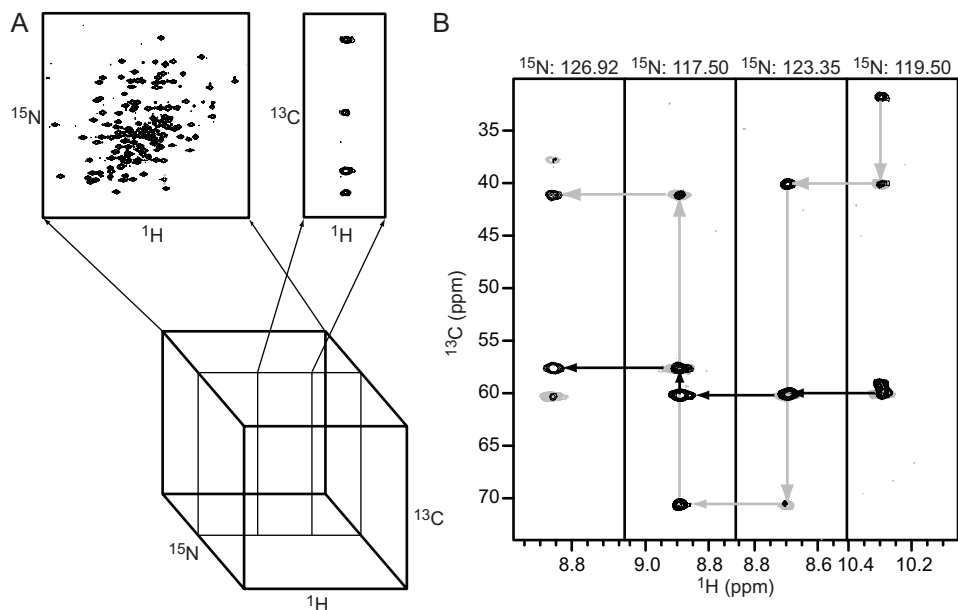


**Figure 2.13.** 3D triple resonance ( $^1\text{H}$ ,  $^{15}\text{N}$ ,  $^{13}\text{C}$ ) experiments. (A) 3D spectral cube. Projection along the  $^{13}\text{C}$  axis would yield the  $^{15}\text{N}$ -HSQC spectrum (indicated). Spectra are often represented as strips showing the resonances belonging to one residue. (B) Four strips displaying the overlay of CBCA(CO)NH (grey) and HNCACB (black) of the second calcium binding domain of the  $\text{Na}^+/\text{Ca}^{2+}$ -exchanger. Together these spectra allow sequential backbone assignment as indicated by the arrows. Black and grey arrows follow the  $\text{C}^\alpha$  and  $\text{C}^\beta$  sequential link, respectively.

$\alpha$  and  $\beta$  protons. Any spin of which the chemical shifts are not evolved (*i.e.* they do not appear in the spectrum), are put between parentheses. For example, the HN(CO)CA experiment correlates the amide proton and its attached nitrogen (HN), via the carbonyl carbon (CO) of the previous residue whose frequency is not recorded, with the  $\text{C}^\alpha$  of the previous residue. Each peak in the 3D cube shows the chemical shift of a specific  $\text{H}^\text{N}$ , N and  $\text{C}^\alpha$ . The 3D experiment is usually displayed as a set of 2D planes stacked onto each other or as a collection of strips (cf. Figure 2.13).

The ability to connect HN resonances of residue  $i$  to a nucleus of the same or previous residue is the essence of the backbone assignment, as it identifies so-called sequential connectivities. The sequential backbone assignment will be explained on the basis of the HNCACB and CBCA(CO)NH experiments (cf. Figure 2.13B), but the principle applies to other combinations of complementary triple resonance experiments as well (Table 2.3, *vide infra*). The sequential backbone assignment commonly starts with matching the 2D peaks in the  $^{15}\text{N}$ -HSQC spectrum to the 3D peaks in the other two spectra on the basis of

the two dimensions in common ( $^{15}\text{N}$  and  $^1\text{H}^{\text{N}}$ ). The 3D spectra are then represented into small pseudo 1D strips based on their  $^1\text{H}^{\text{N}}$  and  $^{15}\text{N}$  shifts. Thus, barring overlap in these latter two dimensions, each strip originates from one amide. The nature of the HNCACB experiment dictates that the HNCACB strip of the  $i^{\text{th}}$  residue will display four peaks: *i.e.* those belonging to the  $\text{C}_i^\alpha$ ,  $\text{C}_{i-1}^\alpha$ ,  $\text{C}_i^\beta$  and  $\text{C}_{i-1}^\beta$  nuclei. The inter-residue peaks can be distinguished from the intra-residue peaks by comparing the HNCACB strips with the corresponding strips from the CBCA(CO)NH spectrum. These strips will only display two intra-residue peaks, *i.e.* those belonging to the  $\text{C}_{i-1}^\alpha$  and  $\text{C}_{i-1}^\beta$  nuclei. Searching for strips that connect inter-residual with the intra-residual peaks will then yield the sequential connectivities.

Once the sequential connectivities have been established, the resonances have to be assigned to residues. This is not trivial, because the sequential linkage can have several gaps due to lack of sensitivity, *i.e.* missing peaks, or as result of peak overlap. Even a complete sequential linkage will typically contain multiple segments, because prolines do not contain an amide proton. To resolve the ambiguities and to map the segments to the amino acid sequence it is advantageous to identify amino acid types based on their chemical shifts. For example, a glycine residue can be easily recognized based on its the upfield  $\text{C}^\alpha$  chemical shift (*i.e.* low ppm, cf. Figure 2.9). Alanine and threonine residues are also characterized by distinct  $\text{C}^\alpha/\text{C}^\beta$  chemical shift values and serve as valuable anchor points connecting the sequentially linked patterns to the primary sequence. Statistical analysis has shown that fragments of four sequential residues can be unambiguously mapped on the primary sequence on the basis of their  $\text{C}^\alpha/\text{C}^\beta$  chemical shift values (Grzesiek and Bax, 1993).

It is not always possible to complete the backbone assignment from the HNCACB / CBCA(CO)NH experiments alone and then additional experiments are required. For example, the HNCACB experiment is rather insensitive for proteins above 15 kDa and the more sensitive HNCA / HN(CO)CA combination can be used in addition. To complete the backbone assignment, the  $\text{H}^\alpha$  nuclei need to be assigned as well. Therefore, the data are typically complemented with the HN(CA)HA and HBHA(CBCACO)NH experiments to obtain the  $\text{H}^\alpha$  and  $\text{H}^\beta$  resonances, which will also further facilitate the sequential backbone assignment in case of ambiguity. In addition, the HNCO experiment that correlates the  $\text{H}_i$ ,  $\text{N}_i$  and the  $\text{C}_{i-1}'$ , is usually recorded, because it has the highest sensitivity of all triple-resonance experiments (cf. Table 2.1) and yields spectra with an overall high cross-peak dispersion. As this experiment can be recorded in a very limited amount of time it is therefore also a good starting point for the backbone assignment, since it can augment



the  $^{15}\text{N}$ -HSQC. Unfortunately, the HN(CA)CO experiment, which acts as the HNCO counterpart for a sequential backbone assignment, is rather insensitive and will often be only useful in combination with a deuterated protein.

### *Sidechain assignment*

The sequential backbone assignment already yields information on the  $\text{H}^{\alpha}$  and  $\text{C}^{\alpha}$  chemical shifts as well as those of  $\text{C}^{\beta}$  and  $\text{H}^{\beta}$ . This information is not only useful for elucidating the sequential backbone assignment, but also forms the starting point for a complete side chain assignment. The so-called HCCH-TOCSY (Total Correlation Spectroscopy) experiment (Bax *et al.*, 1990; Olejniczak *et al.*, 1992) is used to correlate all aliphatic  $^1\text{H}$  and  $^{13}\text{C}$  resonances (*vide infra*). During a TOCSY experiment, magnetization transfer is between  $J$ -coupled nuclei, and even two distant nuclei without direct  $J$ -interaction can be correlated through an intermediate nuclei, provided these have  $|J| > 0$ . The key component in the TOCSY experiment is the isotropic mixing time, during which a sequence of low power RF-pulses induce the magnetization transfer between the nuclei. The length of the mixing time determines the extent of the transfer. A short mixing time will result in partial transfer, resulting in a limited number of correlations measured. Longer mixing time increases the number of correlations, however, the mixing time cannot be too long, because the signal will recede due to transverse relaxation.

Two commonly used variations of the 3D HCCH-TOCSY experiment establish different correlation patterns between the nuclei. The 3D H(C)CH-TOCSY experiment correlates the  $^1\text{H}$ ,  $^{13}\text{C}$ ,  $^1\text{H}$  nuclei, whereas the (H)CCH-TOCSY correlates  $^{13}\text{C}$ ,  $^{13}\text{C}$ ,  $^1\text{H}$ . The observed sidechain resonance patterns can now be connected to the amides via the  $\text{H}^{\alpha}$  and  $\text{C}^{\alpha}$  and possibly the  $\text{H}^{\beta}$  and  $\text{C}^{\beta}$ , as these have been obtained during the sequential backbone assignment. The number and chemical shifts of sidechain resonance patterns will also help identify the amino acid type and complete the assignment.

Unfortunately, some residues with long aliphatic chains, such as Lys or Arg, will often still display significant overlap in resonances (Bax *et al.*, 1990). To alleviate this problem, the sidechain nuclei can also be correlated to the amide moiety. In the (H)CC(CO)NH-TOCSY experiment the aliphatic sidechain carbons of the previous residue are connected to the amide of the next, whereas the H(CCCO)NH-TOCSY does likewise for the aliphatic sidechain protons (Sattler *et al.*, 1999).

### *Automated methods*

The sequential and straightforward nature of the sequential assignment process makes it highly suitable for automation and numerous programs have been developed for this purpose (for a recent review see (Güntert, 2009) and Table 2.4). Generally, similar steps are performed by these programs, which include peak picking, grouping of resonances, pattern linking and assignment.

The first step, peak picking, is the identification of NMR signals in multi-dimensional spectra. Although this task seems easily automated, even sophisticated recognition methods often fail due to peak overlap, noise and artifacts (Güntert, 2009). Therefore, most automated protocols include some filtering step in which real and noise peaks are distinguished (Altieri and Byrd, 2004). Additionally, some programs also perform a referencing step of the spectra, to ensure that the referencing in all spectra is exactly identical. After peak-picking, the resonances are grouped into spin systems, which contain all resonances that can be related to one amino acid. Usually the  $^1\text{H}$ - $^{15}\text{N}$  resonances, as derived from either the  $^{15}\text{N}$ -HSQC spectrum or the 3D HNCO spectrum, are used as basis for the linking step, since all triple resonance experiments contain these resonances.

The third step entails the linking of the different patterns, potentially in combination with assignment of these patterns to the primary sequence. Several methods have been developed using different principles, such as simulated annealing, best-first approaches, Monte Carlo or data base searches. Although there are considerable differences between all these methods, they share some general properties. Often they require peak lists from a specific set of NMR spectra as input and produce lists of chemical shifts as output (Güntert, 2009). The correctness and completeness of the assignment is strongly dependent on the quality of the spectra and the obtained peak lists. Severe resonance overlap will also considerably hamper the automated assignment and therefore automated backbone assignments work best for smaller proteins (< 15kDa, Williamson and Craven, 2009).

Extending the automated protocols to include the complete side-chain assignment has proven to be more difficult, owing to increased peak overlap and missing peaks due to incomplete TOCSY transfer (Williamson and Craven, 2009). Thus, the current general consensus is that the automated procedures provide for a good starting point, but manual assignment and verification is in most cases still necessary (Altieri and Byrd, 2004), in particular for the spectroscopically troublesome regions.

## Fast Methods

Whereas automated methods of chemical shift assignment and structure calculation have decreased the time necessary to generate a protein structure significantly, the measurement times in multidimensional NMR can still be a limiting factor. While a simple one-dimensional spectrum (1D) is recorded directly and only requires a few seconds, a two-dimensional (2D) spectrum is constructed from a series of 1D data and already requires several minutes up to one or two hours. The 3D experiments described in the previous section often require hours to days of measuring time. Even higher dimensional experiments could be beneficial, but would require unreasonable amounts of time. Furthermore, long measurement times also require protein samples to be stable over long periods and prevent high-throughput methods. Therefore, reducing the experimental time (or increasing S/N-

**Table 2.4.** List of automated assignment programs and their required experiments.

Program / author	Experiments required	Type	Ref.
AutoAssign	HA(CA)(CO)NH, HA(CA)NH, CA(CO)NH, CANH, HNCO, HN(CA)CO, CBCA(CO)NH, CBCANH	Best-first approach	(Zimmerman <i>et al.</i> , 1997)
PASTA	HNCA, HN(CO)CA, HNCACB, CBCA(CO)NH, HNCO, HNHA, HCACO	Simulated annealing-like method	(Leutner <i>et al.</i> , 1998)
Lukin <i>et al.</i>	HNCA, HN(CA)CO, HN(CA)HA, HNCACB, COCAH, HCA(CO)N, HNCO, HN(CO)CA, HN(COCA)HA, CBCA(CO)NH	Simulated-annealing-like method	(Lukin <i>et al.</i> , 1997)
Buchler <i>et al.</i>	HNCA, HN(CO)CA, HA(CA)(CO)NH, HN(CA)HA, CP-(H)CCH-TOCSY, CP-(H)C(CA)(CO)NH-TOCSY	Mean-field on simulated annealing	(Buchler <i>et al.</i> , 1997)
BATCH	HADAMAC, HNCA, HNCA(time shifted), HNCB, HNCO	Best-first approach	(Lescop and Brutscher, 2009)
MARS	Any experiment containing $H^N(i)$ , $N(i)$ and $C^\alpha(i)/C^\alpha(i-1)$ , $C^\beta(i)/C^\beta(i-1)$ or both	Simulated annealing-like method	(Jung and Zweckstetter, 2004; Li and Sanctuary, 1997b)
Li and Sanctuary	Any experiment containing $H(Ni)$ , $N(i)$ and $C^\alpha(i)/C^\alpha(i-1)$ , $C^\beta(i)/C^\beta(i-1)$ or both	Best-first approach	(Li and Sanctuary, 1997b; a)
GARANT	Any NMR experiment	Genetic algorithm	(Bartels <i>et al.</i> , 1996; Bartels <i>et al.</i> , 1997)

ratio in equal amount of time) would be highly beneficial and new spectroscopic methods, so called fast methods, are actively being developed (see (Felli and Brutscher, 2009) for a recent review on the topic).

### *Sparse sampling*

There are many techniques to reduce the acquisition time of multi-dimensional spectroscopy and they can be divided into two classes, namely sparse sampling or fast pulsing. The aim of sparse sampling is to reduce the number of data points in the indirect dimensions, without loss of resolution. There are many reduced sampling techniques, such as optimized linear under-sampling, non-uniform random data sampling, radial data sampling (also termed projection reconstruction), Hadamard spectroscopy, G-matrix combined Fourier Transform or spatial frequency encoding. Although these techniques are technically- and conceptually different, they share two common features. The number of indirect data points is reduced and in subsequent analysis all information is retrieved through computational efforts. The techniques usually require more complex and elaborate processing or prior knowledge of the sample. It is beyond the scope of this review to fully explain all techniques, however, optimized linear under-sampling, sparse non-uniform data sampling and radial data sampling are described as examples.

Conceptually the easiest way to reduce the experimental time is optimized linear under-sampling. Simply increasing the time increment between successive data points reduces the number of scans. However, the time increment determines the spectral width of the experiment as result of the Nyquist condition and decreasing the number of points will thus decrease the spectral width. If the spectral width is smaller than the chemical shift range, peaks that have frequencies outside the spectral width will still appear in the spectrum, only at higher or lower frequency. This phenomenon is called spectral aliasing or folding and leads to more complicated spectra and potential loss of information due to peak overlap. The spectral width can be optimized to yield the lowest number of data points without introducing significant peak overlap. Especially for heteronuclear experiments these optimized under-sampling methods can reduce the experimental time by a factor of four or higher (Bax *et al.*, 1991).

Sparse non-uniform random data sampling and radial data sampling are two other approaches to reduce the number of data points in the indirect dimensions. Unlike in the linear- under-sampling approach, the time increment between two consecutive data points is not uniform. In sparse non-uniform random data sampling the experimental time

is reduced by randomly selecting only 10-30% of the data points normally recorded (Felli and Brutscher, 2009). The acquired data can no longer be processed by regular Fourier transformation, but should be processed by means of spectral reconstruction methods such as maximum entropy reconstruction (Hoch and Stern, 2001), filter diagonalization method (Chen *et al.*, 2000) and numerical Fourier integration (Kazimierczuk *et al.*, 2006). Although the experimental time is reduced significantly, processing the data is not completely straightforward and most of these methods rely on fitting procedures and require some parameter adjustment either from prior knowledge or by trial and error (Felli and Brutscher, 2009). The approach of radial data sampling is slightly different. The joint incrementation of  $t_1$  and  $t_2$  in a 3D experiment effectively results in radial data sampling. The acquired data are essentially a set of 2D projections of the 3D spectrum. Several different projection-reconstruction methods can subsequently retrieve the full spectrum. This method can reduce the experimental time especially in case of 4D and higher dimensional spectroscopy (Felli and Brutscher, 2009). The technique is highly suitable for small- and medium sized proteins, for larger proteins the reconstruction becomes less reliable due to extensive peak overlap.

### *Fast pulsing techniques*

Reducing the measurement time can also be achieved by reducing the total time required for recording the individual scans. Each scan is followed by the so-called recycle delay, during which the z-magnetization is restored by longitudinal relaxation. Although the recycle delay is relatively long ( $\sim 1$ s) compared to the duration of the actual pulses and acquisition ( $\sim 100$  ms), the time is typically insufficient to fully restore the equilibrium magnetization. As a result, the system will evolve to a steady-state with somewhat less than maximal Z-magnetization at the start of every scan. It was already realized in the early days of NMR, that the total amount of signal averaged over several transients could be enhanced by exciting the spins with an RF pulse  $< 90^\circ$ , the so-called Ernst angle.

Recently, more elaborate methods that facilitate relaxation have been developed. In the longitudinal relaxation enhancement (LRE) approach (Pervushin *et al.*, 2002), the relaxation times of the  $^1\text{H}$  spins are reduced using nearby unperturbed spins. LRE exploits the NOE phenomenon that causes spins relax faster to thermal equilibrium when nearby spins are unperturbed. The method requires that only a small subset of the  $^1\text{H}$  spins, for example the amide protons, are excited by the pulse sequence, whereas all other spins must remain unperturbed. This is usually achieved by employing selective pulses. In the

SOFAST experiment, the combined use of LRE with the Ernst flip angle allows the recording of 2D  $^1\text{H}$ - $^{15}\text{N}$  or  $^1\text{H}$ - $^{13}\text{C}$  correlation spectra in several seconds (Schanda *et al.*, 2005). Implementation of similar methods can significantly decrease the measurement times of HSQC based triple resonance experiments (Diercks *et al.*, 2005).

## Structure Determination

Obtaining a chemical shift assignment is not goal in itself and is usually used in conjunction with other experiments to obtain a protein structure. In principle, all NMR observables, such as  $J$ -coupling, NOE, residual dipolar coupling and even chemical shifts, provide information on the protein conformation. This section describes how all these NMR-data can be transformed into structural restraints and how these restraints are then used in the structure calculation protocol.

### Restraints

An NMR observable of major importance for a structure determination is the Nuclear Overhauser Effect (NOE). The NOESY spectrum contains distance information, as a cross-peak will only occur if two protons are close enough in space ( $r < 5\text{\AA}$ ). The unambiguous identification of the NOE cross-peak is a crucial prerequisite for its proper translation into a structural restraint. Unfortunately, obtaining a comprehensive set of distance restraints from a NOESY spectrum, using the previously obtained chemical shift assignment is not straightforward (Güntert, 2009), mainly because the number of cross-peaks is typically very large. Therefore, iterative (semi)-automated approaches have been adopted (CANDID, ARIA), in which a preliminary structure is calculated based on a first set of unambiguous NOE assignments. Subsequently, the preliminary structure is used to assign more cross-peaks in the NOESY spectrum and increase the number of restraints. A new structure can then be calculated, which serves as the input for the next iteration. Thus, the NOESY assignments and the structure converge during a number of such iterative cycles (Williamson and Craven, 2009).

The more recent NOESY assignment procedures include the idea of ambiguous NOEs, as first introduced in the program ARIA (Nilges *et al.*, 1997). In many instances a NOE cross-peak can have more than one possible assignment and such cross-peaks are treated as an  $r^{-6}$  weighted average of all the possible assignments. This so-called ambiguous restraint will always be satisfied, provided that the correct assignment included as one of the possibilities. Another key feature of most automated assignment procedures is the

concept of ‘network anchoring’. In this procedure the correctness of a NOE assignment is estimated on the basis of other structural restraints *i.e.* an NOE assignment is more likely to be correct when supported by other related distance restraints.

Fortunately, NOEs are not the only source of structural restraints and are commonly supplemented by several others, such as those derived from  $J$ -couplings, chemical shifts or residual dipolar couplings (RDCs). Chemical shift derived restraints are most easily obtained, because these do not require extra experimentation. The backbone chemical shifts report on the type of secondary structure elements in the protein. Programs like TALOS+ (Shen *et al.*, 2009) give detailed information, using the chemical shifts of a three-residue fragment to derive dihedral angle restraints (cf. Chemical shift). Dihedral restraints can also be obtained from  $J$ -coupling values, but this requires additional experiments. Finally, structural restraints can be derived from RDC measurements and proton solvent exchange (cf. Scalar coupling, NOE, and residual dipolar coupling).

### *Structure calculation*

The NMR structure calculation protocol involves a customized simulated annealing protocol, typically in torsion-angle space, where restraints are included as pseudo-harmonic potentials (Güntert *et al.*, 1997; Nilges *et al.*, 1988). During an initial high temperature phase (*in silico*), the protein is allowed to fold under the influence of a force field in which the pseudo-harmonic experimental potentials drive the trajectory. In a subsequent cooling stage, gradually more terms of the force field, such as the non-bonded terms, become active, thus assuring a proper annealing into a realistic structure. For NMR, the main programs to perform the NMR structure calculations are Xplor\_NIH (Schwieters *et al.*, 2003), Cyana (Güntert *et al.*, 1997) and Aria/CNS (Brünger, 2007; Rieping *et al.*, 2007). The initial calculation is preferentially followed by a refinement in explicit water using an even more extended force field that also includes electrostatics (Linge *et al.*, 2003; Nabuurs *et al.*, 2004; Spronk *et al.*, 2002). The structure calculation and refinement procedure is typically repeated 20-100 times with different starting conditions, to generate a collection of structures. These are then scored according to one or more criteria, such as root mean square difference (rmsd) of the distance restraints, restraint energy or overall energy, and ordered. Usually the best twenty structures are then selected, and together they are called the structure ensemble. The individual structures of the ensemble are commonly denoted as models.

It is the recommendation of the protein data bank (wwPDB) that the first model

of the ensemble corresponds to the best structure and that the models have a common orientation. To achieve the latter, they need to be superposed. As the different models of the ensemble will contain regions of structural variability, originating from either the lack of data or from genuine conformational heterogeneity, a choice has to be made regarding the regions to include in the superposition. Unfortunately, no consensus exists about the criteria for such a choice. Choosing the residues in regular secondary structural elements is often used as a criterion. Alternatively, an algorithm based upon the backbone  $\phi$ ,  $\psi$  dihedral angle order parameters has been proposed for this purpose. Clustering algorithms for identifying core atom sets and for assessing the precision of protein structure ensembles (Snyder and Montelione, 2005). Most NMR structure calculation programs are capable of superposing the models in an NMR structure ensemble. Alternatively, external programs, such as PROFIT ([www.bioinf.org.uk/programs/profit](http://www.bioinf.org.uk/programs/profit)), or molecular viewers such as YASARA ([www.yasara.org](http://www.yasara.org)) or MolMol (Koradi *et al.*, 1996), can be used.

## Structure Validation

The determination of protein structures by NMR spectroscopy is the result of an elaborate process with many experimental- and computational steps. Consequently, the resulting structure ensembles will contain errors (Bhattacharya *et al.*, 2007; Hooft *et al.*, 1996; Nabuurs *et al.*, 2006). Our analyses even showed that a wrongly folded structure is not identified by the NMR parameters commonly reported in the literature (Nabuurs *et al.*, 2005). It is therefore essential that a proper quality assessment of both input data and resulting structures is made, as integral part of the whole structure determination process (cf. Figure 2.1).

The structure validation process can be (arbitrarily) divided into the validation of experimental data, typically in relation to the structural result, and the structural validation in relation to our prior knowledge contained in structural databases such as the wwPDB.

Experimental NMR derived restraints originate from different sources (NOE spectra,  $J$ -couplings, RDCs, chemical shifts, SAXS data), which report on both local- and global properties and are conformationally averaged over different timescales. In addition, the structural information content is very different between the different restraint types and even differs vastly for restraints within a single kind (Nabuurs *et al.*, 2003).



### *Validation of experimental data*

Typically, the structure calculation programs already report metrics (rmsd values, number of violations, Q-factors, etc.) on the agreement between the experimental restraints and the resulting structure ensemble. Consistent and/or large violations of experimental restraints are usually indicative for significant problems that should be remedied (Spronk *et al.*, 2004). More sophisticated methods assess the experimental data within context. For example, the program WATTOS computes the completeness score, defined as the fraction of observed *versus* expected NOE restraints on the basis of the structural ensemble (Doreleijers *et al.*, 1999). A similar analysis is performed by the program RPF (Huang *et al.*, 2005), but now based upon assigned peaks and short-distance networks and the resulting scores describe the extent to which the NOE peak-list either has too many or too few peaks in relation to the experimental NMR ensemble. Whereas the WATTOS and the RPF algorithms do involve a comparison with the calculated structural ensemble, the program QUEEN (Nabuurs *et al.*, 2003) evaluates distance- and dihedral restraints without knowledge of the structural ensemble. The program defines two quantities for every restraint that identify the importance of the restraint in defining the fold of the protein and the degree of support by the other experimental data. High importance and low support values are indicative of troublesome restraints (Nabuurs *et al.*, 2003; Nabuurs *et al.*, 2005).

### *Structural validation*

Comparison of a structural ensemble in relation to the chemical knowledge regarding biomolecules, provides for a powerful way of detecting errors. Proper covalent geometry, such as bond lengths, bond angles, and planarity, can easily be checked for on the basis of their known distributions and average values (the ‘Engh and Huber’ parameters, Engh and Huber, 1991). The dihedral angles define the conformational space accessible for the biomolecules. The wwPDB, a database for the curation of biomolecular structural data, contains over 60,000 entries from which a subset of high-resolution X-ray structures is extracted. From this subset distributions for individual- or pairwise combinations of dihedral angles are derived, which then serve as references to establish the likelihood of the experimental NMR structure ensemble.

### *Cross validation*

Cross validation presents the most unbiased way to establish the merit of the

NMR-derived structure ensemble (Brünger *et al.*, 1993). In a cross-validation procedure, the experimental data are partitioned in a working set and a smaller fraction (typically ~10 %) that comprises the test set. The NMR structure ensemble is calculated using the working set. The data from the test set are then used to establish the quality of the result, by comparing their values with the corresponding values back-calculated from the structure ensemble. An improved agreement between test set data and back-calculated data denotes an improved result. NMR specific aspects, such as the varying information content of the experimental data, requires that this procedure is repeated numerous times, with different partitioning of the working- and test sets.

### *Validation programs*

Validation of NMR-derived structures requires dedicated programs that can accommodate both the multitude of different experimental data, as well as being capable of properly handling multi-model ensembles in their analysis routines. WHAT IF (Vriend, 1990) is a program designed initially for the validation of X-ray structures, but now also capable of handling a NMR ensemble. WHAT IF performs a knowledge-based analysis and does not analyze the experimental NMR input data. Its output is extensive, but hard to evaluate. In contrast, PROCHECK\_NMR (Laskowski *et al.*, 1996) can analyze both the structure ensemble as well as distance- and dihedral experimental restraints. The program has proven quite popular, as it produces relatively easy accessible graphical output, but is no longer maintained and already outdated. The protein structure validation suite (PSVS (Bhattacharya *et al.*, 2007) is an interface to a number of structure validation programs and routines, including PROCHECK\_NMR and RPF. It treats both the structure ensemble and the input data and produces reports that can be accessed through the web.

Our own validation approach is called CING (pronounced 'king') for Common Interface for NMR structure Generation (Vuister *et al.*, in preparation) (<http://nmr.cmbi.ru.nl/cing>). The CING software provides a comprehensive analysis of both the structure ensemble and experimental data, which includes the results of as many as 25 different programs or routines, including WHAT IF and PROCHECK\_NMR. The results are presented in a single, HTML/WEB 2.0, interactive comprehensive report.

### *The quality of NMR structures*

We recently completed the remediation of >5,000 NMR data entries contained within the Biological Magnetic Resonance Bank (Markley *et al.*, 2008), which resulted

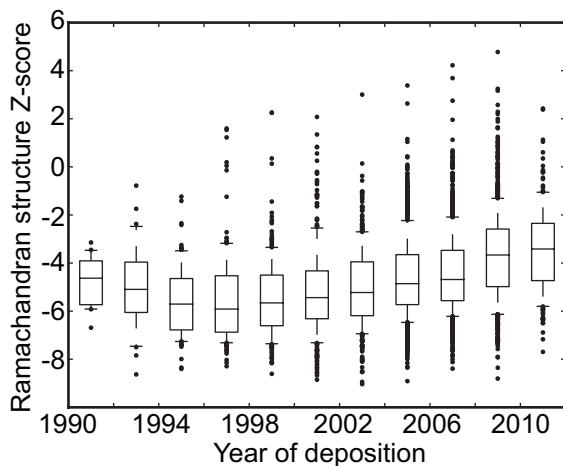


**Figure 2.14.** Boxplots showing the 10, 25, 50, 75 and 90 percentiles of the WHAT IF Ramachandran quality score distribution as a function of year of deposition. Ramachandran quality scores  $< -4$  are considered to indicate significant problems, particularly for a fully structured protein (domain). The data were derived from  $>5000$  entries from the NRG-CING (<http://nmr.cmbi.ru.nl/NRG-CING>) archive.

in the NMR Restraints Grid (NRG) (Doreleijers *et al.*, 2009). All the entries in NRG were combined with the relevant PDB coordinate data and subjected to a CING analysis. This yielded a new archive called NRG-CING <http://nmr.cmbi.ru.nl/NRG-CING>. The NRG-CING was used to assess the overall quality of the experimental NMR structures. Figure 2.14 shows a distribution plot of a commonly accepted quality criterion, the WHAT IF Ramachandran quality, as a function of year of deposition. The plot illustrates three important aspects regarding the quality of NMR structures. First, there is a large variation in this quality parameter, irrespective of the year of deposition. This illustrates, that the NMR method is still highly non-uniform in the quality of the structural results that are obtained. Second, even nowadays there is a substantial fraction of the deposited entries that are likely to have significant problems. A more detailed analysis shows that increased data content, in particularly the usage of RDCs, improves the quality of the structural result. Third, over the years there is a gradual trend towards better structures, suggesting that the advancements in the technique are being applied by the NMR community at large. This hopeful finding can serve as a stimulus for the application of proper validation tools as integral part of the structure determination process.

Proper validation often allows remediation of potential- and commonly encountered problems and more reliable NMR structures will be generated. We therefore encourage the application of structure validation software by all NMR spectroscopists prior to deposition in the wwPDB repositories.

## Relaxation and dynamical processes

Inevitably any system in contact with its surroundings will return to equilibrium

after a perturbation. In the NMR equilibrium state the energy levels  $\alpha$  and  $\beta$  are populated according to the Boltzmann distribution and there is no transverse magnetization. The return to equilibrium is called relaxation and has major practical importance: e.g. it determines how fast an experiment can be repeated and determines the line widths of the peaks in the spectrum. Relaxation is not instantaneous but occurs as function of time and the relaxation rate is influenced by many factors, such as the field strength, sample properties and the size and mobility of the molecule. The theory of NMR relaxation is complex and comprises both quantum mechanics and statistical mechanics. In the next section relaxation will be described phenomenologically with the emphasis on practical applications. For a more thorough description the reader is referred to other texts (Cavanagh *et al.*, 2007).

### *Spin-lattice and spin-spin relaxation*

NMR relaxation involves two distinct processes, the so-called spin-lattice relaxation and spin-spin relaxation. Spin-lattice relaxation, also named longitudinal relaxation or  $T_1$ -relaxation, is the process in which the ensemble of spins returns to their Boltzmann distribution of spin states. In thermal equilibrium, a bulk magnetization in the direction of the magnetic field exists, as on average slightly more spins are in the lower energy state  $\alpha$ . Application of an  $180^\circ$  RF-pulse to the sample will invert this distribution of spin states, and the  $\beta$  state now has the highest population. The sample is no longer in thermal equilibrium and the number of transitions from the  $\alpha$  to the  $\beta$  state becomes slightly lower than the number of  $\beta$  to  $\alpha$  transitions. As a result the bulk magnetization will slowly return (relax) back to its thermal equilibrium magnitude (Figures 15A,B). The kinetics of this relaxation process are described by a single exponential:

$$M_z(t) = [M_z(0) - M_z^{thermal}] \exp\left(-\frac{t}{T_1}\right) + M_z^{thermal} \quad (2.11)$$

with  $M_z(t)$  the magnetization along the z-axis at time  $t$ ,  $M_z^{thermal}$  the bulk magnetization at thermal equilibrium and  $T_1$  the spin-lattice or longitudinal relaxation time. Instead of the relaxation time  $T_1$  the relaxation rate ( $R_1 = 1/T_1$ ) can be reported as well.

The second relaxation process is the spin-spin relaxation, also known as transverse relaxation or  $T_2$ -relaxation. After applying a  $90^\circ$  RF-pulse, the bulk magnetization points along either the x- or y-axis, and the individual spins will start precessing, essentially rotating the bulk magnetization around the static magnetic field. For bulk magnetization to exist, all spins must rotate with the same frequency and with the same phase and this specific

condition is known as coherence. Unfortunately, over time each spin will acquire a slightly different phase and therefore the coherence is lost (cf. Figure 15C,D). The decay is again described by a single exponential decay with a time constant  $T_2$  or rate  $R_2 (= 1/T_2)$ :

$$(M_x(t)^2 + M_y(t)^2)^{1/2} = (M_x(0)^2 + M_y(0)^2)^{1/2} \exp\left(-\frac{t}{T_2}\right) \quad (2.12)$$

with  $M_x$  and  $M_y$  the x and y-components of the transverse magnetization. Transverse relaxation times are always shorter than longitudinal relaxation times. Both longitudinal- and transverse relaxation processes have important practical consequences. First, the rate of decay observed for the FID (Figure 2.3A) is determined by  $T_2$ . Longer  $T_2$  values yield longer-lived signals and sharper peaks in the resulting spectrum. Unfortunately, the value of  $T_2$  is inversely proportional to the size of the molecule (*vide infra*), which renders NMR spectroscopy on large proteins much more difficult. Second, the longitudinal relaxation rate determines the speed by which the bulk z-magnetization can be restored. It is therefore imperative to wait at least the duration of several times  $T_1$  between recording the successive FIDs.

### Origins of relaxation

Completely isolated spins would have near infinite relaxation times as relaxation requires interaction with the environment. In reality, the relaxation of individual spins

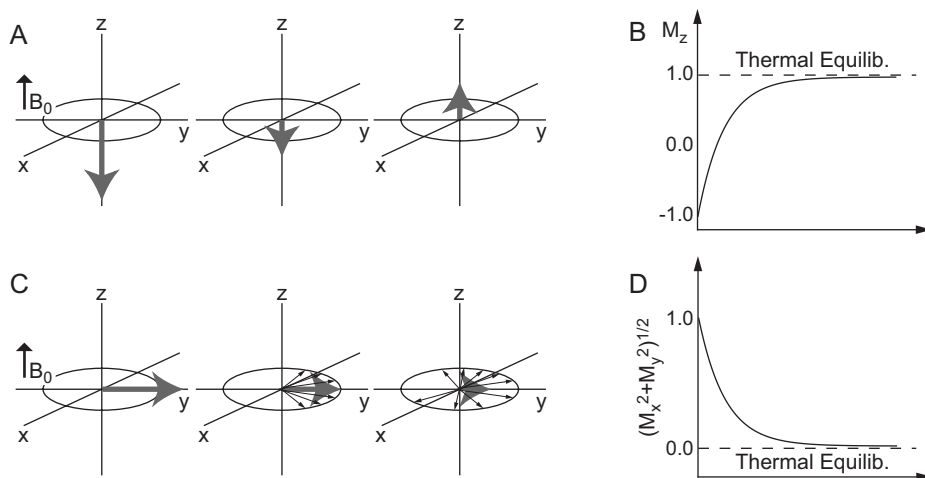


**Figure 2.15.** Pictorial representation of longitudinal (A) and transverse (C) relaxation processes. Time dependence of the  $M_z$  (B) and transverse ( $M_x, M_y$ ) (D) magnetization terms.

is strongly enhanced through interactions with inter- and intramolecular spins and their dynamic properties. The spatial interaction between spins through their dipolar coupling presents one of the dominant relaxation mechanisms and results in transverse relaxation, longitudinal relaxation and the NOE effect. Replacing hydrogen atoms with deuterium atoms effectively reduces the dipolar contribution to the relaxation rates. Equation 2.8 shows the rate of cross-relaxation to be proportional to the square of both  $\gamma$ 's of the cross relaxing nuclei. Replacing most  $^1\text{H}$  with  $^2\text{D}$  decreases the  $\gamma$  by a factor of 6.5, effectively reducing the cross relaxation rates. Similar reasoning applies to the other relaxation rates.

A second important contributing mechanism to the rate of relaxation is the chemical shift anisotropy (CSA). The fluctuating anisotropic magnetic fields generated by the dynamic molecule can induce transitions and destroy coherence. The mechanism is dependent upon the magnitude of the CSA and proportional to the strength of the static magnetic field. The  $^{31}\text{P}$  and  $^{13}\text{C}$  nuclei for example, have large CSA's and suffer from significantly increased relaxation rates with increasing field strength.

### TROSY

The dipolar and CSA contributions to the relaxation rate can either constructively interfere, increasing relaxation rates, or destructively interfere, reducing relaxation rates. Exactly this phenomenon is exploited in the Transverse Relaxation Optimized Spectroscopy (TROSY) experiment (Pervushin *et al.*, 1997). In a regular  $^{15}\text{N}$ -HSQC spectrum, the effects of  $^1J_{\text{NH}}$  couplings are suppressed by spectroscopic techniques, resulting in cross-peaks without splitting in the 2D spectrum. In absence of this suppression, each amide would give rise to four peaks, as result of the splitting by  $^1J_{\text{NH}}$  in both dimensions. It can be shown that as result of dipolar and CSA interference, these four different peaks have experienced different relaxation rates and only for one of the four peaks this interference is destructive, thereby decreasing the relaxation rate. For larger molecules, it becomes advantageous to leave out the decoupling and collapse into a single peak, but rather select for the single component with the favorable relaxation properties.

For large deuterated molecules, the TROSY experiment yields much sharper peaks in the spectrum as compared to the regular  $^{15}\text{N}$ -HSQC experiment (see for excellent review, Fernández and Wider, 2003). As the  $^{15}\text{N}$ -HSQC forms the basis of all triple resonance experiments, special TROSY triple resonance experiments have been developed to exploit this mechanism in the sequential backbone assignment (Konrat *et al.*, 1999; Salzman *et al.*, 1998; Salzman *et al.*, 1999; Yang and Kay, 1999). Furthermore, after

the introduction of the  $^{15}\text{N}$ -HSQC-TROSY other variants emerged, exploiting in essence the same phenomenon on for example methyls (methyl-TROSY, Ollerenshaw *et al.*, 2003; Pervushin *et al.*, 1998; Tugarinov *et al.*, 2004). TROSY, in combination with deuterium labeling, has increased the size of proteins amenable to NMR up to 82 kDa (Tugarinov *et al.*, 2005).

### Dynamics

Although relaxation processes can be considered an unfavorable phenomenon, they contain valuable information on the dynamical processes of the whole molecule. Protein dynamics contribute to the thermodynamic stability of functional states and play an important role in molecular recognition and enzymatic activity (Atkinson and Kieffer, 2004; Mittermaier and Kay, 2006). The dynamics can be probed by the measurement of relaxation rates. For example,  $^{15}\text{N}$  relaxation rates are commonly used to derive protein backbone dynamics (Kay *et al.*, 1989; Palmer *et al.*, 2001) and their measurement has become a standard technique. Other nuclei, such as  $^{13}\text{C}$  can be used as well and are specifically useful to probe side-chain dynamics from methyl moieties (Millet *et al.*, 2002; Skrynnikov *et al.*, 2002).

The  $^{15}\text{N}$  relaxation rates are usually recorded using as series of modified  $^{15}\text{N}$ -HSQC experiments, each with a different time  $t$  during which longitudinal or transverse relaxation is allowed to occur. The resulting spectra are regular 2D  $^{15}\text{N}$ -HSQCs, in which the intensity of the cross-peak is dependent on the time  $t$  and the relaxation rate. Fitting the cross-peak intensities as function of  $t$  with a single exponential decay will give the relaxation rates  $R_1$  or  $R_2$  of individual amides. For practical reasons, the  $R_2$  relaxation rates are usually replaced by the highly similar  $R_{1\rho}$  rates, as these are easier to measure reliably. Finally, a specific NOE experiment, called the steady state  $\{^1\text{H}-^{15}\text{N}\}$ -NOE experiment, is also recorded to extract the cross-relaxation rate. Together the three rates can be used to determine both global tumbling and local backbone dynamics.

The relaxation rates report on the overall tumbling of the molecule. As an example, Figure 2.16B shows a histogram of the  $^{15}\text{N}$   $T_2$  values measured for the Vta1p, a 20 kD protein fused to a GB1 tag. Clearly, the  $T_2$  values originating from the GB1 tag are significantly higher as compared to the values from Vta1p, indicating increased mobility of the tag relative to the protein domain. In addition, a rather large spread in the measured values of Vta1p suggests anisotropic tumbling of the molecule. Analogous to the RDC values, the relaxation rates then become dependent on the orientation of the amide bond vector

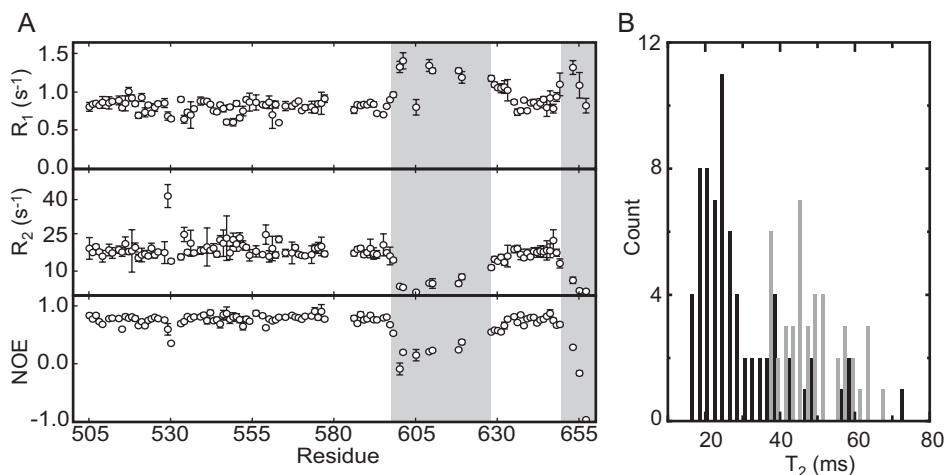


**Figure 2.16.** (A)  $^{15}\text{N}$  backbone relaxation rates of  $R_1$  (upper),  $R_2$  (middle) and NOE (bottom) versus residue of the  $\text{Ca}^{2+}$  free form of the second calcium binding domain. Grey areas indicate highly flexible regions. (B) Histogram of  $^{15}\text{N}$ - $T_2$  values of yeast Vta1p protein fused to GB1 tag. Clearly, GB1  $^{15}\text{N}$ - $T_2$  values (grey) are significantly higher compared to those of the Vta1p protein (black).

with respect to molecular tumbling frame (Figure 2.10C). On the basis of the relaxation rates and the 3D protein structure, the molecular tumbling tensor can be calculated. In addition, it is also possible to compare this outcome with the prediction of programs such as HYDRONMR (de la Torre *et al.*, 2000).

Beyond overall tumbling, the relaxation rates will also report on local backbone dynamics (Kay, 1998; Palmer, 1997). More flexible and unstructured parts of a molecule will generally have lower  $R_2$  and higher  $R_1$  rates as compared to more structured parts of the same protein. Figure 2.16A shows an example for the second calcium binding domain of the  $\text{Na}^+/\text{Ca}^{2+}$ -exchanger, which clearly shows an less-structured loop and C-terminus.

The mathematical description and analysis of relaxation rates into local backbone motion is very complex and dependent on the exact geometrical motional model. The most commonly used analysis is the Modelfree approach, first described by Lipari and Szabo (Lipari and Szabo, 1982a; b). In this approach, the local motion of the amide bond vector is assumed independent of the overall global motion. The local motional properties are characterized by a generalized order parameter  $S^2$  and a characteristic internal correlation time  $\tau_i$ . This type of analysis can nowadays routinely be performed using specific software tools such as MODELFREE (Mandel *et al.*, 1995; Palmer *et al.*, 1991) or TENSOR2 (Dosset *et al.*, 2000).



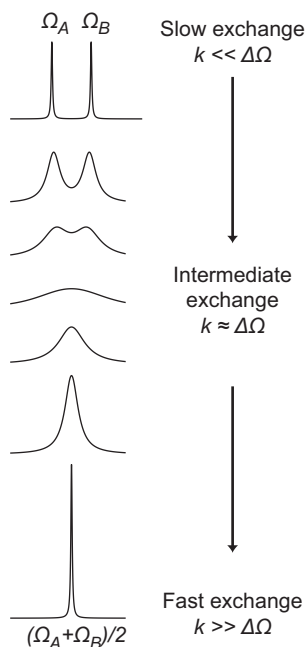


**Figure 2.17.** Spectra of a single spin in a simple two-site chemical exchange process at seven different relative exchange rates, assuming equal populations.

### Chemical Exchange

In addition to transverse relaxation, chemical exchange processes can have a large effect on the appearance and linewidths of the NMR spectra. For simplicity, assume a simple two-site exchange (Equation 2.13), for example a small loop that has two conformations.



We assume that the same nucleus in each conformation will have a different resonance frequency, denoted as  $\Omega_A$  and  $\Omega_B$ , for conformations  $A$  and  $B$ , respectively. The effect of the exchange process on the resulting spectrum depends on the difference in chemical shift frequencies  $\Delta\Omega = |\Omega_A - \Omega_B|$  and the exchange rate  $k$  (cf. Figure 2.17). If the exchange rate is much faster than the chemical shift difference (*i.e.*  $k \gg \Delta\Omega$ ), a single resonance will be observed (so-called fast exchange regime). This can be understood by realizing that during the measurement the resonance frequency of the observed nucleus is

continuously changing from  $\Omega_A$  and  $\Omega_B$  and back. In the opposite situation, when the exchange rate is much slower than the chemical shift difference (*i.e.*  $k < \Delta\Omega$ ), two peaks will be observed. In this slow exchange regime, part of the molecules will be in conformation  $A$  and will give rise to a peak at  $\Omega_A$ , whereas the another part of the molecules will be in conformation  $B$  and will give rise to a peak at  $\Omega_B$ . The intensities of the two peaks will reflect the population of the two conformations. In the particular situation that the exchange rate is approximately as large as the chemical shift difference ( $k \approx \Delta\Omega$ ), then the nucleus is said to be in intermediate exchange. In this situation the linewidths of the observed peaks will broaden, often beyond detection.

## Protein Interactions

Protein-protein and protein-ligand interactions play an essential role in cellular processes and structural information is often essential in understanding these interactions.

The majority of our structural knowledge regarding complexes originates from X-ray crystallography. However, the technique is generally limited to well-structured, high-affinity complexes (O'Connell *et al.*, 2009). In other situations, such as complexes involving highly disordered proteins or interactions with weak affinities, NMR is the only technique that can provide detailed structural information. Furthermore, NMR can also give detailed information on the kinetic aspects and affinity of the interaction.

There are several different methods to study protein-protein and protein-ligand interactions by NMR. For example, inter-domain NOEs yield valuable inter-domain distance restraints. Unfortunately, these NOEs are not easily obtained, especially in the case of weak interactions (Simon *et al.*, 2010). Other methods rely on RDC measurements or paramagnetic relaxation studies (cf. Protein folding). However, the most commonly used method to study protein-ligand interactions is chemical shift perturbation (CSP) (O'Connell *et al.*, 2009). In this method several spectra are recorded with different concentrations of a ligand present in the sample. Commonly, the  $^{15}\text{N}$ -HSQC experiment is used because the chemical shift of the amide is very sensitive to the chemical environment. The presence of a ligand will be immediately translated in to a perturbation of the chemical shift of nearby amides.

The CSP of the second calcium binding domain (CBD2) upon binding of  $\text{Ca}^{2+}$  is used to illustrate the method (Breukels and Vuister, 2010). Figure 2.18A displays an overlay of two  $^{15}\text{N}$ -HSQC spectra in the absence and presence of 10 mM  $\text{CaCl}_2$ . Clear dif-

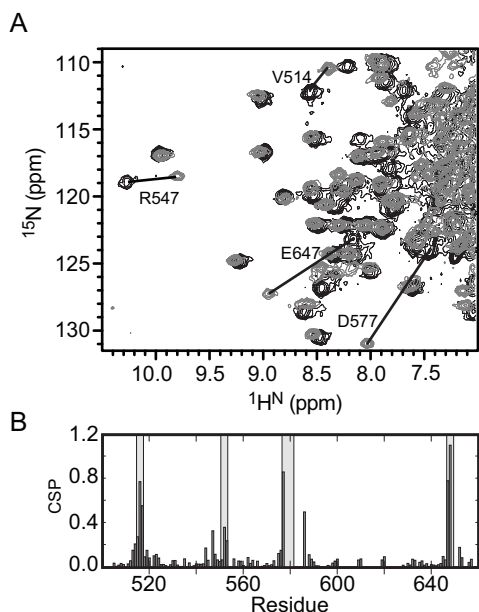


**Figure 2.18.** Chemical shift perturbation (CSP) of the second calcium binding domain of the  $\text{Na}^+/\text{Ca}^{2+}$ -exchanger. (A) Overlay of two  $^{15}\text{N}$ -HSQC spectra recorded in the absence (black) and presence (grey) of 10 mM  $\text{CaCl}_2$ . Several residues show large CSP as indicated by lines. (B) A bar diagram of the combined CSP of  $\text{H}^{\text{N}}$ , N,  $\text{C}^{\alpha}$  and  $\text{C}'$  as function of residue number. Grey areas indicate residues involved in  $\text{Ca}^{2+}$ -binding.

ferences in the spectra are observed for specific residues between the apo and  $\text{Ca}^{2+}$ -bound form of CBD2. Bound  $\text{Ca}^{2+}$  alters the local structure and generates a local electrostatic field, which both change the chemical shift. Thus, maximum CSP values are expected for residues nearby the  $\text{Ca}^{2+}$ , whereas residues far away would remain unperturbed. Mapping the CSP values onto the primary sequence of the protein immediately identifies the structural parts that form the  $\text{Ca}^{2+}$ -binding pocket (Figure 2.18B). In more detail CSP can be used to measure the binding affinity and even binding kinetics, when spectra are recorded at multiple protein ligand concentrations.

CSP identifies the binding interface, however, the CSP is unable to reveal the relative orientation of two binding partners in case of protein-protein interaction. For these complexes several computational data-driven docking approaches have been developed. These programs, such as TreeDock (Fahmy and Wagner, 2002) and Haddock (Dominguez *et al.*, 2003), use the apo-structures of the complex forming proteins and the available interaction, as data measured by CSP or RDC. A model of the complex is subsequently calculated using the CSP and RDC data as restraints, similar to the normal structure calculation procedure. Although these docking routines generate models that are generally of lower resolution compared to X-ray crystallography, they do contain valuable information on the complex interface that could not be obtained otherwise.

## **Protein folding**

### *NMR and protein folding*

NMR spectroscopy is one of the best tools to gain detailed structural and dynamical information about folding states. Non-native states of proteins do not adopt unique three-dimensional structures as folded proteins do, but instead are ensembles of molecules with rapidly fluctuating conformations. Despite their conformational heterogeneity, unfolded and intermediate folding states can be studied by different NMR techniques. However, the dynamical behaviour of unfolded proteins and folding intermediates usually differs substantially. Unfolded proteins exhibit very rapid dynamics and conformational exchange on the (sub)nanosecond timescale, resulting in long transverse relaxation times and hence yielding very sharp cross-peaks in the NMR spectra. In contrast, the ensemble of conformations that forms a folding intermediate or “molten globule” state are characterized by exchange between conformations on the micro- to milli-second timescale, which leads to extensive broadening of the corresponding NMR resonances. The different states and processes in protein folding all demand a different approach; some of these methods

are described in this section.

## Methods

Structural- or dynamical characteristics of unfolded proteins can be determined using straightforward NMR techniques.  $^{15}\text{N}$ -HSQC spectra of unfolded proteins typically show poor dispersion in the  $\text{H}^{\text{N}}$  dimension (Figure 2.6B). In contrast, the dispersion in the  $^{15}\text{N}$  direction is quite good and together with the well-dispersed  $\text{C}'$  resonances they are used for sequential resonance assignments. Backbone resonances of unfolded proteins have chemical shifts close to random coil chemical shifts. Despite the small secondary shifts ( $< 1$  ppm and often a few tenths of a ppm), transient helices formed in unfolded states can be identified using  $\text{C}\alpha$  secondary shifts (Yao *et al.*, 2001). While  $\text{C}'$  chemical shift deviations from random coil values are as sensitive to structure formation as the  $\text{C}\alpha$  chemical shifts are, the sequence dependency of the  $\text{C}'$  random coil values renders their usage problematic. Fortunately, intrinsic referencing, *i.e.* using random coil values of the same polypeptide, solves this problem (Modig *et al.*, 2007). Figure 2.19A shows the  $\text{C}\alpha$  secondary chemical shift of *Azotobacter vinelandii* flavodoxin unfolded in 3.4 M GuHCl as function of residue number (Nabuurs *et al.*, 2008). The chemical shifts of the same protein unfolded in 6.0 M GuHCl were used as random coil values. Three transient helical regions can clearly be identified in this unfolded protein.

Long-range interactions in (partially) unfolded proteins can be probed by using covalently attached nitroxide spin labels at specific sites of a protein. These paramagnetic spin labels cause a distance dependent broadening (PRE) of the resonances of the nuclear spins within a radius of about 15 Å of the label (Schmidt and Kuntz, 1984). The

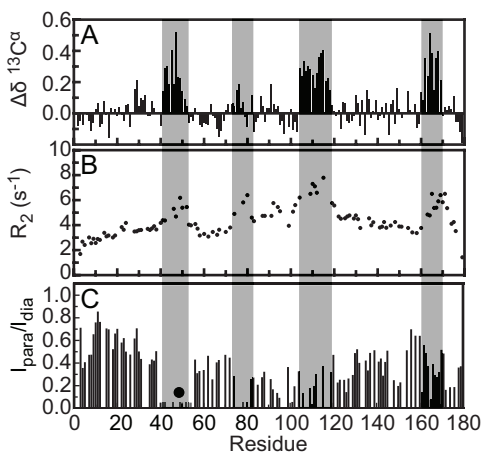


**Figure 2.19.** Residue specific properties of apo-flavodoxin unfolded in 3.4 M guanidine hydrochloride (GuHCl). (A)  $^{13}\text{C}\alpha$  secondary shifts calculated by intrinsic referencing; three regions with transient helical structures are clearly visible. (B)  $R_2$  relaxation rates, four regions are found to be less flexible in unfolded apo-flavodoxin. (C) PRE of amide protons of CMTSL labeled Q48C apo-flavodoxin. The black dot indicates the position of the spin label and dark grey bars indicate residues of which the corresponding cross-peaks have completely disappeared in the paramagnetic state.

$^{15}\text{N}$ -HSQC (or other) spectra of the protein with the label in the paramagnetic (oxidized spin label) and diamagnetic (reduced spin label) state are recorded. The differences between the two spectra in the line widths or intensities of the cross-peaks give an estimate of the average distance between the spin label and any given amide. Figure 2.19C shows the PRE effects originating from the attachment of a spin label at Cys<sup>48</sup> as function of residue number. Not only residues in the direct vicinity of the spin label are affected, but also residues in the other “structured” regions of the unfolded protein show PRE effects, suggesting transient interactions between these regions in the unfolded state (Nabuurs *et al.*, 2010).

Quenched-flow hydrogen-deuterium (H/D) exchange experiments can be used to study molten globule states that give poor NMR spectra and therefore cannot be studied directly (Nabuurs and Van Mierlo, 2010; Nishimura, 2005). The intermediate state of a protein is trapped in D<sub>2</sub>O, for instance by changing the solvent or pH, and after time  $t$  the protein is folded to its native state (quenched) in which no (or very slow) hydrogen exchange occurs. Multiple  $^1\text{H}$ - $^{15}\text{N}$  HSQC spectra of the native protein, recorded for different times  $t$ , allow for extraction of the exchange rates of the intermediate folding state. Partly folded proteins contain secondary structure and amide protons in these structured regions will be protected against exchange (Baum *et al.*, 1989). Rare folding species or partly unfolded forms (PUFs) of a protein can also be detected by H/D experiments using folded proteins (Bai *et al.*, 1995).

Relaxation dispersion experiments constitute variants of the regular  $T_1$  and  $T_2$  relaxation experiments and can be used to detect intermediate folding states that are populated at low levels (*i.e.* at about 0.5 % or higher). Similar to the H/D exchange experiment, information about the intermediate- or unfolded states is obtained indirectly from the resonances of the folded state. Both chemical shift differences between two states as well as (un)folding kinetics can be extracted from the experimental data (Tollinger *et al.*, 2001). For example, the folding intermediate of the Fyn SH3 domain was detected using this technique. By deriving the chemical shifts in combination with RDC data, this even allowed for the determination of an atomic model of the folding intermediate of the FF domain from HYPA/FBP11 (Korzhev *et al.*, 2010).

Protein folding can also be studied at the residue level by measuring a series of  $^{15}\text{N}$  HSQC spectra of protein samples with increasing concentrations of urea or GuHCl as chemical denaturants and following the intensities and chemical shifts of backbone amide resonances. Such experiments have shown that molten globule states do not fold cooperatively as most native states do (Nabuurs *et al.*, 2009; Schulman *et al.*, 1997).

## Conclusions

In this review we have given an overview on the methodology and current practices of biomolecular NMR spectroscopy. NMR spectroscopy not only provides the data to determine high-resolution three-dimensional protein structures, but also yields essential information on dynamics, interactions and kinetics. Development of new NMR experiments is a very active field of research and new techniques continuously emerge. New isotopic labeling schemes, hardware, NMR experiments and computational methods have increased the size of proteins amenable to NMR spectroscopy as well as the quality of the obtained 3D structures, while the time necessary to obtain and analyze all data has decreased. Unfortunately, space limitations refrained us to touch upon promising developments such as  $^{13}\text{C}$  direct detection methods (Felli and Brutscher, 2009), in-cell NMR (Selenko and Wagner, 2007) and dispersion relaxation methods to characterize low-populated protein states (Vallurupalli *et al.*, 2008).

A current challenge concerns characterizing protein complexes. Especially for weak interacting protein complexes, which are difficult to crystallize, NMR will be an essential tool. Obtaining valuable structural and dynamical information will require a combination of different techniques. An excellent example of this current development is the new protocol by Sattler and co-workers, combining both PRE and RDC data (Simon *et al.*, 2010). Another very promising development is the combination of NMR with small angle X-ray or neutron scattering (SAXS/SANS) (Grishaev *et al.*, 2005; Grishaev *et al.*, 2008; Sunnerhagen *et al.*, 1996; Wang *et al.*, 2009). SAXS allows the determination of the overall envelope of the protein complex, whereas NMR can provide detailed information on the individual domains and their relative orientation. Similar combination of techniques can be expected with cryo-electron microscopy or mass spectrometry. Thus, advances in solution NMR spectroscopy as a useful tool in structural biology will not only lie in the development of more powerful experiments, but also in the progress of integrating NMR with other methods.

## Acknowledgements

We thank Wouter Touw for critical reading of the manuscript and Karin Berntsen for help with Figure 2.14. This research was supported by the Netherlands Organization for Scientific Research (NWO) grants 700.55.443 and 700.57.101



# 3

*Binding of calcium is sensed structurally and dynamically throughout the second calcium-binding domain of the sodium/calcium exchanger*

Vincent Breukels and Geerten W. Vuister

*Proteins* (2010) **78**: 1813-1824



## Abstract

We report the effects of  $\text{Ca}^{2+}$  binding on the backbone relaxation rates and chemical shifts of the AD and BD splice variants of the second  $\text{Ca}^{2+}$ -binding domain (CBD2) of the sodium-calcium exchanger. Analysis of the  $\text{Ca}^{2+}$ -induced chemical shifts perturbations yields similar  $K_D$  values of 16 - 24  $\mu\text{M}$  for the two CBD2-AD  $\text{Ca}^{2+}$  binding sites and significant effects are observed up to 20 Å away. To quantify the  $\text{Ca}^{2+}$ -induced chemical shift changes, we performed a comparative analysis of eight  $\text{Ca}^{2+}$ -binding proteins that revealed large differences between different protein folds. The CBD2  $^{15}\text{N}$  relaxation data show the CBD2-AD  $\text{Ca}^{2+}$ -coordinating loops to be more rigid in the  $\text{Ca}^{2+}$ -bound state, as well as to affect the FG-loop located at the opposite side of the domain. The equivalent loops of the CBD2-BD splice variant do not bind  $\text{Ca}^{2+}$  and are much more dynamic relative to both the  $\text{Ca}^{2+}$ -bound and apo forms of CBD2-AD. A more structured FG-loop in CBD2-BD is suggested by increased  $S^2$  order parameter values relative to both forms of CBD2-AD. The chemical shift and relaxation data together indicate that, in spite of the small structural changes, the  $\text{Ca}^{2+}$  binding event is felt throughout the molecule. The data suggests that the FG-loop plays an important role in connecting the  $\text{Ca}^{2+}$ -binding event with the other cytosolic domains of the NCX, in line with *in-vivo* and *in-vitro* biochemical data as well as modeling results that connect the CBD2 FG-loop with the first  $\text{Ca}^{2+}$ -binding domain of NCX.

## Introduction

The calcium ion ( $\text{Ca}^{2+}$ ) is an essential messenger molecule, regulating virtually every process in the cell (Berridge *et al.*, 2003; Carafoli, 2002). Spatial and temporal changes of the cellular  $\text{Ca}^{2+}$  concentration are the trigger for various responses, such as neuronal excitation and muscle contraction. To regulate these responses requires controlled  $\text{Ca}^{2+}$  in- and efflux mechanisms, which is achieved through the integrated action of channels, pumps and exchangers (see Clapham for a review, Clapham, 2007). For example in heart cells,  $\text{Ca}^{2+}$  enters the cytoplasm through  $\text{Ca}^{2+}$  channels leading to muscle contraction. Subsequently, the  $\text{Ca}^{2+}$  needs to be removed to allow for muscle relaxation. In cardiomyocytes the dominant efflux mechanism across the plasma membrane is the  $\text{Na}^+/\text{Ca}^{2+}$ -exchanger (NCX)(Egger and Niggli, 1999) and in its major transport mode it extrudes one  $\text{Ca}^{2+}$  for the counter transport of three  $\text{Na}^+$  (Kang and Hilgemann, 2004).

The NCX protein family comprises four members, three of which are expressed in mammals, i.e. NCX1 (Nicoll *et al.*, 1990), NCX2 (Li *et al.*, 1994) and NCX3 (Nicoll

*et al.*, 1996b), whereas the fourth, NCX4, has only been identified in fish (Marshall *et al.*, 2005). NCX1 is ubiquitously expressed and at least 17 different tissue specific splice variants have been identified. In contrast, NCX2 and NCX3 are mainly expressed in brain and skeletal muscle (Lee *et al.*, 1994; Nicoll *et al.*, 1996b) and no splice variants exists for NCX2 and only three variants are known for NCX3 (Quednau *et al.*, 1996).

Structurally, the NCX is predicted to have nine transmembrane helices (TM) with a large approximately 500 amino acid long cytosolic loop (Iwamoto *et al.*, 1999; Nicoll *et al.*, 1999b). This cytosolic loop contains two Ca<sup>2+</sup>-binding domains, subsequently denoted as CBD1 and CBD2, as well as a third domain tentatively called a-catenin like domain (CLD) (Hilge *et al.*, 2006) of yet unknown function. Structural data at atomic detail of the NCX is currently limited to the two CBD's of NCX1 (Besserer *et al.*, 2007; Hilge *et al.*, 2006; Nicoll *et al.*, 2006) and the closely related Calx- $\beta$  domain of *Drosophila melanogaster* (Wu *et al.*, 2009). Both CBD1 and CBD2 comprise a Calx- $\beta$  motif and exhibit an immunoglobulin fold, composed of a seven-stranded  $\beta$ -sandwich of two anti-parallel  $\beta$ -sheets (cf. Figure 3.1B). CBD1 binds four Ca<sup>2+</sup> ions, mainly coordinated by acidic side chain carboxylate groups located in its AB, CD- and EF-loops connecting the  $\beta$ -strands. In the apo form CBD1 partly unfolds due to repulsion of these negative charges, a process that can be partially alleviated by high salt concentrations (Johnson *et al.*, 2008). In contrast, the CBD2 AD splice variant (CBD2-AD) only binds two Ca<sup>2+</sup> ions with lower affinity and remains structured even in its apo form (Hilge *et al.*, 2006; Hilge *et al.*, 2009) (cf. Figure 3.1C). The carboxyl groups of Glu<sup>516</sup>, Asp<sup>578</sup>, Glu<sup>648</sup> and the carbonyl of Glu<sup>580</sup> form the first Ca<sup>2+</sup> binding site (site I). Site II coordinates the Ca<sup>2+</sup> ion by the carboxyl groups of Asp<sup>552</sup> and Asp<sup>578</sup>. CBD2-AD does not unfold in the apo form, as its crucial Lys<sup>585</sup> points into site II, forming a salt bridge with Asp<sup>552</sup>, thus preventing unfolding.

The activity of the exchanger is carefully regulated by several factors including Na<sup>+</sup> and Ca<sup>2+</sup> itself (Dipolo, 1979; Dipolo and Beauge, 2006; He *et al.*, 2000; Hilgemann, 1990; Hilgemann *et al.*, 1992b; Hilgemann and Ball, 1996). Activation of the exchanger is achieved by binding of Ca<sup>2+</sup> to its binding domains, while high Na<sup>+</sup> can lead to the so-called Na<sup>+</sup>-dependent or I<sub>1</sub>-inactivation. CBD1 has the highest affinity for Ca<sup>2+</sup> with an approximate dissociation constant of 200-800 nM and all its crucial coordinating residues are strictly conserved in all exchangers (Hilge *et al.*, 2006). Therefore, CBD1 is regarded as the primary sensor and binding of Ca<sup>2+</sup> is required for exchanger activation.

Unlike CBD1, CBD2 is subject to alternative splicing in six exons, denoted A to F. Exons A and B are mutually exclusive, whereas the so-called cassette exons C-F can be

combined freely (Kofuji *et al.*, 1994). The important Asp<sup>552</sup>, Asp<sup>578</sup> and Lys<sup>585</sup> residues vary between the different isoforms and splice variants, thereby varying the number of Ca<sup>2+</sup> binding sites between zero and three (Hilge *et al.*, 2009). It is hypothesized that the number and affinity of the Ca<sup>2+</sup> binding sites determines the capability of the exchanger to overcome Na<sup>+</sup>-dependent inactivation. Thus, the differentially expressed CBD2 domains would allow tissue specific alteration of exchange activity to accommodate cell-type specific Ca<sup>2+</sup> needs.

Here, we report results on the NCX1 CBD2-AD and NCX1 CBD2-BD splice variants, also known as NCX1.4 and NCX1.3. Although the CBD2-BD form only differs by twenty-one residues from the CBD2-AD variant, it is unable to bind Ca<sup>2+</sup>. This major difference is a direct consequence of the Asp<sup>578</sup> to Arg substitution in the CBD2-BD variant that abolishes both its Ca<sup>2+</sup> binding sites. NCX1 containing CBD2-BD splice variants have been shown incapable of overcoming Na<sup>+</sup>-dependent inactivation (Dyck *et al.*, 1999; Hurtado *et al.*, 2006), which appears to be a direct consequence of this inability to bind Ca<sup>2+</sup>.

To further explore the detailed mechanisms of Ca<sup>2+</sup> binding in CBD2 we have studied the structural- and dynamical effects of Ca<sup>2+</sup> binding using chemical shift perturbations (CSP) and <sup>15</sup>N relaxation studies by NMR. Significant changes are observed for the residues in the three Ca<sup>2+</sup>-binding loops as well as for residues Met<sup>521</sup> and Val<sup>523</sup> in  $\beta$ -strand B, which are as much as 20 Å away from the Ca<sup>2+</sup> binding site. In order to assess the significance of the observed changes, we compared these with values reported for seven other Ca<sup>2+</sup> binding proteins. Although the Ca<sup>2+</sup> at site I is coordinated by four more carboxylate groups as compared to site II, the binding affinities of both sites are highly similar. Furthermore, we report that the protein backbone motion of CBD2-AD becomes significantly more restricted upon Ca<sup>2+</sup> binding not only in the Ca<sup>2+</sup> binding loops, but also at the C-terminal tail and at the FG-loop located at the opposite site of the domain.

## Methods and Materials

### *Sample preparation*

Samples of CBD2-AD and CBD2-BD of canine NCX were made as previously described (Hilge *et al.*, 2006). In short, nucleotide sequences encoding residues 501–657 of canine NCX1 (accession code P23685; CBD2-AD and CBD2-BD splice variants) were cloned into a pET23b vector and expressed in *E. coli* BL21(DE3) at 37 °C until a optical

density ( $OD_{600}$ ) of 0.8-1.0 was reached. Protein expression was then induced for 3 hrs using 1 mM isopropyl 1-thio- $\beta$ -D-galactopyranoside. Purification was facilitated by N-terminal His tags and anion-exchange chromatography (MonoQ, Amersham-Pharmacia). Purity of all samples was >95% as judged by SDS-PAGE and <sup>15</sup>N-HSQC spectra.

For the relaxation studies the uniformly <sup>15</sup>N/<sup>13</sup>C labeled CBD2-AD sample and the uniformly <sup>15</sup>N labeled CBD2-BD (concentrations of 0.5-1.0 mM) contained 10 mM CaCl<sub>2</sub> (CBD2-AD bound and CBD2-BD) or 10 mM EDTA (CBD2-AD apo). All samples contained 20 mM HEPES pH 7.0, 20 mM  $\beta$ -mercaptoethanol in 95%/5% H<sub>2</sub>O/D<sub>2</sub>O and 0.02% (w/v) NaN<sub>3</sub> as preservative.

Prior to the Ca<sup>2+</sup> titration, the CBD2-AD containing 10 mM EDTA sample was washed using a 10 kDa cut-off centricon filter (Amicon, Millipore). Complete removal of EDTA was confirmed by NMR.

### NMR spectroscopy

All NMR spectra were acquired at 33 °C on Varian Inova 600MHz or 800MHz spectrometers equipped with a standard triple resonance probe and a cold-probe, respectively. For the Ca<sup>2+</sup> titration measurements standard 3D HNCA, HNCOC and 2D <sup>15</sup>N-HSQC experiments were performed.

The  $T_1$ ,  $T_{1\rho}$  and {<sup>1</sup>H,<sup>15</sup>N}-NOE experiments were recorded at 18.8 T in an interleaved fashion. The recorded time intervals for the  $T_1$  and  $T_{1\rho}$  were 16, 256, 384, 512, 1024 ms and 16, 32, 48, 64, 96, 128 ms, respectively. The time delay between saturated and unsaturated parts in the {<sup>1</sup>H,<sup>15</sup>N}-NOE experiments was 13s. All data were processed using the NMRPipe program suite (Delaglio *et al.*, 1995) and analyzed using the program Analysis (Vranken *et al.*, 2005).

### Chemical shift analysis

For CBD2-AD the 3D HNCA, HNCOC and 2D <sup>15</sup>N-HSQC experiments were recorded at seven Ca<sup>2+</sup> to protein ratios: 0:1, 0.52:1.0, 1.55:1, 2.07:1, 3.11:1, 6.21:1, 20.70:1. The protein concentration of was ~480  $\mu$ M at the start of the titration. The backbone chemical shifts were subsequently determined and the total chemical shift perturbation,  $\Delta\delta_{Tot}$ , was calculated according to (Ayed *et al.*, 2001):

$$\Delta\delta_{Tot} = \sqrt{(W_H\Delta\delta_H)^2 + (W_N\Delta\delta_N)^2 + (W_{C\alpha}\Delta\delta_{C\alpha})^2 + (W_{CO}\Delta\delta_{CO})^2} \quad (3.1)$$

with the weight factors  $W_H = 1.000$ ,  $W_N = 0.154$ ,  $W_{Ca} = 0.276$ ,  $W_{CO} = 0.341$ .

Additional  $\text{Ca}^{2+}$ -binding proteins (Figure 3.2) were selected on the basis of available  $\text{H}^N$ ,  $\text{N}$  and  $\text{C}^\alpha$  chemical shifts of  $\text{Ca}^{2+}$ -bound and apo forms in the BMRB databank (Ulrich *et al.*, 2008) (cf. Table S3.2) and availability of a structural ensemble of the  $\text{Ca}^{2+}$ -bound form. The total CSP was determined according to Equation 3.1, without using the carbonyl chemical shifts ( $W_{CO} = 0$ ), as these were not available for all proteins. All selected proteins bind more than one  $\text{Ca}^{2+}$  ion and therefore an average distance for each residue  $i$ ,  $r_{av,i}$ , was defined as:

$$\frac{1}{r_{av,i}^2} = \frac{1}{r_{1,i}^2} + \frac{1}{r_{2,i}^2} + \frac{1}{r_{3,i}^2} + \dots \quad (3.2)$$

where  $r_{1,i}$ ,  $r_{2,i}$ ,  $r_{3,i}$  denote the distance of each of the individual  $\text{Ca}^{2+}$  ions to the  $\text{C}^\alpha$  of residue  $i$ . On the basis of the two proteins with the smallest conformational changes (CBD1 at high salt and the C2 domain of synaptotagmin I) we estimated the CSP to be insignificant at a value of 0.068. For the residues of these two proteins with  $r_{av,i}$  values  $\geq 15.0 \text{ \AA}$ , more than 95% have CSP values  $\leq 0.068$ . To guide the eye in Figure 3.2 the curves  $8.228/r^2$  are displayed, for which the CSP at  $11.0 \text{ \AA}$  equals 0.068.

The binding affinities were determined using an in-house written Mathematica routine. The fitting routine used a two-site independent binding model as described by André and Linse (André and Linse, 2002). Backbone nuclei with significant CSP values ( $^1\text{H}^N > 0.05$ ,  $^{15}\text{N} > 0.35$ ,  $^{13}\text{C}^\alpha > 0.18$  and  $^{13}\text{C}' > 0.15$ ) were used for analysis. All residues were partitioned into three groups: group I sensing  $\text{Ca}^{2+}$  binding site I (residues 515 – 523 and 645 – 654), group II sensing  $\text{Ca}^{2+}$  site II or (residues 544 – 556) and group III sensing both (residues 574 – 576). All CSP values were normalized to 1.0 and subsequently averaged over each group, which were then used for fitting. Errorbars indicate standard error of mean.

In several cases cross-peaks were missing in the second titration point (molar ratio 0.52) due to exchange line broadening. From this observation the exchange rate  $k$  and the lower limit of  $k_{off}$  can be estimated. In the simplest case of one-to-one binding, the exchange rate of the second order reaction is given by:

$$k = k_{off} \left( 1 + \frac{p_{bound}}{p_{free}} \right) \quad (3.3)$$

with  $p_{bound}$  and  $p_{free}$  the fractions of bound and free protein.

Exchange line-broadening is most prominent when:

$$k \approx |\delta_{bound} - \delta_{free}| \quad (3.4)$$

with the  $\delta_{bound}$  and  $\delta_{free}$  the chemical shift of the bound and free species. Under the assumption that at the second titration point all Ca<sup>2+</sup> ions bind to the same site, the upper limit of  $p_{bound}/p_{free}$  is given by  $0.52/0.48 = 1.08$ , yielding a  $k_{off} = 0.48 k$ . However, as both sites have almost identical binding affinities (*vide infra*), a more realistic estimate would be assuming that at most only half the Ca<sup>2+</sup> occupies that given site, thus  $p_{bound}/p_{free} = 0.26/0.74 = 0.35$ , yielding a  $k_{off} = 0.74 k$ .

### Backbone dynamics analysis

Cross-peak intensities and error estimates were obtained by fitting the spectra using the nlinLS routine in NMRPipe (Delaglio *et al.*, 1995). Intensities were subsequently fitted to a single exponential using the modelXY routine in NMRPipe. Error estimates in the rates were obtained using Monte Carlo simulations from the measured intensity errors. Duplicate time points provided internal test for heating effects and other instabilities. Model-free parameters were obtained with the program Tensor2 (Dosset *et al.*, 2000) with a 1.02 Å N-H bond vector length and a CSA of 170 ppm as in the standard treatment. The inherent variation of the CSA tensor was not taken into account. The protein structures used in this analysis were the lowest energy conformers of 2FWU, 2KLS and 2KLT for Ca<sup>2+</sup>-bound CBD2-AD, apo CBD2-AD and CBD2-BD, respectively. The overall tumbling was best fit using an axial symmetric tensor and  $\tau_{av,aniso} = 1/(2D_{||} + 4D_{\perp})$ . The diffusion tensor values were calculated using the appropriate routine in Tensor2 with the core residues in the  $\beta$ -sandwich as input. Subsequently, all model free parameters were determined. Overall average  $S^2$  parameters appear to be too high, with an average of  $S^2$  value of 0.96 for the core residues of Ca<sup>2+</sup>-bound CBD2-AD. The high  $S^2$  are a consequence of too high {<sup>1</sup>H-<sup>15</sup>N}-NOE values, presumably due to incomplete proton saturation. However, the average  $S^2$  values for the  $\beta$ -sandwich core fall within  $\pm 0.02$  for all three samples (cf. Table 3.2), in line with the structurally conserved nature of this scaffold. Furthermore, simulation of the potential errors in  $S^2$  values also showed to have insignificant effects on individual  $\Delta S^2$  values. Therefore comparison of the three samples by using  $\Delta S^2$  values is still valid.

After complete model free analysis the diffusion tensor was calculated again using

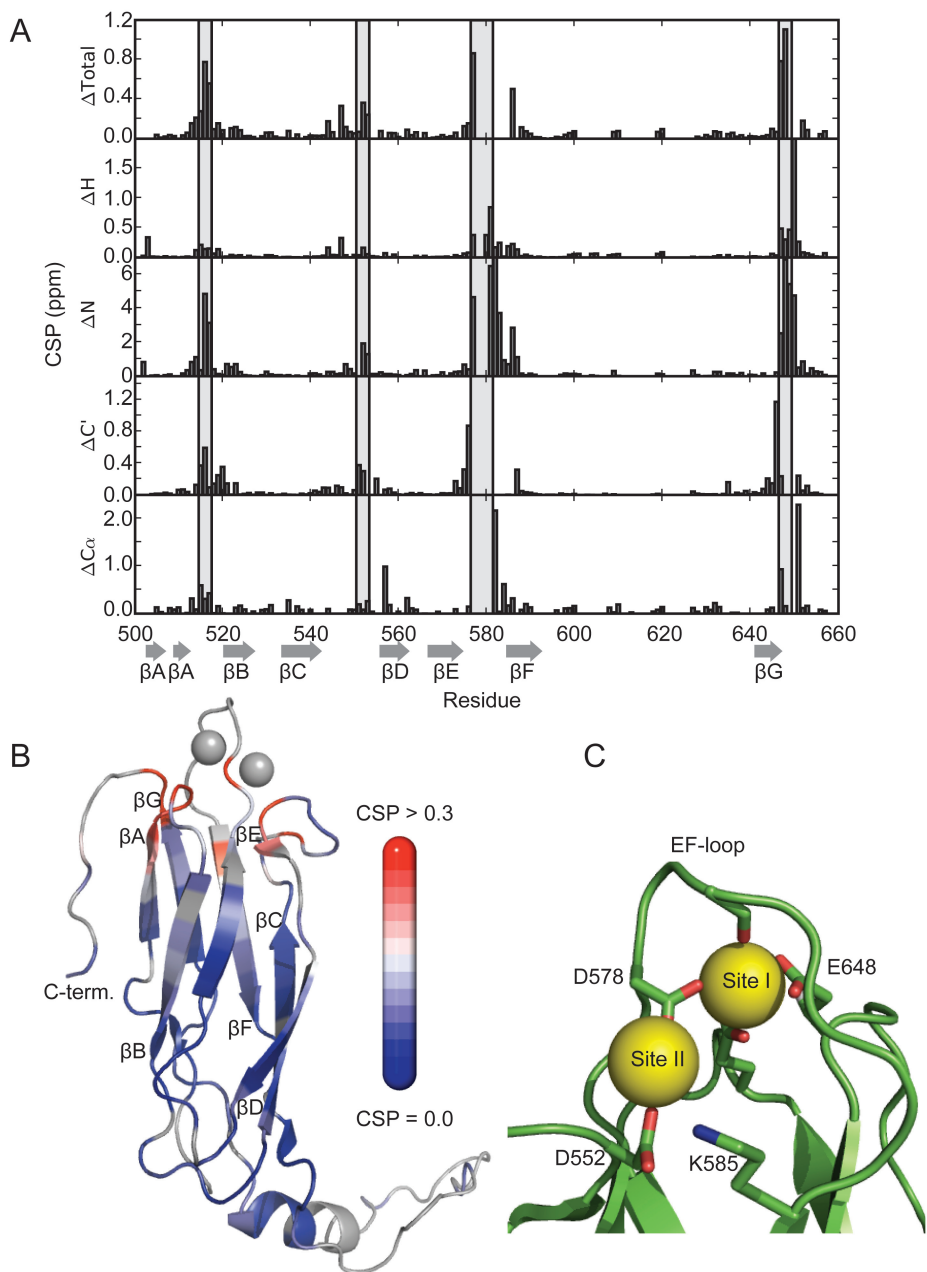


**Figure 3.1.** Chemical shift perturbation (CSP) of NCX1-CBD2-AD. (A) Bardigram of (top to bottom): The total,  $H^N$ , N, C' and  $C^\alpha$  chemical shift perturbation. Total CSP per residue is calculated according to Equation 3.1, using the  $i-1$  backbone carbonyl. The arrows at the bottom indicate  $\beta$ -strands A-F. The light-grey boxes surround the coordinating and adjoining  $Ca^{2+}$ -binding residues (515 – 517, 551 – 553, 577 – 581, 647 – 649). (B) Total CSP mapped on the structure of  $Ca^{2+}$ -bound CBD2-AD, spheres represent  $Ca^{2+}$  ions. (C)  $Ca^{2+}$ -coordinating loops of CBD2-AD with the coordinating carboxylates of Glu<sup>516</sup>, Asp<sup>552</sup>, Asp<sup>578</sup>, Glu<sup>648</sup> (side-chain) and Glu<sup>580</sup> (main chain) and the salt-bridge forming Lys<sup>585</sup> represented as sticks.

all residues that are adequately described by a model using only the single  $S^2$  parameter (the so-called model 1) with  $S^2 > 0.95$ . This procedure was performed iteratively until convergence of the model parameters was reached. Error estimates were calculated on the basis of 100 Monte Carlo cycles using the relaxation rate error as input. All structures showed an anisotropic overall tumbling with  $D_{\parallel}/D_{\perp}$  between 1.4 – 2.0. The data for Ca<sup>2+</sup>-bound CBD2-AD were measured in duplo on two different samples.

The hydrodynamic calculations were performed using fast-HYDRONMR (Ortega and de la Torre, 2005) with the temperature set at 306 K, viscosity at 0.00747 poises, the number of values for the radius of the minibeads at 7, the minimum radius at 1.2 and maximum radius at 2.18. The complete diffusion tensor had highly identical  $D_x$  and  $D_y$  values (within 5%) in all cases, indicating an axial symmetry. Subsequently  $D_{\perp} = (D_x + D_y)/2$  was used to determine the  $\tau_{av,aniso}$  value and the  $D_{\parallel}/D_{\perp}$  ratio. The calculations were performed on all twenty conformers of the same pdb-files used for the <sup>15</sup>N relaxation analysis and were subsequently used to calculate mean and standard deviation of the derived parameters. Visualization and drawing of molecules were done using the program Pymol (Schrödinger, 2010).

## Results

### *Chemical shift perturbation*

Figure 3.1 displays the chemical shift perturbation (CSP) upon Ca<sup>2+</sup> binding as function of residue number. In the upper panel the total CSP is shown, calculated according to Equation 3.1. Large CSP values are observed for residues in the binding loops of CBD2 (cf. Figures 3.1 A and B), with maximum values between 0.35 and 1.10 ppm for residues Ser<sup>517</sup>, Asp<sup>552</sup>, Asp<sup>577</sup>, Lys<sup>585</sup>, Glu<sup>647</sup> and Glu<sup>648</sup>. To assess the magnitude of these changes we examined other Ca<sup>2+</sup> binding proteins for which both structural data and backbone chemical shifts of the apo and Ca<sup>2+</sup>-bound form were available. In Figure 3.2 the total CSP per residue of CBD2-AD and seven other Ca<sup>2+</sup> binding proteins is displayed as function of the  $r^2$ -averaged distance to the Ca<sup>2+</sup> ions (cf. Equation 3.2). The seven proteins, S100A1, S100A13 and CaBP1 (panels A-C), M-crystallin and Tetranectin (panels D, E) and CBD1, C2-domain of synoptotagmin I comprise at least three different classes of Ca<sup>2+</sup>-binding motifs. As expected, the data in Figure 3.2 shows residues near the Ca<sup>2+</sup> binding sites to have the highest CSP and almost all residues with an average distance smaller than 5 Å have a CSP values larger than zero. With the exception of Tetranectin, the magnitude of the largest effect also appears similar between domains of different classes.



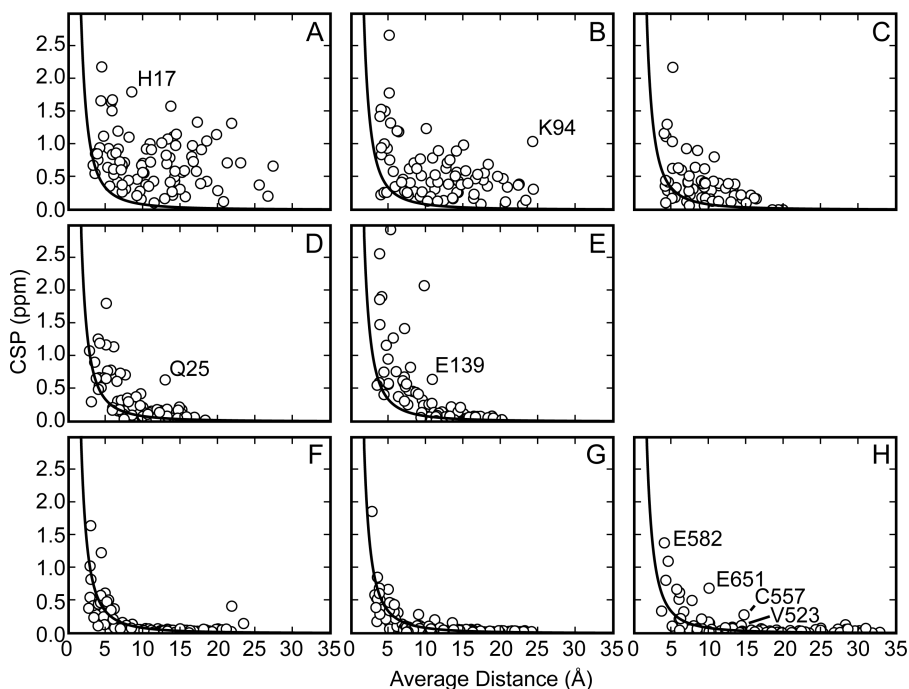


**Figure 3.2.** CSP of eight  $\text{Ca}^{2+}$  binding proteins versus the average distance to the  $\text{Ca}^{2+}$  ions. Black curves are to guide the eye and represent  $8.228/r^2$ , for which the CSP at 11.0 Å becomes insignificant (cf. Methods and Materials). (A) S100A1 (PDB 1zfs)(Baldissieri *et al.*, 1999; Wright *et al.*, 2005), (B) S100A13 (PDB 1yut)(Arnesano *et al.*, 2005), (C) CaBP1 (PDB 2k7d)(Li and Ames, 2008), (D) M-crystallin (PDB 2k1w)(Barnwal *et al.*, 2006; Barnwal *et al.*, 2009), (E) Tetranectin (PDB 1tn3)(Nielbo *et al.*, 2004), (F) CBD1 (PDB 2dpk)(Hilge *et al.*, 2006; Johnson *et al.*, 2008), (G)  $\text{C}_2$  domain of synaptotagmin I (PDB 1byn) (Shao *et al.*, 1997) and (H) CBD2-AD (PDB 2fwu).

Interestingly, the CSP of the individual nuclei ( $\text{N}$ ,  $\text{C}^\alpha$ ,  $\text{H}^\text{N}$ ) can be very small even at short distance of the binding sites (cf. Figure S3.1) and only if the total CSP is taken a non-zero perturbation is observed.

A comparison of the results for the different classes of  $\text{Ca}^{2+}$ -binding proteins reveals distinct differences. For EF-hand containing proteins significant CSP extend to distances up to 20 Å away from the binding site (Figures 3.2A-C), whereas the CSP at this distance is typically negligible for proteins containing the Calx- $\beta$  motif (Figures 3.2F-H).  $\text{Ca}^{2+}$  binding to EF-hand containing proteins is known to induce large conformational changes, whereas the conformational changes for the other proteins are modest (Figures 3.2D,E) or even minor (Figures 3.2F-H).

Ca<sup>2+</sup>-titration

The ability to measure chemical shift perturbations at range of Ca<sup>2+</sup> concentrations enables the determination of site-specific effects of Ca<sup>2+</sup>-binding. We measured <sup>15</sup>N-HSQC, HNCA and HNCOC spectra at seven different protein to Ca<sup>2+</sup> ratios (cf. Methods and materials) and followed <sup>1</sup>H<sup>N</sup>, <sup>15</sup>N, <sup>13</sup>C', <sup>13</sup>C<sup>α</sup> chemical shifts as function of Ca<sup>2+</sup> concentration. Figure 3.3A shows the overlay of <sup>15</sup>N-HSQC spectra recorded at six different protein to Ca<sup>2+</sup> ratios. Surprisingly, the cross-peaks in the spectra shift in an almost uni-directional fashion. This even applies to cross-peaks of residues that are in spatial proximity of both Ca<sup>2+</sup> ions, such as residues Ile<sup>576</sup> and Ile<sup>577</sup>. These two residues precede residue Asp<sup>578</sup> that is involved in the bi-dente coordination of both Ca<sup>2+</sup> ions (cf. Figure 3.1C). This finding is a strong indication that the two binding events have similar binding constants, as for two binding events to give near uni-directional shifts for all cross peaks, both sites need to be approximately equally populated with Ca<sup>2+</sup> at all titration points or Ca<sup>2+</sup> needs to be in fast chemical exchange between the two sites. Furthermore, the cross-peaks of residue that are relative close to either site I or site II shift in a similar fashion.

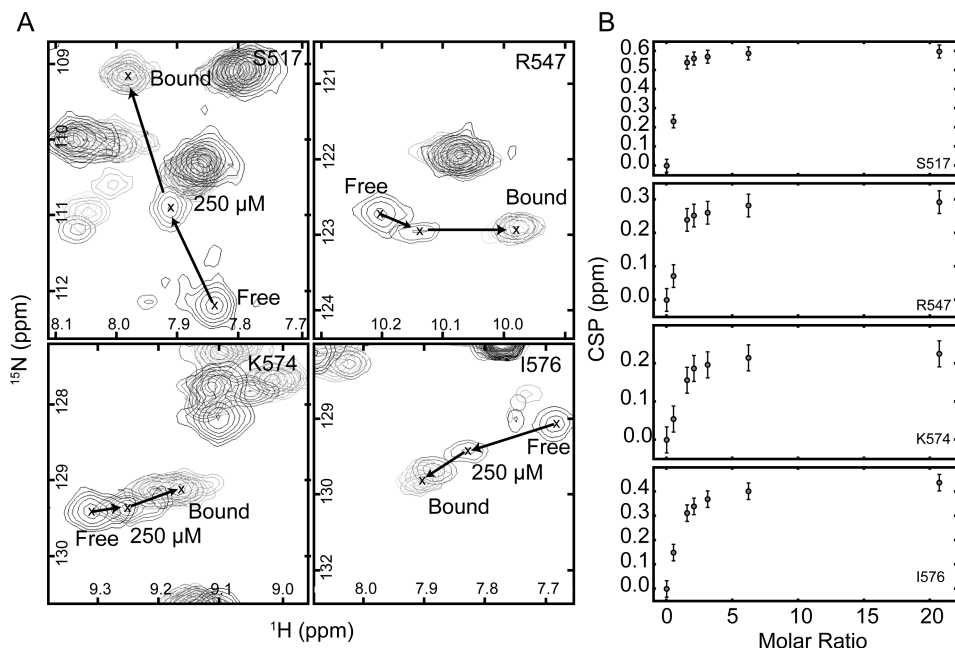


**Figure 3.3** Ca<sup>2+</sup> titration of CBD2. (A) Overlay of six <sup>15</sup>N-HSQC spectra at varying [Ca<sup>2+</sup>] taken in the regions of Ser<sup>517</sup>, Arg<sup>547</sup>, Lys<sup>574</sup> and Ile<sup>576</sup>. (B) Total CSP (cf. Equation 3.1) as function of the protein to Ca<sup>2+</sup> molar ratio for the same residues.

In an effort to quantify the binding events and to try to dissect the binding events into two independent processes, we grouped the residues into three classes. Residues residing in either the A, B or G  $\beta$ -strands or AB-loop (Figure 3.4A, blue) are mainly affected by the binding event at  $\text{Ca}^{2+}$  site I, whereas the residues in the C or D  $\beta$ -strands or CD-loop (Figure 3.4A, red) predominantly are affected by  $\text{Ca}^{2+}$  site II. The residues in the E or F  $\beta$ -strands (Figure 3.4A, yellow) are affected by both binding events. Figure 3.4B shows the relative summed CSP values for residues of these three different classes as function of  $\text{Ca}^{2+}$  to protein ratio. The values are highly similar for the three classes indicating again that the binding affinities of the two sites must be in the same order of magnitude.

To quantify the binding we used a two site independent binding model in which CBD2 can occur in four different states: apo CBD2-AD,  $\text{Ca}^{2+}$  bound to site I,  $\text{Ca}^{2+}$  bound to site II and fully bound CBD2-AD with populations  $P$ ,  $PCa_I$ ,  $PCa_{II}$  and  $PCa_I Ca_{II}$ , respectively, that depend on the affinities of the two sites and the  $\text{Ca}^{2+}$  concentration. We tried to fit the data for each class of residues to this model. The fit yielded  $K_D$  values of 16  $\mu\text{M}$  and 24  $\mu\text{M}$  for site I and II, respectively. The resulting curves are also displayed in Figure 3.4B.

Several residues, e.g. Glu<sup>516</sup>, Asp<sup>577</sup> and Glu<sup>648</sup>, have large <sup>15</sup>N chemical shift differences between apo and  $\text{Ca}^{2+}$ -bound states of 5.1, 4.8 and 6.9 ppm, respectively, resulting in significant exchange broadening during the titration. For these residues the cross-peaks were broadened beyond detection at the second titration point (molar ratio 0.52). The intensity of the cross-peaks is dependent on the exchange rate and chemical shift difference between the holo and apo forms. The exchange rate in turn is protein-ligand concentration dependent. For significant line-shape broadening to occur the exchange rate of the protein ligand binding reaction must be in the order of the chemical shift difference. From these assumptions we determined the exchange regime of the binding event and derived the lower limit of  $k_{\text{off}}$  rates of the exchange reaction (cf. Methods and Materials). We estimate the  $k_{\text{off}}$  values in the order of 197 – 304, 186 – 287 and 268 – 413  $\text{s}^{-1}$  for residues Glu<sup>516</sup>, Asp<sup>577</sup> and Glu<sup>648</sup>, respectively. These values are in good agreement with the values derived previously from a <sup>45</sup>Ca binding assay (Boyman *et al.*, 2009)

### <sup>15</sup>N Relaxation analysis

To gain detailed insight in the mechanisms involved in  $\text{Ca}^{2+}$  binding we also measured the longitudinal ( $T_1$ ) and transversal ( $T_{1\rho}$ ) relaxation times and the steady state <sup>1</sup>H-<sup>15</sup>N nuclear Overhauser effects of CBD2-AD in the  $\text{Ca}^{2+}$ -bound and apo forms and of

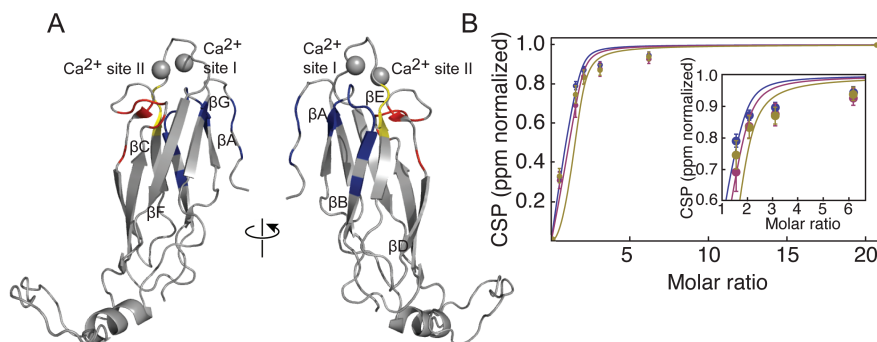


**Figure 3.4.** Partitioning of the residues into the three different subsets differentially responsive to the Ca<sup>2+</sup> binding sites (cf. Methods). (A) Group I: residues in  $\beta$ -strand A, B or G or the AB loop (blue), group II: residues in  $\beta$ -strand C or D or the CD-loop (red) and group III: residues in  $\beta$ -strand E or F (yellow). (B) Chemical shift perturbation of the residues the three groups normalized to 1.0. Lines: Model fit of the three different groups as determined by an in-house written Mathematica script, using the color coding as in (A). Inset displays the expanded region between molar ratio 1 to 6.

a non-binding splice variant, denoted as CBD2-BD (cf. Figure S3.2). We then analyzed these data using the model-free analysis described by Lipari and Szabo (Lipari and Szabo, 1982a; b). This analysis assumes that the local motion is independent of the global motion of the protein and that these occur on substantially different time scale so that they can be separated. The values of the resulting  $S^2$ ,  $\tau_{\text{local}}$  and  $R_{\text{ex}}$  parameters are shown in Figure S3.3.

### Overall tumbling of CBD2

The overall rotational correlation times and the anisotropy ratios were determined from the <sup>15</sup>N relaxation measurements for apo CBD2-AD, Ca<sup>2+</sup>-bound CBD2-AD and CBD2-BD as described in the methods sections and are listed in Table 3.1. Overall tumbling of all three forms of CBD2 is best described by an axial symmetric diffusion tensor with an estimated overall correlation time  $\tau_{\text{av,aniso}}$  of  $\sim 12$  ns and a  $D_{\parallel}/D_{\perp}$  ratio of  $\sim 1.7$ . We also estimated the overall correlation times by hydrodynamic calculations using the program fast-HYDRONMR (Ortega and de la Torre, 2005) (cf. Table S3.1). The values predicted by fast-HYDRONMR are in good agreement with the experimentally derived values.

**Table 3.1** Summary of the overall tumbling motion of Ca<sup>2+</sup>-bound CBD2-AD, apo CBD2-AD and the non-Ca<sup>2+</sup> binding splice variant CBD2-BD

	Ca <sup>2+</sup> -bound CBD2-AD	Apo CBD2-AD	CBD2-BD
$\tau_{\text{anis}} \text{ (ns)}$	13.1 ± 0.9	11.4 ± 2.3	11.8 ± 2.4
$D_{\parallel}/D_{\perp}$	2.08 ± 0.14	1.40 ± 0.28	1.46 ± 0.30

### Local motion

The generalized order parameter  $S^2$  reports on the amplitude of internal motion of the N-H bond vector and its values were determined using the anisotropic tumbling model. Figure 3.5 reports on the changes in  $S^2$  values ( $\Delta S^2$ ) observed between Ca<sup>2+</sup>-bound CBD2-AD and apo CBD2-AD (Figures 3.5A,B) and Ca<sup>2+</sup>-bound CBD2-AD and CBD2-BD (Figures 3.5C,D). As Ca<sup>2+</sup> binding rigidifies the coordinating residues, the largest differences in dynamics were expected to be observed for the binding loops. Indeed,  $S^2$  values increase significantly for residues Arg<sup>547</sup>, Glu<sup>551</sup>, Glu<sup>648</sup> and Ser<sup>649</sup> (Figure 3.5A). Unfortunately, no data is available for residues 578 to 584 in apo CBD2-AD due to missing resonances as a consequence of the increased flexibility and peak overlap. However, for the average  $\Delta S^2$  of the segments surrounding the coordinating residues (residues 516, 517, 551-553, 577 and 647-649) we calculate a value of 0.055 (Table 3.2).

A comparison of the binding loops of Ca<sup>2+</sup>-bound CBD2-AD with the same loops in CBD2-BD again shows increased  $S^2$  values for the former. With an average  $\Delta S^2$  value of 0.22, the difference between Ca<sup>2+</sup>-bound CBD2-AD and CBD2-BD is much larger than the differences between the Ca<sup>2+</sup>-bound and apo forms of CBD2-AD.

Based on the NMR structure ensemble of CBD2 (Hilge *et al.*, 2009) the FG-loop and C-terminus are expected to behave dynamically different from the  $\beta$ -sandwich core. Indeed the average  $S^2$  values of the FG-loop of Ca<sup>2+</sup>-bound CBD2-AD, apo CBD2-AD and CBD2-BD are significantly lower when compared to those of the  $\beta$ -sandwich (Table 3.2). Clearly, the FG-loop of CBD2-BD is distinctly different from both apo and Ca<sup>2+</sup>-bound CBD-AD (Figures 5C,D) with an average  $S^2$  value that is 0.18 and 0.21 higher, respectively.

## Discussion

Ca<sup>2+</sup> binding proteins have been extensively studied using solution NMR spectroscopy (Capozzi *et al.*, 2006; Jensen *et al.*, 2007), but most of these studies involved proteins containing the so-called EF-hand Ca<sup>2+</sup>-binding motif, such as calmodulin, calbindin D<sub>9k</sub>

**Table 3.2** Mean  $S^2$  values of selected fragments of Ca<sup>2+</sup>-bound CBD2-AD, apo CBD2-AD and the non-Ca<sup>2+</sup> binding splice variant CBD2-BD

	Ca <sup>2+</sup> -bound CBD2-AD	Apo CBD2-AD	CBD2-BD
Ca <sup>2+</sup> -binding loops <sup>1)</sup>	0.96 ± 0.05	0.91 ± 0.06	0.75 ± 0.04
β-sandwich <sup>2)</sup>	0.96 ± 0.04	0.95 ± 0.04	0.97 ± 0.05
FG-loop <sup>3)</sup>	0.42 ± 0.26	0.45 ± 0.32	0.63 ± 0.27

<sup>1)</sup> Residues 516, 517, 551-553, 577 and 647-649

<sup>2)</sup> Residues 503-507, 511-515, 520-528, 535-542, 558-562, 586-591, 593-596, 635-637, and 640-647

<sup>3)</sup> Residues 597-632

or S100. Binding of Ca<sup>2+</sup> results in a conformational change for these proteins, thereby transducing the chemical signal of increased Ca<sup>2+</sup> concentration. The Calx-β motif of CBD2, however, is in fold and binding geometry very different from the EF-hand-motif. Structurally, CBD2 is more related to the C<sub>2</sub>-domain, which consists of a β-sandwich of eight anti-parallel β-strands with the L1, L2 and L3 loops connecting the β-strands coordinating the Ca<sup>2+</sup> ions (Shao *et al.*, 1998). The Ca<sup>2+</sup> binding event does not induce large conformational changes, but rather the Ca<sup>2+</sup> binding signal is transduced through an electrostatic switch mechanism (Murray and Honig, 2002), and a similar mechanism has been hypothesized for CBD2 (Hilge *et al.*, 2009).

Using a database approach, we quantified the CSP values of seven Ca<sup>2+</sup>-binding proteins in addition to the values obtained for CBD2. For atoms close to or directly involved in coordination of the Ca<sup>2+</sup> ions, large CSP are typically observed as result of conformational changes and changes in the electronic environments of the nuclei involved. For atoms not directly involved in coordination of the Ca<sup>2+</sup> ions, chemical shift changes upon Ca<sup>2+</sup> binding occur as result of both the structural changes and the effects of the electrostatic field generated by the charges of the ions. The latter changes the polarization of the electrons in the chemical bonds, thus altering the chemical shifts of the nuclei. It is impossible to dissect these individual contributions to the total CSP. However, the direct polarization is not expected to extend beyond a few chemical bonds whereas the electrostatic contribution to the chemical shift is in first approximation dependent on the magnitude of the electric field generated by the charge of the Ca<sup>2+</sup> ion. Therefore, its contribution is expected to depend on  $1/r^2$ , where  $r$  is the distance of the residue to the Ca<sup>2+</sup> ion. Using this assumption and the results of Figure 3.2 we can estimate the spatial upper limit to which the electrostatic effect contributes to the chemical shift. Based on the

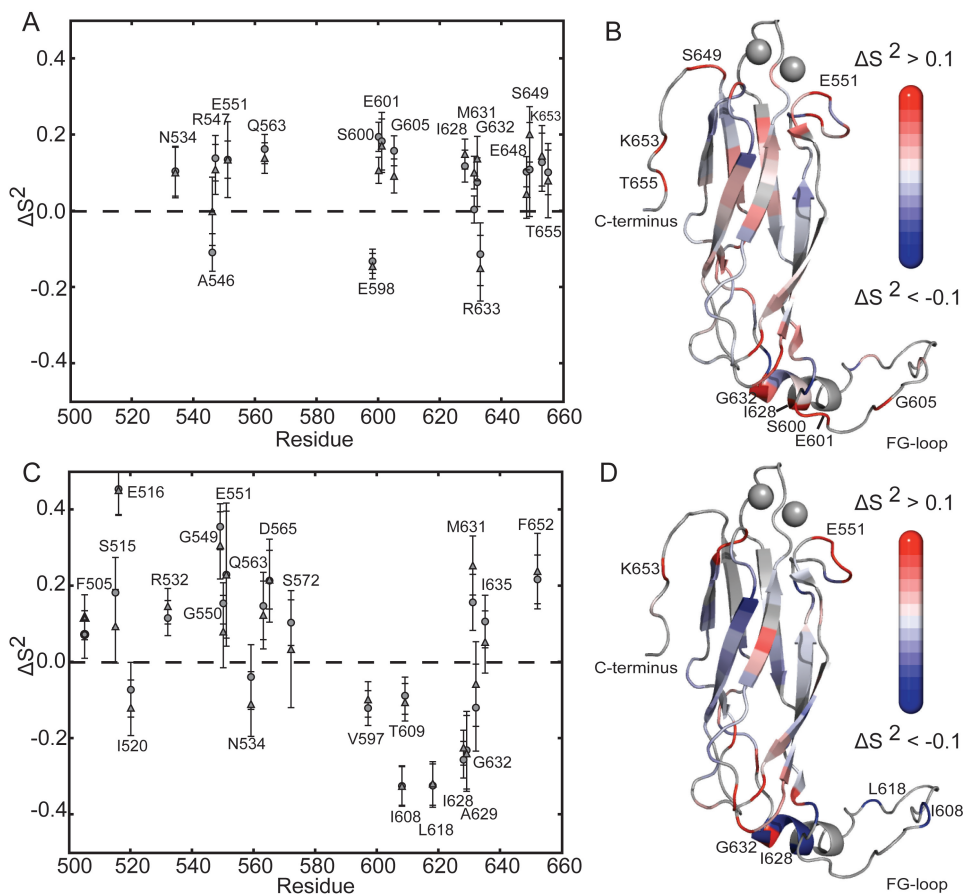


**Figure 3.5.** Change in order parameter ( $\Delta S^2$ ) for Ca<sup>2+</sup>-bound CBD2-AD minus apo CBD2-AD (A,B) and Ca<sup>2+</sup>-bound CBD2-AD minus CBD2-BD (C,D). Panels (A,C) display  $\Delta S^2$  as function of residue (errorbars indicate variation in  $\Delta S^2$  as determined by Monte Carlo simulations, cf. Methods and Materials). For clarity only residues with  $|\Delta S^2| > 0.1$  are shown. Circles and triangles denote duplicate measurements. Panels (C,D) show  $\Delta S^2$  mapped upon the protein backbone with blue to red color coding as indicated.

Calx- $\beta$  proteins that exhibit the smallest conformational changes and the least extended CSP, we estimate this upper limit to  $\sim 11.0$  Å. Larger than anticipated CSP values, i.e. those residues to the right of the black lines in Figure 3.2, identify interesting residues that potentially experience conformational and/or dynamical changes. The data for the EF-hand proteins are self evident: residue His<sup>17</sup> of S100A1 for example (Figure 3.2A), becomes part of an  $\alpha$ -helix, whereas residue Lys<sup>94</sup> of S100A13 (Figure 3.2B) becomes solvent exposed upon Ca<sup>2+</sup>-binding. M-crystallin displays a much more modest conformational

change upon Ca<sup>2+</sup>-binding when compared to the EF-hand proteins, but Gln<sup>25</sup> is a clear outlier (Figure 3.2D). Comparison of the apo and Ca<sup>2+</sup>-bound structures of M-crystallin shows a large displacement of Gln<sup>25</sup>. The CSP of Glu<sup>139</sup> of Tetranectin also is much larger as expected, which can be explained by a considerable change in dynamics between apo and Ca<sup>2+</sup>-bound forms (Nielbo *et al.*, 2004).

In CBD2 the largest displacement is found for Glu<sup>582</sup>, located close to both Ca<sup>2+</sup> ions. The backbone CSP of Glu<sup>651</sup> is much higher than expected for a residue at an effective average distance of 10.1 Å away from the Ca<sup>2+</sup>-binding sites. Likely, this is consequence of the strongly altered dynamics of the C-terminal tail, which becomes much more restricted upon Ca<sup>2+</sup> binding (Figure 3.5). The large CSP of Cys<sup>557</sup> has no biological relevance, but is likely the result of a different oxidation state of the cysteine due to different sample conditions. Finally, Val<sup>523</sup> displays a slightly higher CSP as expected, which is primarily the result of an decreased <sup>15</sup>N chemical shift. Such changes could originate from an altered hydrogen bonding network of the βB and βE-strands.

Using a Ca<sup>2+</sup> titration we monitored the CSP values of CBD2 as function of increasing Ca<sup>2+</sup> concentration. By partitioning the residues affected by Ca<sup>2+</sup>-binding into three classes, we derived  $K_D$  values for the individual binding events. We obtained  $K_D$  values that are a factor 3 to 4 higher than values derived previously by isothermal titration calorimetry (Hilge *et al.*, 2006) and the fit to our simplified two-site model clearly deviates from the experimental data. A more complicated model (eg. a model including intermediate or pre-formed states) might be able to fit this data more accurately. The increase in the number of fit variables and the limited number of titration points does not allow for such derivation. However, it is evident that the binding affinities of both sites are highly similar, which is unexpected from a structural viewpoint. The Ca<sup>2+</sup> ion at binding site I is coordinated by six carboxylate moieties (Figure 3.1C) and hence was expected to have a higher binding affinity when compared to site II, which is only coordinated by two carboxylate groups. How these Ca<sup>2+</sup>-sites can have such similar binding affinities remains unclear, but we speculate entropic contributions to play an important role as the motional properties of the binding loops change upon Ca<sup>2+</sup>-binding (*vide infra*).

The  $k_{off}$  rates of the Ca<sup>2+</sup> binding event compare well with values derived from a <sup>45</sup>Ca binding assay (Boyman *et al.*, 2009). Using the  $K_D$  values of 16 and 24 μM the  $k_{on}$  values are in the order of  $2 \cdot 10^7 \text{ M}^{-1}\text{s}^{-1}$ , which is significantly slower than expected for a purely diffusion-controlled reaction.

Protein motion plays an important role in molecular recognition (Atkinson and



Kieffer, 2004) and the determination of  $^{15}\text{N}$  relaxation rates is commonly employed method to probe such motions (Markwick *et al.*, 2008; Mittermaier and Kay, 2006) including in  $\text{Ca}^{2+}$  binding proteins (Barbato *et al.*, 1992; Tjandra *et al.*, 1996). Upon protein-ligand interactions, such as  $\text{Ca}^{2+}$  binding, changes in the dynamics often occur and are nowadays considered important for the binding process.

The  $^{15}\text{N}$  relaxation data of the three forms of CBD2 were used to determine overall and local motional parameters. The overall tumbling motion of all three forms of CBD2 (Table 3.1) is best described by an axial symmetric diffusion tensor with an estimated overall correlation time  $\tau_{av,aniso}$  of  $\sim 12$  ns and a  $D_{\parallel}/D_{\perp}$  ratio of  $\sim 1.7$ . The  $D_{\parallel}/D_{\perp}$  ratios show that the overall tumbling of CBD2 is highly anisotropic. However, both the anisotropy and the  $\tau_{av,aniso}$  values are considerably higher in the  $\text{Ca}^{2+}$ -bound CBD2-AD when compared to its apo form. This increase was not predicted by the hydrodynamic calculations (Table S3.1), but is in-line with previous findings on CBD1, where the  $\text{Ca}^{2+}$  bound form also displayed higher values relative to the apo form (Johnson *et al.*, 2008). The decrease in anisotropy of the apo state is most likely a consequence of the increased mobility in the binding loops (Figure 3.5), rendering the molecule more isotropic.

The  $\tau_{av,aniso}$  and  $D_{\parallel}/D_{\perp}$  values of CBD2-BD are comparable to those of apo CBD2-AD. However, CBD2-BD does not display significant  $\text{Ca}^{2+}$  binding as judged from chemical shift and ITC data (not shown). Like apo CBD2-AD the structure of CBD2-BD displays flexible  $\text{Ca}^{2+}$  binding loops that similarly would render the molecule more isotropic. The higher flexibility of both apo CBD2-AD and CBD2-BD also explains the differences between the measured and calculated anisotropies, because flexible parts of the protein can be problematic for hydrodynamic calculations (de la Torre *et al.*, 2000).

Multimerization is an often-occurring effect at the relatively high protein concentrations needed for the recording of NMR spectra and potentially of biological significance. As small-angle X-ray scattering (SAXS) data recorded for the combined construct of CBD1, CBD2 and CLD indicated multimerization effects (M. Hilge personal communication), it appeared likely that the individual domains already could display a similar tendency. Dimerization was also reported for the structurally related CAD domains of E-cadherin (Häussinger *et al.*, 2002). In the latter study two CAD domains linked together were reported to form homodimers in their  $\text{Ca}^{2+}$  bound state. However, for CBD2 the  $\tau_{av,aniso}$  values indicate that all three forms are most likely in a monomeric state, as they compare well to those obtained for similar sized proteins.

The  $S^2$  values report on the fast time-scale local motions of the different CBD2

molecules. For all three forms, their values are highly similar for residues located in the  $\beta$ -sandwich core, but significant differences are observed for the Ca<sup>2+</sup> binding loops, the FG-loop and the C-terminus (Figure 3.5, Table 3.2). Upon Ca<sup>2+</sup> binding, the residues in the Ca<sup>2+</sup>-binding loops of CBD2 become more rigid as their average  $\Delta S^2$  value increases by 0.055. This value compares well with the average  $\Delta S^2$  values observed for the Ca<sup>2+</sup>-coordinating segments of the EF-hand motif, which was shown to vary between 0.03 – 0.05 (Maler *et al.*, 2000; Spyrapopoulos *et al.*, 1998). Whereas the EF-hand motif is structurally unrelated to the Calx- $\beta$  fold of CBD2, the first calcium binding domain of NCX1 (CBD1) is structurally very similar. The average  $\Delta S^2$  across the major acidic segment of CBD1 is 0.048 (Johnson *et al.*, 2008), which is less than the value observed for CBD2. As CBD1 partially unfolds upon Ca<sup>2+</sup> depletion and unstructured parts of a protein generally display very low  $S^2$  values a higher average  $\Delta S^2$  would appear logical for CBD1. However, in the study of CBD1 high salt conditions were used in order to enhance the life-time of the sample. We hypothesize that the higher salt content stabilized the highly charged binding loops in the apo form and therefore reduced the differences in the observed  $\Delta S^2$  for CBD1 relative to CBD2 for which the data were recorded at low ionic strength buffer.

Changes in the amplitude of fast time scale dynamics is not restricted to the Ca<sup>2+</sup>-binding loops alone. The FG-loop and C-terminus are also expected to behave dynamically different from the  $\beta$ -sandwich core and these two regions also display a near lack of electron density in the X-ray structures (Besserer *et al.*, 2007). Although no significant difference in the average  $S^2$  values between Ca<sup>2+</sup>-bound CBD2-AD and apo CBD2-AD is observed for residues in the FG loop, Ser<sup>600</sup>, Glu<sup>601</sup>, Gly<sup>605</sup> and Ile<sup>628</sup>, Met<sup>631</sup>, Gly<sup>632</sup> located at the beginning and end of the FG-loop, become more flexible upon Ca<sup>2+</sup>-depletion (Figure 3.5). A similar effect was observed for CBD1 where Ca<sup>2+</sup> depletion resulted in increased mobility for residues located at the opposite end relative to the Ca<sup>2+</sup>-binding site.

The  $S^2$  values of residues Lys<sup>653</sup> and Thr<sup>655</sup> in the C-terminus of CBD2-AD become significantly higher upon Ca<sup>2+</sup>-binding. Although the C-terminus appears to be unstructured in the NMR ensemble of Ca<sup>2+</sup>-bound CBD2-AD (Hilge *et al.*, 2006), these current data indicate that the C-terminus in the Ca<sup>2+</sup>-bound form becomes more structured. Also the CSP data support such Ca<sup>2+</sup> induced changes, as significant chemical shift perturbations are found up to residue Ser<sup>654</sup>.

CBD2-BD differs from CBD2-AD in only twenty-one residues, seven of which are located in the FG-loop and the remainder in the preceding  $\beta$ E and  $\beta$ F-strands and EF loop.  $S^2$  values of the Ca<sup>2+</sup> binding loops in CBD2-BD are much lower as compared

to both  $\text{Ca}^{2+}$ -bound CBD2-AD and apo CBD2-AD (Figures 5C,D; Table 3.2), indicative of a much more disordered state of CBD2-BD. Indeed, the  $\text{Ca}^{2+}$ -binding loops in the CBD2-BD NMR ensemble show considerable more structural variation as compared to apo CBD2-AD as illustrated by their pairwise  $\text{C}^\alpha$  RMSD of  $3.3 \pm 0.3 \text{ \AA}$  and  $1.1 \pm 1.4 \text{ \AA}$  for CBD2-BD and apo CBD2-AD, respectively.

Surprisingly, increased  $S^2$  values were observed for the FG-loop of CBD2-BD relative to both  $\text{Ca}^{2+}$ -bound and apo CBD2-AD (Figure 3.5), even though the twenty-one different residues of CBD2-BD reside in the  $\beta\text{E}$  and  $\beta\text{F}$  strands. These increased  $S^2$  values suggest a potential differential role for this loop in CBD2-BD compared to CBD2-AD. Mutational studies on the FG-loop of other proteins with the immuno-globular fold have reported similar effects and have also shown that their dynamical differences alter receptor specificity (Carr *et al.*, 1997; Cota *et al.*, 2000; Siggers *et al.*, 2007). Furthermore, although the FG loop is largely unstructured in the isolated CBD2 domain, in the intact exchanger the FG-loop is modeled to be near the  $\text{Ca}^{2+}$  binding sites of CBD1. The interaction between the FG-loop of CBD2 with the binding sites of CBD1 is shown to increase the affinity of these binding sites (Hilge *et al.*, 2009) *in vitro*. *In vivo* recordings showed that response of NCX 1 is 10-times faster for ACDEF variant, which has an elongated FG loop in CBD2, as opposed to the AD variant (Dyck *et al.*, 1999). It is thus tempting to speculate that the influence of the FG-loop on the binding sites of CBD1 is different for BD containing NCX splice variants compared to AD variant due to the altered motion properties of CBD2-BD.

## Conclusions

Our chemical shift data show highly similar  $\text{Ca}^{2+}$  affinities of both binding sites even though the primary site has six coordinating carboxylates and secondary site only two. Significant chemical shift perturbations in response to  $\text{Ca}^{2+}$ -binding are observed for residues up to 20  $\text{\AA}$  away from the binding site. Analysis of the  $^{15}\text{N}$  relaxation data not only shows altered backbone dynamics in the  $\text{Ca}^{2+}$  coordinating loops, but also in the opposite-located FG loop. The dynamics of this same loop is also altered for the BD splice variant relative to the AD variant, albeit in an opposite fashion. Together these data indicate that, in spite of the small structural changes of the CBD2  $\beta$ -barrel core, the  $\text{Ca}^{2+}$  binding event is felt throughout the molecule. Moreover, the data also suggest that, in contrast to a previous study (Ottolia *et al.*, 2009), the FG-loop plays an important role in connecting the  $\text{Ca}^{2+}$ -binding event with the other cytosolic domains of the NCX. However, this notion is

in-line with *in-vitro* data that show the CBD1 Ca<sup>2+</sup>-affinity to be modulated by the presence of cassette exons that change the FG-loop. Modeling of the combined CBD1-CBD2 domains also positions the CBD2 FG-loop in close proximity to the CBD1 Ca<sup>2+</sup>-binding sites, thus providing for a mechanism that can explain the *in-vivo* observed dependence of the regulatory behavior of the NCX on the nature of the CBD2 FG-loop and the saturation of its Ca<sup>2+</sup>-binding sites.

## Acknowledgements

We thank Dr. Mark Hilge for critical discussions and Mr. Jan Aelen for expert assistance with the CBD2 production and purification. This research was supported by the Netherlands Organization for Scientific Research (NWO) grants 700.55.443 and 700.57.101.

## Supplementary Information: Figures and Tables

**Table S3.1.** Summary of the results of hydrodynamic calculations on the overall rotational correlation time and anisotropy using all structures in the ensemble.

	Ca <sup>2+</sup> -bound CBD2-AD	Apo CBD2-AD	CBD2-BD
$\tau_c$ (ns)	12.1 ± 0.1	13.2 ± 0.3	12.6 ± 0.1
$D_{\parallel}/D_{\perp}$	1.74 ± 0.29	1.68 ± 0.42	1.73 ± 0.12

**Table S3.2.** List of all BMRB and PDB databank entries used for Figure 3.2.

Name	BMRB entry <sup>1)</sup> (apo)	BMRB entry <sup>1)</sup> (holo)	PDB entry <sup>2)</sup>
S100A1	4285	6583	1zfs
S100A13	6532	6531	1yut
CaBP1	15197	15623	2k7d
M-crystallin	6903	6904	2k1w
Tetranectin	6007	6008	1tn3
CBD1	15764	7009	2dpk
C2 domain of synaptotagmin I	4039	4041	1byn
CBD2 <sup>3)</sup>	This work	7009	2fwu <sup>3)</sup>

<sup>1)</sup> <http://www.bmrw.wisc.edu/>

<sup>2)</sup> <http://www.rcsb.org/pdb/home/home.do>

<sup>3)</sup> Structure 2fwu is the NMR structure of CBD2-AD. In this study an improved NMR structure is used.

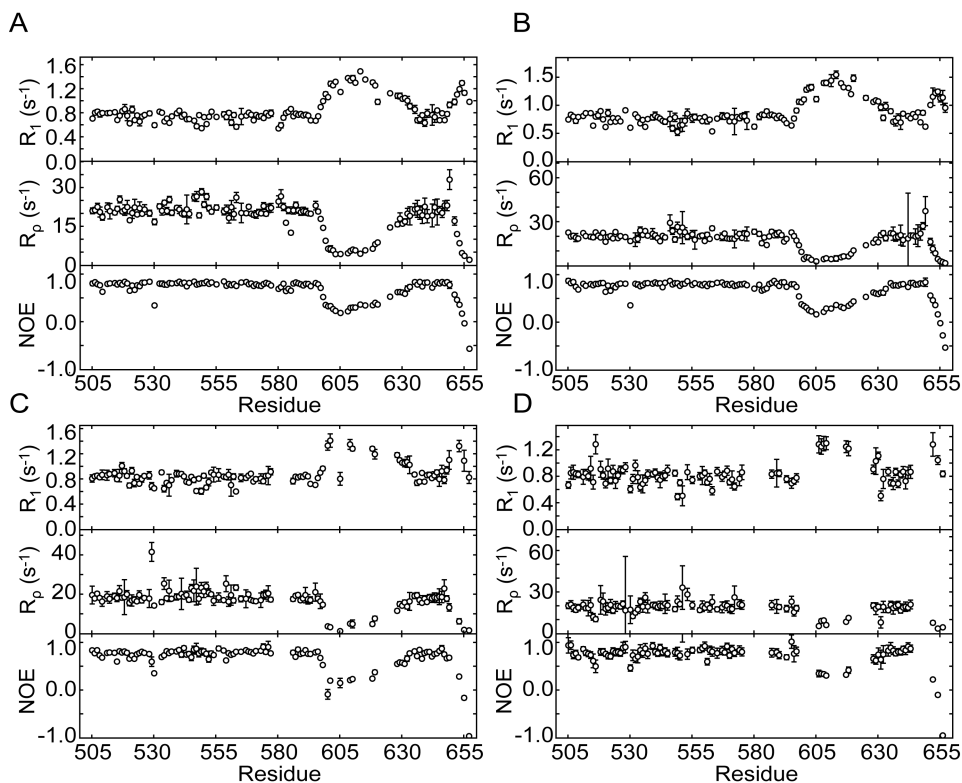
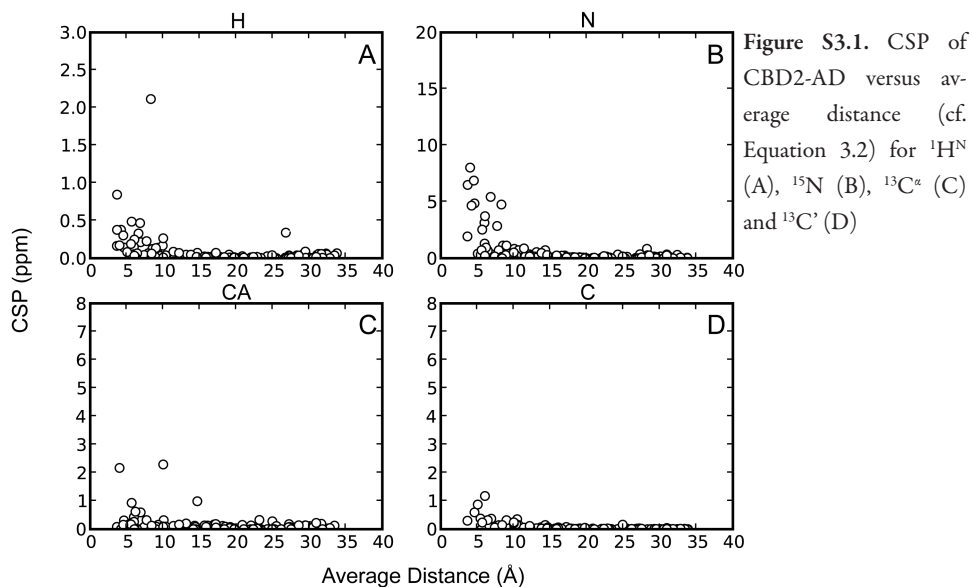


**Figure S3.2.**  $^{15}\text{N}$  backbone relaxation rates of  $R_1$  (upper),  $R_{\rho}$  (middle) and NOE (bottom) versus residue of  $\text{Ca}^{2+}$ -bound CBD2-AD (A and B, duplicate measurements on two different samples), apo CBD2-AD (C) and CBD2-BD (D).

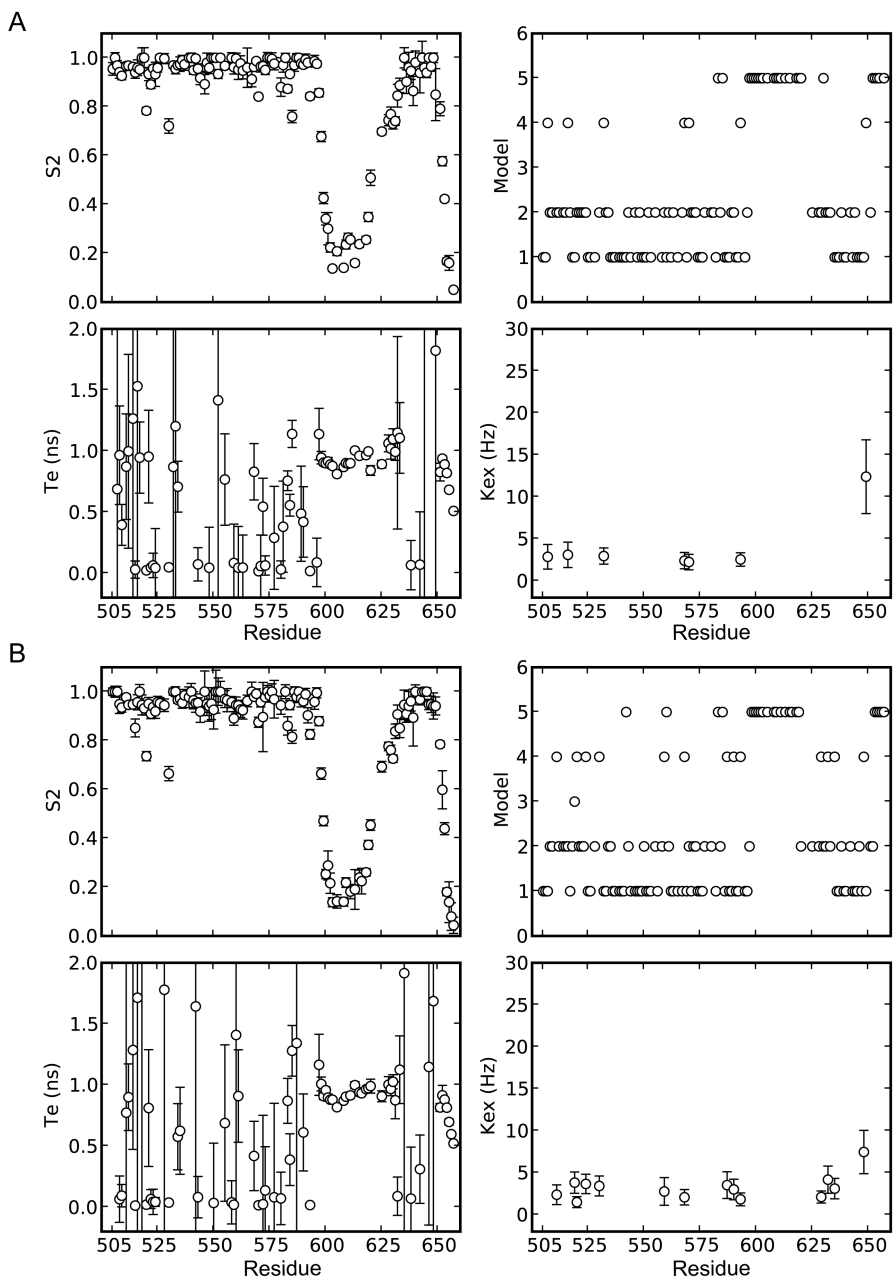


**Figure S3.3.** Model parameters  $S^2$  (upper left),  $\tau_c$  (bottom left), Model (upper right) and  $R_{ex}$  (bottom left) of CBD2 residue of Ca<sup>2+</sup>-bound CBD2-AD (A and B), apo CBD2-AD (C) and CBD2-BD (D).

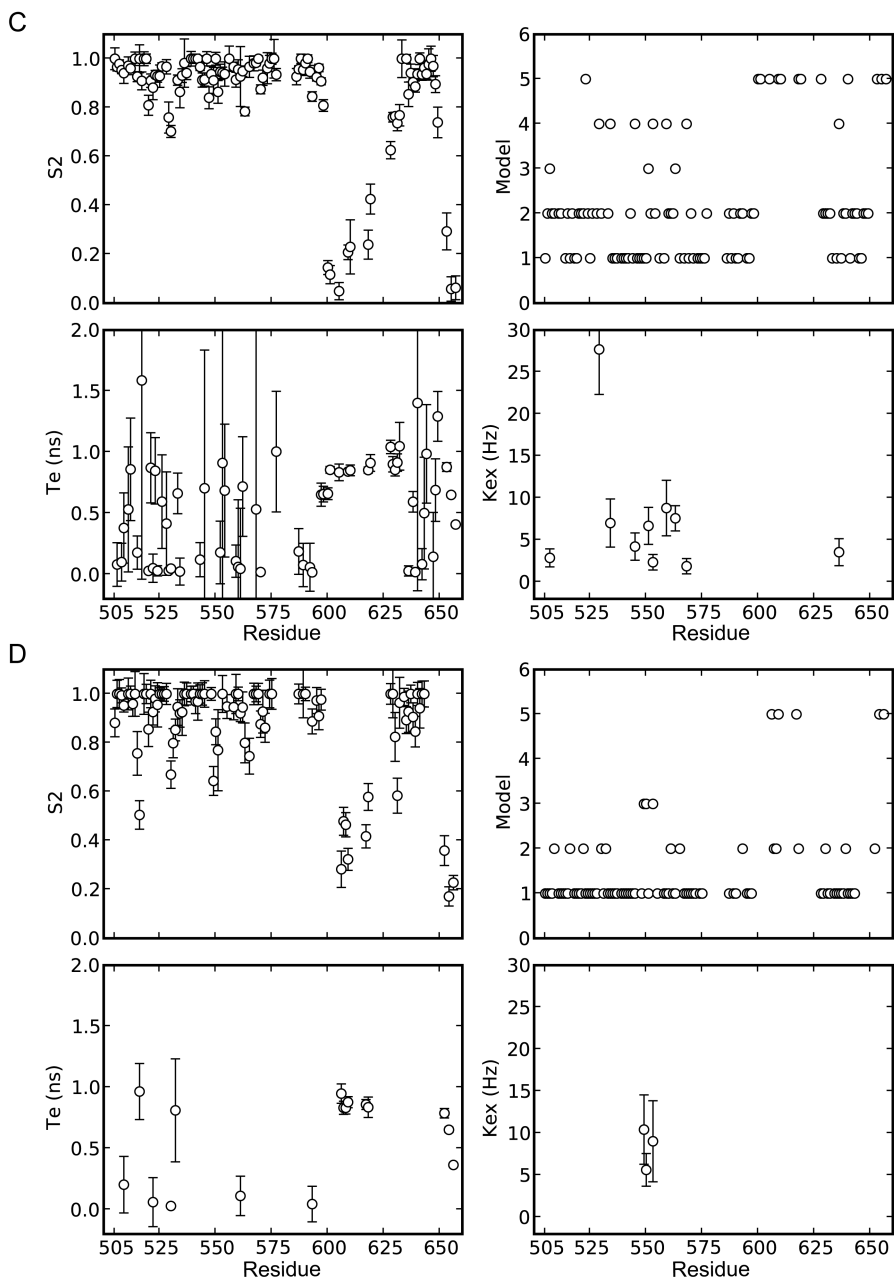


**Figure S3.3.** Model parameters  $S^2$  (upper left),  $\tau_e$  (bottom left), Model (upper right) and  $R_{ex}$  (bottom left) of CBD2 residue of  $\text{Ca}^{2+}$ -bound CBD2-AD (A and B), apo CBD2-AD (C) and CBD2-BD (D).

# 4

*The second  $\text{Ca}^{2+}$ -binding domain of NCX1 binds  $\text{Mg}^{2+}$  with high affinity*

Vincent Breukels, Albert Konijnenberg, Sanne M. Nabuurs, Wouter G. Touw and Geerten W. Vuister

*Biochemistry* (2011) **50**: 8804-8812



## Abstract

We report the effects of  $Mg^{2+}$ -binding to the second  $Ca^{2+}$ -binding domain (CBD2) of the sodium-calcium exchanger. CBD2 is known to bind two  $Ca^{2+}$  ions using its  $Ca^{2+}$ -binding sites I and II. Here, we show by nuclear magnetic resonance (NMR), circular dichroism, isothermal titration calorimetry and mutagenesis, that CBD2 also binds  $Mg^{2+}$  at both sites, but with significantly different affinities. The results from  $Mg^{2+}/Ca^{2+}$  competition experiments show that  $Ca^{2+}$  can replace  $Mg^{2+}$  from site I, but not site II and that  $Mg^{2+}$  binding affects the affinity for  $Ca^{2+}$ . Furthermore, thermal unfolding circular dichroism data demonstrate that  $Mg^{2+}$  binding stabilizes the domain. NMR chemical shift perturbations and  $^{15}N$  relaxation data reveal that the  $Mg^{2+}$ -bound CBD2 adopts a state intermediate between the apo- and fully  $Ca^{2+}$ -loaded forms. Together, the data show that at physiological  $Mg^{2+}$  concentrations CBD2 is loaded with  $Mg^{2+}$  preferentially at site II, thereby stabilizing and structuring the domain and altering its affinity for  $Ca^{2+}$ .

## Introduction

The  $Na^+/Ca^{2+}$ -exchanger (NCX) is a near-ubiquitous plasma membrane protein that plays a major role in the extrusion of  $Ca^{2+}$ . With three mammalian isoforms and numerous splice variants known, the exchanger is expressed in virtually every tissue (Egger and Niggli, 1999; Quednau *et al.*, 1996). To remove  $Ca^{2+}$  against the electrochemical gradient, the exchanger utilizes the energy stored in the  $Na^+$ -gradient generated by the  $Na^+/K^+$ -ATPase (Lytton, 2007). In its dominant mode, NCX exchanges one  $Ca^{2+}$  ion for the uptake of three  $Na^+$  ions (Kang and Hilgemann, 2004) and the activity is strictly regulated. Only low concentrations above basal levels of the intracellular  $[Ca^{2+}]$  are required for activation, whereas increased intracellular  $Na^+$ -concentrations leads to a process called  $Na^+$ -dependent inactivation (Hilgemann *et al.*, 1992b). The allosteric activation by  $Ca^{2+}$  is exclusively ascribed to binding of  $Ca^{2+}$  ions to two  $Ca^{2+}$ -binding domains (subsequently denoted as CBD1 and CBD2), whereas the exact site of  $Na^+$  interaction remains to be established. CBD1 and CBD2 reside in the  $\sim 500$  amino acid long cytosolic loop between transmembrane helices five and six (Iwamoto *et al.*, 1999; Nicoll *et al.*, 1999a), which further contains a third domain tentatively named  $\alpha$ -catenin like domain (CLD) (Hilge *et al.*, 2006).

The ion affinity of calcium binding proteins must be highly specific for  $Ca^{2+}$  as opposed to  $Mg^{2+}$ . Cytosolic levels of free  $[Mg^{2+}]$  range between 0.5 - 1.0 mM (Saris *et al.*, 2000), whereas cytosolic levels of free  $[Ca^{2+}]$  are around  $\sim 100$  nM, which increase

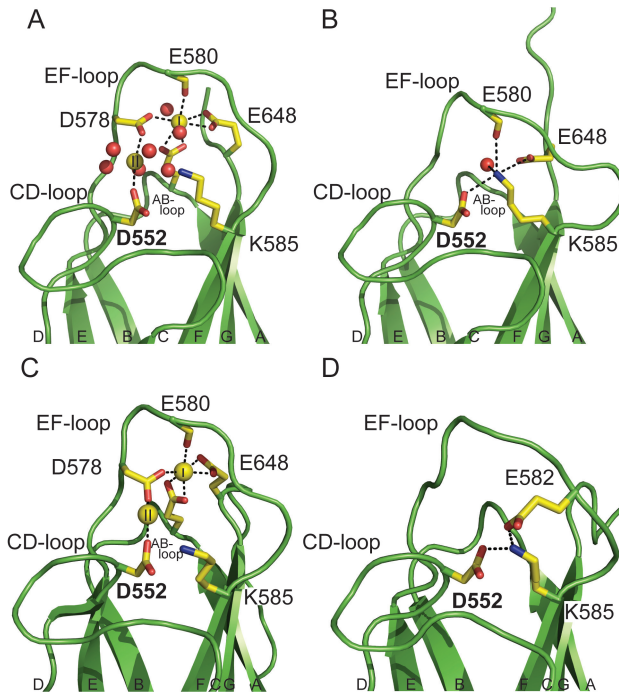


**Figure 4.1.** Ribbon diagrams of the X-ray and NMR structures of the apo- and Ca<sup>2+</sup>-bound forms of the wt-CBD2. Main chain shown in green ribbon, red spheres indicate water molecules, yellow spheres the primary (I) and secondary (II) Ca<sup>2+</sup> ions and strand labels are indicated at the bottom. (A) Ca<sup>2+</sup>-bound form X-ray structure (PDB: 2QVM); coordination depicted with dashed lines and coordinating residues as yellow sticks. (B) Ca<sup>2+</sup>-free form X-ray structure (PDB: 2QVK); Lys<sup>585</sup> points towards the secondary Ca<sup>2+</sup> binding site, forming salt-bridges to Asp<sup>552</sup> and Glu<sup>648</sup> and a hydrogen bond to Glu<sup>580</sup>, as indicated with dashed lines. (C) Ca<sup>2+</sup>-bound NMR structure (refined (Spronk *et al.*, 2002) using original restraints of PDB entry 2FWU and Ca<sup>2+</sup>-coordination derived from 1QVM) (D) Ca<sup>2+</sup>-free form NMR structure (PDB: 2KLS); Lys<sup>585</sup> forms a salt bridge with Asp<sup>552</sup> and Glu<sup>582</sup>, but not with Glu<sup>648</sup>.

up to levels of  $\sim 2 \mu\text{M}$  near the membrane during processes such as neuronal excitation or muscle contraction (Laude and Simpson, 2009). To be functional Ca<sup>2+</sup> sensors, Ca<sup>2+</sup> binding proteins must have at least a three order of magnitude higher affinity for Ca<sup>2+</sup> over Mg<sup>2+</sup>. Furthermore, Mg<sup>2+</sup> concentrations are known to fluctuate under physiological conditions and in dialyzed axons (DiPolo and Beauge, 2008), as well as in cardiomyocytes. NCX activity is decreased by high intracellular [Mg<sup>2+</sup>], possibly by competing with Ca<sup>2+</sup> at the regulatory sites (Levitsky *et al.*, 1994; Wei *et al.*, 2002). A more recent *in vitro* study showed that in both CBD1 and CBD2, Mg<sup>2+</sup> competes for Ca<sup>2+</sup> (Boyman *et al.*, 2009), however with striking differences between the two domains. For CBD1 the apparent af-

finity for  $\text{Ca}^{2+}$  decreases at high  $\text{Mg}^{2+}$  concentrations (5 mM  $\text{MgCl}_2$ ), but the number of  $\text{Ca}^{2+}$  ions bound by CBD1 remains the same. In CBD2, high  $[\text{Mg}^{2+}]$  results in the binding of only one instead of two  $\text{Ca}^{2+}$  ions, even at elevated  $[\text{Ca}^{2+}]$  and the apparent affinity for  $\text{Ca}^{2+}$  at the remaining binding site increases.

To date detailed atomic structural information for the NCX is limited to CBD1 and CBD2 (Besserer *et al.*, 2007; Hilge *et al.*, 2006; Hilge *et al.*, 2009; Nicoll *et al.*, 2006; Wu *et al.*, 2009; Wu *et al.*, 2010) and the exact mechanism by which they jointly regulate the exchanger in its cellular context remains poorly understood. The NMR and X-ray structures revealed a large structural similarity between CBD1 and CBD2, both consisting of a seven-stranded  $\beta$ -sandwich with the connecting loops forming the  $\text{Ca}^{2+}$  binding sites. In NCX 1, CBD1 binds four  $\text{Ca}^{2+}$  ions with high affinity and is considered the primary  $\text{Ca}^{2+}$  sensor activating the exchanger, whereas CBD2 is capable of binding two  $\text{Ca}^{2+}$ -ions (cf. Figure 4.1) and deemed responsible for the secondary response (Hilge *et al.*, 2009). Recently, we postulated that CBD1 and CBD2 activate the exchanger by acting as an electrostatic switch (Hilge *et al.*, 2009). In the electrostatic switch mechanism, binding of  $\text{Ca}^{2+}$  leads to a significantly more positive electrostatic potential of the domain, thereby changing the electrostatic interactions with nearby domains. Small angle X-ray scattering data on the NCX showed that the angle between CBD1 and CBD2 changes upon binding of  $\text{Ca}^{2+}$  and we proposed that this is due to the altered electrostatic potential of CBD1. By the same mechanism, binding of  $\text{Ca}^{2+}$  to CBD2 would induce changes to the nearby CLD or membrane part, thereby overcoming the  $\text{Na}^+$ -inactivation at elevated cytosolic  $\text{Ca}^{2+}$  levels (Hilge *et al.*, 2009). Binding of  $\text{Mg}^{2+}$  to CBD2 would be an additional factor in the electrostatic regulating mechanism, as this also introduces positive charge into CBD2.

We have investigated, using NMR, mutational analysis, circular dichroism (CD) and isothermal titration calorimetry (ITC), the  $\text{Mg}^{2+}$  binding properties of CBD2. We show that  $\text{Mg}^{2+}$  preferentially binds to the site II of CBD2 and with a much lower affinity to site I. Binding of  $\text{Mg}^{2+}$  leads to significant structural rearrangements that stabilize the domain. Furthermore, the overall tumbling and backbone dynamics of  $\text{Mg}^{2+}$ -CBD2 determined using  $^{15}\text{N}$  relaxation measurements reflect an intermediate bound state of  $\text{Mg}^{2+}$ -CBD2 when compared to its apo- and  $\text{Ca}^{2+}$ -bound forms. Finally, the results show that under physiological conditions, site II of CBD2 is preferentially loaded with one  $\text{Mg}^{2+}$  ion.

## Methods and Materials

### *Expression and purification*

NMR, CD and ITC samples of canine NCX1 CBD2 were made as described previously (Hilge *et al.*, 2006). In short, all samples were derived from the nucleotide sequences encoding residues 501–657 of canine NCX1 (accession code P23685) that were cloned into a pET23b vector and expressed in *Escherichia coli* BL21(DE3). Cultures were grown at 37 °C until an optical density (OD<sub>600</sub>) of 0.8–1.0 was reached. Protein expression was then induced for 3 h using 1 mM isopropyl 1-thio- $\beta$ -D-galactopyranoside. Purification was facilitated by N-terminal His-tags and anion-exchange chromatography (MonoQ, Amersham-Pharmacia). Purity of all samples was >95% as judged by SDS-PAGE and <sup>15</sup>N-HSQC spectra.

### *ITC*

To minimize contaminating divalent cations all samples were produced in minimal M9 medium with FeSO<sub>4</sub> as the only trace element and concentrated in 2.5 mM HEPES pH 7.0 (Sigma, Ultrapure) and 2.5 mM  $\beta$ -mercaptoethanol. The buffers contained less than 12.5 ppb (~310 nM) contaminating Ca<sup>2+</sup> as measured by inductively coupled plasma optical emission spectrometry (iCAP 6300, ThermoScientific). 1, 2 or 10 mM CaCl<sub>2</sub> and 1 or 10 mM MgCl<sub>2</sub> containing solutions were prepared in identical buffer as the protein. All ITC measurements were performed at 25 °C using an ITC<sub>200</sub> (MicroCal) device. In all cases, 90  $\mu$ M protein sample was used, as determined using a Nanodrop spectrophotometer ND1000 (Isogen Lifescience). After thermal equilibration the samples were titrated with 38 times 1  $\mu$ L injections with 5 min spacing and at 500 rpm stirring speed. To correct for background heat, we also titrated divalent cation containing buffer into buffer. All measurements were performed at least in duplo to confirm reproducibility. All data was analyzed using the one site independent binding model implemented in Origin 7.0 (MicroCal) with the exception of the Ca<sup>2+</sup> titration to wt-CBD2 for which a two-site independent model was used.

### *NMR*

All NMR samples were identically prepared as the ITC samples and concentrated in 20 mM HEPES pH 7.0 (Sigma; Ultrapure), 20 mM  $\beta$ -mercaptoethanol and 0.03 w/v % NaN<sub>3</sub> as a preservative to ~440  $\mu$ M protein concentration. All <sup>15</sup>N-HSQC spectra were acquired on a Bruker Avance III 600 MHz or a Varian Inova 800 MHz spectrometer, both

equipped with a triple-resonance cryogenic probe. All data were recorded at 33 °C and processed using the NMRPipe program suite (Delaglio *et al.*, 1995) and analyzed using the program Analysis (Vranken *et al.*, 2005). Visualization and drawing of molecules were done using the program Pymol (Schrödinger, 2010).

To assign the  $^{15}\text{N}$ -HSQC spectra of D552V-CBD2 we recorded the standard triple resonance experiments (CBCA(CO)NH, HNCACB, HN(CA)HA and HBHA(CBCACO)NH), which yielded unambiguous resonance identification for 113 of the 157 amides. Significant resonance overlap prohibited complete assignment of D552V-CBD2. A secondary structure prediction was performed using the TALOS+ web server (Shen *et al.*, 2009), which shows that the  $\beta$ -sandwich core of D552V-CBD2 is still intact (cf. Figure S4.5). To determine the total chemical shift perturbation (CSP) we normalized the  $^1\text{H}$  and  $^{15}\text{N}$  dimensions according to (Ayed *et al.*, 2001):

$$\Delta\delta_{Tot} = [(W_H\Delta\delta_H)^2 + (W_N\Delta\delta_N)^2]^{1/2} \quad (4.1)$$

with the weighting factors  $W_H = 1.00$  and  $W_N = 0.154$ .

Samples of  $\sim 440$   $\mu\text{M}$  of either wt-CBD2 or D552V-CBD2 were titrated with  $\text{MgCl}_2$  in ten steps from 0 to 10 mM ( $\text{Mg}^{2+}$  to protein ratio of 0:1, 0.23:1, 0.47:1, 0.96:1, 1.44:1, 2.05:1, 3.02:1, 4.60:1, 10.4:1, 26.4:1). Subsequently the sample was titrated in ten steps to 10 mM  $\text{CaCl}_2$  ( $\text{Ca}^{2+}$  to protein ratio of 0:1, 0.26:1, 0.54:1, 0.96:1, 1.09:1, 1.66:1, 2.25:1, 3.42:1, 5.20:1, 11.7:1, 29.6:1) whilst keeping the  $\text{MgCl}_2$  constant. To obtain per residue  $K_D$  values the CSP data were fitted using a in-house written Python routine, assuming a simple one-to-one binding as described by André and Linse (André and Linse, 2002), using the first nine titration points. (See also Supplementary Information).

The  $^{15}\text{N}$ - $T_1$ ,  $^{15}\text{N}$ - $T_{1\rho}$  and  $\{^1\text{H}$ - $^{15}\text{N}\}$ -NOE experiments were recorded at 18.8 T in an interleaved fashion, using commonly accepted pulse sequences. The relaxation delays for the  $T_1$  and  $T_{1\rho}$  experiments were 16, 256 384, 512, and 1024 ms and 16, 32, 48, 64, 96, and 128 ms, respectively. The time delay between saturated and unsaturated parts in the  $\{^1\text{H}$ - $^{15}\text{N}\}$ -NOE experiments was set to 13 s. The relaxation data were analyzed as previously described (Breukels and Vuister, 2010) using Tensor2 (Dosset *et al.*, 2000).

### Far-UV CD

CD data displayed in Figures 3A and B were acquired using a Jasco J715 spectropolarimeter. Thermal unfolding of CBD2 was followed at 230 nm. Temperature was

increased from 12 or 20 °C to 95 °C at a rate of 1 °C/min in a 1.5 ml stirred quartz cuvette (path-length 0.4 cm). All CD-samples contained 10 μM protein and 1 mM CaCl<sub>2</sub>, MgCl<sub>2</sub> or EDTA in a 1 mM HEPES pH 7.0 and 100 μM β-mercaptoethanol.

To study the ligand concentration dependence of the melting temperature ( $T_m$ ), we measured the thermal unfolding at 1, 5, 10, 25, 100, 250, 500 and 1000 μM MgCl<sub>2</sub> or CaCl<sub>2</sub>, while adjusting the choline chloride concentration to keep the ionic strength constant. The CD-measurements were acquired using a Jasco J810 spectropolarimeter and thermal unfolding was followed at 235 nm. All samples contained 10 μM protein in a 1.5 ml stirred quartz cuvette (path-length 1.0 cm). To reduce the background effects of the buffer all samples contained 1 mM HEPES pH 7.0 and 100 μM β-mercaptoethanol. Fitting of the thermal unfolding data assumed a two-state unfolding mechanism (cf. Supplementary Information).

## Results

### ITC

The AD-exon containing CBD2 splice variant (wt-CBD2) has the ability to bind two Ca<sup>2+</sup> ions. In the crystal structure of CBD2, Ca<sup>2+</sup> at site I is coordinated by six carboxylates whereas Ca<sup>2+</sup> at site II is coordinated by only two (Asp<sup>552</sup> and Asp<sup>578</sup>, cf. Figure 4.1A). However, we previously showed that both sites have similar binding affinities, likely as a result of positive cooperativity (Breukels and Vuister, 2010). To obtain insight in the ion specificity of wt-CBD2 we have measured its binding affinities for both Mg<sup>2+</sup> and Ca<sup>2+</sup> using ITC. To differentiate between the two sites, we also investigated a CBD2 mutant in which we mutated Asp<sup>552</sup> to Val (D552V-CBD2), thus lacking a crucial carboxylate coordinating the Ca<sup>2+</sup> ion in site II. Although mutating an Asp to a Val is not a conserved mutation, this particular D552V mutant has been previously studied with electrophysiology (Besserer et al., 2007) and was shown to constitute a functional exchanger. Figure 4.2A shows the ITC Ca<sup>2+</sup>-binding curve of wt-CBD2 (blue squares) and D552V-CBD2 (red triangles). The binding curve of wt-CBD2 shows a clear two-to-one binding stoichiometry with binding heats in the order of approximately -6 kcal/mol, as can be judged from the molar ratio at half maximum and the  $\Delta H$  at the first injection, respectively. These results are in accordance with the previously measured data (Hilge et al., 2006). The actual binding stoichiometry ( $n = 1.89$ ) is slightly lower than the ideal binding stoichiometry ( $n = 2.0$ ) expected from the crystal structure (Besser *et al.* 2007) and this small deviation might originate from residual Ca<sup>2+</sup> residing in the sample buffer. As anticipated, the mutant has

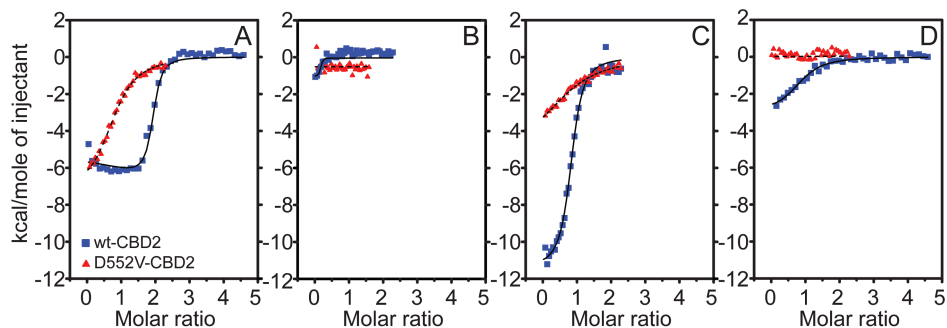


**Figure 4.2.** Comparison of the binding thermodynamics of wt-CBD2 (blue squares) and D552V-CBD2 (red triangles), using ITC. (A) Binding isotherms for 2 mM  $\text{CaCl}_2$  (wild-type) or 1 mM  $\text{CaCl}_2$  (D552V mutant). (B) Binding isotherm of 1 mM  $\text{MgCl}_2$  to protein. (C) Binding isotherm of 1mM  $\text{CaCl}_2$  to protein in the presence of 2 mM  $\text{MgCl}_2$ . (D) Binding isotherm of 1 mM  $\text{MgCl}_2$  in the presence of 90  $\mu\text{M}$   $\text{CaCl}_2$ .

only one binding site and displays a slightly increased  $\Delta H$  of  $-7.4 \pm 0.2$  kcal/mol (cf. Table 4.1), indicating that binding site I in D552V-CBD2 remains intact.

The intracellular free  $\text{Mg}^{2+}$  concentration in the cell can reach levels up to several millimolar (Saris *et al.*, 2000) and we tested  $\text{Mg}^{2+}$  as a ligand for CBD2.  $\text{Mg}^{2+}$  appears to bind to wt-CBD2 but not to D552V-CBD2 (cf. Figure 4.2B). Binding of  $\text{Mg}^{2+}$  to wt-CBD2, however, results in much smaller enthalpic effects compared to the  $\text{Ca}^{2+}$  binding. Furthermore, the  $\text{Mg}^{2+}$  binding stoichiometry is far below a predicted one-to-one binding ( $n=0.16 \pm 0.04$ ) and the binding isotherm starts exothermic to become endothermic after the first seven additions. This indicates that at least two processes are involved and in combination with the small  $\Delta H$  of the exothermic reaction, this results in the low stoichiometry and a poor fit to the model used. We hypothesize that the endothermic reaction is a low affinity, nonspecific  $\text{Mg}^{2+}$ -binding process. Moreover, measurements performed at a 10-fold increased ion concentration show that for both  $\text{Ca}^{2+}$  and  $\text{Mg}^{2+}$  the endothermic reaction occurs, in the wild-type as well as in the D552V mutant (cf. Figure S4.1).

Under physiological conditions,  $\text{Ca}^{2+}$  binding occurs in competition with an excess  $\text{Mg}^{2+}$ . Therefore, we measured the  $\text{Ca}^{2+}$ -binding in the presence of 2 mM  $\text{MgCl}_2$  (cf. Figure 4.2C). Remarkably, at this high  $[\text{Mg}^{2+}]$  condition, we observe a  $\text{Ca}^{2+}$  binding stoichiometry of  $0.85 \pm 0.01$ . Interestingly, the enthalpy of this single binding event ( $\Delta H = -11.4 \pm 0.2$  kcal/mol) is much higher when compared to the  $\text{Ca}^{2+}$ -binding in the absence of  $\text{MgCl}_2$ . In contrast to the wild-type, the  $\text{Ca}^{2+}$ -binding stoichiometry for the mutant

remains one-to-one. We observe, however, a loss of binding heat, decreasing from  $\Delta H = -7.4 \pm 0.2$  kcal/mol without Mg<sup>2+</sup> to  $\Delta H = -5.3 \pm 0.6$  kcal/mol in the presence of 2 mM MgCl<sub>2</sub>. To test if the altered Ca<sup>2+</sup>-binding at 2 mM MgCl<sub>2</sub> is a result of the increased ionic strength, we have also measured Ca<sup>2+</sup>-binding for both molecules in the presence of 2 mM choline chloride. We observed that choline chloride does not alter the binding thermodynamics of Ca<sup>2+</sup> in either of the two molecules (cf. Figure S4.2) and therefore exclude the effects of ionic strength as the cause of the observed differences.

In an effort to determine the relative binding affinity of Mg<sup>2+</sup>, we also performed the reverse competition experiment, titrating Mg<sup>2+</sup> to a partially Ca<sup>2+</sup>-loaded protein (cf. Figure 4.2D). At a Ca<sup>2+</sup>-to-protein ratio of one-to-one, both binding sites are expected to be approximately half filled (Breukels and Vuister, 2010). Under this condition, we observe Mg<sup>2+</sup>-binding to wt-CBD2 with a binding stoichiometry of one-to-one. Compared to the non-competitive Mg<sup>2+</sup>-binding experiment, the binding heat is increased to  $\Delta H = -3.4 \pm 0.2$  kcal/mol. For D552V-CBD2, no binding is observed in the reverse competition experiment. Taken together, the ITC data show that Mg<sup>2+</sup> cannot displace Ca<sup>2+</sup> from site I and can only bind at site II.

To compare the results in a more quantitative way, we also fitted all data using the MicroCal Origin package (cf. Methods and Materials). Affinities, binding enthalpies and binding entropies are summarized in Table 4.1. For the wild-type, the affinity for Ca<sup>2+</sup> is between 0.4 and  $1.0 \pm 1.4$   $\mu$ M, which is slightly lower than previously reported ITC values of  $0.8 \pm 0.5$   $\mu$ M and  $8.6 \pm 1.1$   $\mu$ M (Hilge *et al.*, 2006). The  $K_D$  values presented here are measured with twice as many data points and considered to be more accurate. However, the two site independent binding model can give indistinguishable binding curves with completely different enthalpies and affinities (Freire *et al.*, 2009). The resulting affinities and enthalpies are therefore only approximate, as indicated by the large standard deviations. In the presence of 2 mM MgCl<sub>2</sub> the Ca<sup>2+</sup> affinity of the remaining site is  $3.4 \pm 0.4$   $\mu$ M and the apparent affinity for Mg<sup>2+</sup> in the presence of 90  $\mu$ M CaCl<sub>2</sub> is  $14.6 \pm 3.4$   $\mu$ M. The Ca<sup>2+</sup> binding affinity for the mutant is  $16.1 \pm 1.4$   $\mu$ M in the absence of MgCl<sub>2</sub> and  $53.5 \pm 9.70$   $\mu$ M in the presence of 2 mM MgCl<sub>2</sub>. Unlike wt-CBD2, the D552V mutant does not display a Mg<sup>2+</sup> binding isotherm in the presence of 90  $\mu$ M CaCl<sub>2</sub>.



**Table 4.1.** Thermodynamic  $\text{Ca}^{2+}$  and  $\text{Mg}^{2+}$  binding parameters for wt-CBD2 and D552V-CBD2 obtained by isothermal titration calorimetry.

Sample	Ligand	N	$K_D$ ( $\mu\text{M}$ )	$\Delta H$ ( $\text{kcal mol}^{-1}$ )	$\Delta S$ ( $\text{cal mol}^{-1} \text{deg}^{-1}$ )
90.0 $\mu\text{M}$ wild-type	2 mM $\text{CaCl}_2$	$1.89 \pm 0.05$	$0.4 \pm 1.2^{1)}$	$-5.2 \pm 3.55^{1)}$	$11.7^{1)}$
			$1.1 \pm 1.4^{1)}$	$-7.0 \pm 3.57^{1)}$	$4.0^{1)}$
90.0 $\mu\text{M}$ wild-type	1 mM $\text{CaCl}_2$	$0.85 \pm 0.01$	$3.4 \pm 0.4$	$-11.4 \pm 0.2$	-13.3
	2 mM $\text{MgCl}_2$				
90.0 $\mu\text{M}$ wild-type	1 mM $\text{MgCl}_2$	$0.89 \pm 0.05$	$14.6 \pm 3.4$	$-3.4 \pm 0.2$	11.9
90.0 $\mu\text{M}$ D552V	1 mM $\text{CaCl}_2$	$0.87 \pm 0.01$	$16.1 \pm 1.4$	$-7.4 \pm 0.2$	-4.7
90.0 $\mu\text{M}$ D552V	1 mM $\text{CaCl}_2$	$0.94 \pm 0.07$	$53.5 \pm 9.7$	$-5.3 \pm 0.6$	1.8
	2 mM $\text{MgCl}_2$				

<sup>1)</sup> The two-site binding model gives unreliable results (cf. Results).

### Far-UV Circular Dichroism

In the absence of  $\text{Ca}^{2+}$ , Asp<sup>552</sup> forms a salt bridge with Lys<sup>585</sup> and this interaction is deemed important for stabilizing CBD2 (Besserer *et al.*, 2007; Hilge *et al.*, 2006). To measure the stability of both wild-type and D552V-CBD2, we followed the thermal unfolding using far-UV CD spectropolarimetry. We determined the melting temperature ( $T_m$ ) of both molecules in the presence of 1 mM EDTA,  $\text{CaCl}_2$  or  $\text{MgCl}_2$  (cf. Table 4.2, Figure 4.3).

As expected, the  $T_m$  of the mutant in the apo-form is lower than that of the wild-type ( $30.9 \pm 1.1$  °C and  $39.4 \pm 1.1$  °C, respectively), confirming the stabilizing function of Asp<sup>552</sup>. Cation binding is also known to stabilize proteins (Pace, 1990) and in accordance we observe an increase in  $T_m$  from  $39.4 \pm 1.1$  °C to  $70.0 \pm 0.1$  °C when  $\text{Ca}^{2+}$  is bound to wt-CBD2. The  $T_m$  of  $\text{Ca}^{2+}$ -bound D552V-CBD2 is  $57.1 \pm 0.1$  °C, which is much lower than that of the  $\text{Ca}^{2+}$ -bound form of the wild-type. In the presence of 1 mM  $\text{MgCl}_2$  the  $T_m$  of wt-CBD2 is  $55.8 \pm 0.1$  °C, an increase of 16.4 °C. Surprisingly, a similar increase in  $T_m$  of 17.5 °C is observed for D552V-CBD2 in the presence of 1 mM  $\text{MgCl}_2$ , as the mutant is not expected to bind  $\text{Mg}^{2+}$  in site II.

The increase in  $T_m$  at high  $\text{Ca}^{2+}$  and  $\text{Mg}^{2+}$  is due to binding of the ligand to the protein and therefore is expected to be ligand concentration dependent. We followed the thermal unfolding using far-UV CD spectropolarimetry of both wild-type and mutant at eight different  $\text{Mg}^{2+}$  or  $\text{Ca}^{2+}$  concentrations at constant total ionic strength and derived  $T_m$ ,  $\Delta H_m$  and  $\Delta C_p$  from the fits of the data (cf. Methods and Materials). Figure 4.3C shows  $1/T_m$  versus the common logarithm of the  $\text{Ca}^{2+}$  or  $\text{Mg}^{2+}$  concentration, whereas

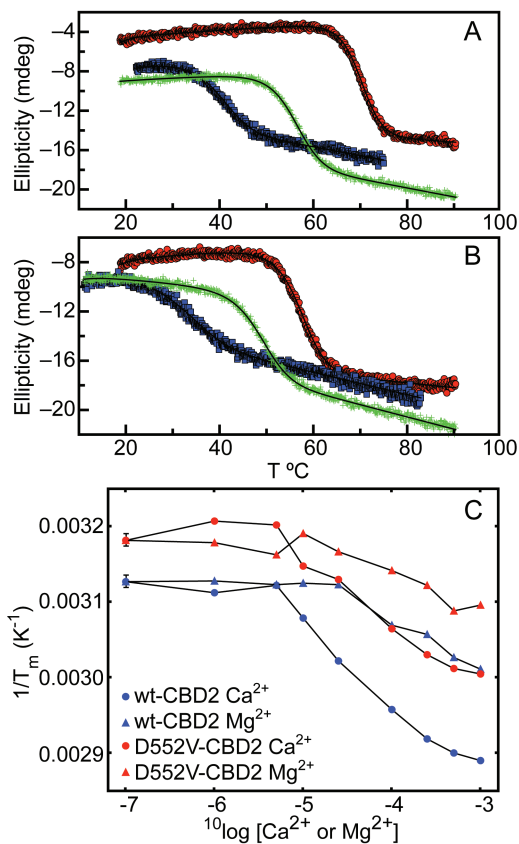


**Figure 4.3.** Thermal unfolding of wt-CBD2 (A) or D552V-CBD2 (B), examined by circular dichroism spectropolarimetry, in the presence of 1 mM CaCl<sub>2</sub> (red circles), 1 mM MgCl<sub>2</sub> (green crosses) or 1 mM EDTA (blue squares). (C) Ligand concentration dependence of  $T_m$  for Ca<sup>2+</sup> (circles) and Mg<sup>2+</sup> (triangles) for wt-CBD2 (blue symbols) and D552V-CBD2 (red symbols), where the 0 mM CaCl<sub>2</sub> or MgCl<sub>2</sub> has been plotted at 10<sup>-7</sup> M. The error estimates in  $T_m$  for all points are between 0.1 and 0.8 °C, which in most cases is smaller than the marker symbol. Hence for clarity only the largest error estimate is shown at the first data point.

Figure S4.4 displays the values for  $\Delta H_m$  and  $\Delta C_p$ . As expected, we observe a strong ligand concentration dependence of the  $T_m$ . In addition, for both the wild-type and the mutant the first point that displays a significant decrease in  $1/T_m$  is at 10  $\mu$ M CaCl<sub>2</sub>, whereas for MgCl<sub>2</sub> this point is at 100  $\mu$ M. This indicates that the affinity for Mg<sup>2+</sup> is much lower than that for Ca<sup>2+</sup>.

## NMR

To study the residue-specific effects of Mg<sup>2+</sup> and Ca<sup>2+</sup> binding, we measured the chemical shift perturbations (CSPs) on wt-CBD2 and D552V-CBD2, as induced by Mg<sup>2+</sup> and Ca<sup>2+</sup> using <sup>15</sup>N-HSQC NMR spectroscopy. Spectra of both wt-CBD2 and D552V-CBD2 were measured at ten different Mg<sup>2+</sup>-to-protein ratios, starting at 0:1 up to 26.4:1 (cf. Methods and Materials). Subsequently, we performed a second titration using CaCl<sub>2</sub>, in the presence of 10 mM MgCl<sub>2</sub>, mimicking the ITC competition experiment described

**Table 4.2.** Melting temperatures ( $T_m$ ) determined by CD spectropolarimetry at 1 mM  $\text{CaCl}_2$ , 1 mM  $\text{MgCl}_2$  or 1 mM EDTA for wt-CBD2 and D552V-CBD2. D552V-CBD2 obtained by isothermal titration calorimetry.

Condition	$T_m$ (°C)	$T_m$ (°C)
1 mM EDTA	$39.4 \pm 1.1$	$30.9 \pm 1.1$
1 mM $\text{MgCl}_2$	$55.8 \pm 0.1$	$48.4 \pm 0.1$
1 mM $\text{CaCl}_2$	$70.0 \pm 0.1$	$57.1 \pm 0.1$

above (cf. Figure S4.3).

To obtain residue  $^{15}\text{N}$ -HSQC assignment of D552V-CBD2, we recorded the standard triple resonance experiments on D552V-CBD2 at 10 mM  $\text{CaCl}_2$  (cf. Methods and Materials) and have assigned 113 of the 157 amides. Chemical shift information can be used to identify secondary structure elements and we used the  $\text{H}^{\text{N}}$ ,  $\text{H}^{\alpha}$ ,  $\text{N}$ ,  $\text{C}^{\alpha}$ ,  $\text{C}^{\beta}$  and CO assignments of D552V-CBD2 to perform a TALOS+ (Shen *et al.*, 2009) analysis. Even though the Asp<sup>552</sup> to Val mutation destabilizes the CBD2 domain, the TALOS+ derived  $\phi$ ,  $\psi$  backbone and  $S^2$  order parameter predictions (cf. Figure S4.5) show that the  $\beta$ -sandwich core remains intact.

Figure 4.4 displays the total CSP (cf. Methods and Materials) upon the addition of 10 mM  $\text{MgCl}_2$  (panels A, B) and upon the subsequent addition of 10 mM  $\text{CaCl}_2$  (panels C, D) as a function of residue number for wt-CBD2 and D552V-CBD2. The  $\text{Mg}^{2+}$ -induced CSPs observed in wt-CBD2 are not only around the CD-binding loop (residues Glu<sup>543</sup> to Thr<sup>556</sup>) but also in the AB-binding loop (residues Ser<sup>515</sup> to Gly<sup>519</sup>) located opposite of the CD-loop (cf. Figure 4.1). Similarly, we find  $\text{Mg}^{2+}$ -induced CSPs for D552V-CBD2 in the AB-loop. Subsequent addition of  $\text{CaCl}_2$  leads to chemical shift changes both in the wild-type and in the mutant, indicating that  $\text{Ca}^{2+}$ -binding still occurs even at high levels of  $[\text{Mg}^{2+}]$ , a result that is in accordance with the ITC data. Furthermore, with the exception of Gly<sup>548</sup> and Val<sup>575</sup>, the largest CSPs during the  $\text{Ca}^{2+}$  titration are observed in the AB-loop, located near  $\text{Ca}^{2+}$  binding site I. Finally, when we derive the CSP as the difference between the apo and  $\text{Ca}^{2+}$ -bound form at high  $[\text{Mg}^{2+}]$ , we observe values that are comparable with those reported previously (Breukels and Vuister, 2010) for the  $\text{Ca}^{2+}$ -bound form at zero  $[\text{Mg}^{2+}]$  (Figure 4.4C). This indicates that at 10 mM  $\text{MgCl}_2$  and 10 mM  $\text{CaCl}_2$ , the binding sites are structurally similar as in the fully  $\text{Ca}^{2+}$ -bound form without  $\text{Mg}^{2+}$ .

Studying  $\text{Mg}^{2+}$  binding in more detail for wt-CBD2 we observe major differences

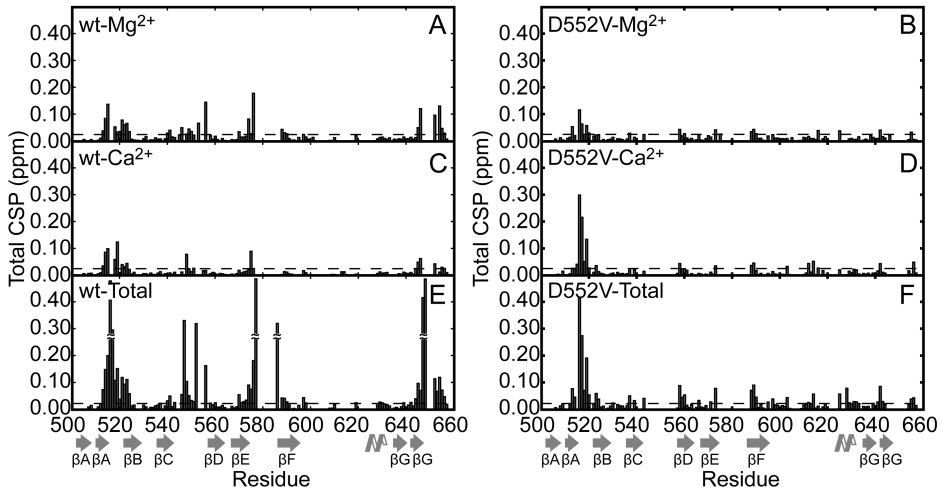


**Figure 4.4.** (A, B) CSP values as function of residue number, resulting from the difference between 0 mM MgCl<sub>2</sub> (*i.e.* apo form) and 10 mM MgCl<sub>2</sub>. (C, D) CSP values resulting from the difference between 10 mM MgCl<sub>2</sub> and 10 mM CaCl<sub>2</sub> in the presence of 10 mM MgCl<sub>2</sub>. (E, F) The total CSP as the difference between 0 mM MgCl<sub>2</sub> and 10 mM CaCl<sub>2</sub> in the presence of 10 mM MgCl<sub>2</sub>. For clarity the bars of Glu<sup>516</sup>, Ser<sup>517</sup>, Asp<sup>577</sup>, Thr<sup>586</sup>, Glu<sup>647</sup> and Glu<sup>648</sup> have been reduced as indicated in the plot as these values exceed 0.5. These residues are not observed under 10 mM MgCl<sub>2</sub> conditions of (C) (see also Results). Grey arrows indicate  $\beta$ -strands, with the  $\alpha$ -helix between  $\beta$ -strand F and G.

between different residues. Six residues, Glu<sup>516</sup>, Ser<sup>517</sup>, Asp<sup>552</sup>, Asp<sup>577</sup>, Glu<sup>647</sup> and Glu<sup>648</sup>, have large <sup>15</sup>N perturbations between the apo and fully ion-bound states and show significant exchange broadening during the Mg<sup>2+</sup>-titration. For these residues, the cross-peaks were broadened beyond detection at the third titration point (0.47:1 molar ratio) and re-appear at the Ca<sup>2+</sup>-bound position after titration of an excess CaCl<sub>2</sub> (*cf.* Figures 5A and B). Three of these residues, Glu<sup>516</sup>, Asp<sup>577</sup> and Glu<sup>648</sup>, also showed exchange line broadening beyond detection in the regular Ca<sup>2+</sup> titration, reported previously (Breukels and Vuister, 2010). The cross-peaks of several other residues, for example Ile<sup>518</sup> and Gly<sup>548</sup>, are clearly present at 10 mM Mg<sup>2+</sup> and are approximately mid-way between the apo and Ca<sup>2+</sup>-bound forms (*cf.* Figures 5C and D). Both types indicate that at high [Mg<sup>2+</sup>] the wt-CBD2 is in an intermediate state between an apo and fully ion-bound form. The most striking residues, however, show strongly curved trajectories during the Ca<sup>2+</sup> titration. These residues, for example Thr<sup>556</sup> and Lys<sup>653</sup> (*cf.* Figures 5E and F), reveal that during the Ca<sup>2+</sup>-titration multiple processes occur, *e.g.* the binding of Ca<sup>2+</sup> to site I and competition between Ca<sup>2+</sup> and Mg<sup>2+</sup> at site II and/or at site I at high [Ca<sup>2+</sup>].

To quantify the CBD2 affinity for Mg<sup>2+</sup>, we fitted a one-to-one binding model

to the total CSPs of the selected individual residues (cf. Methods and Materials). Some typical curves and the distribution of the resulting  $K_D$  values are shown in Figure S4.6. The average  $K_D$  is  $390 \pm 260 \mu\text{M}$ . The large variation possibly originates from the fact that the chemical shift is sensitive to the structural, dynamical and electronical environment of the nucleus, which do not affect all residues equally. The  $K_D$  of  $390 \pm 260 \mu\text{M}$  is not comparable to the ITC determined  $K_D$ . However, in contrast to the ITC experiment, where  $\text{Ca}^{2+}$  is present in a one to one ( $\text{Ca}^{2+}$  to protein) ratio, the  $K_D$  values determined by NMR are derived under  $\text{Ca}^{2+}$  free condition. The strongly curved trajectories during the subsequent  $\text{Ca}^{2+}$  titration prohibited fitting of these curves to derive a  $\text{Ca}^{2+}$  affinity in presence of  $10 \text{ mM MgCl}_2$ .

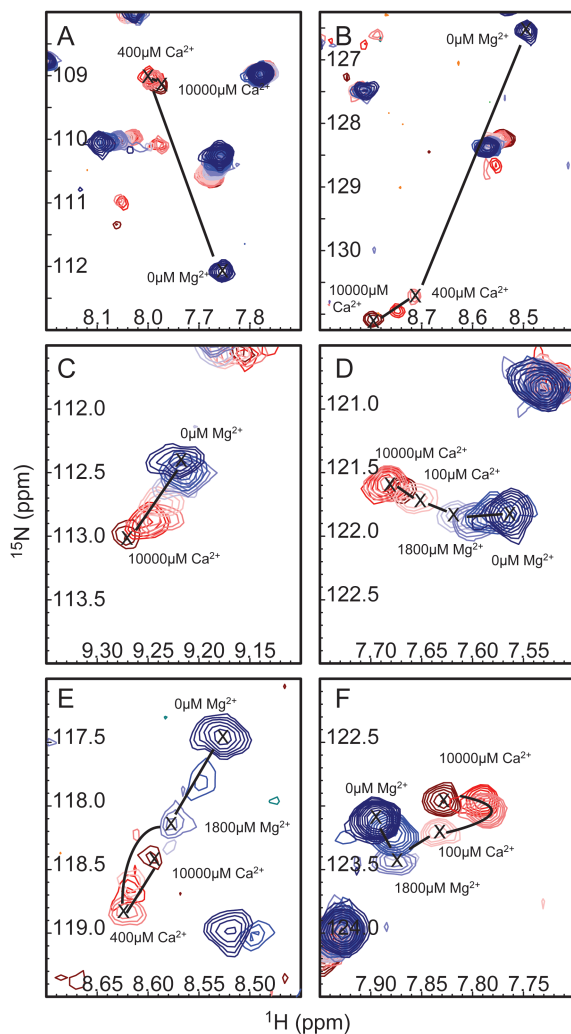


**Figure 4.5.**  $\text{Mg}^{2+}$  and  $\text{Ca}^{2+}$  titration of wt-CBD2 showing the overlays of eight  $^{15}\text{N}$ -HSQC spectra in the region of Ser $^{517}$  (A), Asp $^{577}$  (B), Ile $^{518}$  (C), Gly $^{548}$  (D), Thr $^{556}$  (E) and Lys $^{653}$  (F). In all panels concentrations are 0, 400, 1800 and 10000  $\mu\text{M MgCl}_2$  (dark blue to light blue) and 100 400, 1800, 10000  $\mu\text{M CaCl}_2$  (light pink to red).

**Table 4.3.** Overall rotational correlation time and anisotropy of Ca<sup>2+</sup>-bound, Mg<sup>2+</sup>-bound and apo wt-CBD2.

	Ca <sup>2+</sup> -bound CBD2-AD	Mg <sup>2+</sup> -bound CBD2-AD	Apo CBD2-AD <sup>1)</sup>
$\tau_{av,aniso}$ (ns)	13.1 ± 0.9	12.1 ± 0.9	11.4 ± 2.3
$D_{  }/D_{\perp}$	2.08 ± 0.14	1.85 ± 0.33	1.40 ± 0.28

<sup>1)</sup>Data from (Breukels and Vuister 2010)

The apo and fully Ca<sup>2+</sup>-bound form of CBD2 are both structurally- and dynamically different.<sup>28</sup> In the apo-form the binding loops of wt-CBD2 are more flexible and show decreased  $S^2$  order parameter values when compared to the Ca<sup>2+</sup>-bound form. As a consequence, the overall tumbling is more anisotropic and the rotational correlation time is higher in the Ca<sup>2+</sup>-form compared to the apo-form. We also tested the dynamical properties of the Mg<sup>2+</sup>-bound form of wt-CBD2 and therefore measured the longitudinal ( $T_1$ ) and transversal ( $T_{1\rho}$ ) 15N-relaxation times and the steady-state <sup>1</sup>H-<sup>15</sup>N nuclear Overhauser effects of Mg<sup>2+</sup>-bound wt-CBD2 (cf. Figure S4.7). Analysis using Tensor2 (Dosset *et al.*, 2000) (cf. Methods and Materials) yielded the values for  $\tau_{av,aniso}$  and  $D_{||}/D_{\perp}$  (cf. Table 4.3), which show that the Mg<sup>2+</sup>-bound form is dynamically intermediate between the apo and fully Ca<sup>2+</sup>-bound form (cf. Figure S4.8). The mean  $S^2$  value for the residues in the  $\beta$ -sandwich amounts to  $0.95 \pm 0.02$ , which is identical to the other two forms. The mean  $S^2$  value for the CD-binding loop, however, is slightly increased compared to the apo-form. The  $S^2$  values for the other binding loops cannot be determined for the Mg<sup>2+</sup>-bound form, as those peaks are missing due to exchange line broadening (*vide supra*).

## Discussion

Mg<sup>2+</sup> is chemically very similar to Ca<sup>2+</sup> and many Ca<sup>2+</sup>-binding proteins are known to bind Mg<sup>2+</sup> to some extent. Thus far, most studies on ion specificity focused on EF-hand containing proteins such as the calcium- and integrin-binding protein 1 parvalbumin (CIB1, see (Gifford *et al.*, 2007) for a review). CIB1 for example, not only binds Mg<sup>2+</sup> at a similar position as Ca<sup>2+</sup>, but the Mg<sup>2+</sup>-CIB1 complex is well folded and structurally and dynamically very similar to the Ca<sup>2+</sup>-CIB1 (Yamniuk *et al.*, 2008), which raised the question if CIB even can act as a Ca<sup>2+</sup>-sensor under physiological conditions (Yamniuk and Vogel, 2005). In contrast, the Mg<sup>2+</sup>-bound thymic avian hormone  $\beta$ -parvalbumin, is structurally distinctly different from its Ca<sup>2+</sup>-bound form (Tan and Henzl, 2009) and the two forms therefore have different binding partners.

How proteins are able to differentiate their affinities for different metal cations

is still not fully understood, but based on computational- and experimental studies some general trends have been indentified. Both  $Mg^{2+}$  and  $Ca^{2+}$  are preferentially coordinated by carboxyl, carbonyl and hydroxyl atoms (Dokmanic *et al.*, 2008). However,  $Mg^{2+}$  strongly favors oxygen atoms in an octahedral fashion, whereas for  $Ca^{2+}$  this can vary between six and eight. In addition,  $Mg^{2+}$  likes to retain several water molecules in its coordination sphere and prefers monodentate coordination of the sidechain carboxylates. In contrast,  $Ca^{2+}$  has a lower affinity for water and has a tendency for coordination by bidentate carboxylates (Dudev and Lim, 2003). In accordance with this theory, it is to be expected that  $Mg^{2+}$  ions prefer site II over site I, as site II coordinates  $Ca^{2+}$  in a pentagonal bi-pyramidal fashion with five waters in plane and the monodentate side-chain oxygen atoms at almost perfect opposite positions (cf. Figure 4.1A, Besserer *et al.*, 2007). It is reasonable to assume that  $Mg^{2+}$  at site II binds in a similar coordination, albeit with four instead of five waters, thereby maintaining its preferred octahedral coordination. For  $Mg^{2+}$  to bind at site I is much less optimal, as the coordination is far from octahedral and two bidentate coordination side-chains are involved.

The ITC, CD and NMR results of this study show that wt-CBD2 indeed binds  $Mg^{2+}$ , a finding in accordance with the results of Boyman *et al.* (Boyman *et al.*, 2009). To identify the binding site of  $Mg^{2+}$  and to obtain insight into the relative affinities of the two sites for the two ions, we constructed an Asp<sup>552</sup> to Val mutant (D552V-CBD2), thereby removing one of the only two carboxylates coordinating the ion in site II. This mutation was previously shown to constitute a functional exchanger (Besserer *et al.*, 2007) and the NMR data showed the overall fold of the D552V mutant to be similar to wt-CBD2, with only modest changes in the  $Ca^{2+}$ -binding loops (cf. Figure S4.5). Furthermore, the ITC results show that the D552V-CBD2 mutant only binds one  $Ca^{2+}$ , which demonstrates that site II has become non-functional and site I is still intact.

Direct titration of  $Mg^{2+}$  to wt-CBD2 only gives modest effects in the ITC (cf. Figure 4.2B), with a very low binding heat, possibly originating from energetically unfavourable breaking of the Asp<sup>552</sup> to Lys<sup>585</sup> salt bridge. However, high  $[Mg^{2+}]$  reduces the  $Ca^{2+}$ -binding stoichiometry of wt-CBD2 to one, whereas the stoichiometry of D552V-CBD2 remains one under the same conditions. This effect can only be reconciled by a  $Ca^{2+}$  bound in site I and a  $Mg^{2+}$  ion in site II, which cannot be displaced by  $Ca^{2+}$ . The reverse experiment, titrating  $Mg^{2+}$  to a partially  $Ca^{2+}$ -loaded protein, resulted in a  $Mg^{2+}$ -binding stoichiometry of one for wt-CBD2 and no binding was observed for D552V-CBD2. Under these conditions, the ITC results show that  $Mg^{2+}$  binds at site II with a  $K_D$

of  $14.6 \pm 3.4 \mu\text{M}$ .

Using far UV-CD spectroscopy we tested for the thermal stability of the two domains in response to varying concentrations of Ca<sup>2+</sup> or Mg<sup>2+</sup>. The CD results show that Mg<sup>2+</sup> stabilizes wt-CBD2 compared to the apo form, with an increase of 16.4 °C in  $T_m$ , whereas for the fully Ca<sup>2+</sup>-bound form a 30.6 °C higher  $T_m$  is observed. Both the Mg<sup>2+</sup> and Ca<sup>2+</sup> induced increase in  $T_m$  is strongly concentration dependent. Even though an accurate determination of the binding affinities and stoichiometries from these data is not possible due to the large increase in  $\Delta H_m$  (cf. Figure S4.4)(Greenfield, 2006), Figure 4.3C clearly shows that for wt-CBD2 the affinity for Ca<sup>2+</sup> is significantly higher than for Mg<sup>2+</sup>. Surprisingly, a similar concentration dependent increase in  $T_m$  at high MgCl<sub>2</sub> is found for D552V-CBD2 compared to wt-CBD2. This result indicates that also D552V-CBD2 is able to bind Mg<sup>2+</sup>, resulting in increased stability of the domain. The exact location of this binding site is unclear; it could be at site I, at the defunct site II or at the a-specific site also observed with the ITC at very high Ca<sup>2+</sup> or Mg<sup>2+</sup> concentrations (Figure S4.1). However, the NMR chemical shift data of the mutant shows significant CSP between 0 and 10 mM MgCl<sub>2</sub> for the residues in the AB-loop (Val<sup>514</sup> - Ile<sup>518</sup>), which suggests that in the mutant Mg<sup>2+</sup> binds at site I, but with much lower affinity as Ca<sup>2+</sup> can still replace the Mg<sup>2+</sup>. This finding also explains the decrease in Ca<sup>2+</sup> binding affinity and enthalpy for D552V-CBD2 at high MgCl<sub>2</sub> (cf. Table 4.1). The competition experiment allows for an estimate of the Mg<sup>2+</sup> binding affinity for site I in D552V-CBD2 ( $K_D \sim 860 \mu\text{M}$ , cf. Equation S4.8 Malmendal *et al.*, 1999), which is in a similar range as the residue-specific  $K_D$  values derived from NMR.

Together the ITC, NMR and CD data show that Mg<sup>2+</sup> binds to both site I and II, albeit with significantly different affinities. Binding to site II is preferred by Mg<sup>2+</sup> and displays the highest affinity ( $K_D \sim 15 \mu\text{M}$ ), whereas site I has a much lower estimated Mg<sup>2+</sup>-binding affinity ( $K_D \sim 300 - 800 \mu\text{M}$ ). Furthermore, in the Mg<sup>2+</sup>-bound form of CBD2 (Mg<sup>2+</sup>-CBD2), we observe many cross-peaks in the <sup>15</sup>N-HSQC that are approximately mid-way between the apo and Ca<sup>2+</sup>-bound forms. The results of the NMR relaxation studies show  $\tau_{av,anis}$  and  $D_{||}/D_{\perp}$  values that are exactly between the apo and fully Ca<sup>2+</sup>-bound forms. This indicates that Mg<sup>2+</sup>-CBD2 is in a state intermediate between the apo and fully Ca<sup>2+</sup>-bound forms. Finally, the NMR results show that wt-CBD2 at high [Ca<sup>2+</sup>] and [Mg<sup>2+</sup>], a condition in which wt-CBD2 is bound by one Mg<sup>2+</sup> and one Ca<sup>2+</sup>, is structurally very similar to the fully Ca<sup>2+</sup> bound form.

Previously it was shown that the  $k_{on}$  rate for binding Ca<sup>2+</sup>-binding to wt-CBD2



increases by more than a factor of two and the  $k_{off}$  rate decreases by almost 30% in the presence of  $Mg^{2+}$  (Boyman *et al.*, 2009), effectively increasing the affinity for  $Ca^{2+}$  by a factor of 2.5. Our results can explain these differences as  $Mg^{2+}$  binding to site II also pre-forms site I. Both the NMR and X-ray structure of the apo-CBD2 (cf. Figures 1B and 1D) show that, in the absence of  $Ca^{2+}$ , the side chain of Lys585 orients towards to the now free site II, forming salt bridges with Asp552. In addition, in the X-ray structure determined at pH 4.9, Lys585 forms another salt bridge with and Glu648 and is hydrogen bonded to the carbonyl oxygen of Glu580, displacing the EF-loop towards the CD-loop (Besserer *et al.*, 2007). In spite of explicit examination of the relevant regions in the NOESY spectra of apo-CBD2 recorded at pH 7.0, contacts of Lys<sup>585</sup> to either Glu<sup>580</sup> or Glu<sup>648</sup> were not found (Hilge *et al.*, 2009). Instead, NOEs to Glu<sup>582</sup> were observed and in the resulting NMR-ensemble of the apo-CBD2 Lys<sup>585</sup> is also engaged in a second salt bridge with Glu<sup>582</sup>. This salt bridge occurs only in 8 out of 20 structures of the ensemble as a result of a very flexible EF loop (Breukels and Vuister, 2010). In either case, with  $Mg^{2+}$  bound at site II the side-chain of Lys585 will be displaced from the binding pocket, as a result of steric effects and repulsive interaction.  $Mg^{2+}$  binding at site II stabilizes the EF-loop and Asp<sup>578</sup> (coordinating  $Ca^{2+}$  in site I and II in  $Ca^{2+}$ -CBD2) will be correctly oriented for coordination at site I. Therefore,  $Ca^{2+}$  can bind more easily at site I, explaining the higher  $k_{on}$  rate.

CBD2 plays an important role in the kinetic effects of NCX activation and displays a tight interplay with the  $Na^{+}$ -dependent inactivation. Upon activation the exchanger current rapidly increases and then slowly decreases to a steady-state value as a result of  $Na^{+}$ -dependent inactivation. It has been postulated that at elevated  $[Ca^{2+}]$ , the  $Na^{+}$ -dependent inactivation is reduced through interactions with CBD2 (Hilge *et al.*, 2009). Assuming a cellular  $Mg^{2+}$  concentration of  $\sim 1.0$  mM and  $Ca^{2+}$  concentrations between 100 nM at rest and 2.0  $\mu$ M in the excited state, the apo form of CBD2 is hardly present under physiological conditions. Instead, the majority of the exchangers will have site II of CBD2 occupied with  $Mg^{2+}$ , which raises the question whether this site is involved in the  $Ca^{2+}$ -regulation of the intact NCX. More likely, site II bound by  $Mg^{2+}$  has a structuring role, increasing the  $Ca^{2+}$  binding rate of site I. In electrophysiological studies Besserer *et al.* observed strongly altered  $Ca^{2+}$ -regulation as results of mutations affecting site I, whereas they did not observe significant effects for the D552V mutation (Besserer *et al.*, 2007). Unfortunately, in that study as well as many others on the NCX, the concentrations of  $Mg^{2+}$  were not experimentally controlled. It would be interesting to know if and how these electrophysiological results would change in the presence of  $Mg^{2+}$ , especially with the respect to the rate of the

regulatory response. The increase in affinity for Ca<sup>2+</sup> under high [Mg<sup>2+</sup>] (Boyman *et al.*, 2009) could also have an important effect in alleviating Na<sup>+</sup>-dependent inactivation. We therefore hypothesize that under high [Mg<sup>2+</sup>] condition the steady-state current of wt-CBD2 will be increased even at a lower [Ca<sup>2+</sup>] condition, whereas high [Mg<sup>2+</sup>] will not exert any effect on the D552V mutant.

A constitutively bound Mg<sup>2+</sup> at site II also affects the hypothesis of the electrostatic switch mechanism previously proposed, because apo-CBD2 is not present under physiological conditions. If Ca<sup>2+</sup> regulation occurs via electrostatic interactions, then differences in the electrostatic potential must be compared between one ion Mg<sup>2+</sup>-bound and fully Ca<sup>2+</sup>-bound CBD2. Calculating the electrostatic potential by ABPS (Baker *et al.*, 2001) using one ion present at site II shows that differences still exist between Mg<sup>2+</sup>-bound CBD2 and Ca<sup>2+</sup>-bound CBD2, however, the differences are much smaller compared to apo-CBD2 (Figure S4.9). Another complicating factor is the protonation state of the charged residues. In the electrostatic calculations all Asp and Glu side-chains are fully deprotonated, as the predicted pKa of all Asp and Glu side-chains is smaller than 4.8 (calculated using PROPKA (Bas *et al.*, 2008; Li *et al.*, 2005), data not shown). However, a recent study shows that the Ca<sup>2+</sup> affinity of CBD2 decreases 24% when the pH is lowered from 7.2 to 6.9 (Boyman *et al.*, 2011). Possibly not all side-chains are actually fully deprotonated at decreased pH and the authors further suggest that protonation state changes upon Ca<sup>2+</sup> binding. Unfortunately no data is available on interactions between H<sup>+</sup> and Mg<sup>2+</sup>, but we speculate that proton sensitivity decreases with Mg<sup>2+</sup> bound at site II, as binding of the first ion may deprotonate (or keep deprotonated) the coordinating residues of the other site.

## Conclusion

Our study unequivocally shows that CBD2-AD of NCX1 binds Mg<sup>2+</sup> at concentration far below the physiological concentration of ~1 mM MgCl<sub>2</sub>. Both site I and site II bind Mg<sup>2+</sup>, although with significantly different affinities. The different isoforms and splice variants of the NCX change the number of Ca<sup>2+</sup> ions bound by CBD2, likely altering the regulation to tissue specific needs. Whether Mg<sup>2+</sup> will bind to CBD2 of other NCX isoforms as well as to CBD1 and transport sites remains to be established. Finally, our study shows that Mg<sup>2+</sup> has a stabilizing and structural effect on CBD2 of NCX1 and we suggest that physiological experiments should be performed under controlled Mg<sup>2+</sup> concentrations for obtaining relevant results regarding regulation of the exchanger.

## Acknowledgement

We thank Ing. Nathalie Schilderink for expert assistance with the CBD2 production and purification and Marco Felici for help with the backbone assignment of D552V-CBD2.

## Supplementary Information: Methods and Materials

### NMR-titration

The concentrations bound and unbound protein for a simple one-to-one binding model can be calculated according to:

$$[PL] = [P]_0[L]_0K_D^{-1} \quad (S4.1)$$

$$[P]_0 = [P]_{Total} / (1 + K_D^{-1}[L]_0) \quad (S4.2)$$

$$[L]_0 = -1/2([P]_{Total} + K_D - [L]_{Total}) \pm \frac{1}{4}\sqrt{([P]_{Total} + K_D - [L]_{Total})^2 + [L]_{Total}K_D} \quad (S4.3)$$

With  $[PL]$  the concentration of protein bound with ligand,  $[P]_0$  and  $[L]_0$  the free protein and ligand concentration,  $[P]_{Total}$  and  $[L]_{Total}$  the total protein and ligand concentration.

The spectroscopic signal under fast exchange conditions at titration point  $i$ ,  $S_{meas,i}$ , is the chemical shift difference between the cross-peak at zero ligand concentration and ligand concentration at point  $i$ . The calculated signal,  $S_{calc,i}$  is given by:

$$S_{calc,i} = S_{max} \frac{[PL]_i}{[P]_{Total}} \quad (S4.4)$$

With  $S_{max}$  the maximum signal when the protein is fully bound and  $[PL]_i$  a function of  $K_D$ ,  $[P]_{Total}$  and  $[L]_{Total}$ . The titration is subsequently fitted by minimizing the chi-squared value:

$$\chi^2 = \sum_{i=1} \left( \frac{S_{meas,i} - S_{calc,i}}{\sigma_i} \right)^2 \quad (S4.5)$$

With  $\sigma_i$  the estimated error on the individual data point.

The error estimates in the fitted  $K_D$  and  $S_{max}$  values are estimated by recalculating the fit values 45 times with randomly varying the individual data points (one at a time) assuming normal distributed error and taking the standard deviation of the resulting fit values.

### CD thermal unfolding

The change in free energy for thermal-induced protein unfolding,  $\Delta G(T)$ , is described by the modified Gibbs-Helmholtz equation:

$$\Delta G(T) = \Delta H_m(1 - T/T_m) - \Delta C_p[(T_m - T) + T \ln(T/T_m)] \quad (S4.6)$$

where  $\Delta H_m$  is the enthalpy change for unfolding measured at  $T_m$ ,  $T$  is the absolute temperature,  $T_m$  the temperature at the midpoint of the transition, and  $\Delta C_p$  is the difference in heat capacity between the unfolded and folded state (Becktel and Schellman, 1987; Pace and Laurents, 1989). Under the assumption that  $\Delta C_p$  is temperature independent (Privalov and Khechinashvili, 1974), a two-state mechanism of unfolding can be fitted to individual thermal unfolding curves:

$$Y_{obs} = (a_U + b_U T) + \frac{(a_N + b_N T) - (a_U + b_U T)}{1 + \exp((-\Delta H_m/R)(1/T - 1/T_m) + (\Delta C_p/R)((T_m/T - 1) + \ln(T/T_m)))} \quad (S4.7)$$

where  $Y_{obs}$  is the measured far-UV CD or fluorescence signal,  $R$  is the gas constant,  $a$  and  $b$  the intercepts and slopes of the pre- and post unfolding baselines, respectively. Error estimates in the fit values are estimated by recalculating the fit 100 times selecting randomly 90 percent of all data points and taking the standard deviation of the resulting fit values.

### Estimating Mg<sup>2+</sup> binding affinity

To calculate the Mg<sup>2+</sup> binding affinity from the determined Ca<sup>2+</sup> binding affinities in the absence and presence of 2 mM MgCl<sub>2</sub> (adapted from Malmendal *et al.*, 1999):

$$K_{Mg} = \left( \frac{K_{Ca}}{K_{Ca,app}} - 1 \right) / [Mg^{2+}] \quad (S4.8)$$

in which  $K_{Mg}$  and  $K_{Ca}$  are the Mg<sup>2+</sup> and Ca<sup>2+</sup> association constants and  $K_{Ca,app}$  is the apparent Ca<sup>2+</sup> association constant in the presence of Mg<sup>2+</sup>. With  $K_{Ca} = 1 / (16.1 \cdot 10^{-6})$ ,  $K_{Ca,app} = 1 / (53.5 \cdot 10^{-6})$  and  $[Mg^{2+}] = 2.0 \cdot 10^{-3}$  this yields in a  $K_{Mg}$  of 1161.5 M<sup>-1</sup> which is a  $K_{D,Mg}$  of 860.9  $\mu$ M.

### Electrostatic Potential Calculation

All electrostatic potentials were calculated using the program APBS (Baker *et al.*, 2001) and PDB2PQR (Dolinsky *et al.*, 2004) and visualized using PMV (Sanner, 1999). All calculations were performed in the presence of 150 mM KCl. Both  $\text{Ca}^{2+}$  and  $\text{Mg}^{2+}$  ions were modeled with an ionic charge of  $+2.0 e$  and an ionic radius of  $1.0 \text{ \AA}$ . The structures with PDB codes 2QVM and 2KLS were used for the calculation of CBD2 coordinating two  $\text{Ca}^{2+}$  and zero ions, respectively. The structure of  $\text{Mg}^{2+}$ -CBD2 was obtained by removing  $\text{Ca}^{2+}$  from site I of the  $\text{Ca}^{2+}$ -bound CBD2 structure (PDB code 2QVM) and a subsequent energy minimization in vacuum using standard YASARA protocols and the YASARA2 force field (www.yasara.org). Further minimization in explicit water resulted in large deviations from both the apo and fully  $\text{Ca}^{2+}$ -bound structure. Therefore, the initial energy-minimized structure was chosen for calculation of the electrostatic potential.

## Supplementary Information: Figures and Tables

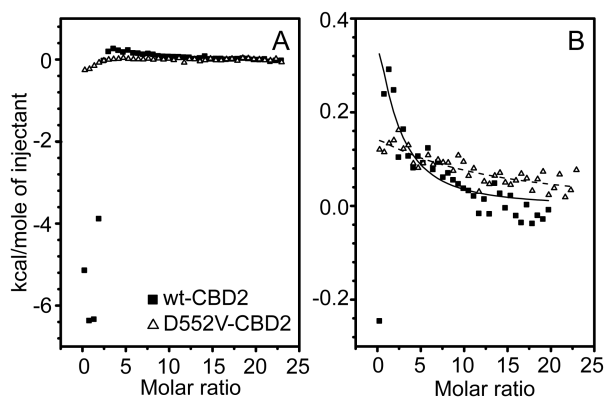


**Figure S4.1.** Comparison of the binding thermodynamics of wt-CBD2 (filled squares) and D552V-CBD2 (open triangles), using ITC and 10 mM  $\text{CaCl}_2$  (A) or  $\text{MgCl}_2$  (B) injections (10-fold higher compared to the experiments displayed in Figure 4.2).

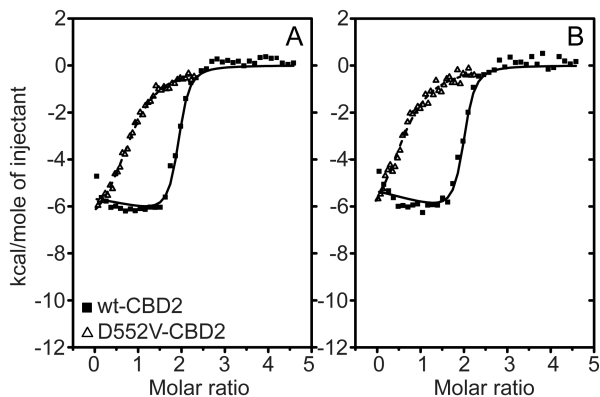


**Figure S4.2.** Comparison of the binding thermodynamics of wt-CBD2 (filled squares) and D552V-CBD2 (open triangles), using ITC. Binding isotherms with 1 or 2 mM  $\text{CaCl}_2$  in the absence (A) or presence of 2 mM choline chloride (B).

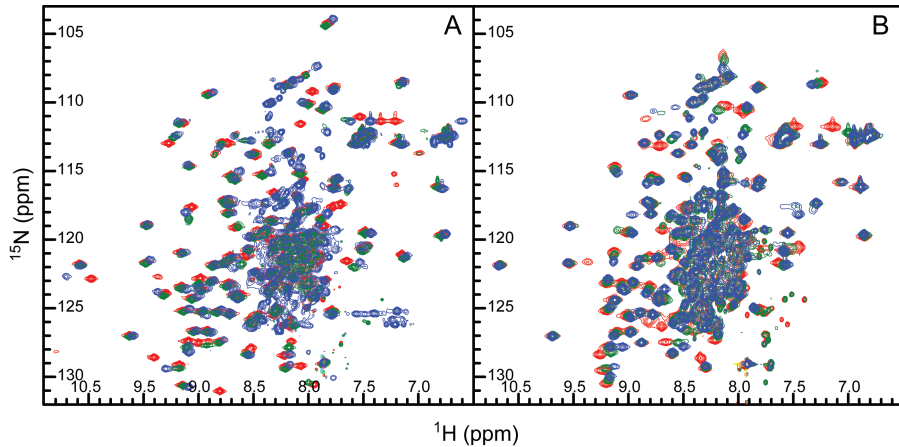


**Figure S4.3.** <sup>15</sup>N-HSQC overlays of wt-CBD2 (A) or D552V-CBD2 (B) at 0 mM (blue), 10 mM MgCl<sub>2</sub> (green) and 10 mM MgCl<sub>2</sub> and CaCl<sub>2</sub> (red).

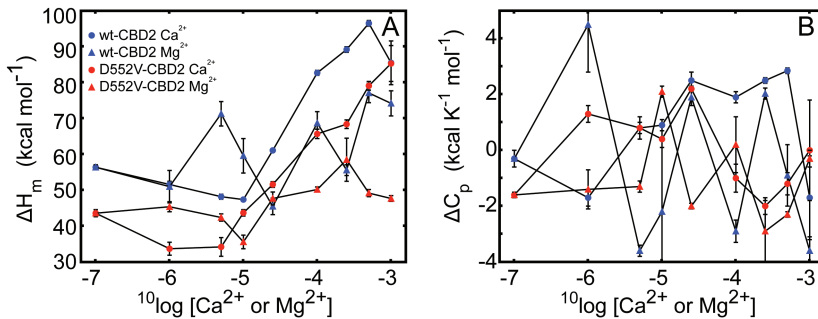


**Figure S4.4.** The ligand concentration dependence of  $\Delta H_m$  (A) and  $\Delta C_p$  (B) for Ca<sup>2+</sup> (circles) and Mg<sup>2+</sup> (triangles) for wt-CBD2 (blue symbols) and D552V-CBD2 (red symbols)

The curves show that for  $\Delta H_m$  we observe a ligand concentration dependent increase, albeit with a larger spread compared to  $T_m$ . For  $\Delta C_p$  no concentration dependence is observed; the data is almost randomly scattered between  $-4.5$  to  $4.5$  kcal K<sup>-1</sup> mol<sup>-1</sup>, which indicates that determining  $\Delta C_p$  from far-UV CD thermal unfolding curves is very difficult, as previously reported (Puglisi and Tinoco, 1989). Determining both  $T_m$  and  $\Delta H_m$  with  $\Delta C_p$  fixed at 0, as previously suggested (Puglisi and Tinoco, 1989), gives very similar results (data not shown).

At ligand concentrations much larger than the protein concentration,  $1/T_m$  is expected to be linear with  $\log([\text{Mg}^{2+}])$  (Puglisi and Tinoco, 1989). For RNA or DNA unfolding, the number of Mg<sup>2+</sup> binding sites have been estimated from the slope of this plot. However, this is under the assumption of small difference between  $\Delta H_m$  in the bound

and unbound form, an assumption that is not fulfilled for CBD2. Likewise, the affinity of binding can only be derived if the difference in  $\Delta H_m$  between the ligand bound form and free form is small.

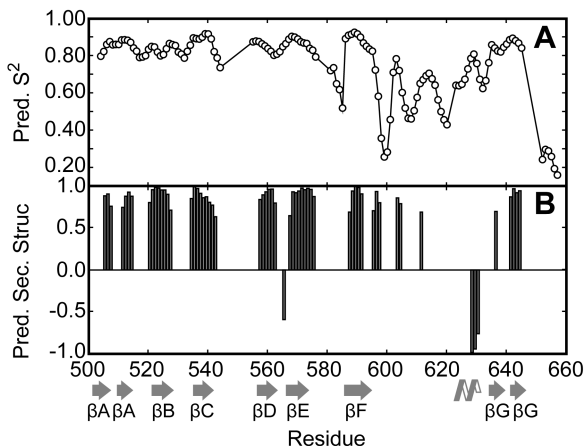


**Figure S4.5.** Order parameter  $S^2$  (A) and secondary structure elements (B) of D552V-CBD2 as a function of residue number as predicted by TALOS+ (Shen *et al.*, 2009). Grey arrows indicate  $\beta$ -strands in wt-CBD2, with the  $\alpha$ -helix between  $\beta$ -strand F and G. No marker in panel A means no assignment, positive or negative score in panel B reflects the probability assigned by TALOS+ for the  $\beta$ -strand or  $\alpha$ -helix, respectively.

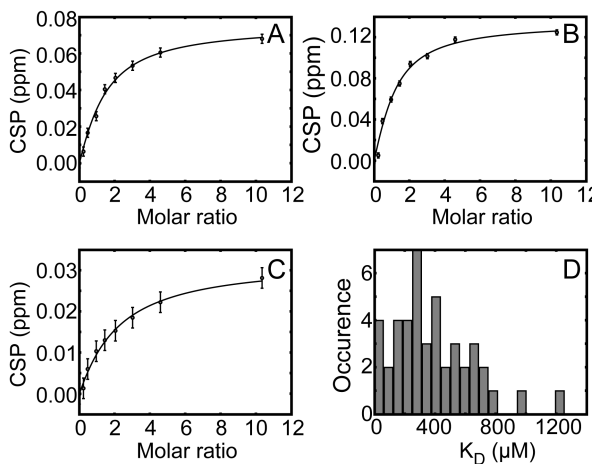


**Figure S4.6.** Three typical examples of  $\text{Mg}^{2+}$  chemical shift perturbation (CSP) binding curves of wt-CBD2: Met<sup>521</sup> (A), Thr<sup>556</sup> (B) and Thr<sup>570</sup> (C). (D) Overall distribution of the fitted  $\text{Mg}^{2+}$  binding  $K_D$  values.

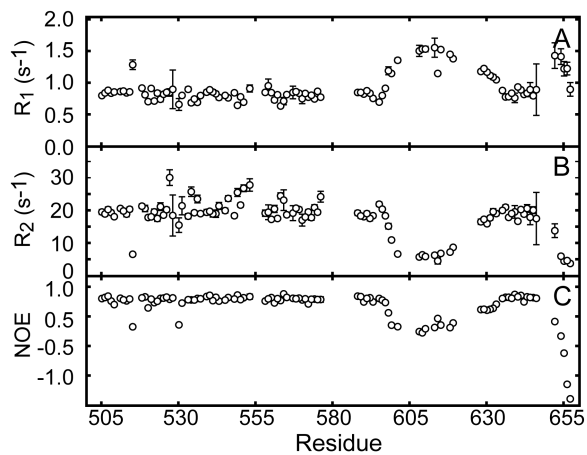


**Figure S4.7.** <sup>15</sup>N backbone relaxation rates of  $R_1$  (A),  $R_{1\rho}$  (B) and NOE (C) versus residue number of Mg<sup>2+</sup>-bound wt-CBD2-AD.

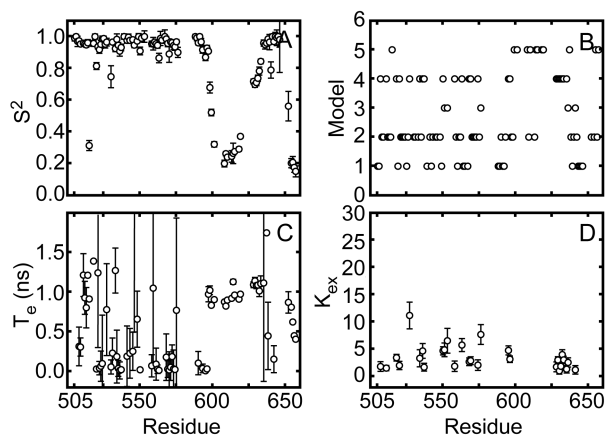


**Figure S4.8.** Model parameters  $S^2$  (A),  $\tau_c$  (B), Model (C) and  $R_{ex}$  (D) versus residue number of Mg<sup>2+</sup>-bound wt-CBD2.



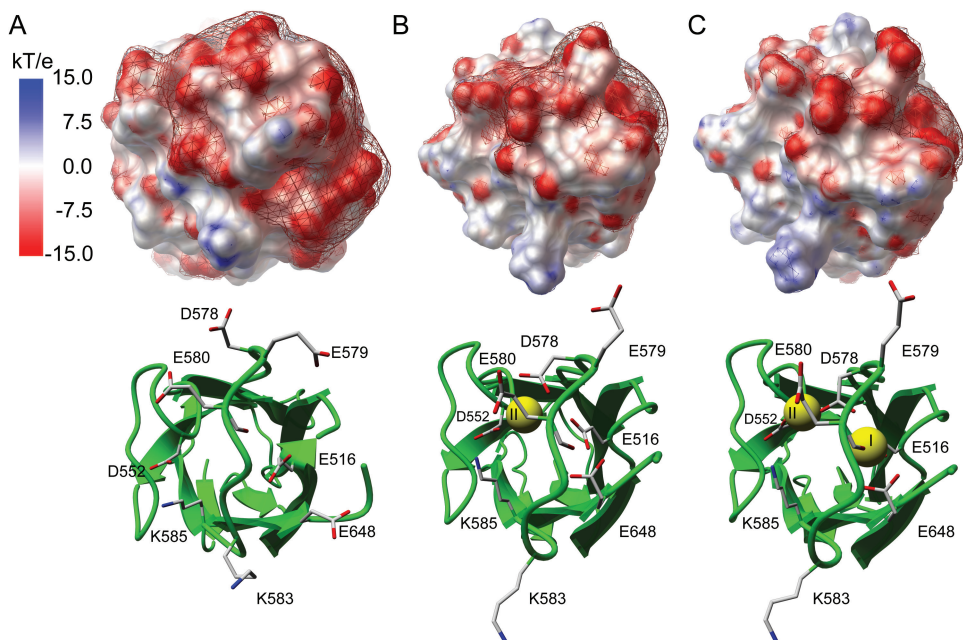


**Figure S4.9.** Electrostatic potentials of the CBD2 Ca<sup>2+</sup>-binding sites in the presence of zero (A), one (B) and two (C) divalent ions (cf. Supplementary Information: Methods and Materials), with the orientation depicted below. All surfaces are colored by electrostatic potential as indicated in panel A and the red and blue meshes represent isocontours of the electrostatic potential at -5 kT/e and +5 kT/e, respectively. Using the latest version of APBS almost identical electrostatic potentials were obtained for (A) and (C) compared to the results previously reported (Hilge *et al.*, 2009). The electrostatic potential of a one Mg<sup>2+</sup>-bound CBD2 deviates both from apo-CBD2 and the fully Ca<sup>2+</sup>-bound CBD2.

# 5

*Solution structure of the second  $\text{Ca}^{2+}$ -binding domain of the B variant of the third isoform of the  $\text{Na}^+/\text{Ca}^{2+}$ -exchanger*

Vincent Breukels, Wouter G. Touw and Geerten W. Vuister

*Manuscript in preparation*

## Abstract

We have determined the solution structure of the B variant of the second  $\text{Ca}^{2+}$ -binding domain of the third isoform of the  $\text{Na}^+/\text{Ca}^{2+}$ -exchanger (NCX3-CBD2-B) in the calcium bound form. The structure is elucidated using NOE, dihedral and RDC restraints. NCX3-CBD2-B displays the Calx- $\beta$  fold with a characteristic  $\beta$ -sandwich comprised of seven  $\beta$ -strands. NCX3-CBD2-B is structurally very similar to the solution structure of the CBD2-AD variant of NCX1 (NCX1-CBD2-AD), which shows that the  $\alpha$ -helix and the  $\beta$ -bulges are conserved within these different isoforms of the exchanger. However, the NCX3-CBD2-B structure is distinct from NCX1-CBD2-AD in the orientation of the  $\alpha$ -helix with respect to the  $\beta$ -sandwich. The current RDC and NOE data are only consistent with a conformation in which the helix axis in NCX3-CBD2-B is almost co-axial with the longitudinal axis of the  $\beta$ -sandwich. Most likely, this represents a biologically more relevant conformation than the helix orientation reported for NCX1-CBD2-AD.

## Introduction

The  $\text{Na}^+/\text{Ca}^{2+}$ -exchanger (NCX) is an omnipresent plasma membrane protein that catalyzes the removal of intracellular  $\text{Ca}^{2+}$  for the uptake of  $\text{Na}^+$  (see for review; Lytton, 2007). Mammals express three isoforms, denoted as NCX1, NCX2, or NCX3, which also display alternative splicing. The exchanger is activated by allosteric  $\text{Ca}^{2+}$  binding to  $\text{Ca}^{2+}$ -binding domains 1 and 2 (CBD1 and CBD2) located in the large cytosolic loop between transmembrane helix 5 and 6. CBD1 binds four  $\text{Ca}^{2+}$  ions, irrespective of the isoform and is considered the primary  $\text{Ca}^{2+}$  sensor. The number of  $\text{Ca}^{2+}$  ions that bind to CBD2 depends on the isoform and splice variant. It is hypothesized that the number of binding sites determines the ability of the exchanger to overcome the  $\text{Na}^+$  dependent inactivation (Hilge *et al.*, 2009).

NCX1 is thus far the best-studied isoform and solution and X-ray structures of NCX1 CBD1 and CBD2 have been determined (Besserer *et al.*, 2007; Hilge *et al.*, 2006; Hilge *et al.*, 2009; Nicoll *et al.*, 2006). CBD1 and CBD2 display an immunoglobulin like fold comprised of seven  $\beta$ -strands. The  $\text{Ca}^{2+}$  binding pocket is formed by the loops connecting the  $\beta$ -strands  $\beta\text{A}-\beta\text{B}$ ,  $\beta\text{C}-\beta\text{D}$  and  $\beta\text{E}-\beta\text{F}$  together with the residues C-terminally of  $\beta\text{G}$ . CBD2 of NCX1 is further characterized by an  $\alpha$ -helix in the large, otherwise unstructured FG-loop opposite to the  $\text{Ca}^{2+}$  binding pocket as well as by two  $\beta$ -bulges disrupting the hydrogen bonding pattern of strands  $\beta\text{A}$  and  $\beta\text{G}$ .

The third mammalian isoform of the NCX (NCX3) is mainly found in brain and skeletal muscle (Nicoll *et al.*, 1996b). NCX3 is subject to alternative splicing that involves exons A, B and C. The alternative splicing region affects CBD2 and alters the number of Ca<sup>2+</sup> binding sites. NCX3-CBD2-AC binds two Ca<sup>2+</sup>, whereas NCX3-CBD2-B and NCX3-CBD2-BC bind three Ca<sup>2+</sup> ions (Hilge *et al.*, 2009). Here, we present the solution structure of NCX3-CBD2-B.

## Methods and Materials

### *Protein expression and purification*

The CBD2-B construct was derived from *mus musculus* NCX3 (accession code: Q7TS90) and cloned into a pET23b vector as previously described (Hilge *et al.*, 2009). Uniformly <sup>15</sup>N and <sup>15</sup>N/<sup>13</sup>C labelled protein was obtained by growing *Escherichia coli* BL21(DE3) in 800 mL of minimal M9 medium in the presence of <sup>15</sup>N ammonium chloride and <sup>13</sup>C-glucose (Cambridge Isotope Laboratories Inc.) at 37 °C and induction by 1mM IPTG for ~4 hrs at an OD<sub>600</sub> of 1.0. Purification was facilitated by N-terminal His tags and anion-exchange chromatography (MonoQ, Amersham-Pharmacia). Purity of all samples was >95% as judged by SDS-PAGE and <sup>15</sup>N-HSQC spectra. The samples were concentrated using a 10 kDa molecular weight cut off Vivaspin 6 (GE Healthcare) and contained ~0.5 mM protein in 20 mM HEPES (pH 7.0), 20 mM β-mercaptoethanol, 10 mM CaCl<sub>2</sub> buffer prepared in 95%/5% H<sub>2</sub>O/D<sub>2</sub>O with 0.03% NaN<sub>3</sub> as preservative. The alignment medium used for Residual Dipolar Coupling (RDC) measurements contained 8 mg/mL of Pf1 phage (ASLA Biotech) and 0.3 mM protein in an otherwise identical buffer. Under these conditions a quadrupolar splitting of 3.4 Hz was observed in the <sup>2</sup>H NMR spectrum. All chemicals were obtained from Sigma Aldrich unless stated otherwise.

### *NMR spectroscopy and structure determination*

NMR spectra were acquired at 306 K on Varian Inova 600 and 800 MHz spectrometers equipped with a standard triple resonance probe and a cold probe, respectively. Backbone resonance assignment was obtained using the following experiments: <sup>15</sup>N-HSQC, HNCO, HNCACB, CBCA(CO)NH and HN(CA)HA. The side chain chemical shifts were obtained using the experiments: HBHA(CO)NH, C(CO)NH, H(C)CH-TOCSY, (H)CCH-TOCSY. Side-chain assignments were improved by analyzing NOE resonances predicted from preliminary structures calculated using distance, dihedral and RDC restraints. Aromatic side chain assignments were obtained from the

$^{13}\text{C}$ -NOESY-HSQC (aromatic). All spectra were processed with the NMRPipe program (Delaglio *et al.*, 1995) and analyzed with CCPN Analysis (Vranken *et al.*, 2005).

RDCs were obtained by in-phase/anti-phase  $^{15}\text{N}$ -HSQC experiments by comparing the peak positions of the up-field and down-field components measured in isotropic solution and the dilute liquid crystalline phase.

$T_\rho$ ,  $T_{1\rho}$  and  $^1\text{H}$ - $^{15}\text{N}$  steady state NOE experiments were recorded at 18.8 T in an interleaved fashion. The recorded time intervals for the  $T_1$  and  $T_{1\rho}$  were 16, 256, 384, 512, 768 and 1024 ms and 16, 32, 48, 64, 96 and 128 ms, respectively. The time delay between the saturated and unsaturated parts in the NOE experiments was 13 s. The relaxation rates were determined as previously described (Breukels and Vuister, 2010) and amide backbone dynamics were derived according to the model-free analysis formulated by Lipari and Szabo implemented in the program Tensor2 (Dosset *et al.*, 2000).

Distance restraints for structure calculation were derived from  $^{13}\text{C}$ -NOESY-HSQC (aliphatic and aromatic) and  $^{15}\text{N}$ -NOESY-HSQC spectra recorded with 80 ms NOE-mixing time. For structure determination the NOESY cross peaks were automatically picked and integrated by CCPN Analysis and manually checked for artefacts and genuinely missed peaks. The input data for CYANA3.0 (Güntert *et al.*, 1997; Güntert, 2009) consisted of the chemical shifts obtained from the resonance assignment, the unassigned peak positions and volumes of the NOESY spectra, 186 backbone dihedral restraints based on the chemical shift information from the program TALOS+ (Shen *et al.*, 2009), and 81  $^1\text{H}$ - $^{15}\text{N}$  RDCs. The NOESY peak lists were automatically assigned during seven cycles of automated assignment and structure calculation. In each cycle one hundred structures were generated and energy minimized using 15,000 steps of simulated annealing. The NOE calibration parameters were automatically determined in the first cycle. In the final cycle 4983 of the 7431 NOESY peaks were assigned. The 20 lowest energy conformers were subsequently subjected to a final round of refinement in explicit solvent using the YASARA force field and the YASARA software ([www.yasara.org](http://www.yasara.org)), in which RDC restraints were not included.

## Results

Protein resonance assignments were achieved for 83.1% of all backbone atoms and 77.4% for all H side-chain assignments. Backbone and side-chain resonance assignments were missing for residues 605 to 610 in the EF-loop and 665 to 669 near the C-terminus. These residues are near the  $\text{Ca}^{2+}$  binding pocket and are in chemical exchange between the

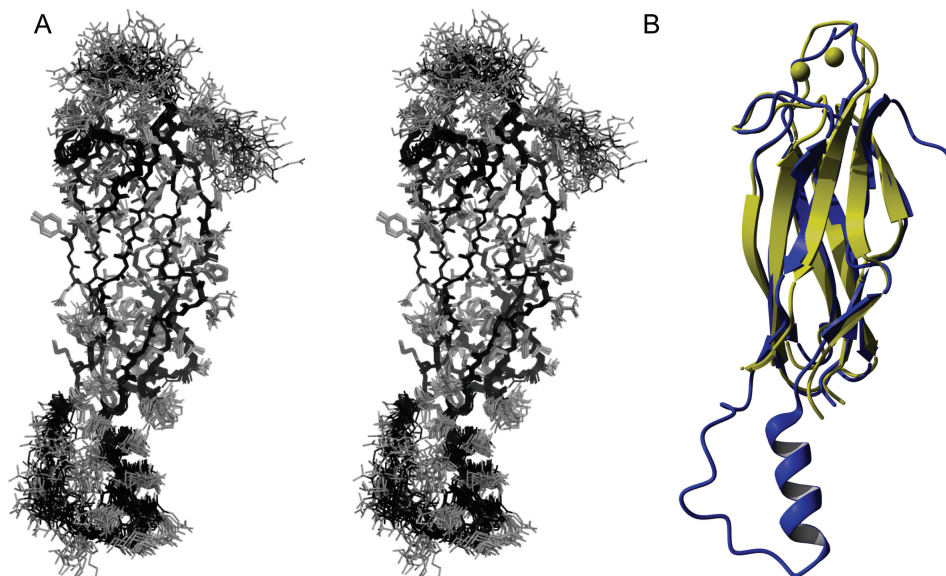


**Figure 5.1.** Solution structure of NCX3-CBD2-B. (A) Stereo view of the structural ensemble. Backbone and side chains are represented as black and grey sticks, respectively. (B) Structural alignment of the lowest-energy conformer (blue) and NCX1-CBD2-AD (2QVM, yellow).  $\text{Ca}^{2+}$  ions are only shown for the crystal structure because crucial resonances were missing in the  $\text{Ca}^{2+}$  binding pocket of NCX3-CBD2-B. The alignment was based on residues in the  $\beta$ -sandwich. Residues 571 to 575 in NCX3-CBD2-B were omitted from (A) and (B) for clarity. Figures created with Pymol ([www.pymol.org](http://www.pymol.org)) and YASARA ([www.yasara.org](http://www.yasara.org)).

apo- and  $\text{Ca}^{2+}$ -form bound form. Possibly, the missing resonances are exchange line broadened beyond detection (cf. Discussion).

The solution structure of NCX3-CBD2-B displays the Calx- $\beta$  fold (Figure 5.1A). The core of NCX3-CBD2-B is formed by seven  $\beta$ -strands (labelled  $\beta\text{A}$  to  $\beta\text{F}$ ). The overall structural statistics of the final water-refined structure are shown in Table 5.1. The  $\text{Ca}^{2+}$  ions were not modelled in the structure because of missing resonance assignments in the  $\text{Ca}^{2+}$  binding pocket.

Similarly to the previously reported structures of CBD2, two  $\beta$ -bulges in NCX3-CBD2-B disrupt the hydrogen-bonding pattern of strands  $\beta\text{A}$  and  $\beta\text{G}$  (labelled  $\beta\text{A}/\beta\text{A}'$  and  $\beta\text{G}/\beta\text{G}'$ ). The strands form a  $\beta$ -sandwich comprised of two  $\beta$ -sheets consisting of strands GABE and strands DCFG'A'. Although the first part of the FG-loop is largely unstructured, an  $\alpha$ -helix is present in the second part of the FG-loop (residues 638-650). NCX3-CBD2-B is nine residues shorter compared to NCX1-CBD2-AD and outside the FG-loop the two proteins display a sequence identity of  $\sim 76\%$ . The N-terminal signal se-

**Table 5.1.** Structural statistics of the 20 lowest energy structures of NCX3-CBD2-B after water-refinement in YASARA

<b>Number of NOE restraints</b>	
2901	Total NOE restraints
1333	Short range ( $ i - j  \leq 1$ )
279	Medium range ( $1 <  i - j  \leq 5$ )
1289	Long range ( $ i - j  > 5$ )
<b>Distance restraints violations</b>	
0	In six or more structures $> 0.2 \text{ \AA}$
0	In six or more structures $> 0.3 \text{ \AA}$
$0.004 \pm 0.001$	r.m.s.
<b>TALOS+ derived restraints</b>	
93	$\phi$
93	$\psi$
<b>Dihedral violations</b>	
1	In six or more structures $> 5^\circ$
$1.71 \pm 0.05$	r.m.s.
<b>Number of RDC restraints</b>	
81	$^1\text{H-}^{15}\text{N}$
<b>RDC violations</b>	
2	In six or more structures $> 5 \text{ Hz}$
$1.74 \pm 0.09$	r.m.s.
$34.5 \pm 1.5$	Q-factor
<b>Ramachandra plot (%)</b>	
80.9	Residues in the most favored region
15.6	Residues in the additionally allowed region
2.2	Residues in the in the generously allowed region
1.3	Residues in the disallowed region
<b>Cing ROG scores</b>	
24.3 / 32/4 / 43.3	ROG (%)
r.m.s.d. to the average coordinates for $\beta$ -sandwich	Residues: 531-542, 546-556, 561-570, 581-589, 594-602, 612-624, 638-665
$0.37 \pm 0.07$	Backbone heavy atom
$0.75 \pm 0.07$	All heavy atom

quence of NCX1 is cleaved off during maturation (Durkin *et al.*, 1991). In contrast, a similar cleavage has not been biochemically verified for NCX3 to date. Therefore, equivalent residues in both proteins have a numbering offset of 27 in the structure reported here. A structural alignment (Figure 5.1B) shows that NCX3-CBD2-B is structurally very similar resulting in a heavy atom backbone r.m.s.d. of  $1.11 \pm 0.04$  Å for the  $\beta$ -sandwich residues relative to NCX1-CBD2-AD.

116  $^1\text{H}$ - $^{15}\text{N}$  RDCs were obtained of which 81 RDCs were measured for residues in the  $\beta$ -sandwich, the  $\alpha$ -helix, and the very short stretch connecting the helix to  $\beta\text{G}$  (Figure 5.2A). This subset, referred to as the ‘standard RDC set’, was used to restrain the orientation of amide bond vectors relative to a common alignment frame during the CYANA structure calculation protocol. The correlation between observed and predicted RDCs is shown in Figure 5.2B for the lowest-energy conformer after refinement in explicit water. RDCs and alignment tensors were fitted to the structure in CYANA3.0 using singular value decomposition. The Q factor (Cornilescu *et al.*, 1998) calculated for the NCX3-CBD2-B ensemble is  $34.5 \pm 1.3$  %.

### Backbone dynamics

The rotational diffusion anisotropy of NCX3-CBD2-B was best described by an axial symmetric diffusion tensor, characterized by a  $D_{\parallel}/D_{\perp}$  ratio of  $1.68 \pm 0.03$  and an overall tumbling correlation time  $\tau_{av,aniso}$  of  $11.6 \pm 0.14$  ns. The generalized order parameter  $S^2$  is plotted as a function of residue number in Figure 5.2C. The mean  $S^2$  values are 0.94, 0.80, and 0.55 in the  $\beta$ -sandwich,  $\alpha$ -helix, and the first part the FG-loop before the helix, respectively.

We observed internal motion in the FG-loop characterized by an internal correlation time  $\tau_i$  of  $0.96 \pm 0.48$  ns. An extra apparent conformational exchange contribution of  $1.6 \pm 1.5$  s $^{-1}$  was sufficient for the helix but not the rest of the FG loop to explain the measured relaxation data (Figure S5.1). The dynamics of the first part of the FG loop could only be accurately described by a modified Lipari-Szabo model that includes both motions on a time-scale much faster than the overall protein rotation, and slower internal dynamics with a correlation time comparable to  $\tau_{av,aniso}$ .

### Water refinement and structure validation

The water refinement of the protein structure was performed in YASARA. Unfortunately, YASARA only restrains inter-atomic distances and dihedral angles but



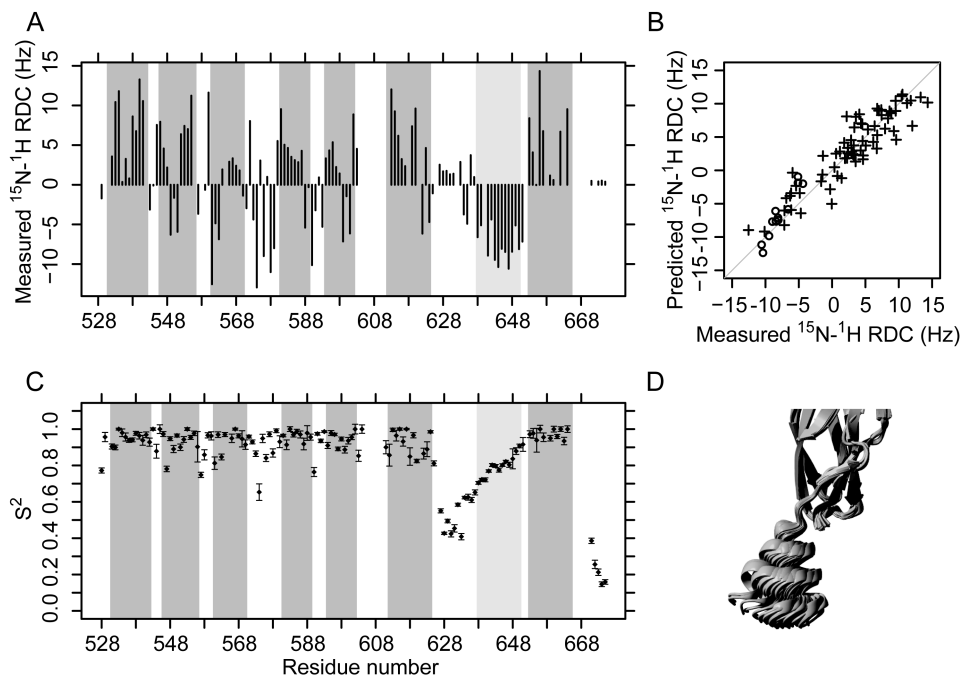


Figure 5.2. (A) Measured  $^1\text{H}$ - $^{15}\text{N}$  RDC values as function of residue number. The estimated uncertainty is 0.8 Hz. Secondary structure elements are represented by dark ( $\beta$ -strands) and light ( $\alpha$ -helix) grey rectangles. (B) Correlation between measured and back-calculated RDCs using the lowest-energy conformer of the structural ensemble. Circles indicate  $\alpha$ -helix residues, crosses indicate residues in  $\beta$  strands and residues connecting the  $\alpha$ -helix to  $\beta$ G. The grey line represents a perfect correlation. (C) Generalized order parameter,  $S^2$ , as function of residue number. Background as in (A). (D) Comparison of  $\alpha$ -helix orientations in eight separate structure determinations calculated with different sets of  $\alpha$ -helix RDC restraints, but using otherwise identical RDC restraints for all other residues. All structures were aligned using backbone heavy-atoms in the  $\beta$ -sandwich

not the orientation of amide bond vectors. Xplor-NIH (Schwieters *et al.*, 2006) can use RDC potentials during the simulated annealing protocol. To investigate whether structures could be improved relative to YASARA-refined structures, we subjected the 20 lowest-energy conformers of CYANA to explicit water refinement in Xplor-NIH using a standard protocol that included RDC potentials. In our hands the standard Xplor-NIH water-refinement protocol over-refines the RDCs at the cost of very high dihedral and Ramachandran energies. Scaling of the RDC potentials did reduce the high dihedral and

Ramachandran energies, but at the cost of increased RDC Q-factors and violations of distance restraints. In summary, the best structures in terms of fit with the experimental data and common criteria for structural quality were obtained when the CYANA structure calculation using distance, dihedral and RDC restraints, was followed by a refinement protocol in explicit water using the YASARA force-field. The overall improved structural quality was indicated by a better definition of secondary structure elements, 70 to 80 % less distance, dihedral, van der Waals, and RDC violations when compared to the best Xplor-NIH runs. Juxtaposed to the CYANA output (not water-refined), all but the RDC quality criteria are better for YASARA-refined structures. The reported structures were validated using the iCING web server (Vuister, et al., Manuscript in preparation). Overall validation statistics are reported in Table 5.1.

In this study, we selected  $^1\text{H}$ - $^{15}\text{N}$  RDCs to restrain the orientation of amide bond vectors of residues in the  $\beta$ -sandwich, the  $\alpha$ -helix, and of residues between the helix and strand  $\beta\text{G}$ . To validate the orientation of the helix with respect to the  $\beta$ -sandwich, we performed several additional structure calculations using different RDC restraint sets. First, we calculated a structure with RDC restraints only from residues in the  $\beta$ -sandwich, but with the identical distance and dihedral restraints as used for the reported structure. A comparable structure was obtained and the orientation of the  $\alpha$ -helix was similar. However, when  $\alpha$ -helix RDC restraints were included in the structure calculation a better agreement between the measured and predicted RDCs in both helix and strands was observed, as reflected in the Q factors of  $36.5 \pm 2.0$  % and  $34.5 \pm 1.3$  %, respectively. Before water-refinement the difference in correlation between observed and fitted RDCs from structures calculated with the two RDC sets was more distinct and the Q-factors were lower; the calculated Q was  $31.1 \pm 2.7$  % for structures where only RDCs  $\beta$ -sandwich residues were used as restraints, but improved to  $15.2 \pm 0.5$  % for the standard restraint set inclusive of  $\alpha$ -helix residues.

A similar comparison was made between structures calculated with the standard restraint set and in addition to using RDC restraints of residues having an  $S^2 > 0.7$ . The set included 20 extra residues in the loops connecting strands  $\beta\text{A}$  to  $\beta\text{F}$ . Some of these additional residues were found to be relatively rigid, having even higher  $S^2$  values when compared to residues in the  $\alpha$ -helix. The structures obtained using this extended restraints set displayed a similar helix orientation, but the use of RDCs in loops gave rise to a small deterioration of structural quality indicators.

Finally, to further investigate the robustness of the  $\alpha$ -helix orientation and the

information content of RDC restraints in this part of the structure, we calculated several structures, each time using a different set of RDC restraints as input. The seven different sets consisted of standard RDC restraints but only eleven  $\alpha$ -helix RDC restraints. Two helical RDC restraints were left out consistently. The discarded RDC restraints were the first two residues of the  $\alpha$ -helix (638/639), the last two residues (649/650), two residues in the middle (643/644), and four other pairs (641/645, 642/647, 646/648, 648/649). The helix orientations of the resulting structures are shown in Figure 5.2D. Before refinement in explicit solvent, the Q factors calculated for all RDC restraints in the standard set, thus including all thirteen  $\alpha$ -helix RDC restraints, varied between 15 and 23 %, indicating a comparable agreement between observed and fitted RDC restraints. The helix thus samples a number of conformations that fit similarly well to the observed RDC restraints. The relaxation data supports the existence of multiple conformations, because a conformational exchange contribution to the motion of the helix was observed.

## Discussion

In this study we present the first structure of the second  $\text{Ca}^{2+}$ -binding domain of the third NCX isoform. NCX3-CBD2-B employs the Calx- $\beta$  comprised of seven  $\beta$ -strands forming a  $\beta$ -sandwich. The Calx- $\beta$  motif has been structurally characterized in the calcium binding domains of NCX1 (Besserer *et al.*, 2007; Hilge *et al.*, 2006; Hilge *et al.*, 2009; Nicoll *et al.*, 2006) and the *Drosophila melanogaster*  $\text{Na}^+/\text{Ca}^{2+}$ -exchanger (CALX; Wu *et al.*, 2009; Wu *et al.*, 2010), as well as in human integrin  $\beta 4$  (Alonso-García *et al.*, 2009). In the CBDs of NCX1 the loops connecting the  $\beta$ -strands  $\beta A$ - $\beta B$ ,  $\beta C$ - $\beta D$  and  $\beta E$ - $\beta F$  form the  $\text{Ca}^{2+}$  binding pocket. Our structure shows that the  $\beta$ -bulges are conserved between the various NCX isoforms suggesting a potential role in NCX functioning, although their role is currently unclear.

Like the calcium binding domains of other NCX isoforms, NCX3-CBD2-B has a highly anisotropic prolate diffusion tensor indicated by a  $D_{\parallel}/D_{\perp}$  ratio of  $\sim 1.7$ . The overall tumbling of  $\text{Ca}^{2+}$ -bound NCX3 ( $\sim 11.6$  ns) is slightly faster than the  $\text{Ca}^{2+}$ -bound forms of NCX1 CBD1 ( $\sim 12.5$  ns, Johnson *et al.*, 2008) and CBD2-AD ( $\sim 13.1$  ns, Breukels and Vuister, 2010), consistent with the higher  $D_{\parallel}/D_{\perp}$  ratio ( $\sim 2.1$ ) of NCX1 domains compared to NCX3 ( $\sim 1.7$ ). Surprisingly, the  $D_{\parallel}/D_{\perp}$  ratio and  $\tau_{av,aniso}$  values correlate well with the apo form of NCX1-CBD2-AD ( $\sim 1.4$  and 11.4 ns) and NCX1-CBD2-BD ( $\sim 1.5$  and 11.8 ns; Breukels and Vuister, 2010), a splice variant unable to bind  $\text{Ca}^{2+}$ . The loops in the  $\text{Ca}^{2+}$  binding pocket of the apo form of NCX1-CBD2-AD and NCX1-CBD2-B are more

flexible and therefore these variants have a less anisotropic diffusion tensor (Breukels and Vuister, 2010). Strikingly, no resonances are observed in NCX1-CBD2-B spectra for residues 577 to 585 which reside in the EF-loop (Hilge *et al.*, 2009). In NCX3-CBD2-B we are also unable to find resonances in the same EF-loop, as well as the residues in the C-tail. Furthermore, isothermal titration calorimetry (ITC) data of NCX3-CBD2-B shows that the three  $\text{Ca}^{2+}$  ions have macroscopic dissociation constants ( $K_D$ ) of 3.9, 8.3 and 19  $\mu\text{M}$ , which is almost ten times higher than the  $\text{Ca}^{2+}$  affinity of NCX1-CBD2-AD ( $K_D$  of 0.4 and 1.1  $\mu\text{M}$ ). The decreased affinity either originates from a lower  $k_{on}$  or higher  $k_{off}$  and the latter would result in an increased chemical exchange. We observed high chemical exchange rates in for residues in the CD  $\text{Ca}^{2+}$  binding loop (2 - 12.5  $\text{s}^{-1}$ ). Therefore, the  $\text{Ca}^{2+}$  binding affinity together with the relaxation data strongly support the hypothesis that the resonances of residues in the EF-loop and C-tail are exchange line broadened beyond detection as a result of exchange between the apo and  $\text{Ca}^{2+}$  bound form even at an excess of 10 mM  $\text{CaCl}_2$ .

The entire FG-loop is absent in the crystal structure of NCX1-CBD2-AD due to lack of electron density. Although the FG-loop is very flexible, an  $\alpha$ -helix is present in the second half of the loop, as shown by the previous solution structures of NCX1-CBD2 and this work on NCX3-CBD2. In the NMR structure of NCX1-CBD2-AD the  $\alpha$ -helix is oriented almost perpendicular to the longitudinal axis of the  $\beta$ -sandwich. In contrast, the  $\alpha$ -helix was found to be much more co-axial with the  $\beta$ -core in the structure of NCX3-CBD2-B reported here. This orientation was validated by fitting two separate alignment tensors to the  $\beta$ -sandwich and the  $\alpha$ -helix and exploring the relative orientations that best fit all observed RDCs. The two tensors differed significantly when the helix had the orientation as observed for NCX1-CBD2-AD. Furthermore, such an orientation resulted in a systematic offset in the correlation between observed and predicted RDCs from both helical and  $\beta$ -sandwich residues. In contrast, the two alignment tensors were virtually the same in the structure reported here.

The previously determined NMR structures were obtained without the usage of RDC restraints, which could explain the differences between the NCX3-CBD2-B and the other CBD2 NMR structures. The relaxation data show that the FG-loop is flexible and therefore all structures lack long range NOEs in this part of the molecule. The different orientation of the  $\alpha$ -helix in NCX1-CBD2-AD and NCX1-CBD2-B might originate from lack of RDC data rather than genuine differences between the isoforms and we speculate that the  $\alpha$ -helix is similarly oriented in all isoforms.

In the intact exchanger a very short linker of three residues connects CBD1 to CBD2. In NCX1 the last  $\text{Ca}^{2+}$  coordinating residue is Asp<sup>500</sup> and the  $\beta\text{A}$  strand of CBD2 starts at Gly<sup>503</sup>. Hence, the  $\text{Ca}^{2+}$  binding sites of CBD1 are in close proximity of the BC, DE and FG-loops of CBD2. An NMR study on NCX1 using RDC restraints shows that CBD1 and CBD2 adopt a very elongated orientation with an angle of almost 180 degrees between the long axes of CBD1 and CBD2. In the apo form this orientation is very flexible, however binding of  $\text{Ca}^{2+}$  rigidifies the linker and restricts the motion of both domains (Salinas *et al.*, 2011). Interestingly, chemical shift differences between the individual domains and the CBD12 construct implicated the presence of several residues in the CBD2-FG-loop at the CBD12 interface.

In contrast to the NCX, the FG-loop of the second  $\text{Ca}^{2+}$ -binding domain of *Drosophila melanogaster*  $\text{Na}^+/\text{Ca}^{2+}$ -exchanger (CALX-CBD2) is observed in the crystal structure (Wu *et al.*, 2009). This FG-loop has two  $\alpha$ -helices, one at the end of the  $\beta\text{F}$ -strand (H1) and one in front of the  $\beta\text{G}$ -strand (H2). In the CALX-CBD2 structure H2 adopts an orientation parallel to the long axis of the  $\beta$ -sandwich (Wu *et al.*, 2009), very similar to orientation of the  $\alpha$ -helix we report for NCX3-CBD2-B. A very recent X-ray study on a CALX-CBD12 constructed showed that the two CBDs also adopt an elongated orientation like NCX-CBD12 (Wu *et al.*, 2011). In this structure H2 is at the CBD12 interface and very close to the  $\text{Ca}^{2+}$  binding sites of CBD1. ITC and mutational analysis showed that several residues in H2 influence the  $\text{Ca}^{2+}$  binding of CBD1.

## Conclusions

In summary, we have determined the solution structure of NCX3-CBD2-B. The  $\beta$ -sandwich core of the protein is structurally very similar to previously reported NCX CBDs. Our structure is distinct from NCX1-CBD2-AD in the orientation of the  $\alpha$ -helix in the FG-loop with respect to the  $\beta$ -sandwich. Although this orientation is dynamical, our RDC data shows that it adopts an orientation that is primarily parallel to the  $\beta$ -sandwich. We speculate that a similar helix orientation would be present in the other variants of CBD2. Finally, recent studies show that this  $\alpha$ -helix is part of the CBD12 interface and influences the  $\text{Ca}^{2+}$  binding sites of CBD1. Our study shows the conformation of the  $\alpha$ -helix in NCX3-CBD2-B, which is more likely to represent a biologically relevant conformation than the helix orientation reported for NCX1-CBD2-AD.

## Acknowledgements

We thank Jurgen Doreleijers for assistance with Xplor-NIH and iCing, Gjalt van Rутten for support with using the HPC Cloud infrastructure at BitBrains. This work was supported by grants from the Netherlands Organization for Scientific Research (NWO): 700.55.443.700.57.101.

## Supplementary Information: Figures

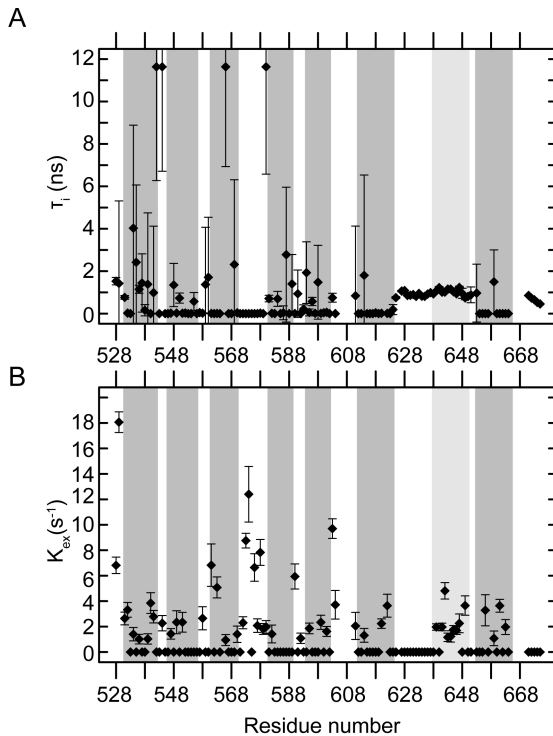
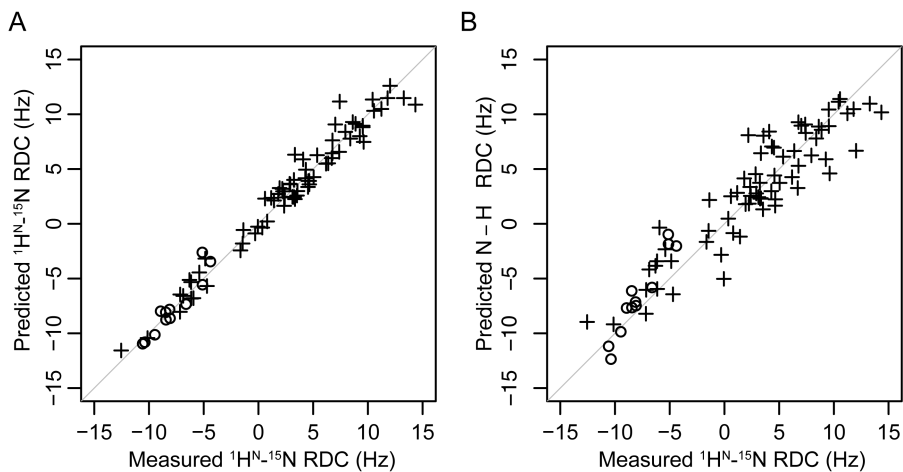


Figure S5.1.  $^{15}\text{N}$  backbone dynamical parameters. (A) Correlation time for internal motion as a function of residue number. (B) Chemical exchange contribution per residue.



**Figure S5.2.** Correlation between observed  $^1\text{H}$ - $^{15}\text{N}$  RDCs and RDCs fitted to the lowest energy conformer of NCX3-CBD2-B before (A) and after (B) refinement in explicit water refinement using YASARA. Note that YASARA only restrains inter-atomic distances and dihedral angles but not the orientation of amide bond vectors. Circles indicate  $\alpha$ -helix residues, crosses are from residues in  $\beta$  strands and residues connecting the  $\alpha$ -helix to  $\beta$ G. The grey lines represent a perfect correlation.

# 6

## **Discussion**

*Structural and dynamic aspects of  $\text{Ca}^{2+}$  and  $\text{Mg}^{2+}$  binding of the regulatory domains of the sodium-calcium exchanger*

Vincent Breukels, Wouter G. Touw and Geerten W. Vuister

*Biochem. Soc. Trans. in press*



## Abstract

Intracellular  $\text{Ca}^{2+}$  regulates the activity of the  $\text{Na}^+/\text{Ca}^{2+}$ -exchanger through binding to the cytosolic  $\text{Ca}^{2+}$ -binding domains, CBD1 and CBD2. *In vitro* studies of the structure and dynamics of CBD1 and CBD2, as well as studies of their kinetics and thermodynamics of  $\text{Ca}^{2+}$  binding, greatly enhanced our understanding of NCX regulation. We describe the fold of the CBDs in relation to other known structures and review  $\text{Ca}^{2+}$  binding of the different CBD variants from a structural perspective. We also report on new findings concerning  $\text{Mg}^{2+}$  binding to the CBDs and finally we discuss recent results on CBD1-CBD2 inter-domain interactions.

## Introduction

The  $\text{Na}^+/\text{Ca}^{2+}$ -exchanger (NCX) is a crucial membrane protein controlling cytosolic  $\text{Ca}^{2+}$  levels. In cardiomyocytes and neurons  $\text{Na}^+/\text{Ca}^{2+}$  exchange is the main extrusion mechanism across the plasma membrane (Lyttton, 2007; Reeves and Condrescu, 2008). Four NCX genes (NCX1-4; Li *et al.*, 1994; Marshall *et al.*, 2005; Nicoll *et al.*, 1990; Nicoll *et al.*, 1996b) are presently known and together constitute the NCX family (ie. Solute Carrier eight or SLC8; On *et al.*, 2008; Quednau *et al.*, 2004). NCX1 and NCX3 have 17 and 3 splice variants, respectively, whereas NCX2 does not display alternative splicing (Quednau *et al.*, 1997).

The exchanger is regulated by both  $\text{Na}^+$  and  $\text{Ca}^{2+}$  and by other factors such as  $\text{H}^+$ , phosphatidylinositol bisphosphate ( $\text{PIP}_2$ ) and a large number of interacting proteins (Dipolo and Beauge, 2006). The regulation occurs through interactions with the large cytosolic loop connecting transmembrane helices 5 and 6 (cf. Figure 6.1A). The loop starts with the 20 residue long exchanger inhibitory peptide (XIP) (Li *et al.*, 1991); so-called because exogenous XIP is a potent exchanger inhibitor. The XIP-region is thought to be involved in both  $\text{Na}^+$  and  $\text{PIP}_2$  regulation (He *et al.*, 2000; Matsuoka *et al.*, 1997). The XIP sequence is followed by a domain of yet unknown function modeled to be similar to  $\alpha$ -catenin and subsequently denoted CLD for catenin-like domain (Hilge *et al.*, 2006). The best-studied region comprises the two  $\text{Ca}^{2+}$ -binding domains (CBD1 and CBD2) residing C-terminally of the CLD (Besserer *et al.*, 2007; Hilge *et al.*, 2006; Hilge *et al.*, 2009; Nicoll *et al.*, 2006). Allosteric binding of  $\text{Ca}^{2+}$  to these domains is required for NCX to turn into the active state (Dipolo and Beauge, 2006). Importantly, the region affected by alternative splicing resides in CBD2 changing the  $\text{Ca}^{2+}$  binding capabilities (Quednau *et al.*, 1997) and NCX response *in vivo* (Dyck *et al.*, 1999).

### CBD1 and CBD2

To date, only CBD1 (Hilge *et al.*, 2006; Nicoll *et al.*, 2006) and CBD2 (Besserer *et al.*, 2007; Hilge *et al.*, 2006; Hilge *et al.*, 2009) of NCX1 have been structurally characterized. Both CBD1 and CBD2 comprise a Calx- $\beta$  motif. Figure 6.1C shows a structure-based sequence alignment of selected Calx- $\beta$  domains. The Calx- $\beta$  motif displays an immunoglobulin fold with a characteristic  $\beta$ -sandwich comprised of seven  $\beta$ -strands denoted A-G (cf. Figure 6.1B). In both CBD1 and CBD2 the hydrogen-bonding pattern in strand A is locally disrupted by a  $\beta$ -bulge separating the strand into two parts (A and A'). In strand G, a cis-proline is observed in CBD1 while a  $\beta$ -bulge is observed in CBD2 at the same location again splitting the strand in two parts (G and G'). The function of these bulges in CBD1 and CBD2 is at present unclear, but edge strand  $\beta$ -bulges may prevent oligomerization of immunoglobulin domains (Park and Saven, 2006).

The seven  $\beta$ -strands are arranged in two  $\beta$ -sheets consisting of strands GABE and strands DCFG'A' (cf. Figure 6.1B) that together form a hydrophobic core made up of several relatively conserved aromatic amino acids. The  $\beta$ -sandwich is also stabilized by salt-bridges at the surface. The sandwich has a cylinder-like shape with a long axis of about 45 Å and a diameter of 25 Å. The N- and C-termini of the domain are positioned at opposite sides of the two sheets and the Ca<sup>2+</sup> binding sites are located C-terminally of strand A with the coordinating residues residing in loops AB, CD, and EF (displayed for NCX1-CBD1 and CBD2-AD in Figure 6.2).

Other protein domains, such as the human integrin  $\beta$ 4, VLGR1, or both calcium binding domains of the *Drosophila melanogaster* Na<sup>+</sup>/Ca<sup>2+</sup>-exchanger (CALX) also employ the Calx- $\beta$  motif. However, the Calx- $\beta$  domain of integrin  $\beta$ 4 does not bind calcium as Arg<sup>1003</sup> (equivalent to Glu<sup>385</sup>/Glu<sup>516</sup>, Figures 1C and 2) stabilizes the acidic region by occupying the position structurally similar to Ca<sup>2+</sup> (Alonso-García *et al.*, 2009). Similarly, two lysine residues neutralize the acidic residues of CALX1.1-CBD2 (Wu *et al.*, 2009) and only CALX-CBD1 binds calcium (Wu *et al.*, 2010).

The Calx- $\beta$  domains belong to the superclass of immunoglobulin-like folds, which also comprises other members such as C2, cadherin, and immunoglobulin domains. The C2-domains, present in phospholipases, protein kinases C, and synaptotagmins, are not only structurally homologous, but also bind Ca<sup>2+</sup>. Although the Calx- $\beta$  and C2-domains bear structural homology, the domains are usually classified as different motifs in domain databases such as SCOP (Murzin *et al.*, 1995). The  $\beta$ -sandwich of C2-domains is composed of 8 strands instead of the 7 strands that build up the sandwich of the Calx- $\beta$

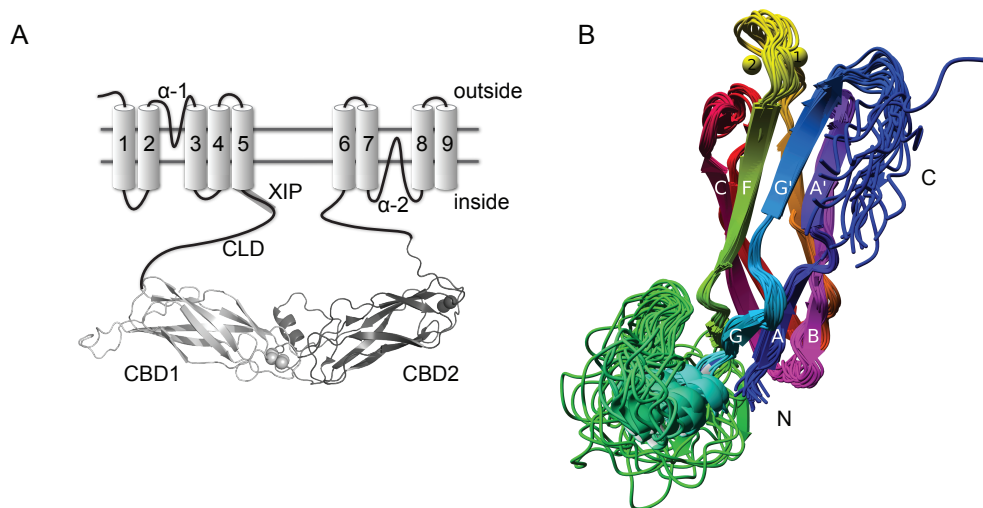
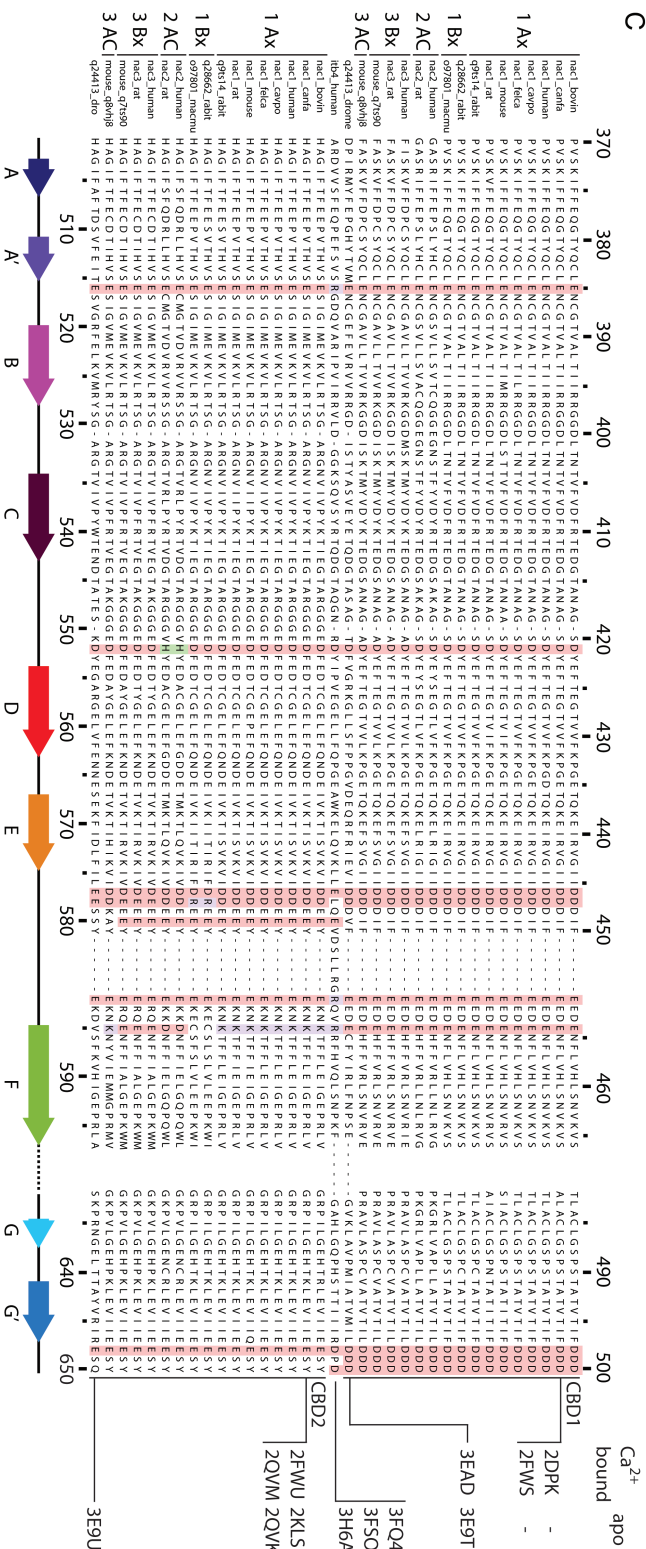


**Figure 6.1.** (A) Predicted topology of NCX, including the transmembrane helices (cylinders), XIP,  $\alpha$ -catenin-like domain (CLD) and both Calcium Binding Domain 1 (CBD1; PDB: 2DPK) and Calcium Binding Domain 2 (CBD2; PDB: 2FWU). The individual domains are not drawn to scale. CBD1 and CBD2 adopt an elongated conformation. (B) NMR structure of the second calcium binding domain of the sodium-calcium exchanger (NCX1-CBD2-AD). 20 superposed models of the ensemble are shown (PDB: 2FWU). Strand labels are indicated. For clarity, only the calcium ions (yellow spheres 1 and 2) of the first model are shown. Figure generated with YASARA ([www.yasara.org](http://www.yasara.org)) (C, on the next page) Structure-based sequence alignment of Calx- $\beta$  domains in NCX, Calx1.1, and integrin  $\beta 4$ . Only a selection is shown of all the Calx- $\beta$  sequences that were used in the alignment.  $\text{Ca}^{2+}$  coordinating positions are colored (Asp/Glu: red, Arg/Lys: blue, His: green). Strand names and colors in the topology diagram below the alignment correspond to the structure displayed in (B). The FG loop has been omitted from the alignment and topology diagram for clarity. NCX splice variants are indicated on the left. Exon A or B containing variants are grouped as Ax or Bx, respectively. Sequence names correspond to Swiss-Prot or TrEMBL entry names. NCX1-CBD1 residue numbers are shown above the alignment. The numbering shown below the alignment is based on NCX1-CBD2-AD. All numbering in this paper is based on the canine NCX1-AD splice variant (NCX1.4). Available PDB structures and the reported  $\text{Ca}^{2+}$  state are shown on the right.

domains. Furthermore, a multiple structural alignment of several representative C2- and Calx- $\beta$  domains using MUSTANG (Konagurthu *et al.*, 2006) shows that the  $\text{Ca}^{2+}$  binding sites are located at opposite sites of the  $\beta$ -sandwich. The 'BC' (L2) and 'FG' loops (L5) of C2 bind  $\text{Ca}^{2+}$ , while the AB, CD, and EF loops bind  $\text{Ca}^{2+}$  in Calx- $\beta$  domains.



### $Ca^{2+}$ binding properties of CBD1 and CBD2

NCX1-CBD1 binds four  $Ca^{2+}$  ions (subsequently referred to as  $Ca^{2+}$  I-IV), irrespective of the isoform. NCX1-CBD2-AD binds two  $Ca^{2+}$  ions (denoted as  $Ca^{2+}$  1 and 2). A structural alignment of the crystal structures of  $Ca^{2+}$ -bound NCX1-CBD1 and CBD2-AD (cf. Figure 6.2) shows that the calcium binding sites in both domains are characterized by a high number of structurally conserved glutamate and aspartate residues that coordinate  $Ca^{2+}$  in a mono- or bi-dentate fashion. A few residues even coordinate multiple  $Ca^{2+}$  ions and some  $Ca^{2+}$  ions are bound by backbone carbonyl moieties in addition to side chain carboxylates. The coordination number of the different  $Ca^{2+}$  ions varies from five to eight with water molecules coordinating ions II, 1 and 2. The  $Ca^{2+}$  1 and III and  $Ca^{2+}$  2 and II ions occupy comparable structural positions.

A structural comparison between the apo forms of CBD1 and CBD2 is difficult due to the lack of an apo structure of CBD1, as CBD1 appears partly unstructured in the absence of  $Ca^{2+}$  (Hilge *et al.*, 2006; Nicoll *et al.*, 2006). This loss of structural integrity is probably caused by electrostatic repulsion between the acidic residues in the  $Ca^{2+}$  binding loops of CBD1. In contrast, apo NCX1-CBD2-AD remains structured as result of the stabilizing salt-bridge between Lys<sup>585</sup> and Asp<sup>552</sup>. Glu<sup>454</sup> in CBD1 is orthologous to Lys<sup>585</sup> in CBD2 (cf. Figures 1C and 2) and CBD1 obtains CBD2-like properties when Glu<sup>454</sup> is mutated to a lysine (Chaptal *et al.*, 2009). The lysine residue replaces  $Ca^{2+}$  I and forms salt-bridges with residues coordinating  $Ca^{2+}$  in wild-type CBD1 (Chaptal *et al.*, 2009).

Isothermal titration calorimetry (ITC) showed that all three mammalian isoforms of CBD1 bind  $Ca^{2+}$  with comparable affinities. The first two binding events have a relatively high affinity ( $K_D \sim 200 - 500$  nM), whereas the latter two binding events occur only at elevated  $Ca^{2+}$  concentrations ( $K_D \sim 10$   $\mu$ M) (Hilge *et al.*, 2009). In contrast, the different isoforms and splice variants of CBD2 bind between zero and three  $Ca^{2+}$  ions (Hilge *et al.*, 2009) and the affinities vary between 0.2 – 20  $\mu$ M. With the exception of Asp<sup>578</sup>, all residues involved in  $Ca^{2+}$  coordination at site 1 are conserved within the NCX (cf. Figure 6.1C). The residues that largely determine the number of bound  $Ca^{2+}$  ions of CBD2 (sites 2,3) are found at positions 552, 578 and 585. NCX1-CBD2 variants containing exon B do not bind any  $Ca^{2+}$ , because Arg<sup>578</sup> replaces the crucial aspartate involved in coordinating both  $Ca^{2+}$  ions in exon A containing variants. Other changes are present in NCX isoforms 2 and 3. NCX2-CBD2 lacks binding site 2, because it has a histidine residue at position 552 and an aspartate residue at the orthologous position 585 (cf. Figure 6.1C) (Hilge *et al.*, 2009). NCX3-CBD2-AC binds two ions and is very similar to CBD2-AD of NCX1,

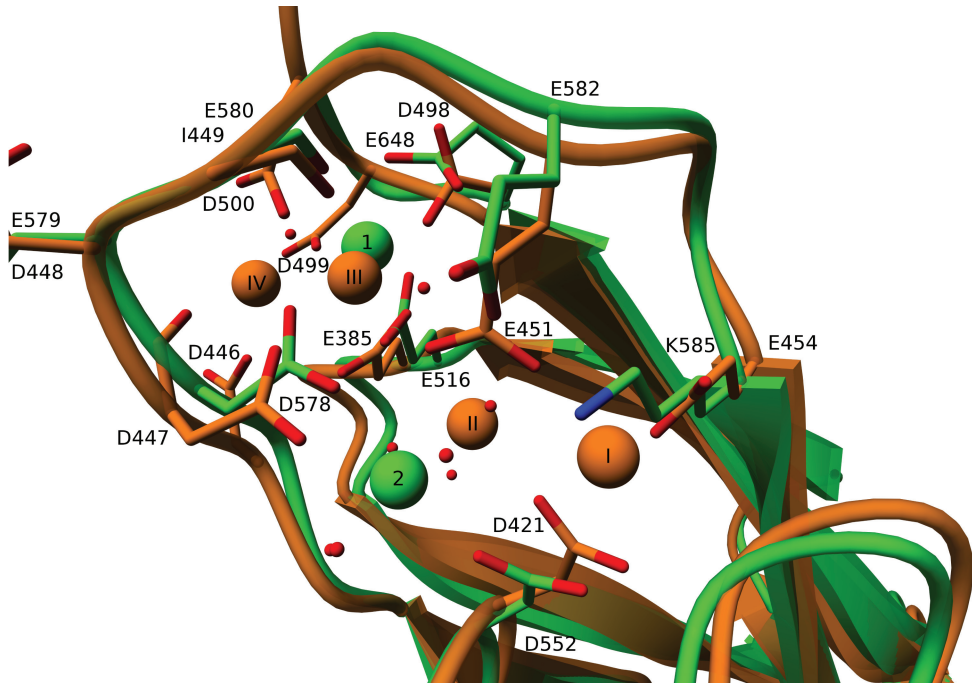


**Figure 6.2.**  $\text{Ca}^{2+}$  coordination of NCX-CBD1 (orange, PDB: 2DPK) and NCX1-CBD2-AD (green, PDB: 2QVM). Spheres indicate  $\text{Ca}^{2+}$  of CBD1 (I-IV) and CBD2 (1-2).  $\text{Ca}^{2+}$  II, 1, and 2 are coordinated by 3, 2 and 5 water molecules (red spheres), respectively.

whereas NCX3-CBD2-B has glutamate residue at position 585 thereby introducing a third binding site (Hilge *et al.*, 2009). Mutating His<sup>552</sup> to Asp and Asp<sup>585</sup> to Lys in NCX2-CBD2 and Glu<sup>585</sup> to Lys in NCX3-CBD2-B results in  $\text{Ca}^{2+}$  binding properties very similar to wild-type NCX1-CBD2-AD (Hilge *et al.*, 2009), underscoring the crucial role of these structural positions in determining the  $\text{Ca}^{2+}$  binding stoichiometries.

The relative importance of the  $\text{Ca}^{2+}$  binding sites has been studied by electrophysiological experiments in *Xenopus* oocytes expressing both wild-type and mutant NCX1. Mutants affecting binding sites III and IV of CBD1 decrease the affinity for cytosolic  $\text{Ca}^{2+}$ , whereas disruption of site I and II hardly affects  $\text{Ca}^{2+}$  regulation of NCX (Chaptal *et al.*, 2009; Ottolia *et al.*, 2009). Three mutations in CBD2 (Glu<sup>516</sup> to Leu, Asp<sup>578</sup> to Val or Glu<sup>648</sup> to Val) that disrupt Ca site 1 almost completely, remove the NCX  $\text{Ca}^{2+}$  sensitivity, whereas disrupting site 2 has little effect (Besserer *et al.*, 2007). Interestingly, mutating Glu<sup>516</sup>, Asp<sup>578</sup> or Glu<sup>468</sup> to an arginine in lieu of a leucine or valine residue, partially recovers  $\text{Ca}^{2+}$  regulation even though these arginine mutations do not restore  $\text{Ca}^{2+}$  binding at site 1 of CBD2 (Ottolia *et al.*, 2009). This finding suggests that a positive charge in CBD2 primary binding site is required for CBD1 to activate the exchanger.

*Dynamics and stability*

Although apo-CBD1 partly unfolds, under relatively high salt conditions an NMR study proved the  $\beta$ -sandwich of CBD1 to be intact in the absence of  $\text{Ca}^{2+}$  (Johnson *et al.*, 2008). The binding of  $\text{Ca}^{2+}$  is accompanied by relatively small reorientations of the binding loops and coordinating residues. Consequently, the  $\text{Ca}^{2+}$  binding event of CBD1 has to be relayed to the membrane part of the exchanger by other means such as altered protein dynamics or changes in domain orientation. The NMR studies also showed that binding of  $\text{Ca}^{2+}$  reduces the flexibility of the  $\text{Ca}^{2+}$ -binding loops. For NCX1-CBD2-AD the conformational changes upon  $\text{Ca}^{2+}$  binding are less pronounced than for CBD1, likely because the Lys<sup>585</sup> to Asp<sup>552</sup> salt-bridge that is formed in the absence of  $\text{Ca}^{2+}$ . However, similar to CBD1 the binding of  $\text{Ca}^{2+}$  rigidifies the  $\text{Ca}^{2+}$  binding loops in CBD2. Compared to the apo form,  $\text{Ca}^{2+}$ -bound CBD2 is significantly more elongated (Breukels and Vuister, 2010). Whether the changes in dynamics are transferred to other parts of the exchanger remains to be established, but significantly altered dynamics were observed for the FG-loop in CBD2 located opposite to the  $\text{Ca}^{2+}$ -binding loops in response to  $\text{Ca}^{2+}$  (Breukels and Vuister, 2010).

The stability of CBD1 and CBD2 is strongly dependent on ligand binding. Using far UV circular dichroism spectroscopy we determined the thermal stability of NCX1-CBD2-AD in the presence and absence of ligands. An increase of  $\sim 30$  °C in melting temperature ( $T_M$ ) is observed in the presence of  $\text{Ca}^{2+}$  compared to the apo form of CBD2 [unpublished results Breukels V. Konijnenberg A., Nabuurs S.M., Touw W.G. and Vuister G.W.]. For an Asp<sup>552</sup> to Val mutant we observed a decrease in the  $T_M$  by approximately 12 °C both in the absence and presence of  $\text{Ca}^{2+}$ , which underscored the stabilizing role of the salt-bridge between Asp<sup>552</sup> to Lys<sup>585</sup>.

We also tested whether  $\text{Mg}^{2+}$  can be a ligand for NCX1-CBD2-AD. Using a combination of NMR, ITC and CD spectroscopy we showed that CBD2 binds  $\text{Mg}^{2+}$  and stabilizes CBD2. The affinity of  $\text{Mg}^{2+}$  for site 1 or site 2 is distinctly different. Whereas site 2 has a high affinity for  $\text{Mg}^{2+}$  and is not replaced by  $\text{Ca}^{2+}$  under physiological conditions, site 1 only weakly associates with  $\text{Mg}^{2+}$  and is easily replaced by  $\text{Ca}^{2+}$  (Breukels *et al.*, 2011). The data shows that the  $\text{Mg}^{2+}$  bound form is both dynamically and structurally in an intermediate state that influences the  $\text{Ca}^{2+}$  binding affinity of site I. Furthermore, thermal unfolding showed that  $\text{Mg}^{2+}$  bound CBD2 has a 12 °C increased  $T_M$  compared to the apo form. Together, this prompted the idea that site 2 of CBD2 has structuring rather than regulatory role in the intact exchanger, potentially associated with the requirement for a

**Table 6.1.** Table of Ca<sup>2+</sup> and Mg<sup>2+</sup> binding properties of various CBDs

Variant	Ca <sup>2+</sup> -sites	Ca <sup>2+</sup> affinity K <sub>D</sub> ( $\mu$ M)		Mg <sup>2+</sup> binding
NCX1-CBD1	4	0.2 $\pm$ 0.1	0.6 $\pm$ 0.1	- <sup>1)</sup>
		9.4 $\pm$ 2.2	9.7 $\pm$ 2.4	
NCX1-CBD2-AD	2	0.4 $\pm$ 1.2	1.1 $\pm$ 1.4	+
NCX1-CBD2-BD	0	-		Not tested
NCX2-CBD2	1	12.8 $\pm$ 1.2		+ <sup>1)</sup>
NCX3-CBD2-B	3	4.0 $\pm$ 0.4	8.3 $\pm$ 1.0	+ <sup>1)</sup>
		19.4 $\pm$ 2.9		
NCX3-CBD2-AC	2	0.3 $\pm$ 0.1	15.6 $\pm$ 0.9	- <sup>1)</sup>

Data from (Hilge *et al.*, 2009) and (Breukels *et al.*, 2011). The last column shows detected (+) or undetected (-) interaction with Mg<sup>2+</sup>, and <sup>1)</sup> indicates preliminary results.

positive charge in this domain.

Mg<sup>2+</sup> binding might also be associated with CBD1 and with other variants of CBD2. In a preliminary study we have tested if Mg<sup>2+</sup> interacts with NCX1-CBD1 and four CBD2 variants (cf. Table 6.1) by measuring thermal unfolding using a thermofluor assay. This assay uses a dye, which might influence the binding process; however, the results of the thermal unfolding CD data of NCX1-CBD2-AD were correctly reproduced. We observed that Mg<sup>2+</sup> interacts with NCX2-CBD2 and NCX3-CBD2-B, but not NCX1-CBD1. Surprisingly, Mg<sup>2+</sup> does not bind to NCX3-CBD2-AC even though this variant has the same coordinating residues as NCX1-CBD2-AD and the Ca<sup>2+</sup> coordination is likely to be identical. Possibly the lack of Mg<sup>2+</sup> binding originates from differences in residues in proximity of the coordinating ones, which modulate the ability of the loops to accommodate an Mg<sup>2+</sup> ion. We are currently investigating these issues.

### Inter-Domain Interactions

The individual Ca<sup>2+</sup>-binding domains are now well characterized, however, the exact mechanism by which the domains regulate the intact exchanger is still not resolved. Understanding this process requires experiments in intact exchanger or with multiple domains and some exciting new results have recently been reported.

A very short linker of three amino acids connects CBD1 and CBD2, which restricts the relative orientation of the domains in a head-to-tail fashion (cf. Figure 6.1A). The first *in vitro* study on the combined CBD1 and CBD2 construct (CBD12) using



small angle X-ray scattering indicated that  $\text{Ca}^{2+}$  binding induces changes in the inter-domain orientation (Hilge *et al.*, 2009). These observations have been confirmed by FRET measurements showing an increased distance between the N- and C-termini of CBD12 upon  $\text{Ca}^{2+}$  binding. Intriguingly, the intact NCX most likely exists as a dimer where the distance between the monomers decreases in the presence of  $\text{Ca}^{2+}$  (John *et al.*, 2011). A recent NMR study probably provides for the most detailed report thus far on the relative orientation of CBD12 (Salinas *et al.*, 2011). CBD12 adopts an elongated shape, but in the absence of  $\text{Ca}^{2+}$  the linker is sufficiently flexible allowing CBD12 to assume a wide range of relative orientations. Binding of  $\text{Ca}^{2+}$  to CBD1 constrains the linker and CBD12 forms a more rigid, elongated conformation.

The influence of CBD2 on the  $\text{Ca}^{2+}$  binding sites of CBD1 is still under debate. Several studies have shown that the affinity for  $\text{Ca}^{2+}$  of CBD1 changes in the presence of CBD2, although it is unclear whether the affinity increases (Hilge *et al.*, 2009; Ottolia *et al.*, 2009) or decreases (Giladi *et al.*, 2010). Furthermore, it is also not clear which residues of CBD2 are involved. It is apparent that CBD2 has to be in close proximity, as the introduction of 7 alanine residues in the linker region decreases the  $\text{Ca}^{2+}$  affinity (Ottolia *et al.*, 2010) in a functional exchanger and increases the  $\text{Ca}^{2+}$  dissociation rate of CBD1 (Giladi *et al.*, 2010). It is suggested that the FG-loop of CBD2 is involved; however, deletion of the FG loop residues does not alter the  $\text{Ca}^{2+}$ -dependent regulation of NCX (Ottolia *et al.*, 2009).

We comprehend  $\text{Ca}^{2+}$  binding to the individual CBDs and begin to understand the interplay between CBD1 and CBD2. Unfortunately, a structural view on the transfer of the  $\text{Ca}^{2+}$  binding events in CBD12 towards the ion transport sites near the membrane is still lacking. Future structural studies on the complete cytosolic loop or even on the intact exchanger are needed to answer these outstanding questions regarding our understanding of NCX regulation.

# 7

## References

- Almond, A., and Axelsen, J. B. **2002**. Physical interpretation of residual dipolar couplings in neutral aligned media. *J Am Chem Soc* 124:9986-9987.
- Alonso-García, N., Inglés-Prieto, A., Sonnenberg, A., and de Pereda, J. M. **2009**. Structure of the Calx-beta domain of the integrin beta4 subunit: insights into function and cation-independent stability. *Acta Crystallogr D Biol Crystallogr* 65:858-871.
- Altieri, A. S., and Byrd, R. A. **2004**. Automation of NMR structure determination of proteins. *Curr Opin Struct Biol* 14:547-553.
- André, I., and Linse, S. **2002**. Measurement of Ca<sup>2+</sup>-binding constants of proteins and presentation of the CaLigator software. *Anal Biochem* 305:195-205.
- Andrec, M., Du, P. C., and Levy, R. M. **2001a**. Protein backbone structure determination using only residual dipolar couplings from one ordering medium. *J Biomol NMR* 21:335-347.
- Andrec, M., Du, P. C., and Levy, R. M. **2001b**. Protein structural motif recognition via NMR residual dipolar couplings. *J Am Chem Soc* 123:1222-1229.
- Andronesi, O. C., Becker, S., Seidel, K., Heise, H., Young, H. S., and Baldus, M. **2005**. Determination of membrane protein structure and dynamics by magic-angle-spinning solid-state NMR spectroscopy. *J Am Chem Soc* 127:12965-12974.
- Arnesano, F., Banci, L., Bertini, I., Fantoni, A., Tenori, L., and Viezzoli, M. S. **2005**. Structural interplay between calcium(II) and copper(II) binding to S100A13 protein. *Angew Chem Int Edit* 44:6341-6344.
- Atkinson, R. A., and Kieffer, B. **2004**. The role of protein motions in molecular recognition: insights from heteronuclear NMR relaxation measurements. *Prog Nucl Mag Res Sp* 44:141-187.
- Ayala, I., Sounier, R., Usé, N., Gans, P., and Boisbouvier, J. **2009**. An efficient protocol for the complete incorporation of methyl-protonated alanine in perdeuterated protein. *J Biomol NMR* 43:111-119.
- Ayed, A., Mulder, F. A. A., Yi, G. S., Lu, Y., Kay, L. E., and Arrowsmith, C. H. **2001**. Latent and active p53 are identical in conformation. *Nat Struct Biol* 8:756-760.
- Bagby, S., Tong, K. I., Liu, D., Alattia, J. R., and Ikura, M. **1997**. The button test: a small scale method using microdialysis cells for assessing protein solubility at concentrations suitable for NMR. *J Biomol NMR* 10:279-282.
- Bai, Y., Sosnick, T. R., Mayne, L., and Englander, S. W. **1995**. Protein folding intermediates: native-state hydrogen exchange. *Science* 269:192-197.
- Baker, N. A., Sept, D., Joseph, S., Holst, M. J., and McCammon, J. A. **2001**. Electrostatics of nanosystems: application to microtubules and the ribosome. *P Natl Acad Sci Usa* 98:10037-10041.
- Baker, P. F., Blaustein, M. P., Hodgkin, A. L., and Steinhardt, R. A. **1969**. The influence of calcium on sodium efflux in squid axons. *J Physiol (Lond)* 200:431-458.
- Balambika, R., Inui, T., Sargsyan, H., Arshava, B., Cohen, L. S., Ding, F. X., Becker, J. M., and Naider, F. **2007**. Synthesis of a double transmembrane domain fragment of Ste2p by native chemical ligation. *Int J Pept Res Ther* 13:251-263.
- Baldisseri, D. M., Rustandi, R. R., Zhang, Z. S., Tang, C., Bair, C. L., Landar, A., Landar, A., Zimmer, D. B., and Weber, D. J. **1999**. Letter to the Editor: H-1, C-13 and N-15 NMR sequence-specific resonance assignments for rat apo-S100A1(alpha alpha). *J Biomol NMR* 14:91-92.
- Barbato, G., Ikura, M., Kay, L., Pastor, R., and Bax, A. **1992**. Backbone dynamics of calmodulin studied by N-15 relaxation using inverse detected 2-dimensional NMR-spectroscopy - the central helix is flexible. *Biochemistry* 31:5269-5278.
- Barnwal, R. P., Jobby, M. K., Sharma, Y., and Chary, K. V. R. **2006**. NMR assignment of M-crystallin: a novel Ca<sup>2+</sup> binding protein of the beta gamma-crystallin superfamily from Methanosarcina acetivorans. *J Biomol Nmr* 36:32-32.
- Barnwal, R. P., Agarwal, G., and Sharma, Y. **2009**. Complete backbone assignment of a Ca<sup>2+</sup>-binding protein of the  $\beta\gamma$ -crystallin superfamily from Methanosarcina acetivorans, at two denaturant concentrations. *Biomol Nmr Assignm*.
- Bartels, C., Billeter, M., Güntert, P., and Wüthrich, K. **1996**. Automated sequence-specific NMR assignment of homologous proteins using the program GARANT. *J Biomol NMR* 7:207-213.
- Bartels, C., Güntert, P., Billeter, M., and Wüthrich, K. **1997**. GARANT - A general algorithm for resonance

- assignment of multidimensional nuclear magnetic resonance spectra. *J Comput Chem* 18:139-149.
- Bas, D. C., Rogers, D. M., and Jensen, J. H. 2008. Very fast prediction and rationalization of pKa values for protein-ligand complexes. *Proteins* 73:765-783.
- Baum, J., Dobson, C. M., Evans, P. A., and Hanley, C. 1989. Characterization of a partly folded protein by NMR methods: studies on the molten globule state of guinea pig alpha-lactalbumin. *Biochemistry* 28:7-13.
- Bax, A., Clore, G. M., and Gronenborn, A. M. 1990. 1H-1H correlation via isotropic mixing of 13C magnetization, a new 3-dimensional approach for assigning 1H and 13C spectra of 13C-enriched proteins. *J Magn Reson* 88:425-431.
- Bax, A., Ikura, M., Kay, L. E., and Zhu, G. 1991. Removal of f1-base-line distortion and optimization of folding in multidimensional nmr-spectra. *J Magn Reson* 91:174-178.
- Becktel, W. J., and Schellman, J. A. 1987. Protein stability curves. *Biopolymers* 26:1859-1877.
- Berlin, K., O'Leary, D. P., and Fushman, D. 2009. Improvement and analysis of computational methods for prediction of residual dipolar couplings. *J Magn Reson* 201:25-33.
- Berridge, M. J., Bootman, M. D., and Roderick, H. L. 2003. Calcium signalling: dynamics, homeostasis and remodelling. *Nat Rev Mol Cell Biol* 4:517-529.
- Besserer, G. M., Ottolia, M., Nicoll, D. A., Chaptal, V., Cascio, D., Philipson, K. D., and Abramson, J. 2007. The second Ca2+-binding domain of the Na+-Ca2+ exchanger is essential for regulation: Crystal structures and mutational analysis. *P Natl Acad Sci Usa* 104:18467-18472.
- Bhattacharya, A., Tejero, R., and Montelione, G. T. 2007. Evaluating protein structures determined by structural genomics consortia. *Proteins* 66:778-795.
- Billeter, M., Wagner, G., and Wüthrich, K. 2008. Solution NMR structure determination of proteins revisited. *J Biomol NMR* 42:155-158.
- Blaustein, M. P., Charpentier, T. H., and Weber, D. J. 2007. Getting a grip on calcium regulation. *P Natl Acad Sci Usa* 104:18349-18350.
- Bondos, S. E., and Bicknell, A. 2003. Detection and prevention of protein aggregation before, during, and after purification. *Anal Biochem* 316:223-231.
- Bossuyt, J., Taylor, B. E., James-Kracke, M., and Hale, C. C. 2002. Evidence for cardiac sodium-calcium exchanger association with caveolin-3. *FEBS Lett* 511:113-117.
- Bouchner, W. 1993. Azara. Cambridge: Biochemistry Department.
- Boyman, L., Mikhasenko, H., Hiller, R., and Khananshvil, D. 2009. Kinetic and equilibrium properties of regulatory calcium sensors of NCX1 protein. *J Biol Chem* 284:6185-6193.
- Boyman, L., Hagen, B. M., Giladi, M., Hiller, R., Lederer, W. J., and Khananshvil, D. 2011. Proton-sensing Ca2+ Binding Domains Regulate the Cardiac Na+/Ca2+ Exchanger. *J Biol Chem* 286:28811-28820.
- Breukels, V., and Vuister, G. W. 2010. Binding of calcium is sensed structurally and dynamically throughout the second calcium-binding domain of the sodium/calcium exchanger. *Proteins* 78:1813-1824.
- Breukels, V., Konijnenberg, A., Nabuurs, S. M., Touw, W. G., and Vuister, G. W. 2011. The second Ca(2+)-binding domain of NCX1 binds Mg(2+) with high affinity. *Biochemistry* 50:8804-8812.
- Brünger, A., G. Marius Clore, G. M., Gronenborn, A. M., and Saffrich, R. 1993. Assessing the quality of solution nuclear magnetic resonance structures by complete cross-validation. *Science*.
- Brünger, A. T. 2007. Version 1.2 of the Crystallography and NMR system. *Nat Protoc* 2:2728-2733.
- Bryson, M., Tian, F., Prestegard, J. H., and Valafar, H. 2008. REDCRAFT: A tool for simultaneous characterization of protein backbone structure and motion from RDC data. *J Magn Reson* 191:322-334.
- Buchler, N. E. G., Zuiderweg, E. R. P., Wang, H., and Goldstein, R. A. 1997. Protein heteronuclear NMR assignments using mean-field simulated annealing. *J Magn Reson* 125:34-42.
- Cai, X., and Lytton, J. 2004. The cation/Ca(2+) exchanger superfamily: phylogenetic analysis and structural implications. *Mol Biol Evol* 21:1692-1703.
- Capozzi, F., Casadei, F., and Luchinat, C. 2006. EF-hand protein dynamics and evolution of calcium signal transduction: an NMR view. *J Biol Inorg Chem* 11:949-962.
- Carafoli, E. 2002. Calcium signaling: A tale for all seasons. *P Natl Acad Sci Usa* 99:1115-1122.
- Carr, P. A., Erickson, H. P., and Palmer, A. G. 1997. Backbone dynamics of homologous fibronectin type III

- cell adhesion domains from fibronectin and tenascin. *Structure* 5:949-959.
- Cavalli, A., Eghbali, M., Minosyan, T. Y., Stefani, E., and Philipson, K. D. 2007a. Localization of sarcolemmal proteins to lipid rafts in the myocardium. *Cell Calcium* 42:313-322.
- Cavalli, A., Salvatella, X., Dobson, C. M., and Vendruscolo, M. 2007b. Protein structure determination from NMR chemical shifts. *P Natl Acad Sci Usa* 104:9615-9620.
- Cavanagh, J., Fairbrother, W. J., Palmer, A. G., Rance, M., and Skelton, N. J. 2007. Protein NMR spectroscopy: Principles and Practice 2nd ed, vol. Elsevier Academic Press.
- Chaptal, V., Ottolia, M., Mercado-Besserer, G., Nicoll, D. A., Philipson, K. D., and Abramson, J. 2009. Structure and Functional Analysis of a Ca<sup>2+</sup> Sensor Mutant of the Na<sup>+</sup>/Ca<sup>2+</sup> Exchanger. *J Biol Chem* 284:14688-14692.
- Chen, J. H., Mandelshtam, V. A., and Shaka, A. J. 2000. Regularization of the two-dimensional filter diagonalization method: FDM2K. *J Magn Reson* 146:363-368.
- Clapham, D. E. 2007. Calcium signaling. *Cell* 131:1047-1058.
- Clark, E. 1998. Refolding of recombinant proteins. *Curr Opin Biotechnol* 9:157-163.
- Condrescu, M., Gardner, J. P., Chernaya, G., Aceto, J. F., Kroupis, C., and Reeves, J. P. 1995. ATP-dependent regulation of sodium-calcium exchange in Chinese hamster ovary cells transfected with the bovine cardiac sodium-calcium exchanger. *J Biol Chem* 270:9137-9146.
- Cornilescu, G., Marquardt, J., Ottiger, M., and Bax, A. 1998. Validation of protein structure from anisotropic carbonyl chemical shifts in a dilute liquid crystalline phase. *J Am Chem Soc* 120:6836-6837.
- Cornilescu, G., Delaglio, F., and Bax, A. 1999. Protein backbone angle restraints from searching a database for chemical shift and sequence homology. *J Biomol NMR* 13:289-302.
- Cota, E., Hamill, S., Fowler, S., and Clarke, J. 2000. Two proteins with the same structure respond very differently to mutation: The role of plasticity in protein stability. *J Mol Biol* 302:713-725.
- Cunha, S. R., Bhasin, N., and Mohler, P. J. 2007. Targeting and stability of Na/Ca exchanger 1 in cardiomyocytes requires direct interaction with the membrane adaptor ankyrin-B. *J Biol Chem* 282:4875-4883.
- de la Torre, J. G., Huertas, M. L., and Carrasco, B. 2000. HYDRONMR: Prediction of NMR relaxation of globular proteins from atomic-level structures and hydrodynamic calculations. *J Magn Reson* 147:138-146.
- Delaglio, F., Grzesiek, S., Vuister, G. W., Zhu, G., Pfeifer, J., and Bax, A. 1995. NMRPipe - A multidimensional spectral processing system based on UNIX pipes. *J Biomol NMR* 6:277-293.
- Delaglio, F., Kontaxis, G., and Bax, A. 2000. Protein structure determination using molecular fragment replacement and NMR dipolar couplings. *J Am Chem Soc* 122:2142-2143.
- Diercks, T., Daniels, M., and Kaptein, R. 2005. Extended flip-back schemes for sensitivity enhancement in multidimensional HSQC-type out-and-back experiments. *J Biomol NMR* 33:243-259.
- diGuan, C., Li, P., Riggs, P. D., and Inouye, H. 1988. Vectors that facilitate the expression and purification of foreign peptides in escherichia-coli by fusion to maltose-binding protein. *Gene* 67:21-30.
- Dipolo, R. 1979. Calcium influx in internally dialyzed squid giant axons. *J Gen Physiol* 73:91-113.
- Dipolo, R., and Beauge, L. 2006. Sodium/calcium exchanger: Influence of metabolic regulation on ion carrier interactions. *Physiol Rev* 86:155-203.
- DiPolo, R., and Beauge, L. 2008. In the squid axon Na<sup>+</sup>/Ca<sup>2+</sup> exchanger the state of the Ca<sup>i</sup>-regulatory site influences the affinities of the intra- and extracellular transport sites for Na<sup>+</sup> and Ca<sup>2+</sup>. *Pflug Arch Eur J Phy* 456:623-633.
- Dokmanic, I., Sikic, M., and Tomic, S. 2008. Metals in proteins: correlation between the metal-ion type, coordination number and the amino-acid residues involved in the coordination. *Acta Crystallogr D* 64:257-263.
- Dolinsky, T. J., Nielsen, J. E., McCammon, J. A., and Baker, N. A. 2004. PDB2PQR: an automated pipeline for the setup of Poisson-Boltzmann electrostatics calculations. *Nucleic Acids Res* 32:W665-667.
- Dominguez, C., Boelens, R., and Bonvin, A. M. J. J. 2003. HADDOCK: A protein-protein docking approach based on biochemical or biophysical information. *J Am Chem Soc* 125:1731-1737.
- Dong, H., Dunn, J., and Lytton, J. 2002. Stoichiometry of the Cardiac Na<sup>+</sup>/Ca<sup>2+</sup> exchanger NCX1.1 measured in transfected HEK cells. *Biophys J* 82:1943-1952.

- Doreleijers, J. F., Raves, M. L., Rullmann, T., and Kaptein, R. 1999. Completeness of NOEs in protein structure: a statistical analysis of NMR. *J Biomol NMR* 14:123-132.
- Doreleijers, J. F., Vranken, W. F., Schulte, C., Lin, J., Wedell, J. R., Penkett, C. J., Vuister, G. W., Vriend, G., Markley, J. L., and Ulrich, E. L. 2009. The NMR restraints grid at BMRB for 5,266 protein and nucleic acid PDB entries. *J Biomol NMR* 45:389-396.
- Dosset, P., Hus, J. C., Blackledge, M., and Marion, D. 2000. Efficient analysis of macromolecular rotational diffusion from heteronuclear relaxation data. *J Biomol NMR* 16:23-28.
- Dosset, P., Hus, J. C., Marion, D., and Blackledge, M. 2001. A novel interactive tool for rigid-body modeling of multi-domain macromolecules using residual dipolar couplings. *J Biomol NMR* 20:223-231.
- Dudev, T., and Lim, C. 2003. Principles governing Mg, Ca, and Zn binding and selectivity in proteins. *Chem Rev* 103:773-787.
- Durkin, J. T., Ahrens, D. C., Pan, Y. C., and Reeves, J. P. 1991. Purification and amino-terminal sequence of the bovine cardiac sodium-calcium exchanger: evidence for the presence of a signal sequence. *Arch Biochem Biophys* 290:369-375.
- Durst, F. G., Ou, H. D., Löhner, F., Dötsch, V., and Straub, W. E. 2008. The Better Tag Remains Unseen. *J Am Chem Soc* 130:14932-14933.
- Dyck, C., Omelchenko, A., Elias, C. L., and Quednau, B. D. 1999. Ionic Regulatory Properties of Brain and Kidney Splice Variants of the NCX1 Na<sup>+</sup>-Ca<sup>2+</sup> Exchanger. *J Gen Physiol* 114:701-711.
- Eder, P., Probst, D., Rosker, C., Poteser, M., Wolinski, H., Kohlwein, S. D., Romanin, C., and Groschner, K. 2007. Phospholipase C-dependent control of cardiac calcium homeostasis involves a TRPC3-NCX1 signaling complex. *Cardiovasc Res* 73:111-119.
- Egger, M., and Niggli, E. 1999. Regulatory function of Na-Ca exchange in the heart: milestones and outlook. *J Membr Biol* 168:107-130.
- Engh, R., and Huber, R. 1991. Accurate bond and angle parameters for x-ray protein-structure refinement. *Acta Crystallogr A* 47:392-400.
- Ericsson, U. B., Hallberg, B. M., DeTitta, G. T., Dekker, N., and Nordlund, P. 2006. Thermofluor-based high-throughput stability optimization of proteins for structural studies. *Anal Biochem* 357:289-298.
- Fahmy, A., and Wagner, G. 2002. TreeDock: A tool for protein docking based on minimizing van der Waals energies. *J Am Chem Soc* 124:1241-1250.
- Fedrizzi, L., Lim, D., and Carafoli, E. 2008. Calcium and signal transduction. *Biochem Mol Biol Edu* 36:175-180.
- Felli, I. C., and Brutscher, B. 2009. Recent Advances in Solution NMR: Fast Methods and Heteronuclear Direct Detection. *Chemphyschem* 10:1356-1368.
- Fernandes, M. X., Bernadó, P., Pons, M., and de la Torre, J. G. 2001. An analytical solution to the problem of the orientation of rigid particles by planar obstacles. Application to membrane systems and to the calculation of dipolar couplings in protein NMR spectroscopy. *J Am Chem Soc* 123:12037-12047.
- Fernández, C., and Wider, G. 2003. TROSY in NMR studies of the structure and function of large biological macromolecules. *Curr Opin Struct Biol* 13:570-580.
- Flinders, J., and Dieckmann, T. 2006. NMR spectroscopy of ribonucleic acids. *Prog Nucl Mag Res Sp* 48:137-159.
- Freire, E., Schön, A., and Velazquez-Campoy, A. 2009. Isothermal titration calorimetry: general formalism using binding polynomials. *Method Enzymol* 455:127-155.
- Fujioka, Y., Komeda, M., and Matsuoka, S. 2000. Stoichiometry of Na<sup>+</sup>-Ca<sup>2+</sup> exchange in inside-out patches excised from guinea-pig ventricular myocytes. *J Physiol (Lond)* 523 Pt 2:339-351.
- Gardner, K. H., and Kay, L. E. 1997. Production and incorporation of N-15, C-13, H-2 (H-1-delta 1 methyl) isoleucine into proteins for multidimensional NMR studies. *J Am Chem Soc* 119:7599-7600.
- Gardner, K. H., and Kay, L. E. 1998. The use of 2H, 13C, 15N multidimensional NMR to study the structure and dynamics of proteins. *Annu Rev Biophys Biomol Struct* 27:357-406.
- Gelis, I., Bonvin, A. M. J. J., Keramisanou, D., Koukaki, M., Gouridis, G., Karamanou, S., Economou, A., and Kalodimos, C. G. 2007. Structural basis for signal-sequence recognition by the translocase motor SecA as determined by NMR. *Cell* 131:756-769.
- Gifford, J. L., Walsh, M. P., and Vogel, H. J. 2007. Structures and metal-ion-binding properties of the Ca<sup>2+</sup>-

- binding helix-loop-helix EF-hand motifs. *Biochem J* 405:199-221.
- Giladi, M., Boyman, L., Mikhasenko, H., Hiller, R., and Khananshvil, D. 2010. Essential role of the CBD1-CBD2 linker in slow dissociation of Ca<sup>2+</sup> from the regulatory two-domain tandem of NCX1. *J Biol Chem* 285:28117-28125.
- Ginzinger, S. W., Skočibušić, M., and Heun, V. 2009. CheckShift improved: fast chemical shift reference correction with high accuracy. *J Biomol NMR* 44:207-211.
- Goel, M., Zuo, C.-D., Sinkins, W. G., and Schilling, W. P. 2007. TRPC3 channels colocalize with Na<sup>+</sup>/Ca<sup>2+</sup> exchanger and Na<sup>+</sup> pump in axial component of transverse-axial tubular system of rat ventricle. *Am J Physiol-Heart C* 292:H874-H883.
- Golovanov, A. P., Hautbergue, G. M., Wilson, S. A., and Lian, L.-Y. 2004. A simple method for improving protein solubility and long-term stability. *J Am Chem Soc* 126:8933-8939.
- Goto, N. K., Gardner, K. H., Mueller, G. A., Willis, R. C., and Kay, L. E. 1999. A robust and cost-effective method for the production of Val, Leu, Ile (delta 1) methyl-protonated 15N-, 13C-, 2H-labeled proteins. *J Biomol NMR* 13:369-374.
- Graslund, S., Nordlund, P., Weigelt, J., Bray, J., Hallberg, B. M., Gileadi, O., Knapp, S., Oppermann, U., Arrowsmith, C., Hui, R., Ming, J., dhe-Paganon, S., Park, H.-w., Savchenko, A., Yee, A., Edwards, A., Vincentelli, R., Cambillau, C., Kim, R., Kim, S.-H., Rao, Z., Shi, Y., Terwilliger, T. C., Kim, C.-Y., Hung, L.-W., Waldo, G. S., Peleg, Y., Albeck, S., Unger, T., Dym, O., Prilusky, J., Sussman, J. L., Stevens, R. C., Lesley, S. A., Wilson, I. A., Joachimiak, A., Collart, F., Dementieva, I., Donnelly, M. I., Eschenfeldt, W. H., Kim, Y., Stols, L., Wu, R., Zhou, M., Burley, S. K., Emtage, J. S., Sauder, J. M., Thompson, D., Bain, K., Luz, J., Gheyi, T., Zhang, F., Atwell, S., Almo, S. C., Bonanno, J. B., Fiser, A., Swaminathan, S., Studier, F. W., Chance, M. R., Sali, A., Acton, T. B., Xiao, R., Zhao, L., Ma, L. C., Hunt, J. F., Tong, L., Cunningham, K., Inouye, M., Anderson, S., Janjua, H., Shastry, R., Ho, C. K., Wang, D., Wang, H., Jiang, M., Montelione, G. T., Stuart, D. I., Owens, R. J., Daenke, S., Schutz, A., Heinemann, U., Yokoyama, S., Bussow, K., and Gunsalus, K. C. 2008. Protein production and purification. *Nat Methods* 5:135-146.
- Greenfield, N. J. 2006. Using circular dichroism collected as a function of temperature to determine the thermodynamics of protein unfolding and binding interactions. *Nat Protoc* 1:2527-2535.
- Grishaev, A., Wu, J., Trewheella, J., and Bax, A. 2005. Refinement of multidomain protein structures by combination of solution small-angle X-ray scattering and NMR data. *J Am Chem Soc* 127:16621-16628.
- Grishaev, A., Tugarinov, V., Kay, L. E., Trewheella, J., and Bax, A. 2008. Refined solution structure of the 82-kDa enzyme malate synthase G from joint NMR and synchrotron SAXS restraints. *J Biomol NMR* 40:95-106.
- Grzesiek, S., and Bax, A. 1993. Amino-acid type determination in the sequential assignment procedure of uniformly c-13/n-15-enriched proteins. *J Biomol NMR* 3:185-204.
- Guerini, D., Coletto, L., and Carafoli, E. 2005. Exporting calcium from cells. *Cell Calcium* 38:281-289.
- Güntert, P., Mumenthaler, C., and Wüthrich, K. 1997. Torsion angle dynamics for NMR structure calculation with the new program DYANA. *J Mol Biol* 273:283-298.
- Güntert, P. 2009. Automated structure determination from NMR spectra. *Eur Biophys J Biophys* 38:129-143.
- Harris, R. K., Becker, E. D., de Menezes, S. M. C., Goodfellow, R., and Granger, P. 2002. NMR nomenclature: Nuclear spin properties and conventions for chemical shifts - IUPAC recommendations 2001 (Reprinted from Pure Appl. Chem, vol 73, pg 1795-1818, 2001). *Solid State Nucl Mag* 22:458-483.
- Häussinger, D., Ahrens, T., Sass, H. J., Pertz, O., Engel, J., and Grzesiek, S. 2002. Calcium-dependent homoassociation of E-cadherin by NMR spectroscopy: Changes in mobility, conformation and mapping of contact regions. *J Mol Biol* 324:823-839.
- He, Z. P., Feng, S. Y., Tong, Q. S., Hilgemann, D. W., and Philipson, K. D. 2000. Interaction of PIP2 with the XIP region of the cardiac Na/Ca exchanger. *Am J Physiol-Cell Ph* 278:C661-C666.
- Henzler-Wildman, K. A., Lei, M., Thai, V., Kerns, S. J., Karplus, M., and Kern, D. 2007. A hierarchy of timescales in protein dynamics is linked to enzyme catalysis. *Nature* 450:913-916.
- Herchuelz, A. 2007. Historical note regarding the discovery of the Na/Ca exchanger and the PMCA. *Ann N Y Acad Sci* 1099:xvii-xviii.
- Hilge, M., Aelen, J., and Vuister, G. W. 2006. Ca<sup>2+</sup> regulation in the Na<sup>+</sup>/Ca<sup>2+</sup> exchanger involves two mark-

- edly different Ca<sup>2+</sup> sensors. *Mol Cell* 22:15-25.
- Hilge, M., Aelen, J., Foarce, A., Perrakis, A., and Vuister, G. W. 2009. Ca<sup>2+</sup> regulation in the Na<sup>+</sup>/Ca<sup>2+</sup> exchanger features a dual electrostatic switch mechanism. *P Natl Acad Sci Usa* 106:14333-14338.
- Hilgemann, D. W. 1989. Giant excised cardiac sarcolemmal membrane patches: sodium and sodium-calcium exchange currents. *Pflugers Arch* 415:247-249.
- Hilgemann, D. W. 1990. Regulation and deregulation of cardiac Na<sup>(+)</sup>-Ca<sup>2+</sup> exchange in giant excised sarcolemmal membrane patches. *Nature* 344:242-245.
- Hilgemann, D. W., Collins, A., and Matsuoka, S. 1992a. Steady-state and dynamic properties of cardiac sodium-calcium exchange - secondary modulation by cytoplasmic calcium and atp. *J Gen Physiol* 100:933-961.
- Hilgemann, D. W., Matsuoka, S., Nagel, G. A., and Collins, A. 1992b. Steady-state and dynamic properties of cardiac sodium-calcium exchange - sodium-dependent inactivation. *J Gen Physiol* 100:905-932.
- Hilgemann, D. W., and Ball, R. 1996. Regulation of cardiac Na<sup>+</sup>,Ca<sup>2+</sup> exchange and K-ATP potassium channels by PIP2. *Science* 273:956-959.
- Hoch, J. C., and Stern, A. S. 2001. Maximum entropy reconstruction, spectrum analysis and deconvolution in multidimensional nuclear magnetic resonance. *Method Enzymol* 338:159-178.
- Hoof, R., Vriend, G., Sander, C., and Abola, E. 1996. Errors in protein structures. *Nature* 381:272-272.
- Huang, Y. J., Powers, R., and Montelione, G. T. 2005. Protein NMR recall, precision, and F-measure scores (RPF scores): Structure quality assessment measures based on information retrieval statistics. *J Am Chem Soc* 127:1665-1674.
- Hurtado, C., Prociuk, M., Maddaford, T. G., Dibrov, E., Mesaeli, N., Hryshko, L. V., and Pierce, G. N. 2006. Cells expressing unique Na<sup>+</sup>/Ca<sup>2+</sup> exchange (NCX1) splice variants exhibit different susceptibilities to Ca<sup>2+</sup> overload. *Am J Physiol Heart Circ Physiol* 290:H2155-2162.
- Huth, J. R., Bewley, C. A., Jackson, B. M., Hinnebusch, A. G., Clore, G. M., and Gronenborn, A. M. 1997. Design of an expression system for detecting folded protein domains and mapping macromolecular interactions by NMR. *Protein Sci* 6:2359-2364.
- Ikura, M., Kay, L. E., and Bax, A. 1990. A novel approach for sequential assignment of <sup>1</sup>H, <sup>13</sup>C, and <sup>15</sup>N spectra of proteins: heteronuclear triple-resonance three-dimensional NMR spectroscopy. Application to calmodulin. *Biochemistry* 29:4659-4667.
- Isaacson, R. L., Simpson, P. J., Liu, M., Cota, E., Zhang, X., Freemont, P., and Matthews, S. 2007. A new labeling method for methyl transverse relaxation-optimized spectroscopy NMR spectra of alanine residues. *J Am Chem Soc* 129:15428-15429.
- Ishima, R., and Torchia, D. A. 2000. Protein dynamics from NMR. *Nat Struct Biol* 7:740-743.
- Ito, T., and Wagner, G. 2004. Using codon optimization, chaperone co-expression, and rational mutagenesis for production and NMR assignments of human eIF2 alpha. *J Biomol NMR* 28:357-367.
- Iwamoto, T., Nakamura, T. Y., Pan, Y., Uehara, A., Imanaga, I., and Shigekawa, M. 1999. Unique topology of the internal repeats in the cardiac Na<sup>+</sup>/Ca<sup>2+</sup> exchanger. *FEBS Lett* 446:264-268.
- Iwamoto, T., Uehara, A., Imanaga, I., and Shigekawa, M. 2000. The Na<sup>+</sup>/Ca<sup>2+</sup> exchanger NCX1 has oppositely oriented reentrant loop domains that contain conserved aspartic acids whose mutation alters its apparent Ca<sup>2+</sup> affinity. *J Biol Chem* 275:38571-38580.
- Jeener, J. 1971. Ampère Summer School, Basko Polje, Yugoslavia.
- Jensen, M. R., Hass, M. A. S., Hansen, D. F., and Led, J. J. 2007. Investigating metal-binding in proteins by nuclear magnetic resonance. *Cell Mol Life Sci* 64:1085-1104.
- Joachimiak, A. 2009. High-throughput crystallography for structural genomics. *Curr Opin Struct Biol* 19:573-584.
- John, S. A., Ribalet, B., Weiss, J. N., Philipson, K. D., and Ottolia, M. 2011. Ca<sup>2+</sup>-dependent structural rearrangements within Na<sup>+</sup>-Ca<sup>2+</sup> exchanger dimers. *P Natl Acad Sci Usa* 108:1699-1704.
- Johnson, E., Bruschiweiler-Li, L., Showalter, S. A., Vuister, G. W., Zhang, F., and Bruschiweiler, R. 2008. Structure and dynamics of Ca<sup>2+</sup>-binding domain 1 of the Na<sup>+</sup>/Ca<sup>2+</sup> exchanger in the presence and in the absence of Ca<sup>2+</sup>. *J Mol Biol* 377:945-955.
- Jung, Y.-S., and Zweckstetter, M. 2004. Mars - robust automatic backbone assignment of proteins. *J Biomol NMR* 30:11-23.



- Kainosho, M., Torizawa, T., Iwashita, Y., Terauchi, T., Mei Ono, A., and Güntert, P. 2006. Optimal isotope labelling for NMR protein structure determinations. *Nature* 440:52-57.
- Kang, T. M., and Hilgemann, D. W. 2004. Multiple transport modes of the cardiac Na<sup>+</sup>/Ca<sup>2+</sup> exchanger. *Nature* 427:544-548.
- Karplus, M. 1959. Contact electron-spin coupling of nuclear magnetic moments. *J Chem Phys* 30:11-15.
- Karplus, M. 1963. Vicinal proton coupling in nuclear magnetic resonance. *J Am Chem Soc* 85:2870-2871.
- Katanosaka, Y., Iwata, Y., Kobayashi, Y., Shibasaki, F., Wakabayashi, S., and Shigekawa, M. 2005. Calcineurin inhibits Na<sup>+</sup>/Ca<sup>2+</sup> exchange in phenylephrine-treated hypertrophic cardiomyocytes. *J Biol Chem* 280:5764-5772.
- Kay, L. E., Torchia, D. A., and Bax, A. 1989. Backbone dynamics of proteins as studied by <sup>15</sup>N inverse detected heteronuclear NMR spectroscopy: application to staphylococcal nuclease. *Biochemistry* 28:8972-8979.
- Kay, L. E., Clore, G. M., Bax, A., and Gronenborn, A. M. 1990a. Four-dimensional heteronuclear triple-resonance NMR spectroscopy of interleukin-1 beta in solution. *Science* 249:411-414.
- Kay, L. E., Ikura, M., Tschudin, R., and Bax, A. 1990b. Three-Dimensional triple-resonance nmr-spectroscopy of isotopically enriched proteins. *J Magn Reson* 89:496-514.
- Kay, L. E. 1998. Protein dynamics from NMR. *Nat Struct Biol* 5:513-517.
- Kazimierzczuk, K., Koźmiński, W., and Zhukov, I. 2006. Two-dimensional Fourier transform of arbitrarily sampled NMR data sets. *J Magn Reson* 179:323-328.
- Kelly, A. E., Ou, H. D., Withers, R., and Dötsch, V. 2002. Low-conductivity buffers for high-sensitivity NMR measurements. *J Am Chem Soc* 124:12013-12019.
- Kim, H. J., Howell, S. C., Van Horn, W. D., Jeon, Y. H., and Sanders, C. R. 2009. Recent advances in the application of solution NMR spectroscopy to multi-span integral membrane proteins. *Prog Nucl Mag Res Sp* 55:335-360.
- Kimura, J., Noma, A., and Irisawa, H. 1986. Na-Ca exchange current in mammalian heart cells. *Nature* 319:596-597.
- Kiyoshi, T., Otsuka, A., Kosuge, M., Yuyama, M., Nagai, H., and Matsumoto, F. 2006. Generation of high magnetic fields using superconducting magnets. *Fusion Eng Des* 81:2411-2415.
- Kobashigawa, Y., Kumeta, H., Ogura, K., and Inagaki, F. 2009. Attachment of an NMR-invisible solubility enhancement tag using a sortase-mediated protein ligation method. *J Biomol NMR* 43:145-150.
- Kochendoerfer, G. G., Jones, D. H., Lee, S., Oblatt-Montal, M., Opella, S. J., and Montal, M. 2004. Functional characterization and NMR Spectroscopy on full-length Vpu from HIV-1 prepared by total chemical synthesis. *J Am Chem Soc* 126:2439-2446.
- Kofuji, P., Lederer, W. J., and Schulze, D. H. 1994. Mutually exclusive and cassette exons underlie alternatively spliced isoforms of the Na/Ca exchanger. *J Biol Chem* 269:5145-5149.
- Konagurthu, A. S., Whisstock, J. C., Stuckey, P. J., and Lesk, A. M. 2006. MUSTANG: a multiple structural alignment algorithm. *Proteins* 64:559-574.
- Konrat, R., Yang, D., and Kay, L. 1999. A 4D TROSY-based pulse scheme for correlating (<sup>1</sup>H)-<sup>1</sup>H-<sup>15</sup>N, <sup>15</sup>C-<sup>13</sup>(i)α, <sup>13</sup>C-<sup>13</sup>(i-1) chemical shifts in high molecular weight, N-<sup>15</sup>C-<sup>13</sup>, H-<sup>2</sup> labeled proteins. *J Biomol NMR* 15:309-313.
- Koradi, R., Billeter, M., and Wüthrich, K. 1996. MOLMOL: A program for display and analysis of macromolecular structures. *J Mol Graphics* 14:51-8.
- Korzhev, D. M., Religa, T. L., Banachewicz, W., Fersht, A. R., and Kay, L. E. 2010. A transient and low-populated protein-folding intermediate at atomic resolution. *Science* 329:1312-1316.
- Laskowski, R., Rullmann, J., and MacArthur, M. 1996. AQUA and PROCHECK-NMR: Programs for checking the quality of protein structures solved by NMR. *J Biomol NMR* 8:477-486.
- Laude, A. J., and Simpson, A. W. M. 2009. Compartmentalized signalling: Ca<sup>2+</sup> compartments, microdomains and the many facets of Ca<sup>2+</sup> signalling. *Febs J* 276:1800-1816.
- Lee, A. L., Urbauer, J. L., and Wand, A. J. 1997. Improved labeling strategy for <sup>13</sup>C relaxation measurements of methyl groups in proteins. *J Biomol NMR* 9:437-440.
- Lee, S. L., Yu, A. S. L., and Lytton, J. 1994. Tissue-specific expression of Na<sup>+</sup>-Ca<sup>2+</sup> exchanger isoforms. *J Biol Chem* 269:14849-14852.

- LeMaster, D. M., and Richards, F. M. 1988. NMR sequential assignment of *Escherichia coli* thioredoxin utilizing random fractional deuteration. *Biochemistry* 27:142-150.
- Lencesova, L., O'Neill, A., Resneck, W. G., Bloch, R. J., and Blaustein, M. P. 2004. Plasma membrane-cytoskeleton-endoplasmic reticulum complexes in neurons and astrocytes. *J Biol Chem* 279:2885-2893.
- Lepre, C. A., and Moore, J. M. 1998. Microdrop screening: a rapid method to optimize solvent conditions for NMR spectroscopy of proteins. *J Biomol NMR* 12:493-499.
- Lescop, E., and Brutscher, B. 2009. Highly automated protein backbone resonance assignment within a few hours: the ((BATCH)) strategy and software package. *J Biomol NMR* 44:43-57.
- Leutner, M., Gschwind, R. M., Liermann, J., Schwarz, C., Gemmecker, G., and Kessler, H. 1998. Automated backbone assignment of labeled proteins using the threshold accepting algorithm. *J Biomol NMR* 11:31-43.
- Levitsky, D. O., Nicoll, D. A., and Philipson, K. D. 1994. Identification of the high-affinity Ca<sup>2+</sup>-binding domain of the cardiac Na<sup>+</sup>-Ca<sup>2+</sup> exchanger. *J Biol Chem* 269:22847-22852.
- Levitt, M. H. 2008. Spin dynamics: Basics of Nuclear Magnetic Resonance, 2nd ed, vol. Wiley-Blackwell.
- Li, C., and Ames, J. B. 2008. H-1, N-15, and C-13 chemical shift assignments of calcium-bound calcium-binding protein 1 (CaBP1). *Biomol Nmr Assignm* 2:61-63.
- Li, H., Robertson, A. D., and Jensen, J. H. 2005. Very fast empirical prediction and rationalization of protein pKa values. *Proteins* 61:704-721.
- Li, K.-B., and Sanctuary, B. C. 1997a. Automated resonance assignment of proteins using heteronuclear 3D NMR. 2. Side chain and sequence-specific assignment. *J Chem Inf Comp Sci* 37:467-477.
- Li, K.-B., and Sanctuary, B. C. 1997b. Automated resonance assignment of proteins using heteronuclear 3D NMR. Backbone spin systems extraction and creation of polypeptides. *J Chem Inf Comp Sci* 37:359-366.
- Li, Z., Nicoll, D. A., Collins, A., Hilgemann, D. W., Filoteo, A. G., Penniston, J. T., Weiss, J. N., Tomich, J. M., and Philipson, K. D. 1991. Identification of a peptide inhibitor of the cardiac sarcolemmal Na(+)-Ca<sup>2+</sup> exchanger. *J Biol Chem* 266:1014-1020.
- Li, Z. P., Matsuoka, S., Hryshko, L. V., Nicoll, D. A., Bersohn, M. M., Burke, E. P., Lifton, R. P., and Philipson, K. D. 1994. Cloning of the NCX2 isoform of the plasma-membrane Na<sup>+</sup>-Ca<sup>2+</sup> exchanger. *J Biol Chem* 269:17434-17439.
- Linge, J. P., Williams, M. A., Spronk, C. A. E. M., Bonvin, A. M. J. J., and Nilges, M. 2003. Refinement of protein structures in explicit solvent. *Proteins* 50:496-506.
- Lipari, G., and Szabo, A. 1982a. Model-free approach to the interpretation of nuclear magnetic-resonance relaxation in macromolecules .1. Theory and range of validity. *J Am Chem Soc* 104:4546-4559.
- Lipari, G., and Szabo, A. 1982b. Model-free approach to the interpretation of nuclear magnetic-resonance relaxation in macromolecules .2. Analysis of experimental results. *J Am Chem Soc* 104:4559-4570.
- Lukin, J. A., Gove, A. P., Talukdar, S. N., and Ho, C. 1997. Automated probabilistic method for assigning backbone resonances of (C-13,N-15)-labeled proteins. *J Biomol NMR* 9:151-166.
- Lytton, J. 2007. Na<sup>+</sup>/Ca<sup>2+</sup> exchangers: three mammalian gene families control Ca<sup>2+</sup> transport. *Biochem J* 406:365-382.
- Maack, C., Ganesan, A., Sidor, A., and O'Rourke, B. 2005. Cardiac sodium-calcium exchanger is regulated by allosteric calcium and exchanger inhibitory peptide at distinct sites. *Circ Res* 96:91-99.
- Maler, L., Blankenship, J., Rance, M., and Chazin, W. 2000. Site-site communication in the EF-hand Ca<sup>2+</sup>-binding protein calbindin D-9k. *Nat Struct Biol* 7:245-250.
- Malmendal, A., Linse, S., Evenäs, J., Forsén, S., and Drakenberg, T. 1999. Battle for the EF-hands: magnesium-calcium interference in calmodulin. *Biochemistry* 38:11844-11850.
- Mandel, A. M., Akke, M., and Palmer, A. G. 1995. Backbone dynamics of *escherichia-coli* ribonuclease hi - correlations with structure and function in an active enzyme. *J Mol Biol* 246:144-163.
- Marion, D., Driscoll, P. C., Kay, L. E., Wingfield, P. T., Bax, A., Gronenborn, A. M., and Clore, G. M. 1989. Overcoming the overlap problem in the assignment of 1H NMR spectra of larger proteins by use of three-dimensional heteronuclear 1H-15N Hartmann-Hahn-multiple quantum coherence and nuclear Overhauser-multiple quantum coherence spectroscopy: application to interleukin 1 beta. *Biochemistry* 28:6150-6156.

- Markley, J. L., Ulrich, E. L., Berman, H. M., Henrick, K., Nakamura, H., and Akutsu, H. 2008. BioMagRes-Bank (BMRB) as a partner in the Worldwide Protein Data Bank (wwPDB): new policies affecting biomolecular NMR depositions. *J Biomol NMR* 40:153-155.
- Markwick, P. R. L., Malliavin, T., and Nilges, M. 2008. Structural Biology by NMR: Structure, Dynamics, and Interactions. *Plos Comput Biol* 4:e1000168.
- Marshall, C. R., Pan, T. C., Le, H. D., Omelchenko, A., Hwang, P. P., Hryshko, L. V., and Tibbits, G. F. 2005. cDNA cloning and expression of the cardiac Na<sup>+</sup>/Ca<sup>2+</sup> exchanger from Mozambique tilapia (*Oreochromis mossambicus*) reveal a teleost membrane transporter with mammalian temperature dependence. *J Biol Chem* 280:28903-28911.
- Matsuoka, S., Nicoll, D. A., He, Z. P., and Philipson, K. D. 1997. Regulation of the cardiac Na<sup>+</sup>-Ca<sup>2+</sup> exchanger by the endogenous XIP region. *J Gen Physiol* 109:273-286.
- McDermott, A. 2009. Structure and Dynamics of Membrane Proteins by Magic Angle Spinning Solid-State NMR. *Ann Rev Biophys* 38:385-403.
- Menick, D. R., Renaud, L., Buchholz, A., Müller, J. G., Zhou, H., Kappler, C. S., Kubalak, S. W., Conway, S. J., and Xu, L. 2007. Regulation of Ncx1 gene expression in the normal and hypertrophic heart. *Ann NY Acad Sci* 1099:195-203.
- Millet, O., Muhandiram, D. R., Skrynnikov, N. R., and Kay, L. E. 2002. Deuterium spin probes of side-chain dynamics in proteins. 1. Measurement of five relaxation rates per deuteron in C-13-labeled and fractionally H-2-enriched proteins in solution. *J Am Chem Soc* 124:6439-6448.
- Mittermaier, A., and Kay, L. E. 2006. Review - New tools provide new insights in NMR studies of protein dynamics. *Science* 312:224-228.
- Modig, K., Jürgensen, V. W., Lindorff-Larsen, K., Fieber, W., Bohr, H. G., and Poulsen, F. M. 2007. Detection of initiation sites in protein folding of the four helix bundle ACBP by chemical shift analysis. *FEBS Lett* 581:4965-4971.
- Mohler, P., Davis, J., and Bennett, V. 2005. Ankyrin-B coordinates the Na/K ATPase, Na/Ca exchanger, and InsP(3) receptor in a cardiac T-tubule/SR microdomain. *Plos Biol* 3:2158-2167.
- Moore, E. D., Etter, E. F., Philipson, K. D., Carrington, W. A., Fogarty, K. E., Lifshitz, L. M., and Fay, F. S. 1993. Coupling of the Na<sup>+</sup>/Ca<sup>2+</sup> exchanger, Na<sup>+</sup>/K<sup>+</sup> pump and sarcoplasmic reticulum in smooth muscle. *Nature* 365:657-660.
- Mulder, F. A. A., and Filatov, M. 2010. NMR chemical shift data and ab initio shielding calculations: emerging tools for protein structure determination. *Chem Soc Rev* 39:578-590.
- Muona, M., Aranko, A. S., Raulinaitis, V., and Iwai, H. 2010. Segmental isotopic labeling of multi-domain and fusion proteins by protein trans-splicing in vivo and in vitro. *Nat Protoc* 5:574-587.
- Murphy, E., Cross, H., and Steenbergen, C. 1999. Sodium regulation during ischemia versus reperfusion and its role in injury. *Circ Res* 84:1469-1470.
- Murray, D., and Honig, B. 2002. Electrostatic control of the membrane targeting of C2 domains. *Mol Cell* 9:145-154.
- Murzin, A. G., Brenner, S. E., Hubbard, T., and Chothia, C. 1995. SCOP: a structural classification of proteins database for the investigation of sequences and structures. *J Mol Biol* 247:536-540.
- Nabuurs, S. B., Spronk, C. A. E. M., Krieger, E., Maassen, H., Vriend, G., and Vuister, G. W. 2003. Quantitative evaluation of experimental NMR restraints. *J Am Chem Soc* 125:12026-12034.
- Nabuurs, S. B., Nederveen, A. J., Vranken, W., Doreleijers, J. F., Bonvin, A. M. J. J., Vuister, G. W., Vriend, G., and Spronk, C. A. E. M. 2004. DRESS: a database of Refined solution NMR structures. *Proteins* 55:483-486.
- Nabuurs, S. B., Krieger, E., Spronk, C. A. E. M., Nederveen, A. J., Vriend, G., and Vuister, G. W. 2005. Definition of a new information-based per-residue quality parameter. *J Biomol NMR* 33:123-134.
- Nabuurs, S. B., Spronk, C. A. E. M., Vuister, G. W., and Vriend, G. 2006. Traditional biomolecular structure determination by NMR spectroscopy allows for major errors. *PLoS Comput Biol* 2:e9.
- Nabuurs, S. M., Westphal, A. H., and Van Mierlo, C. P. M. 2008. Extensive Formation of Off-Pathway Species during Folding of an  $\alpha$ - $\beta$  Parallel Protein Is Due to Docking of (Non)native Structure Elements in Unfolded Molecules. *J Am Chem Soc* 130:16914-16920.
- Nabuurs, S. M., Westphal, A. H., and Van Mierlo, C. P. M. 2009. Noncooperative Formation of the Off-

- Pathway Molten Globule during Folding of the  $\alpha$ - $\beta$  Parallel Protein Apoflavodoxin. *J Am Chem Soc* 131:2739-2746.
- Nabuurs, S. M., de Kort, B. J., Westphal, A. H., and Van Mierlo, C. P. M. 2010. Non-native hydrophobic interactions detected in unfolded apoflavodoxin by paramagnetic relaxation enhancement. *Eur Biophys J Biophys* 39:689-698.
- Nabuurs, S. M., and Van Mierlo, C. P. M. 2010. Interrupted Hydrogen/Deuterium Exchange Reveals the Stable Core of the Remarkably Helical Molten Globule of alpha-beta Parallel Protein Flavodoxin. *J Biol Chem* 285:4165-4172.
- Neal, S., Nip, A. M., Zhang, H.-Y., and Wishart, D. S. 2003. Rapid and accurate calculation of protein H-1, C-13 and N-15 chemical shifts. *J Biomol Nmr* 26:215-240.
- Nicoll, D. A., Longoni, S., and Philipson, K. D. 1990. Molecular-cloning and functional expression of the cardiac sarcolemmal Na<sup>+</sup>-Ca<sup>2+</sup> exchanger. *Science* 250:562-565.
- Nicoll, D. A., Hryshko, L. V., Matsuoka, S., Frank, J. S., and Philipson, K. D. 1996a. Mutation of amino acid residues in the putative transmembrane segments of the cardiac sarcolemmal Na<sup>+</sup>-Ca<sup>2+</sup> exchanger. *J Biol Chem* 271:13385-13391.
- Nicoll, D. A., Quednau, B. D., Qui, Z. Y., Xia, Y. R., Lusic, A. J., and Philipson, K. D. 1996b. Cloning of a third mammalian Na<sup>+</sup>-Ca<sup>2+</sup> exchanger, NCX3. *J Biol Chem* 271:24914-24921.
- Nicoll, D. A., Ottolia, M., Lu, L. Y., Lu, Y. J., and Philipson, K. D. 1999a. A new topological model of the cardiac sarcolemmal Na<sup>+</sup>-Ca<sup>2+</sup> exchanger. *J Biol Chem* 274:910-917.
- Nicoll, D. A., Ottolia, M., Lu, L. Y., Lu, Y. J., and Philipson, K. D. 1999b. A new topological model of the cardiac sarcolemmal Na<sup>+</sup>-Ca<sup>2+</sup> exchanger, p. 910-917. *J Biol Chem*, vol. 274.
- Nicoll, D. A., Sawaya, M. R., Kwon, S., Cascio, D., Philipson, K. D., and Abramson, J. 2006. The crystal structure of the primary Ca<sup>2+</sup> sensor of the Na<sup>+</sup>/Ca<sup>2+</sup> exchanger reveals a novel Ca<sup>2+</sup> binding motif. *J Biol Chem* 281:21577-21581.
- Nielbo, S., Thomsen, J. K., and Graversen, J. H. 2004. Structure of the plasminogen kringle 4 binding calcium-free form of the C-type lectin-like domain of tetranectin. *Biochemistry*.
- Nietispach, D., Clowes, R. T., Broadhurst, R. W., Ito, Y., Keeler, J., Kelly, M., Ashurst, J., Oschkinat, H., Domaille, P. J., and Laue, E. D. 1996. An approach to the structure determination of larger proteins using triple resonance NMR experiments in conjunction with random fractional deuteration. *J Am Chem Soc* 118:407-415.
- Nilges, M., Clore, G., and Gronenborn, A. 1988. Determination of three-dimensional structures of proteins from interproton distance data by hybrid distance geometry-dynamical simulated annealing calculations. *FEBS Lett* 229:317-324.
- Nilges, M., Macias, M. J., O'Donoghue, S. I., and Oschkinat, H. 1997. Automated NOESY interpretation with ambiguous distance restraints: the refined NMR solution structure of the pleckstrin homology domain from beta-spectrin. *J Mol Biol* 269:408-422.
- Nishimura, C. 2005. Enhanced picture of protein-folding intermediates using organic solvents in H/D exchange and quench-flow experiments. *P Natl Acad Sci Usa* 102:4765-4770.
- O'Connell, M. R., Gamsjaeger, R., and Mackay, J. P. 2009. The structural analysis of protein-protein interactions by NMR spectroscopy. *Proteomics* 9:5224-5232.
- Olejniczak, E. T., Xu, R. X., and Fesik, S. W. 1992. A 4D-HCCH-TOCSY experiment for assigning the side-chain h-1-resonance and c-13-resonance of proteins. *J Biomol NMR* 2:655-659.
- Ollerenshaw, J., Tugarinov, V., and Kay, L. 2003. Methyl TROSY: explanation and experimental verification. *Magn Reson Chem* 41:843-852.
- On, C., Marshall, C. R., Chen, N., Moyes, C. D., and Tibbits, G. F. 2008. Gene structure evolution of the Na<sup>+</sup>-Ca<sup>2+</sup> exchanger (NCX) family. *Bmc Evol Biol* 8:127.
- Ortega, A., and de la Torre, J. 2005. Efficient, accurate calculation of rotational diffusion and NMR relaxation of globular proteins from atomic-level structures and approximate hydrodynamic calculations. *J Am Chem Soc* 127:12764-12765.
- Otten, R., Chu, B., Krewulak, K. D., Vogel, H. J., and Mulder, F. A. A. 2010. Comprehensive and Cost-Effective NMR Spectroscopy of Methyl Groups in Large Proteins. *J Am Chem Soc* 132:2952-2960.
- Ottolia, M., Nicoll, D. A., and Philipson, K. D. 2005. Mutational analysis of the alpha-1 repeat of the cardiac

- Na(+)-Ca<sup>2+</sup> exchanger. *J Biol Chem* 280:1061-1069.
- Ottolia, M., Nicoll, D. A., and Philipson, K. D. 2009. Roles of Two Ca<sup>2+</sup>-binding Domains in Regulation of the Cardiac Na<sup>+</sup>-Ca<sup>2+</sup> Exchanger. *J Biol Chem* 284:32735-32741.
- Ottolia, M., Nicoll, D. A., John, S., and Philipson, K. D. 2010. Interactions between Ca<sup>2+</sup> binding domains of the Na<sup>+</sup>-Ca<sup>2+</sup> exchanger and secondary regulation. *Channels* 4:159-162.
- Pace, C. N., and Laurents, D. V. 1989. A new method for determining the heat capacity change for protein folding. *Biochemistry* 28:2520-2525.
- Pace, C. N. 1990. Measuring and increasing protein stability. *Trends Biotechnol* 8:93-98.
- Palmer, A. G., Rance, M., and Wright, P. E. 1991. Intramolecular motions of a zinc finger dna-binding domain from xfin characterized by proton-detected natural abundance c-12 heteronuclear nmr-spectroscopy. *J Am Chem Soc* 113:4371-4380.
- Palmer, A. G. 1997. Probing molecular motion by NMR. *Curr Opin Struct Biol* 7:732-737.
- Palmer, A. G., Kroenke, C. D., and Loria, J. P. 2001. Nuclear magnetic resonance methods for quantifying microsecond-to-millisecond motions in biological macromolecules. *Meth Enzymol* 339:204-238.
- Palmer, A. G. 2004. NMR characterization of the dynamics of biomacromolecules. *Chem Rev* 104:3623-3640.
- Parekh, A. B., and Putney, J. W. 2005. Store-operated calcium channels. *Physiol Rev* 85:757-810.
- Park, S., and Saven, J. G. 2006. Simulation of pH-dependent edge strand rearrangement in human beta-2 microglobulin. *Protein Sci* 15:200-207.
- Pervushin, K., Riek, R., Wider, G., and Wüthrich, K. 1997. Attenuated T-2 relaxation by mutual cancellation of dipole-dipole coupling and chemical shift anisotropy indicates an avenue to NMR structures of very large biological macromolecules in solution. *P Natl Acad Sci Usa* 94:12366-12371.
- Pervushin, K., Riek, R., Wider, G., and Wüthrich, K. 1998. Transverse relaxation-optimized spectroscopy (TROSY) for NMR studies of aromatic spin systems in C-13-labeled proteins. *J Am Chem Soc* 120:6394-6400.
- Pervushin, K., Vogeli, B., and Eletsky, A. 2002. Longitudinal H-1 relaxation optimization in TROSY NMR spectroscopy. *J Am Chem Soc* 124:12898-12902.
- Prestegard, J. H., Bougault, C. M., and Kishore, A. I. 2004. Residual dipolar couplings in structure determination of biomolecules. *Chem Rev* 104:3519-3540.
- Privalov, P. L., and Khechinashvili, N. N. 1974. A thermodynamic approach to the problem of stabilization of globular protein structure: a calorimetric study. *J Mol Biol* 86:665-684.
- Puglisi, J. D., and Tinoco, I. 1989. Absorbance melting curves of RNA. *Meth Enzymol* 180:304-325.
- Pulina, M. V., Rizzuto, R., Brini, M., and Carafoli, E. 2006. Inhibitory interaction of the plasma membrane Na<sup>+</sup>/Ca<sup>2+</sup> exchangers with the 14-3-3 proteins. *J Biol Chem* 281:19645-19654.
- Quednau, B. D., Nicoll, D. A., and Philipson, K. D. 1996. Tissue-specific expression of the Na/Ca exchanger isoforms NCX1, NCX2, and NCX3. *Biophys J* 70:MP282-MP282.
- Quednau, B. D., Nicoll, D. A., and Philipson, K. D. 1997. Tissue specificity and alternative splicing of the Na<sup>+</sup>/Ca<sup>2+</sup> exchanger isoforms NCX1, NCX2, and NCX3 in rat. *Am J Physiol* 272:C1250-1261.
- Quednau, B. D., Nicoll, D. A., and Philipson, K. D. 2004. The sodium/calcium exchanger family-SLC8. *Pflugers Arch Eur J Phy* 447:543-548.
- Reeves, J. P., and Sutko, J. L. 1980. Sodium-calcium exchange activity generates a current in cardiac membrane vesicles. *Science* 208:1461-1464.
- Reeves, J. P., and Sutko, J. L. 1983. Competitive interactions of sodium and calcium with the sodium-calcium exchange system of cardiac sarcolemmal vesicles. *J Biol Chem* 258:3178-3182.
- Reeves, J. P., and Hale, C. C. 1984. The stoichiometry of the cardiac sodium-calcium exchange system. *J Biol Chem* 259:7733-7739.
- Reeves, J. P., and Condrescu, M. 2008. Ionic regulation of the cardiac sodium-calcium exchanger. *Channels* 2:322-328.
- Reuter, H., and Seitz, N. 1968. The dependence of calcium efflux from cardiac muscle on temperature and external ion composition. *J Physiol (Lond)* 195:451-470.
- Rieping, W., Habeck, M., Bardiaux, B., Bernard, A., Malliavin, T. E., and Nilges, M. 2007. ARIA2: automated NOE assignment and data integration in NMR structure calculation. *Bioinformatics* 23:381-382.
- Rieping, W., and Vranken, W. F. 2010. Validation of archived chemical shifts through atomic coordinates.

- Proteins* 78:2482-2489.
- Ringer, S. 1882. Concerning the Influence exerted by each of the Constituents of the Blood on the Contraction of the Ventricle. *The Journal of Physiology* 3:380.
- Ringer, S. 1883. A further Contribution regarding the influence of the different Constituents of the Blood on the Contraction of the Heart. *The Journal of Physiology* 4:29.
- Rosen, M. K., Gardner, K. H., Willis, R. C., Parris, W. E., Pawson, T., and Kay, L. E. 1996. Selective methyl group protonation of perdeuterated proteins. *J Mol Biol* 263:627-636.
- Salinas, R. K., Bruschweiler-Li, L., Johnson, E., and Bruschweiler, R. 2011. Ca<sup>2+</sup>-binding alters the inter-domain flexibility between the two cytoplasmic calcium-binding domains in the Na<sup>+</sup>/Ca<sup>2+</sup> exchanger. *J Biol Chem.* 286: 32123-32131
- Salzmann, M., Pervushin, K., Wider, G., Senn, H., and Wüthrich, K. 1998. TROSY in triple-resonance experiments: New perspectives for sequential NMR assignment of large proteins. *P Natl Acad Sci Usa* 95:13585-13590.
- Salzmann, M., Wider, G., Pervushin, K., Senn, H., and Wüthrich, K. 1999. TROSY-type triple-resonance experiments for sequential NMR assignments of large proteins. *J Am Chem Soc* 121:844-848.
- Sanner, M. F. 1999. Python: a programming language for software integration and development. *J Mol Graph Model* 17:57-61.
- Saris, N. E. L., Mervaala, E., Karppanen, H., Khawaja, J. A., and Lewenstam, A. 2000. Magnesium - An update on physiological, clinical and analytical aspects. *Clin Chim Acta* 294:1-26.
- Sattler, M., Schleucher, J., and Griesinger, C. 1999. Heteronuclear multidimensional NMR experiments for the structure determination of proteins in solution employing pulsed field gradients, p. 93-158. *Prog Nucl Mag Res Sp*, vol. 34.
- Schanda, P., Kupce, E., and Brutscher, B. 2005. SOFAST-HMQC experiments for recording two-dimensional heteronuclear correlation spectra of proteins within a few seconds. *J Biomol NMR* 33:199-211.
- Schmidt, P. G., and Kuntz, I. D. 1984. Distance measurements in spin-labeled lysozyme. *Biochemistry* 23:4261-4266.
- SchneiderMuntau, H. 1997. High field NMR magnets. *Solid State Nucl Mag* 9:61-71.
- Schrödinger, LLC. 2010. The PyMOL Molecular Graphics System, Version 0.99rc6.
- Schulman, B. A., Kim, P. S., Dobson, C. M., and Redfield, C. 1997. A residue-specific NMR view of the non-cooperative unfolding of a molten globule. *Nat Struct Biol* 4:630-634.
- Schwarz, E. M., and Benzer, S. 1997. Calx, a Na-Ca exchanger gene of *Drosophila melanogaster*. *P Natl Acad Sci Usa* 94:10249-10254.
- Schwieters, C., Kuszewski, J., Tjandra, N., and Clore, G. 2003. The Xplor-NIH NMR molecular structure determination package. *J Magn Reson* 160:65-73.
- Schwieters, C., Kuszewski, J., and Clore, G. 2006. Using Xplor-NIH for NMR molecular structure determination. *Prog Nucl Mag Res Sp* 48:47-62.
- Selenko, P., and Wagner, G. 2007. Looking into live cells with in-cell NMR spectroscopy. *J Struct Biol* 158:244-253.
- Shao, X., Sudhof, T., and Rizo, J. 1997. Assignment of the H-1, N-15 and C-13 resonances of the calcium-free and calcium-bound forms of the first C-2-domain of synaptotagmin I. *J Biomol Nmr* 10:307-308.
- Shao, X. G., Fernandez, I., Sudhof, T. C., and Rizo, J. 1998. Solution structures of the Ca<sup>2+</sup>-free and Ca<sup>2+</sup>-bound C(2)A domain of synaptotagmin I: Does Ca<sup>2+</sup> induce a conformational change? *Biochemistry* 37:16106-16115.
- Shekhtman, A., Ghose, R., Goger, M., and Cowburn, D. 2002. NMR structure determination and investigation using a reduced proton (REDPRO) labeling strategy for proteins. *FEBS Lett* 524:177-182.
- Shen, Y., Lange, O., Delaglio, F., Rossi, P., Aramini, J., Liu, G., Eletsky, A., Wu, Y., Singarapu, K. K., Lemak, A., Ignatchenko, A., Arrowsmith, C. H., Szyperski, T., Montelione, G., Baker, D., and Bax, A. 2008. Consistent blind protein structure generation from NMR chemical shift data. *P Natl Acad Sci Usa*.
- Shen, Y., Delaglio, F., Cornilescu, G., and Bax, A. 2009. TALOS+: a hybrid method for predicting protein backbone torsion angles from NMR chemical shifts. *J Biomol NMR* 44:213-223.
- Siggers, K., Soto, C., and Palmer, A. G. 2007. Conformational dynamics in loop swap mutants of homologous fibronectin type III domains. *Biophys J* 93:2447-2456.

- Simon, B., Madl, T., Mackereth, C. D., Nilges, M., and Sattler, M. **2010**. An Efficient Protocol for NMR-Spectroscopy-Based Structure Determination of Protein Complexes in Solution. *Angew Chem Int Edit* 49:1967-1970.
- Skrisovska, L., Schubert, M., and Allain, F. H.-T. **2010**. Recent advances in segmental isotope labeling of proteins: NMR applications to large proteins and glycoproteins. *J Biomol NMR* 46:51-65.
- Skrynnikov, N. R., Millet, O., and Kay, L. E. **2002**. Deuterium spin probes of side-chain dynamics in proteins. 2. Spectral density mapping and identification of nanosecond time-scale side-chain motions. *J Am Chem Soc* 124:6449-6460.
- Slaughter, R. S., Sutko, J. L., and Reeves, J. P. **1983**. Equilibrium calcium-calcium exchange in cardiac sarcolemmal vesicles. *J Biol Chem* 258:3183-3190.
- Smith, D. B., and Johnson, K. S. **1988**. Single-step purification of polypeptides expressed in *Escherichia coli* as fusions with glutathione S-transferase. *Gene* 67:31-40.
- Snyder, D. A., and Montelione, G. T. **2005**. Clustering algorithms for identifying core atom sets and for assessing the precision of protein structure ensembles. *Proteins* 59:673-686.
- Solaro, R. J., and Rarick, H. M. **1998**. Troponin and tropomyosin: proteins that switch on and tune in the activity of cardiac myofilaments. *Circ Res* 83:471-480.
- Spronk, C. A. E. M., Linge, J. P., Hilbers, C. W., and Vuister, G. W. **2002**. Improving the quality of protein structures derived by NMR spectroscopy. *J Biomol NMR* 22:281-289.
- Spronk, C. A. E. M., Nabuurs, S. B., Krieger, E., Vriend, G., and Vuister, G. W. **2004**. Validation of protein structures derived by NMR spectroscopy. *Prog Nucl Mag Res Sp* 45:315-337.
- Spyracopoulos, L., Gagne, S., Li, M., and Sykes, B. **1998**. Dynamics and thermodynamics of the regulatory domain of human cardiac troponin C in the apo- and calcium-saturated states. *Biochemistry* 37:18032-18044.
- Sunnerhagen, M., Olah, G. A., Stenflo, J., Forsen, S., Drakenberg, T., and Trehwella, J. **1996**. The relative orientation of Gla and EGF domains in coagulation factor X is altered by Ca<sup>2+</sup> binding to the first EGF domain. A combined NMR small angle X-ray scattering study. *Biochemistry* 35:11547-11559.
- Tan, A., and Henzl, M. T. **2009**. Evidence for a Ca<sup>2+</sup>-Specific Conformational Change in Avian Thymic Hormone, a High-Affinity beta-Parvalbumin. *Biochemistry* 48:3936-3945.
- Terwilliger, T. C., Stuart, D., and Yokoyama, S. **2009**. Lessons from Structural Genomics. *Ann Rev Biophys* 38:371-383.
- Tjandra, N., Szabo, A., and Bax, A. **1996**. Protein backbone dynamics and N-15 chemical shift anisotropy from quantitative measurement of relaxation interference effects. *Journal of the American Chemical Society* 118:6986-6991.
- Tjandra, N., and Bax, A. **1997**. Direct measurement of distances and angles in biomolecules by NMR in a dilute liquid crystalline medium. *Science* 278:1111-1114.
- Tollinger, M., Skrynnikov, N. R., Mulder, F. A., Forman-Kay, J. D., and Kay, L. E. **2001**. Slow dynamics in folded and unfolded states of an SH3 domain. *J Am Chem Soc* 123:11341-11352.
- Tolman, J. R., Flanagan, J. M., Kennedy, M. A., and Prestegard, J. H. **1995**. Nuclear magnetic dipole interactions in field-oriented proteins: information for structure determination in solution. *P Natl Acad Sci Usa* 92:9279-9283.
- Tóth, A., Kiss, L., Varró, A., and Nánási, P. P. **2009**. Potential therapeutic effects of Na<sup>+</sup>/Ca<sup>2+</sup> exchanger inhibition in cardiac diseases. *Curr Med Chem* 16:3294-3321.
- Tugarinov, V., Sprangers, R., and Kay, L. E. **2004**. Line narrowing in methyl-TROSY using zero-quantum H-1-C-13 NMR spectroscopy. *J Am Chem Soc* 126:4921-4925.
- Tugarinov, V., Choy, W. Y., Orekhov, V. Y., and Kay, L. E. **2005**. Solution NMR-derived global fold of a monomeric 82-kDa enzyme. *P Natl Acad Sci Usa* 102:622-627.
- Tycko, R. **2006**. Characterization of amyloid structures at the molecular level by solid state nuclear magnetic resonance spectroscopy. *Method Enzymol* 413:103-122.
- Ulrich, E. L., Akutsu, H., Doreleijers, J. F., Harano, Y., Ioannidis, Y. E., Lin, J., Livny, M., Mading, S., Maziuk, D., Miller, Z., Nakatani, E., Schulte, C. F., Tolmie, D. E., Wenger, R. K., Yao, H., and Markley, J. L. **2008**. BioMagResBank. *Nucleic Acids Res* 36:D402-D408.
- Valafar, H., and Prestegard, J. H. **2004**. REDCAT: a residual dipolar coupling analysis tool. *J Magn Reson*

- 167:228-241.
- Vallurupalli, P., Hansen, D. F., and Kay, L. E. 2008. Probing structure in invisible protein states with anisotropic NMR chemical shifts. *J Am Chem Soc* 130:2734-2735.
- Van Zijl, P., Sukumar, S., Johnson, M., Webb, P., and Hurd, R. 1994. Optimized shimming for high-resolution nmr using 3-dimensional image-based field-mapping. *J Magn Reson Ser A* 111:203-207.
- Vranken, W. F., Boucher, W., Stevens, T. J., Fogh, R. H., Pajon, A., Llinas, P., Ulrich, E. L., Markley, J. L., Ionides, J., and Laue, E. D. 2005. The CCPN data model for NMR spectroscopy: Development of a software pipeline. *Proteins* 59:687-696.
- Vriend, G. 1990. WHAT IF: a molecular modeling and drug design program. *J Mol Graph* 8:52-56.
- Vuister, G. W., Clore, G. M., Gronenborn, A. M., Powers, R., Garrett, D., Tschudin, R., and Bax, A. 1993. Increased resolution and improved spectral quality in 4-Dimensional C-13/C-13-separated HMQC-NOESY-HMQC spectra using pulsed field gradients. *J Magn Reson Ser B* 101:210-213.
- Vuister, G. W., Tessari, M., Karimi-Nejad, Y., and Whitehead, B. 1999. Pulse Sequences for Measuring Coupling Constants. *Biological Magnetic Resonance* 16:195-257.
- Wang, B., Wang, Y., and Wishart, D. S. 2010. A probabilistic approach for validating protein NMR chemical shift assignments. *J Biomol NMR* 47:85-99.
- Wang, J., Zhang, X. Q., Ahlers, B. A., Carl, L. L., Song, J., Rothblum, L. I., Stahl, R. C., Carey, D. J., and Cheung, J. Y. 2006. Cytoplasmic tail of phospholemman interacts with the intracellular loop of the cardiac Na<sup>+</sup>/Ca<sup>2+</sup> exchanger. *J Biol Chem* 281:32004-32014.
- Wang, J., Zuo, X., Yu, P., Byeon, I.-J. L., Jung, J., Wang, X., Dyba, M., Seifert, S., Schwieters, C. D., Qin, J., Gronenborn, A. M., and Wang, Y.-X. 2009. Determination of Multicomponent Protein Structures in Solution Using Global Orientation and Shape Restraints. *J Am Chem Soc* 131:10507-10515.
- Wang, L., and Markley, J. L. 2009. Empirical correlation between protein backbone N-15 and C-13 secondary chemical shifts and its application to nitrogen chemical shift re-referencing. *J Biomol NMR* 44:95-99.
- Wei, S. K., Quigley, J. F., Hanlon, S. U., O'Rourke, B., and Haigney, M. C. P. 2002. Cytosolic free magnesium modulates Na/Ca exchange currents in pig myocytes, p. 334-340. *Cardiovasc Res*, vol. 53.
- Williamson, M. P., and Craven, C. J. 2009. Automated protein structure calculation from NMR data. *J Biomol NMR* 43:131-143.
- Wishart, D. S., Sykes, B. D., and Richards, F. M. 1992. The chemical shift index: a fast and simple method for the assignment of protein secondary structure through NMR spectroscopy. *Biochemistry* 31:1647-1651.
- Wishart, D. S., Bigam, C. G., Yao, J., Abildgaard, F., Dyson, H. J., Oldfield, E., Markley, J. L., and Sykes, B. D. 1995. 1H, 13C and 15N chemical shift referencing in biomolecular NMR. *J Biomol NMR* 6:135-140.
- Wright, N. T., Varney, K. M., Ellis, K. C., and Markowitz, J. 2005. The Three-dimensional Solution Structure of Ca<sup>2+</sup>-bound S100A1 as Determined by NMR spectroscopy. *J Mol Biol*.
- Wu, B., Petersen, M., Girard, F., Tessari, M., and Wijmenga, S. S. 2006. Prediction of molecular alignment of nucleic acids in aligned media. *J Biomol NMR* 35:103-115.
- Wu, M., Wang, M., Nix, J., Hryshko, L. V., and Zheng, L. 2009. Crystal Structure of CBD2 from the Drosophila Na<sup>+</sup>/Ca<sup>2+</sup> Exchanger: Diversity of Ca<sup>2+</sup> Regulation and Its Alternative Splicing Modification. *J Mol Biol* 387:104-112.
- Wu, M., Le, H. D., Wang, M., Yurkov, V., Omelchenko, A., Hnatowich, M., Nix, J., Hryshko, L. V., and Zheng, L. 2010. Crystal Structures of Progressive Ca<sup>2+</sup> Binding States of the Ca<sup>2+</sup> Sensor Ca<sup>2+</sup> Binding Domain 1 (CBD1) from the CALX Na<sup>+</sup>/Ca<sup>2+</sup> Exchanger Reveal Incremental Conformational Transitions. *J Biol Chem* 285:2554-2561.
- Wu, M., Tong, S., Gonzalez, J., Jayaraman, V., Spudich, J. L., and Zheng, L. 2011. Structural Basis of the Ca(2+) Inhibitory Mechanism of Drosophila Na(+)/Ca(2+) Exchanger CALX and Its Modification by Alternative Splicing. *Structure* 19:1509-1517.
- Wüthrich, K. 2003. NMR studies of structure and function of biological macromolecules (Nobel Lecture). *Angew Chem Int Edit* 42:3340-3363.
- Yamniuk, A. P., and Vogel, H. J. 2005. Calcium- and magnesium-dependent interactions between calcium- and



- integrin-binding protein and the integrin alpha IIb cytoplasmic domain. *Protein Sci* 14:1429-1437.
- Yamniuk, A. P., Gifford, J. L., Linse, S., and Vogel, H. J. 2008. Effects of metal-binding loop mutations on ligand binding to calcium- and integrin-binding protein 1. Evolution of the EF-hand. *Biochemistry* 47:1696-1707.
- Yanagisawa, Y., Nakagome, H., Hosono, M., Hamada, M., Kiyoshi, T., Hobo, F., Takahashi, M., Yamazaki, T., and Maeda, H. 2008. Towards beyond-1 GHz solution NMR: Internal H-2 lock operation in an external current mode. *J Magn Reson* 192:329-337.
- Yang, D., and Kay, L. 1999. TROSY triple-resonance four-dimensional NMR spectroscopy of a 46 ns tumbling protein. *J Am Chem Soc* 121:2571-2575.
- Yao, J., Chung, J., Eliezer, D., Wright, P. E., and Dyson, H. J. 2001. NMR structural and dynamic characterization of the acid-unfolded state of apomyoglobin provides insights into the early events in protein folding. *Biochemistry* 40:3561-3571.
- Yee, A., Gutmanas, A., and Arrowsmith, C. H. 2006. Solution NMR in structural genomics. *Curr Opin Struct Biol* 16:611-617.
- Zamparelli, C., Macquaide, N., Colotti, G., Verzili, D., Seidler, T., Smith, G. L., and Chiancone, E. 2010. Activation of the cardiac Na<sup>+</sup>-Ca<sup>2+</sup> exchanger by sorcin via the interaction of the respective Ca<sup>2+</sup>-binding domains. *J Mol Cell Cardiol* 49:132-141.
- Zhou, M. M., Ravichandran, K. S., Olejniczak, E. F., Petros, A. M., Meadows, R. P., Sattler, M., Harlan, J. E., Wade, W. S., Burakoff, S. J., and Fesik, S. W. 1995. Structure and ligand recognition of the phosphotyrosine binding domain of Shc. *Nature* 378:584-592.
- Zhou, P., Lugovskoy, A. A., and Wagner, G. 2001. A solubility-enhancement tag (SET) for NMR studies of poorly behaving proteins. *J Biomol NMR* 20:11-14.
- Zhou, P., and Wagner, G. 2010. Overcoming the solubility limit with solubility-enhancement tags: successful applications in biomolecular NMR studies. *J Biomol NMR* 46:23-31.
- Zimmerman, D. E., Kulikowski, C. A., Huang, Y. P., Feng, W. Q., Tashiro, M., Shimotakahara, S., Chien, C. Y., Powers, R., and Montelione, G. T. 1997. Automated analysis of protein NMR assignments using methods from artificial intelligence. *J Mol Biol* 269:592-610.
- Züger, S., and Iwai, H. 2005. Intein-based biosynthetic incorporation of unlabeled protein tags into isotopically labeled proteins for NMR studies. *Nat Biotechnol* 23:736-740.
- Zuiderweg, E. R., and Fesik, S. W. 1989. Heteronuclear three-dimensional NMR spectroscopy of the inflammatory protein C5a. *Biochemistry* 28:2387-2391.
- Zweckstetter, M., and Bax, A. 2000. Prediction of sterically induced alignment in a dilute liquid crystalline phase: Aid to protein structure determination by NMR. *J Am Chem Soc* 122:3791-3792.
- Zweckstetter, M. 2008. NMR: prediction of molecular alignment from structure using the PALES software. *Nat Protoc* 3:679-690.

# 8

## Summary

The  $\text{Na}^+/\text{Ca}^{2+}$ -exchanger (NCX) has a crucial role in  $\text{Ca}^{2+}$  homeostasis (**Chapter 1**). The NCX is a plasma membrane protein and exploits the large  $\text{Na}^+$  gradient over the plasma membrane to catalyze  $\text{Ca}^{2+}$  extrusion.  $\text{Ca}^{2+}$  carefully regulates the NCX and the allosteric activation is exclusively ascribed to binding of  $\text{Ca}^{2+}$  to two cytosolic  $\text{Ca}^{2+}$ -binding domains (CBD1 and CBD2). This thesis presents a biophysical study of CBD2. The goal of this study was to understand the structural and dynamical effects of  $\text{Ca}^{2+}$  binding on CBD2 and the role of  $\text{Mg}^{2+}$  in the  $\text{Ca}^{2+}$ -binding process. This thesis also presents a new CBD2 structure of the third NCX isoform and compares the  $\text{Ca}^{2+}$ -binding domains with other  $\text{Ca}^{2+}$ -binding proteins.

Nuclear Magnetic Resonance (NMR) is an essential tool to study the structure and dynamics of proteins in solution. **Chapter 2** introduces the basic physical principles of NMR spectroscopy and the steps required for protein structure determination. In addition, the use of NMR to study protein dynamics and protein-ligand interactions is explained.

In **Chapter 3** the detailed mechanisms of  $\text{Ca}^{2+}$  binding to NCX1-CBD2 are explored by  $^{15}\text{N}$  relaxation rate measurements and  $\text{Ca}^{2+}$ -induced chemical shift perturbations (CSP). NCX1-CBD2-AD has two  $\text{Ca}^{2+}$ -binding sites. The chemical shift data indicate highly similar  $\text{Ca}^{2+}$  affinities for both sites, even though the primary site has six coordinating carboxylates and the secondary site only two. The structural changes in CBD2-AD upon  $\text{Ca}^{2+}$  binding are small, but significant CSP effects are observed up to 20 Å away. The NCX1-CBD2-AD  $\text{Ca}^{2+}$ -induced CSP values are compared with CSP values from seven other  $\text{Ca}^{2+}$ -binding proteins. This analysis revealed large differences in CSP values between different protein folds. The  $^{15}\text{N}$ -relaxation data of CBD2-BD,  $\text{Ca}^{2+}$ -bound CBD2-AD and apo CBD2-AD were used to determine overall tumbling and local backbone motion of these domains. For all three forms CBD2 the overall tumbling is best described by an axial symmetric diffusion tensor. In addition, the relaxation data of CBD2-AD show the  $\text{Ca}^{2+}$ -coordinating loops to be more rigid in the  $\text{Ca}^{2+}$ -bound state. The equivalent loops of the CBD2-BD splice variant do not bind  $\text{Ca}^{2+}$  and are much more dynamic relative to both the  $\text{Ca}^{2+}$ -bound and apo form of CBD2-AD. Interestingly, differences in local backbone motion between apo and  $\text{Ca}^{2+}$ -bound form of CBD2-AD are not only observed in the  $\text{Ca}^{2+}$ -coordinating loops, but also in the FG-loop at the opposite side of the domain. The chemical shift and relaxation data together indicate that the  $\text{Ca}^{2+}$ -binding event is felt throughout the molecule. The data suggests an important role for the FG-loop in connecting the  $\text{Ca}^{2+}$ -binding event of CBD2 with the other cytosolic domains of the NCX.

The intracellular  $\text{Mg}^{2+}$  concentration ( $\sim 0.5$  mM) is very high compared to the

cytosolic  $\text{Ca}^{2+}$  concentration ( $\sim 100$  nM). Many  $\text{Ca}^{2+}$ -binding proteins are known to bind  $\text{Mg}^{2+}$  under physiological conditions and NCX activity is affected by high intracellular  $\text{Mg}^{2+}$  concentration. **Chapter 4** describes the  $\text{Mg}^{2+}$ -binding properties of NCX1-CBD2-AD. The NMR, circular dichroism, isothermal titration calorimetry and mutagenesis data show that CBD2-AD binds  $\text{Mg}^{2+}$  at both sites, but with significantly different affinities. The secondary  $\text{Ca}^{2+}$ -binding site is preferred by  $\text{Mg}^{2+}$  and has the highest affinity ( $K_D \sim 15$   $\mu\text{M}$ ), whereas the primary  $\text{Ca}^{2+}$ -binding site has a much lower affinity for  $\text{Mg}^{2+}$  ( $K_D \sim 300$ – $800$   $\mu\text{M}$ ). The results from the  $\text{Mg}^{2+}/\text{Ca}^{2+}$ -competition experiments show replacement of  $\text{Mg}^{2+}$  by  $\text{Ca}^{2+}$  only at the primary binding site. Furthermore,  $\text{Mg}^{2+}$ -binding affects the affinity for  $\text{Ca}^{2+}$  and stabilizes the domain. Finally,  $\text{Mg}^{2+}$ -induced chemical shift perturbations and  $^{15}\text{N}$ -relaxation data reveal the  $\text{Mg}^{2+}$ -bound CBD2 form to adopt a state intermediate between the apo and fully  $\text{Ca}^{2+}$ -loaded forms.

**Chapter 5** presents a solution structure of NCX3-CBD2-B in the  $\text{Ca}^{2+}$ -bound form. The solution structure of NCX3-CBD2-B displays the Calx- $\beta$  fold and is homologous to NCX1-CBD2-AD. These results show that the  $\beta$ -bulges in the  $\beta$ -sandwich and the  $\alpha$ -helix in the otherwise unstructured FG-loop are conserved within the different isoforms of the exchanger. Using residual dipolar couplings (RDCs) the orientation of the  $\alpha$ -helix with respect to the  $\beta$ -sandwich is determined. The  $\alpha$ -helix is oriented almost co-axial with the longitudinal axis of the  $\beta$ -sandwich. This orientation differs from the previously reported structure of NCX1-CBD2-AD in which the  $\alpha$ -helix is oriented perpendicular to the  $\beta$ -sandwich. However, the NMR structure of NCX1-CBD2-AD was determined without the usage of RDC restraints, which could explain these differences. Finally, recent studies show that this  $\alpha$ -helix is part of the CBD1-CBD2 interface and influences the  $\text{Ca}^{2+}$ -binding sites of CBD1. This study shows that the conformation of the  $\alpha$ -helix in NCX3-CBD2-B is more likely to represent a biologically relevant conformation than the helix orientation reported for NCX1-CBD2-AD.

The elucidation of the CBD1 and CBD2 structures greatly enhanced the understanding of NCX regulation. It allowed *in vitro* studies of the dynamics of CBD1 and CBD2, as well as studies of the kinetics and thermodynamics of  $\text{Ca}^{2+}$ -binding. **Chapter 6** gives a structural explanation for the different  $\text{Ca}^{2+}$  binding affinities of the various CBD variants and reviews the fold of the domains in relation to other homologous structures. It concludes with recent results on CBD1-CBD2 inter-domain interactions.



# 9

## **Samenvatting**

Calcium ( $\text{Ca}^{2+}$ ) is een belangrijk signaalmolecuul betrokken bij verschillende cellulaire processen, zoals spiercontractie en neuronale activiteit. Geholpen door verschillende membraaneiwitten stroomt  $\text{Ca}^{2+}$  continu in en uit de cel. De natrium/calcium exchanger (NCX) speelt een belangrijke rol bij het verwijderen van  $\text{Ca}^{2+}$  uit de cel. Dit is energetisch ongunstig omdat de  $\text{Ca}^{2+}$ -concentratie buiten de cel vele malen hoger is dan binnen de cel. Voor de energie die nodig is voor het verwijderen van  $\text{Ca}^{2+}$  gebruikt de NCX natrium ( $\text{Na}^+$ ). Net zoals voor  $\text{Ca}^{2+}$  is de concentratie van  $\text{Na}^+$  hoog buiten en laag binnen de cel. De NCX gebruikt deze  $\text{Na}^+$ -gradiënt voor de uitwisseling (exchange) van  $\text{Na}^+$  met  $\text{Ca}^{2+}$ .  $\text{Na}^+$  stroomt naar binnen en  $\text{Ca}^{2+}$  stroomt naar buiten, vergelijkbaar met een windmolen die dankzij de wind water uit de polder omhoog de boezem in pompt.

De activiteit van de NCX wordt strikt gereguleerd door  $\text{Ca}^{2+}$  en  $\text{Na}^+$  (**hoofdstuk 1**). Een verhoogde intracellulaire  $\text{Ca}^{2+}$ -concentratie activeert de NCX, terwijl verhoogde  $\text{Na}^+$ -concentraties de NCX juist inactieveert. De activatie gebeurt via twee  $\text{Ca}^{2+}$ -bindende domeinen (CBD1 en CBD2), onderdeel van de NCX. De  $\text{Ca}^{2+}$  gebonden aan CBD1 en CBD2 wordt niet getransporteerd en CBD1 en CBD2 fungeren alleen als  $\text{Ca}^{2+}$ -sensor. Dit proefschrift is een biofysische studie naar CBD2. Het doel van deze studie was inzicht verkrijgen in de structurele en dynamische effecten van de  $\text{Ca}^{2+}$ -binding aan CBD2 en de rol van  $\text{Mg}^{2+}$  in de  $\text{Ca}^{2+}$ -bindingsproces. Dit proefschrift beschrijft ook een nieuwe CBD2 structuur van de derde NCX isovorm en vergelijkt de  $\text{Ca}^{2+}$ -bindende domeinen met andere  $\text{Ca}^{2+}$ -bindende eiwitten.

Om de structuur en dynamica van eiwitten te kunnen bestuderen is Nucleaire Magnetische Resonantie (NMR) essentieel. **Hoofdstuk 2** beschrijft de fundamentele fysische principes van NMR en de stappen die nodig zijn om een eiwitstructuur te bepalen. Daarnaast worden verschillende aanvullende NMR technieken uitgelegd, zoals  $^{15}\text{N}$ -relaxatiemetingen en chemical shift perturbations (CSP), alsmede hoe deze gebruikt kunnen worden voor het bestuderen van eiwitdynamiek en eiwit-ligand interacties.

In **hoofdstuk 3** is de precieze werking van de  $\text{Ca}^{2+}$ -binding aan NCX1-CBD2-AD onderzocht met  $^{15}\text{N}$ -relaxatie- en CSP-metingen. NCX1-CBD2-AD heeft twee  $\text{Ca}^{2+}$ -bindingsplaatsen. De CSP-data laten zien dat de  $\text{Ca}^{2+}$ -affiniteit voor beide sites vergelijkbaar is. Dit is verrassend, omdat de primaire bindingsplaats zes coördinerende carboxylgroepen heeft en de secundaire bindingsplaats slechts twee. De structurele veranderingen in CBD2-AD als gevolg van de  $\text{Ca}^{2+}$ -binding zijn klein, maar significante CSP effecten worden waargenomen tot op 20 Å van de  $\text{Ca}^{2+}$ -bindingsplaats. Ter vergelijking hebben we de  $\text{Ca}^{2+}$ -geïnduceerde CSP waarden van zeven andere  $\text{Ca}^{2+}$ -bindende eiwitten geanalyseerd.

seerd. Deze analyse toont aan dat de CSP-waarden sterk verschillen en dat NCX1-CBD2-AD relatief kleine CSP-waarden heeft.

Naast chemical shift-effecten is er in **hoofdstuk 3** ook gekeken naar dynamische verschillen tussen NCX1-CBD2-BD, Ca<sup>2+</sup>-gebonden NCX1-CBD2-AD en apo NCX1-CBD2-AD. De <sup>15</sup>N-relaxatiedata laten zien dat de globale beweging van de drie eiwitten het best beschreven wordt door een axiaal symmetrische diffusie tensor. Tevens laat de data zien dat de eiwitketen meer rigide wordt door Ca<sup>2+</sup>-binding. In NCX1-CBD2-BD, een variant die geen Ca<sup>2+</sup> bindt, is de eiwitketen veel dynamischer dan zowel de Ca<sup>2+</sup>-gebonden als de apo vorm van NCX1-CBD2-AD. Verschillen tussen de Ca<sup>2+</sup>-gebonden en apo structuur van NCX1-CBD2-AD en tussen NCX1-CBD2-AD and NCX1-CBD2-BD zijn niet alleen gevonden vlakbij de Ca<sup>2+</sup>, maar ook in de zogenoemde FG-loop aan de andere kant van het domein. Dit geeft aan dat de Ca<sup>2+</sup>-binding gevoeld wordt door het gehele domein en suggereert een belangrijke rol voor de FG-loop in het doorgeven van de Ca<sup>2+</sup> binding in CBD2 naar de andere cytosolische domeinen.

De intracellulaire Mg<sup>2+</sup>-concentratie (~ 0.5 mM) is zeer hoog in vergelijking met de intracellulaire Ca<sup>2+</sup>-concentratie (~ 100 nM). Het is bekend dat veel Ca<sup>2+</sup>-bindende eiwitten onder deze fysiologische omstandigheden Mg<sup>2+</sup> binden. Eveneens is bekend dat NCX activiteit wordt beïnvloed door een hoge intracellulaire Mg<sup>2+</sup>-concentratie. **Hoofdstuk 4** beschrijft de Mg<sup>2+</sup>-binding van NCX1-CBD2-AD. De NMR, CD, ITC en mutagenese data laten zien dat CBD2-AD Mg<sup>2+</sup> bindt op beide Ca<sup>2+</sup>-bindingsplaatsen, maar met significant verschillende affiniteiten. De secundaire Ca<sup>2+</sup>-bindingsplaats heeft de hoogste affiniteit voor Mg<sup>2+</sup> ( $K_D \sim 15 \mu\text{M}$ ), terwijl de primaire Ca<sup>2+</sup>-bindingsplaats een veel lagere affiniteit heeft ( $K_D \sim 300$  tot  $800 \mu\text{M}$ ). De resultaten van de Mg<sup>2+</sup>/Ca<sup>2+</sup>-competitie-experimenten tonen aan dat Mg<sup>2+</sup> alleen op de primaire bindingsplaats kan worden verdrongen door Ca<sup>2+</sup>. Tevens laten de resultaten zien dat Mg<sup>2+</sup> de affiniteit voor Ca<sup>2+</sup> verandert en het domein stabiliseert. Tot slot, de Mg<sup>2+</sup>-geïnduceerde CSP- en de <sup>15</sup>N-relaxatiedata geven aan de Mg<sup>2+</sup>-gebonden NCX1-CBD2-AD een toestand aanneemt intermediair tussen de apo en de Ca<sup>2+</sup>-gebonden structuur.

**Hoofdstuk 5** beschrijft de structuur van NCX3-CBD2-B in de Ca<sup>2+</sup>-gebonden vorm. De structuur heeft een Calx- $\beta$  vouwing en is homoloog aan NCX1-CBD2-AD. Deze structuur toont aan dat de  $\beta$ -bulges in de  $\beta$ -sandwich en de  $\alpha$ -helix in de verder ongestructureerde FG-loop geconserveerd zijn binnen de verschillende isovormen van de exchanger. Met behulp van Residual Dipolar Couplings (RDC) is de oriëntatie van de  $\alpha$ -helix ten opzichte van de  $\beta$ -sandwich bepaald. De helixoriëntatie is bijna co-axiaal



met de longitudinale as van de  $\beta$ -sandwich. Dit is een groot verschil met de helixoriëntatie in NCX1-CBD2-AD. In dit domein is de oriëntatie van de  $\alpha$ -helix vrijwel loodrecht ten opzichte van de  $\beta$ -sandwich. Echter de structuur van deze isovorm is bepaald zonder RDC-metingen, wat het verschil tussen de isovormen zou kunnen verklaren. Recente studies laten zien dat de  $\alpha$ -helix een belangrijk onderdeel vormt in de koppeling tussen CBD1 en CBD2 en de  $\text{Ca}^{2+}$ -bindingsplaatsen van CBD1 beïnvloedt. De  $\alpha$ -helixoriëntatie in NCX3-CBD2-B is waarschijnlijk de biologisch relevante oriëntatie in tegenstelling tot die van NCX1-CBD2-AD.

Het begrip over NCX-regulatie is sterk verbeterd dankzij de structuuropheldering van CBD1 en CBD2. Hierdoor was het mogelijk om de dynamica domeinen *in vitro* te bestuderen, alsmede de kinetiek en thermodynamica van de  $\text{Ca}^{2+}$ -binding. **Hoofdstuk 6** geeft een structurele verklaring voor de verschillen in  $\text{Ca}^{2+}$ -affiniteiten van de verschillende CBD varianten en geeft een overzicht van de structuur van de domeinen in relatie tot andere homologe structuren. Tot slot worden de laatste bevindingen over de CBD1-CBD2 interdomein interacties beschreven.

# 10

## Epilogue

## Dankwoord

Het geeft me ontzettend veel voldoening dat mijn proefschrift bijna af is en dat ik dit dankwoord mag schrijven. Maar zonder de hulp en aanmoediging van velen, zou ik nooit op dit punt zijn aangekomen.

Geerten, bedankt! Een betere begeleider en promotor heb ik mij niet kunnen wensen. Je had veel tijd voor mij: om resultaten te bespreken, achter de spectrometer te zitten, teksten te corrigeren, enzovoorts. Maar bovenal wil ik je bedanken voor het gevoel dat je gaf een gedeeld doel te hebben, namelijk dit proefschrift. Ik wens je heel veel succes in Leicester en wens je nog vele succesvolle promovendi toe.

I would also like to thank dr. Mark Hilge. You started the NCX project in Nijmegen, without it this thesis would look completely different. You are a dedicated and persistent researcher and I admire your ability to come up with new concepts and ideas. It's a pity you left Nijmegen.

Het produceren van (gelabelde) eiwitten is een vak op zich en ik bedank Jan Aelen ervoor mij de beginselen ervan te leren. Nog meer labondersteuning heb ik gekregen van Nathalie en Nicole. Het is ondanks het gebrek aan zwarte weegschoentjes toch nog goed gekomen. Bedankt voor alle Schwung®!

Gedurende mijn promotie heb ik een viertal bachelor- en masterstudenten begeleid. Ik heb zonder uitzondering ook veel van jullie geleerd. Patty, Michiel, Albert en Wouter, bedankt voor jullie inzet en veel succes met het vervolg van jullie carrière. En dan wil ik uiteraard nog alle andere collega's van de afdeling bedanken. Nadia en Jurgen bedankt voor jullie interesse in mijn project en natuurlijk de goede sfeer op het lab. Sanne, bedankt voor je goede discussies, het was fijn dat ik niet meer de enige was op het NCX- project en ik vond het jammer toen je weer vertrok. Fedir, although we only worked together for less than a year, it was nice not being the only Ph.D. student for a while and I wish you good luck with your project in Leicester.

Protein Biophysics was niet erg honkvast en als gevolg daarvan heeft mijn bureau op drie verschillende plekken gestaan. Dat had ook zo zijn voordelen, zo kon ik op vier verschillende locaties terecht voor mijn gezeur om toegangspassen, sleutels, post-verzendingen, labjournaals, examenpapier en meer van dat alles. Marian, Maria, Els en Barbara, bedankt voor jullie efficiëntie en voor het feit dit soort zaken altijd tussendoor konden.

Een ander voordeel van op veel plekken werken was dat ik heel veel verschillende collega's van verschillende afdelingen heb leren kennen. Allereerst de mensen van 'deze kant van de weg'. De Mol. Biol. groep Robert, Rike, Joke, Kees-Jan, Arjen, Josephine,

Stephanie, en vele andere, bedankt dat jullie onze afdeling zo gastvrij ontvingen toen wij jullie verdieping introkken. Uiteraard ook Siebe bedankt voor je hulp bij de FPLC en Mark en Nanda, bedankt voor het langdurig uitlenen van de bench! En dan is er nog het CMBI: Christof, Gijs, Valère, Isabel, Radek, Jules, Richard, Robin, John, Gert, Martijn en alle anderen, bedankt voor de fijne omgeving en de vele interessante discussies aan de koffietafel.

Er is natuurlijk ook 'de andere kant van de weg'. Er zijn vele vloeistof- en vaste stof-NMR'ers die ik wil bedanken. Allereerst Jan van Os, voor het mij bijbrengen van de meest elementaire kennis op het gebied van de elektronica en je vaardige hulp als de spectrometer niet functioneerde zoals het hoorde. Jack en Ruud, voor jullie hulp bij het opzetten van nieuwe NMR experimenten, vooral op de nieuwe, nog niet door mij omarmde Bruker. Hans Heus voor het delen van jouw inzichten in kinetiek in het algemeen en Mg<sup>2+</sup>-binding in het bijzonder. De collega-AIO's en post-docs Ard, Marc, Chandrakala, Suresh, Margriet, Paul, Dennis, Jacob, Agnieszka, Ramon, Otmar, Paul, Jorge, voor het delen van de stress, gemopper over mislukte experimenten, maar vooral toch voor de lol bij de filmavonden, (tafel-)voetbal, BBQs en vrijdagmiddagborrels. En dan rest mij nog (in willekeurige volgorde) Marco, Frank, Aafke, Ernst, Sybren, Arno, Jan van Bentum, Anna-Jo, Hans Janssen, Gerrit, alle studenten en ieder die ik vergeten ben, zonder twijfel vormt de NMR-groep de meest de gezellige afdeling binnen het instituut.

Het leven bestaat niet alleen uit werken, alle oud-Oud-Beijerlanders, oud-'t-Gildehuizers en oud-NW'ers bedankt voor jullie interesse en het is fijn zoveel mensen te hebben om mee te ontspannen en plezier te hebben. Arend en Michiel, ik vind het erg leuk dat jullie mijn paranimfen zullen zijn en ik hoop van harte dat we, samen met Bram, nog vele avonden spelspelend zullen doorbrengen. Monique, Frederiek en Ingrid, ik ben er nog niet van overtuigd dat op Brinta niet te sleëen valt en stel voor enkele controleproeven te plannen!

Pap, mam, bedankt voor jullie liefde, aanmoedigingen en onvoorwaardelijke steun. Jullie hebben nooit getwijfeld aan de goede afloop. Joost, Erica, Maaïke, Thomas en Linde, ik ben trots dat ik jullie broer, zwager en oom ben! Bedankt voor jullie niet aflatende interesse in mijn onderzoek en ik ga nog één keer uitleggen wat ik heb gedaan, daarna kunnen jullie het zelf nalezen!

Denise, het is af en zonder jou was het nooit gelukt. Niemand weet beter dan jij hoe moeilijk ik het soms vond. Je gaf me het vertrouwen, maar bovenal, de rust om door te gaan. Ik ben er ontzettend trots op dat we nu allebei klaar zijn en dat we het allebei hebben gehaald. Lieve, ik hou van je!

## Curriculum Vitae

Vincent Breukels werd op 19 november 1982 geboren te Rotterdam. Tot en met zijn achttiende woonde hij in Oud-Beijerland. Daar ging hij naar de RSG Hoeksche Waard, waar hij in 2001 cum laude zijn VWO haalde. Hierna verhuisde hij naar Nijmegen om daar Natuurwetenschappen te studeren aan de Radboud Universiteit. Tijdens zijn eerste stage bij Cellulaire Dierfysiologie onder begeleiding van dr. W.J.J.M. Scheenen was zijn interesse voor ionkanalen gewekt en zocht hij een passend vervolg voor zijn tweede stage. Deze vond hij bij Biofysische Chemie onder begeleiding van dr. G.W. Vuister. Daar maakte hij kennis met NMR en het NCX-project. In 2008 behaalde hij zijn doctoraal examen en begon aansluitend zijn promotieonderzoek in de nieuwe, door prof. dr. G.W. Vuister geleide groep Protein Biophysics. De resultaten van dit onderzoek leidden tot dit proefschrift.

## Publicaties

- Zhang H., Langeslag M., Breukels V., Jenks, B.G., Roubos E.W., Scheenen W.J.J.M. **2008**. Calcium channel kinetics of melanotrope cells in *Xenopus laevis* depend on environmental stimulation. *Gen. Comp. Endocr.* 156: 104-112
- Breukels V., Vuister G.W. **2010**. Binding of calcium is sensed structurally and dynamically throughout the second calcium-binding domain of the sodium-calcium exchanger. *Proteins* 78: 1813-1824
- Breukels V., Konijnenberg A., Nabuurs S.M., Touw W.G., Vuister G.W. **2011**. The second  $\text{Ca}^{2+}$  binding domain of NCX1 binds  $\text{Mg}^{2+}$  with high affinity. *Biochemistry* 50: 8804-8812
- Breukels V., Konijnenberg A, Nabuurs S.M., Doreleijers J.F., Kovalevskaya N.V., Vuister G.W. **2011**. Overview on the use of NMR to examine protein structure. *Curr. Protoc. Protein Sci.* 64: 175.1-175.44
- Breukels V., Touw W.G., Vuister G.W. **2012**. Structural and dynamic aspects of  $\text{Ca}^{2+}$  and  $\text{Mg}^{2+}$  binding of the regulatory domains of the sodium-calcium exchanger. *Biochem. Soc. Trans.* In press
- Breukels V., Touw W.G., Vuister G.W. **2012**. Solution structure of the second  $\text{Ca}^{2+}$ -binding domain of the B variant of the third isoform of the  $\text{Na}^+/\text{Ca}^{2+}$ -exchanger. *Manuscript in preparation*